


**CALCULATION OF PERFORMANCE  
AND CAVITATION CHARACTERISTICS  
OF PROPELLERS INCLUDING EFFECTS  
OF NON-UNIFORM FLOW  
AND VISCOSITY**

**DR. IR. P. VAN OOSSANEN**



**PUBLICATION No. 457  
NETHERLANDS SHIP MODEL BASIN  
WAGENINGEN, THE NETHERLANDS**



CALCULATION OF PERFORMANCE AND CAVITATION  
CHARACTERISTICS OF PROPELLERS INCLUDING  
EFFECTS OF NON-UNIFORM FLOW AND VISCOSITY

Bibliotheek van de Afdeling Scheepsbouw- en Scherphoudende Technische Hogeschool	
DOCUMENTATIE	390-457
DATUM	

TECHNISCHE UNIVERSITEIT DELFT	
BIBLIOTHEEK WERKTUIGBOUWKUNDE/MARITIEME-TECHNIEK	
MEKELWEG 2	
2620 CD DELFT	
STAMNFR. :	
SIGN. :	390-112
AUBID :	1265863
GIRAF :	



# CALCULATION OF PERFORMANCE AND CAVITATION CHARACTERISTICS OF PROPELLERS INCLUDING EFFECTS OF NON-UNIFORM FLOW AND VISCOSITY

BY

DR. IR. P. VAN OOSSANEN

TECHNISCHE UNIVERSITEIT DELFT  
BIBLIOTHEEK WERKTUIGBOUWKUNDE/MARITIEME-TECHNIEK  
MEKELWEG 2  
2625 CD DELFT  
STAMNR. :  
SIGN. : 390/112  
AUCID :  
GRAF :

2443  
512  
5

PUBLICATION No. 457  
NETHERLANDS SHIP MODEL BASIN  
WAGENINGEN, THE NETHERLANDS

Bibliotheek TU Delft



C 0003814577

CONTENTS

CHAPTER 1 . . . . .	9
GENERAL INTRODUCTION	
CHAPTER 2 . . . . .	15
CALCULATION OF RADIAL AND CHORDWISE DISTRIBUTIONS OF LOADING ON PROPELLER BLADES IN NON-UNIFORM FLOW	
2.1 Preliminary Considerations . . . . .	15
2.2 Calculation of Radial Load Distribution. . . . .	19
2.2.1 Effect of Free Vortices. . . . .	19
2.2.2 Effect of Bound Vortices . . . . .	36
2.3 Effect of Circumferential-Varying Inflow . . . . .	39
2.4 Calculation of Chordwise Load (Pressure) Distribution . . . . .	43
2.4.1 Description of Theoretical Procedure . . . . .	43
2.4.2 Application to Propeller Blades. . . . .	50
CHAPTER 3 . . . . .	55
ASSESSMENT OF VISCOSITY EFFECTS ON PROPELLER BLADE SECTION CHARACTERISTICS AND LOADING DISTRIBUTIONS	
3.1 Introductory Remarks . . . . .	55
3.2 Calculation of Two-Dimensional Boundary Layer Characteristics. . . . .	58
3.2.1 The Laminar Boundary Layer and Laminar Separation. . . . .	58
3.2.2 Estimation of Laminar-Turbulent Transition . . . . .	60
3.2.3 The Turbulent Boundary Layer and Turbulent Separation . . . . .	60
3.3 Effect of Viscosity on Lift-Curve Slope and Angle of Zero-Lift . . . . .	63
3.3.1 Lift-Curve Slope . . . . .	63
3.3.2 Angle of Zero-Lift . . . . .	70
3.4 Calculation of Drag Coefficient. . . . .	74
3.5 Effect of Viscosity on Chordwise Pressure Distribution . . . . .	83

CHAPTER 4 . . . . .	86
CALCULATION OF CAVITATION PERFORMANCE OF PROPELLERS	
4.1    General Remarks on Types of Cavitation Occurring on Propeller Blades . . . . .	86
4.2    Method for Assessing Cavitation Inception . . . . .	93
4.3    Calculation of Type and Extent of Cavitation. . . . .	103
4.4    Effect of Cavitation on Propeller Performance . . . . .	111
CHAPTER 5. . . . .	130
RESULTS OF CALCULATIONS AND CORRELATION WITH EXPERIMENT	
5.1    Open-Water Propeller Performance: Differences Between Model and Full Scale. . . . .	130
5.2    Type and Extent of Cavitation: Differences Between Model and Full Scale. . . . .	143
5.3    Effect of Cavitation on Propeller Performance . . . . .	153
CHAPTER 6. . . . .	159
FINAL REMARKS AND CONCLUSIONS	
APPENDIX. . . . .	162
POLYNOMIAL REPRESENTATION OF PROPELLER LIFTING SURFACE CORRECTION FACTORS	
REFERENCES. . . . .	219
NOMENCLATURE. . . . .	238
SUMMARY . . . . .	252
SAMENVATTING. . . . .	255
DANKWOORD . . . . .	257
CURRICULUM VITAE. . . . .	259

CHAPTER 1  
GENERAL INTRODUCTION

For the last 75 years, the screw propeller has been the principal propulsion device applied to ships, whether small or large, slow or fast. From the beginning of this period, propeller designers have been confronted with the phenomenon of cavitation, the possible occurrence of which was first discussed by Euler in 1754 [1-1]\*. Its discovery was through the effect it had on the performance of the propeller; it can cause the rotational propeller speed to increase out of all proportion to the applied torque. This phenomenon (subsequently termed the "racing" of screw propellers) was the subject of some memorable papers by Reynolds [1-3,1-4]. Ever since, cavitation on propellers has been the subject of study of many research workers. This is nearly always performed experimentally in so-called cavitation tunnels after the example of Parsons in 1895 [1-2], who first derived in this way an acceptable propeller configuration for his experimental steam turbine ship "Turbinia" which had to perform at speeds in excess of 30 knots. Parsons found that the occurrence of cavitation set a limit to the amount of developed thrust per unit blade area of the propeller. The first criterion of  $11\frac{1}{2}$  lb per sq. in. for this limit was given by Thornycroft and Barnaby [1-5]. Refined forms of this criterion such as the much-used Burrill chart [1-6] and Keller formula [1-7] are still used in propeller design today. Whereas use of such a criterion will avoid the extreme case of racing of the propeller or thrust breakdown, it has been found that more refined criteria are necessary to avoid other consequences of the occurrence of cavitation.

One of these consequences is damage to the propeller in the form of erosion and bent trailing edges. Parsons and Cook [1-8] in 1918 deduced that the observed "pitting" of the blade surfaces was not a result of corrosion but a consequence of cavitation. A typical example of cavitation erosion is shown in Fig. 1. It has since been verified that a large energy is associated with cavitation bubble collapse which can lead to damage when occurring

\*Numbers in parentheses refer to the references listed on page 219.

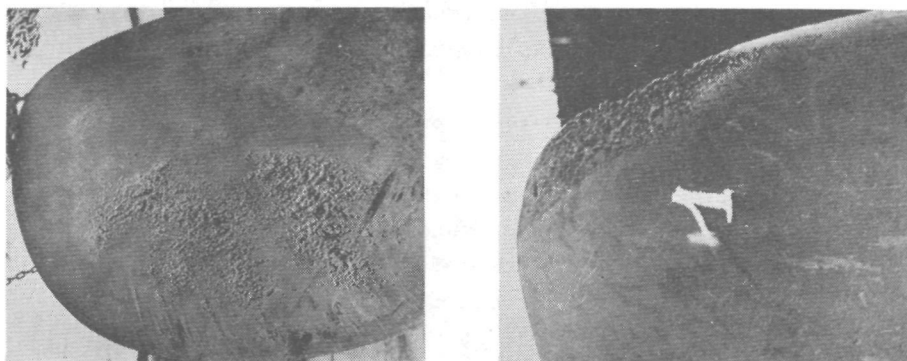


FIG.1 EXAMPLES OF CAVITATION EROSION ON A PROPELLER BLADE.

directly on the blade surface [1-9]. Intense and persistent erosion will sooner or later result in loss of material or even of the loss of a complete propeller blade. Van Manen [1-10] showed that the associated forces, when locally acting in the neighbourhood of the trailing edge, can result in the bending of the trailing edge as shown in Fig. 2.

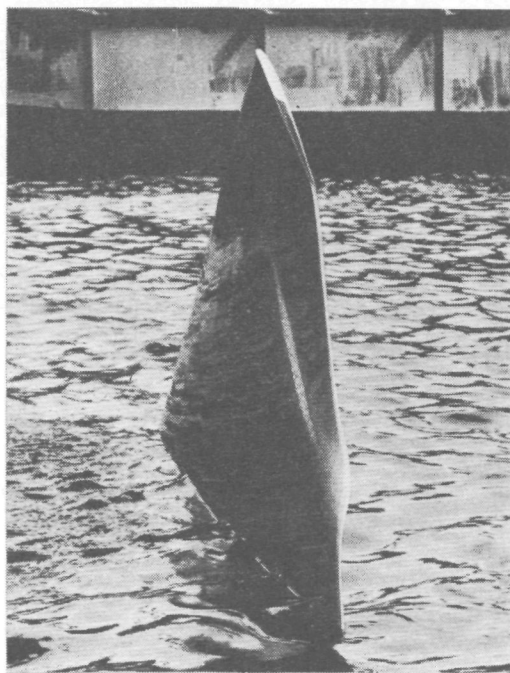


FIG.2 BENT TRAILING EDGE OF PROPELLER BLADE DUE TO CAVITATION.



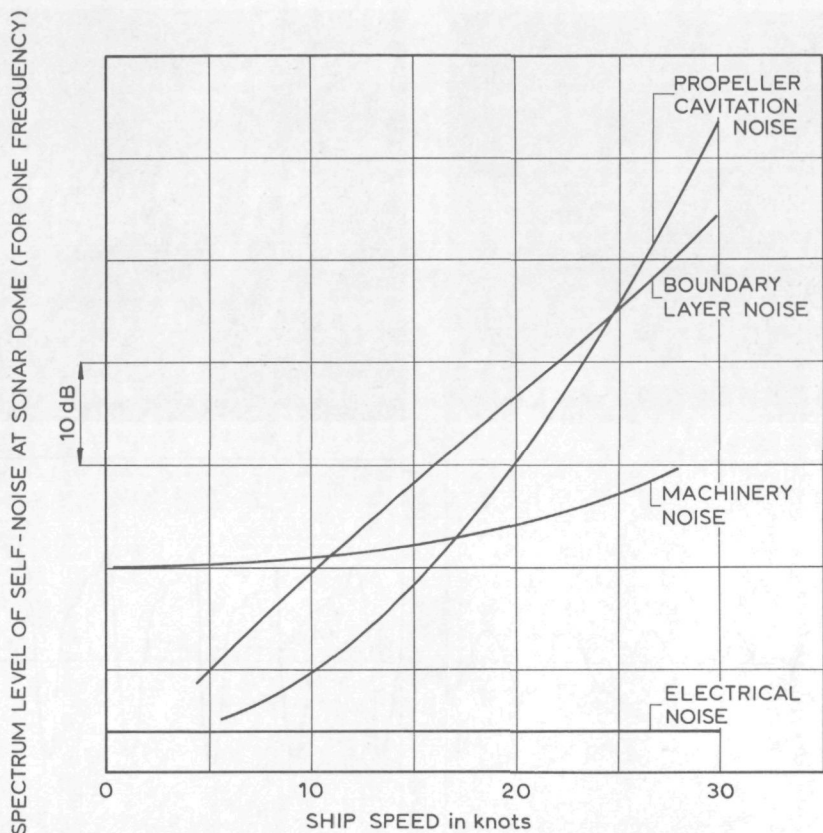


FIG. 3. EXAMPLE OF THE VARIATIONS IN SELF-NOISE AS A FUNCTION OF SHIP SPEED DUE TO PROPELLER, BOUNDARY LAYER AND MACHINERY.

The trend in most ship designs towards higher ship speeds and larger displacements, i.e. towards higher shaft horsepowers, is responsible for the recent study of other detrimental effects of cavitation. These detrimental effects are the noise emitted by a cavitating propeller and the large amplification of propeller-excited hull pressure forces due to cavitation. Studies of this last mentioned effect have been performed by Van Manen [1-11], Huse [1-12], Van Oossanen and Van der Kooy [1-13] and others. Figure 3, taken from Sabathé [1-14], gives an example of the variations in self-noise as a function of ship speed due to propellers, boundary layer and machinery at the sonar dome of a naval vessel. In this figure the relative importance of propeller cavitation noise with respect to boundary layer noise,

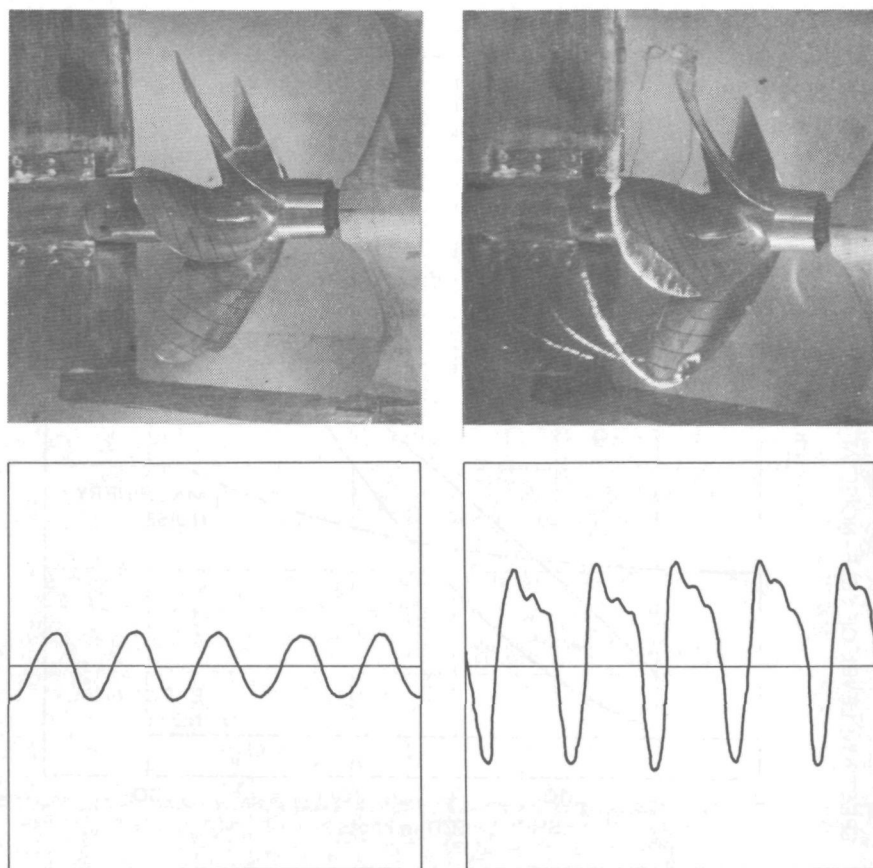


FIG. 4 EXAMPLE OF HULL PRESSURE SIGNAL WITH AND WITHOUT CAVITATION ON PROPELLER.

as represented by the curves, should not be misinterpreted since the propeller is situated relatively far away from the sonar dome while the boundary layer noise is generated directly in the vicinity of the sonar dome. Figure 4, taken from Van Oossanen and Van der Kooy [1-13], gives an example of the increase in hull pressure forces due to cavitation.

To avoid detrimental consequences of cavitation it is now, more than ever, necessary to study experimentally the behaviour of cavitation on propeller models in order to arrive at acceptable cavitation performance. A difficulty which occurs in these experiments is that in order to obtain an adequate simulation of full-scale cavitation behaviour, the wake of the ship in which

the propeller operates must be simulated. Furthermore, the tests to determine the effect of cavitation on propeller-induced hull pressure forces require the inclusion of the ship model in the test set-up. This state of affairs has made it desirable to design and build new cavitation facilities better suited for these tests. For example the Netherlands Ship Model Basin has built a large depressurized towing basin in which the air pressure of the entire facility can be lowered in accordance with the required scaling laws. Other experimental centres have built (or are in the process of building) large free-surface or closed water tunnels. An account of these developments, and some of the motivations for them, has been given by Van Oossanen [1-15].

The increasing difficulties in the design of propeller configurations now urgently requires a theoretical procedure to determine the extent and type of cavitation on propellers. Strictly, such a procedure only needs to be qualitatively correct so that for a particular case the effect of various parameters on the development and formation of cavitation can be assessed, leaving only one or two possible configurations for experimental verification. Moreover, such a theoretical procedure could constitute the starting point for calculations of the effect of cavitation on propeller-hull interaction phenomena. It is this reasoning which has led to more intensive endeavours to derive a suitable calculation method for the determination of the cavitation performance of marine propellers. Attempts to calculate the pressure distribution on propeller blades with the aim of arriving at an assessment of the cavitation properties, such as those of Lockwood-Taylor [1-16], Burrill [1-17], Kafali [1-18] and others, had a number of shortcomings particularly in connection with the actual calculation of cavitation from the approximate pressure distribution. Cavitation was nearly always calculated to occur in that region on the blades where the local value of the pressure is less than the value of the vapour pressure. The more recent approaches of Johnsson [1-19], Holden [1-20] and Johnsson [1-21], constitute an improvement in this regard.

In this thesis, recently obtained results of fundamental cavitation studies on standard bodies are employed to overcome some of the

obstacles still present in the calculation of inception and extent of cavitation. The developed method is practical and straight forward, whereby the complete approach is suitable for engineering applications on an average-size electronic computer. In addition to the performance characteristics and the extent and type of cavitation, the effect of cavitation on thrust, torque and efficiency is considered. Due considerations are given to the effects of viscosity and non-uniform flow. The capabilities of the method are demonstrated by comparing theoretical and experimental results.

CHAPTER 2  
CALCULATION OF RADIAL AND CHORDWISE LOADING  
DISTRIBUTIONS ON PROPELLER BLADES IN NON-UNIFORM FLOW

2.1. Preliminary Considerations

From recent fundamental cavitation studies by Bailey [2-1] and Arakeri [2-2] it has become clear that cavitation inception can be calculated from specific characteristics of the boundary layer. It has also become clear that the change in the performance of lifting surfaces due to cavitation can be calculated from the associated change in the pressure distribution. This has been demonstrated by Van Oossanen [2-3]. To deal with both of these aspects, knowledge of the velocity or pressure distribution over the non-cavitating body is required.

In the case of a screw propeller this means that use must be made of vortex theory in order to determine the relation between the distribution of load or lift on the blade and the associated induced velocities, the so-called downwash. The nature of the present problem of the broad-bladed marine propeller operating in the wake of a ship is such that unsteady lifting surface theory is called for. Yet, in its present stage of development, unsteady lifting surface theory is unsuitable for this purpose. To arrive at numerical solutions it is necessary to linearize the lifting surface equation. Reliable results are hereby only obtained for the lightly loaded propeller for which the shape of the free helical vortex sheets are assumed to be dependent on the undisturbed inflow velocities only. This can be seen from Fig. 5, taken from Kuiper [2-4], in which a comparison is made between experiments and lifting surface theory for the thrust and torque of a propeller of the Wageningen B-series. Most propellers operate at higher loadings, however, for which case the influence of the induced velocities on the pitch of the shed vortex sheets must be included. This is necessary because the directions of a free vortex line or sheet, when not acted on by forces, must assume the direction of the resultant flow at (or just behind) the bound vortices. To overcome this shortcoming of linearization, some lifting surface procedures for the steady case incorporate a lifting line model



of the moderately loaded propeller whereby the correct pitch of the free vortex sheets can be calculated. This was performed by Morgan, Silovic and Denny [2-5], among others.

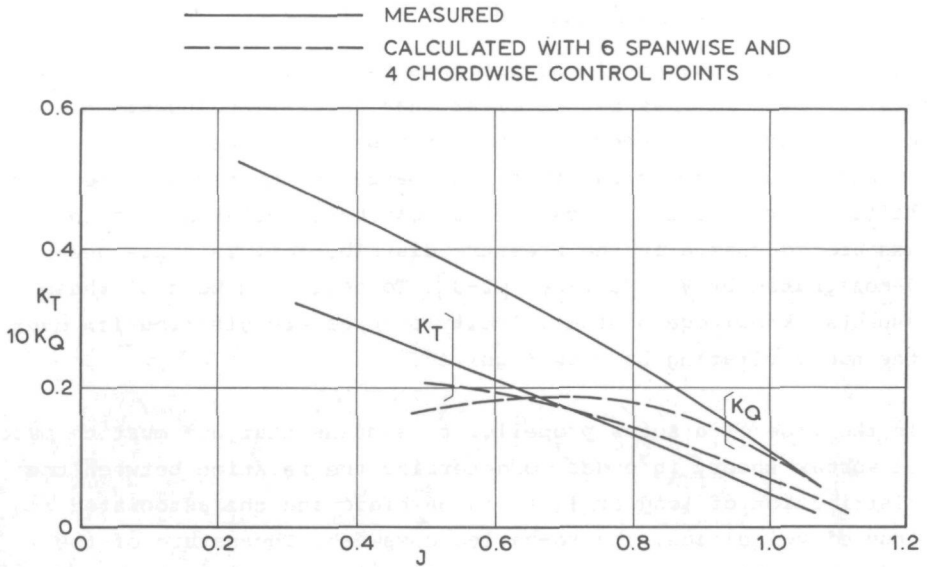


FIG. 5. COMPARISON BETWEEN EXPERIMENTS AND UNSTEADY LIFTING SURFACE THEORY FOR THE MEAN THRUST AND TORQUE OF B3-50 PROPELLER ( $P/D=1.0$ )

In addition, present unsteady lifting surface theories do not include finite thickness effects of the blades whereby the required unsteady pressure distribution on both the back and the face of the blades can be determined. The numerical methods developed at the Stevens Institute of Technology, primarily by Tsakonas [2-6, 2-7, 2-8] and at the Netherlands Ship Model Basin by Verbrugh [2-9], Kuiper [2-10] and Van Gent [2-11], both being representative of the most advanced numerical procedures available, at this time only incorporate blade camber. The amplitude and phase of the pressure difference between face and back of the blades is hereby attained, which is infinite at the leading edge. Finally, the requirement of a long central processor time on all but the largest electronic computers, is a further disadvantage of unsteady lifting surface theory.

Besides steady and unsteady lifting surface theory, another three-dimensional theory is available in the form of a modified Hess and Smith approach [2-12]. In a private communication, Dr. Hess has pointed out that the available program in its present form could be used to calculate the desired flow by inputting all blades and their wakes. He argues, however, that this would be very time-consuming or inaccurate or both, and that a better approach consists in using the fact that in uniform flow (or in a quasi-steady approach for non-uniform flow) all the blades have the same flow fields, the rotational symmetry of which enables use of the symmetry planes of the present theory. The effects of symmetrically placed elements are then added to produce a combined matrix of influence coefficients whose order equals the number of surface elements on a single blade. The only difference from the available program is then that symmetrically placed elements are obtained by rotation instead of by reflection in a plane. Input of only one blade is then required together with its wake. It must be added, however, that the requirement of very large electronic computers to obtain numerical solutions is again a drawback.

Finally, the three-dimensional theory devised by Hoiby [2-13] and used by Holden [2-14] and Johnsson and Sjøntvedt [2-15], based on earlier work by Küchemann and Weber for swept wings [2-16, 2-17], is not refined enough to give more accurate results than a corrected two-dimensional method. This is a consequence of the fact that the assumptions made regarding the distribution of spanwise and chordwise loading, approximately valid for swept wings, can lead to errors when applied to propeller blades.

In a recent study by Johnsson [2-18], it is demonstrated that proper use of an adequate lifting line theory, applied in the quasi-steady sense, can give reliable results for the calculation of the thrust and torque variations experienced by a propeller in a wake for not too high values of the blade area ratio. Such comparisons have also been performed by Tsakonas and Jacobs [2-19], Vedeler [2-20] and very recently by Tanibayashi [2-21] with the same result. In most of these cases the used lifting line theory is rather crude and not refined enough to take into account some

important effects associated with the circumferential variations in the flow into the propeller. One of these is the effect of the varying incidence of the undisturbed flow along the blade section, which effectively changes the blade section camber, as discussed by Kruppa [2-22] and Johnson et al [2-23]. The validity of quasi-steady lifting line theory at high blade area ratios for calculating the variations in thrust and torque is considerably improved when this phenomenon is taken into account. These facts, together with the knowledge that lifting line procedures are extremely versatile, particularly in conjunction with the desire to incorporate viscous effects and the effects of changes in blade section geometry, point to the acceptability of using quasi-steady lifting line theory for the calculation of the circulation distribution along the lifting line and the angle of attack of the resultant inflow at various angular blade positions.

The most rigorous and complete lifting line procedure for the moderately loaded propeller, is the induction factor method developed by Lerbs [2-24]. In its standard form it is adequate to deal with a radially varying wake and a non-optimum radial distribution of the load. For the application of this method in an inverse sense (i.e. to determine induced velocities and circulation distribution when the propeller geometry is given) in a circumferentially varying wake, a number of modifications must be considered. These are presented in the next section.

The lack of a fast and practical procedure for the calculation of the three-dimensional pressure distribution on propeller blades necessitates the use of a two-dimensional approach. This can only lead to satisfactory results when the blade section geometry is effectively distorted and an effective angle of attack is used such that when the pressure difference between back and face of the blade section is integrated over the chord, the three-dimensional value of the lift is obtained. The distortion of blade section geometry may in principle only consist of a decrease of camber to compensate for the effect of the curvature of the induced velocity along the chord and for the decrease in angle of zero lift. This approach is discussed in section 3 of this chapter.

## 2.2 Calculation of Radial Load Distribution

### 2.2.1 Effect of Free Vortices

In lifting line theory of the screw propeller, the blades are presented by vortex lines. The circulation  $\Gamma$  of these vortex or lifting lines are considered to vary with the radial coordinate  $r$ . This variation in  $\Gamma$  prescribes that a free vortex line is shed from the lifting line between the radial stations  $r$  and  $(r+dr)$ , the circulation of which, by Stokes' theorem, is  $d\Gamma/dr$ . The direction of this free vortex line coincides with the direction of the resultant fluid motion behind the lifting line. The assembly of free vortex lines forms a vortex sheet with a general helical surface behind each propeller blade.

The induced velocities caused by this system of trailing vortices must be combined with the undisturbed incoming flow to give the direction of the flow at the lifting line. A change in this flow direction modifies the lift or circulation of the lifting line leading to a change in the strength of the free vortex lines. This will in turn again influence the direction of the incoming flow. This inter-relationship between induced velocities and strength of bound and free vortices makes it necessary in propeller theory to introduce approximations. When the propeller is lightly loaded the influence of the induced velocities of the free vortex sheets on the incoming flow is neglected. In moderately loaded propeller theory this cannot be done and another simplification regarding the shape of the free vortex sheets or the induced velocities is necessary. Betz [2-25] found that when the circulation along the lifting line is such that the kinetic energy within the slipstream is a minimum, the free vortex sheets form true helical sheets with a constant pitch angle. He also found that in this case the resultant of the induced velocities at the propeller is normal to the direction of the vortex sheets. All so-called optimum theories for the moderately loaded propeller in uniform flow such as those of Goldstein [2-26], Lock [2-27], Kramer [2-28] and others, use these results for the form of the free-vortex sheets and the resultant direction of the induced velocities.

In the development of the induction factor method, Lerbs [2-24] only assumes that the free vortex sheets are made up of cylindrical vortex lines, each of constant pitch angle, thereby allowing for a radially varying non-uniform flow and a non-optimum circulation distribution. This method calculates the axial and tangential induced velocities independently and includes the effect of the propeller hub. The lifting lines are considered to be straight, i.e. with no skew or rake. For the calculation of the induced velocities, Lerbs uses the concept of the induction factor as introduced by Kawada [2-29, 2-30]. The induction factor  $I$  represents the ratio of the velocity at a point  $r$  of the lifting line due to the helical vortex  $d\Gamma$  at  $r_0$  and a straight line vortex  $d\Gamma$  at  $r_0$  parallel to the axis. The velocity induced by the straight line vortex is:

$$dU_s = \frac{d\Gamma}{4\pi(r-r_0)} \quad (2-1)$$

where  $dU_s$  is perpendicular to the plane through the free vortex line and the point  $r$  on the lifting line. The velocity induced by the free helical vortex is then:

$$d\bar{U} = \bar{I} \frac{d\Gamma}{dr_0} \frac{dr_0}{4\pi(r-r_0)} \quad (2-2)$$

and the velocity induced by all helical vortices is:

$$\bar{U} = \int_{r_h}^R \bar{I} \frac{d\Gamma}{dr_0} \frac{dr_0}{4\pi(r-r_0)} \quad (2-3)$$

in which  $r_h$  = radius of propeller hub,  
 $R$  = radius of propeller,  
 $\bar{U}$  = induced velocity at  $r$  by all helical vortices,  
and  $\bar{I}$  = induction factor.

On resolving the inflow and induced velocities into axial and tangential components as shown in Fig. 6, and on introducing the non-dimensional value of the radius  $x = r/R$  and the non-dimensional value of the circulation  $G = \Gamma/\pi DV_A$ , where  $V_A$  equals the average



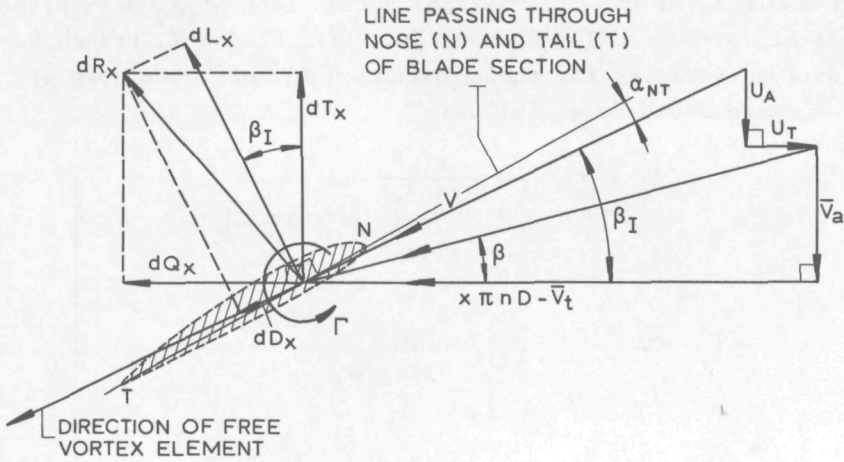


FIG. 6. SCHEME OF VELOCITIES AND FORCES ON PROPELLER BLADE SECTION.

value of the axial inflow velocity over the propeller disc and  $D$  the propeller diameter, the velocity induced by all the free helical vortices at  $x$  is then given by the equations:

$$\frac{U_A}{\bar{V}_A} = \frac{1}{2} \int_{x_h}^1 I_A \frac{dG}{dx_0} \frac{dx_0}{x-x_0} \quad (2-4)$$

$$\text{and } \frac{U_T}{\bar{V}_A} = \frac{1}{2} \int_{x_h}^1 I_T \frac{dG}{dx_0} \frac{dx_0}{x-x_0} \quad (2-5)$$

in which  $U_A, U_T$  = axial and tangential induced velocity at  $x$ ,  
 $I_A, I_T$  = axial and tangential induction factor at  $x$ ,  
 and  $\frac{dG}{dx_0}$  = dimensionless circulation of the free helical vortex at  $x_0$ .

The induction factors  $I_A$  and  $I_T$  are dependent on  $x/x_0$ , on the pitch angle  $\beta_I$  of the free helical vortex line at  $x_0$  and on the number of (symmetrically spaced) propeller blades  $Z$ . Wrench [2-31] has derived formulas for these induction factors. The complete set of expressions is as follows:

$$\left. \begin{aligned} I_A &= (x/x_0 - 1) \frac{Z \cdot A^*}{(\tan \beta_I)} \\ I_T &= (1 - x_0/x) Z(1 + A^*) \end{aligned} \right\} \text{for } x/x_0 > 1$$

$$\left. \begin{aligned} I_A &= \cos \beta_I \\ I_T &= \sin \beta_I \end{aligned} \right\} \text{for } x = x_0$$

$$\left. \begin{aligned} I_A &= (1 - x/x_0) \frac{Z}{(\tan \beta_I)} (1 + B^*) \\ I_T &= (x_0/x - 1) Z B^* \end{aligned} \right\} \text{for } x/x_0 < 1 \quad (2-6)$$

in which  $A^* = f \left[ \frac{1}{u-1} - \frac{1}{24Z} g \cdot \ln \frac{u}{u-1} \right]$

and  $B^* = f \left[ \frac{u}{1-u} + \frac{1}{24Z} g \cdot \ln \frac{1}{1-u} \right]$

where  $f = \sin^{-\frac{1}{2}} \beta_I \cdot p^{-\frac{1}{4}}$

$$g = \sin^3 \beta_I \left[ 2 + \frac{9}{\tan^2 \beta_I} \right] + (3p-5) \cdot p^{-3/2}$$

$$u = \exp \left[ Z \left( \ln \left[ (p^{\frac{1}{2}} - 1) \left( \frac{1}{\sin \beta_I} - 1 \right)^{-1} \cdot x_0/x \right] + p^{\frac{1}{2}} - \frac{1}{\sin \beta_I} \right) \right]$$

$$\text{and } p = 1 + \frac{(x/x_0)^2}{\tan^2 \beta_I}$$

Application of this theory in the inverse sense, i.e. to determine the induced velocities and distribution of circulation along the lifting line when the geometric particulars of the propeller and the velocity field in which the propeller works are known, has

been attempted a number of times up to now. In each case it was reported that the developed method was "unstable" or that the iteration procedure did not converge. In this regard the attempts of Johnsson [2-32] and Höiby [2-33] may be mentioned. The method developed here works very satisfactorily and the results, as demonstrated in chapter 5, are accurate. To apply this theory in the quasi-steady sense in a radially and circumferentially-varying propeller inflow, it is necessary to define the angular blade position of the lifting line  $\theta$ , as shown in Fig. 7 as an extra variable. The average inflow velocity  $V_A$  then becomes a function of  $\theta$ , and  $U_A$ ,  $U_T$ ,  $G$  and  $\beta_I$  become functions of  $x$  and  $\theta$ .

The induction factors  $I_A$  and  $I_T$  are, strictly considered, also functions of  $\theta$  since the Wrench relations (equations 2-6) assume that the  $Z$  free-vortex sheets have the same radial distribution in the pitch angle  $\beta_I$ . The consequence of neglecting this dependency on  $\theta$  in using these relations when the lifting line is positioned in a local region of low intake velocity, for example, is that the calculated values for the induced velocities would be too high, whereby the resulting value for the blade loading becomes too low. This is a result of the fact that in this case it is implicitly assumed that the other  $(Z-1)$  blades experience the same low intake velocities. The omission of the dependency of the induction factors on the angular position of the lifting line in a circumferentially varying velocity field is, however, inherent in the quasi-steady approach. Only an unsteady approach to the problem of the calculation of the induction factors can account for the effect of a variation in the pitch angle of the free vortex sheets with  $\theta$ .

The inaccuracy made in assuming that the pitch angle of the  $Z$  free helical vortex lines at  $x$  is equal to the  $\beta_I$ -value at the lifting line being considered, is small. This is a consequence of the fact that in this way an allowance is made for the lift deficiency due to the circumferential variation in the inflow velocity, particularly at higher values of the reduced frequency, which can only be calculated by unsteady theory or by incorporating a correction factor such as developed by Sears [2-34]. The reduced frequency is defined as  $k = \omega c/2V$ , where  $\omega$  equals the effective angular

velocity experienced by the propeller blade section,  $c$  the chord length and  $V$  the inflow velocity. The fact that when both effects are of equal magnitude, their combined effect on the circulation of the lifting line will be zero, is important to note.

For the numerical solution of equations 2-4 and 2-5 in the inverse application, it should be observed that at a radial station  $x$ , in addition to the induced velocities  $U_A$  and  $U_T$ , the circulation  $G$  and the pitch angle  $\beta_I$  on which the induction factors are dependent, are unknown. For the solution of this problem the following iteration procedure must be used.

The value of the angular position  $\theta$  of the propeller blade (as defined by its generator line) at which the calculations are to be performed, the geometry of the propeller, and the velocity field in which the propeller operates are assumed to be known. The lifting line is defined to pass through the quarter-chord positions of the blade sections as shown in Fig. 7. At the radial stations given by  $x = 0.2 + 0.1j$  where  $j = 0, 1, 2, \dots, 8$ , the average value of the advance angle  $\beta(x, \theta)$ , based on the average

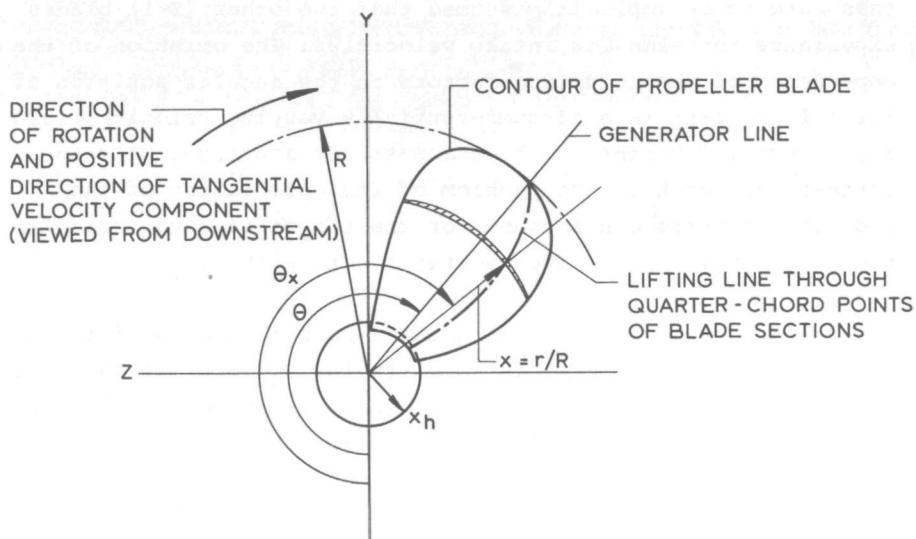


FIG. 7. SCHEME OF NOTATION OF USED POLAR COORDINATE SYSTEM

components of the velocity field between the leading and trailing edge and the rotational propeller speed, is determined. The variation of the advance angle over the chord is accounted for as described in section 3 of this chapter. This angle is calculated by means of the relation:

$$\beta(x, \theta) = \arctan \left[ \frac{\bar{V}_a(x, \theta)}{x\pi nD - \bar{V}_t(x, \theta)} \right] \quad (2-7)$$

In addition, the average (effective) advance velocity along the lifting line can be determined by:

$$V_A(\theta) = 2 \int_0^1 x \bar{V}_a(x, \theta) dx \quad (2-8)$$

In equations 2-7 and 2-8,

$\bar{V}_a(x, \theta), \bar{V}_t(x, \theta)$  = average axial and tangential components of velocity field between the leading and trailing edge of the blade section at  $(x, \theta)$ ,

$n$  = number of propeller revolutions per second, and  $D$  = propeller diameter.

A first value for the hydrodynamic pitch angle  $\beta_I(x, \theta)$  can then be determined by means of an empirical relation given by Sjøntvedt [2-35], viz:

$$\beta_I(x, \theta) \approx \gamma_0(x, \theta) - \left[ \gamma_0(x, \theta) - \beta(x, \theta) \right] \cdot \left[ 0.135 + \frac{0.053}{1.093 - x} \right] \quad (2-9)$$

From Fig 8, it is seen that:

$$\gamma_0(x, \theta) = \arctan \left[ \frac{P(x)}{x\pi D} \right] + \gamma_{NT}(x) - \alpha_0(x, \theta) \quad (2-10)$$

in which  $P(x)$  = pitch of propeller blade section,

$\gamma_{NT}(x)$  = angle, in radians, between chord line of blade section and pitch line at  $x$ ,



and  $\alpha_0(x, \theta)$  = three-dimensional angle of zero-lift in radians in real flow relative to chord line of blade section.

For the sake of calculating a first value of the pitch angle  $\beta_I(x, \theta)$  by means of equation 2-9, the two-dimensional value of the angle of zero-lift of the blade section can be used. The calculation of this two-dimensional angle of zero-lift,  $\alpha_0(x, \theta)$ , is discussed in chapter 3. Alternative use can be made of an empirical relation given by Burrill [2-36], in lieu of equation 2-9, viz:

$$\beta_I(x, \theta) \approx \gamma_0(x, \theta) - [\gamma_0(x, \theta) - \beta_0(x, \theta)] \cdot (0.52 - 0.2x) \quad (2-11)$$

With this first value for  $\beta_I$ , providing a first value for the induction factors  $I_A$  and  $I_T$ , the circulation distribution  $G(x, \theta)$  and the induced velocities  $U_A(x, \theta)$  and  $U_T(x, \theta)$  are found by introducing, after Lerbs [2-24], the variables  $\phi$  and  $\phi_0$  for  $x$  and  $x_0$  such that  $\phi=0$  for  $x=x_h$  and  $\phi=\pi$  for  $x=1$ , as follows:

$$\left. \begin{aligned} x &= \frac{1}{2}(1+x_h) - \frac{1}{2}(1-x_h) \cos \phi \\ \text{and } x_0 &= \frac{1}{2}(1+x_h) - \frac{1}{2}(1-x_h) \cos \phi_0 \end{aligned} \right\} \quad (2-12)$$

Then the circulation  $G(x, \theta)$  can be expanded in a Fourier series such that  $G(x_h, \theta) = 0$  and  $G(1, \theta) = 0$ , viz:

$$G(\phi, \theta) = \sum_{m=1}^{\infty} G_m(\theta) \sin(m\phi) \quad (2-13)$$

and also the induction factors can be expanded in an even Fourier series according to:

$$\left. \begin{aligned} I_A(\phi, \phi_0) &= \sum_{n=0}^{n=\infty} I_n^A(\phi) \cos(n\phi_0) \\ \text{and } I_T(\phi, \phi_0) &= \sum_{n=0}^{\infty} I_n^T(\phi) \cos(n\phi_0) \end{aligned} \right\} \quad (2-14)$$

The Fourier coefficients  $I_n^A(\phi)$  and  $I_n^T(\phi)$  are assumed to be equal to zero for  $n \geq 9$  since 9 radial stations are considered. The values of these 9 coefficients are obtained by inverting the matrix formed by the coefficients in the resulting 9 linear equations.

On substituting equation 2-13 in equations 2-4 and 2-5, it follows that:

$$\left. \begin{aligned} \frac{U_A(\phi, \theta)}{V_A(\theta)} &= \frac{1}{1-x_h} \sum_{m=1}^{\infty} m G_m(\theta) \int_0^{\pi} \frac{I_A(\phi, \phi_0) \cos(m\phi_0)}{\cos\phi_0 - \cos\phi} d\phi_0 \\ \frac{U_T(\phi, \theta)}{V_A(\theta)} &= \frac{1}{1-x_h} \sum_{m=1}^{\infty} m G_m(\theta) \int_0^{\pi} \frac{I_T(\phi, \phi_0) \cos(m\phi_0)}{\cos\phi_0 - \cos\phi} d\phi_0 \end{aligned} \right\} (2-15)$$

The integrals in these expressions can be simplified as follows:

$$\left. \begin{aligned} \text{putting } h_m^A(\phi) &= \int_0^{\pi} \frac{I_A(\phi, \phi_0) \cos(m\phi_0)}{\cos\phi_0 - \cos\phi} d\phi_0 \\ \text{and } h_m^T(\phi) &= \int_0^{\pi} \frac{I_T(\phi, \phi_0) \cos(m\phi_0)}{\cos\phi_0 - \cos\phi} d\phi_0 \end{aligned} \right\} (2-16)$$

and substituting expressions 2-14, we obtain:

$$\left. \begin{aligned} h_m^A(\phi) &= \frac{1}{2} \sum_{n=0}^{\infty} I_n^A(\phi) \left[ \int_0^{\pi} \frac{\cos(m+n)\phi_0}{\cos\phi_0 - \cos\phi} d\phi_0 + \int_0^{\pi} \frac{\cos(m-n)\phi_0}{\cos\phi_0 - \cos\phi} d\phi_0 \right] \\ \text{and } h_m^T(\phi) &= \frac{1}{2} \sum_{n=0}^{\infty} I_n^T(\phi) \left[ \int_0^{\pi} \frac{\cos(m+n)\phi_0}{\cos\phi_0 - \cos\phi} d\phi_0 + \int_0^{\pi} \frac{\cos(m-n)\phi_0}{\cos\phi_0 - \cos\phi} d\phi_0 \right] \end{aligned} \right\} (2-17)$$

The integrals form so-called Glauert integrals. With the known principal value of these integrals, equations 2-17 can be written as:

$$h_m^A(\phi) = \frac{\pi}{\sin\phi} \left[ \sin(m\phi) \sum_{n=0}^m I_n^A(\phi) \cos(n\phi) + \cos(m\phi) \sum_{n=m+1}^{\infty} I_n^A(\phi) \sin(m\phi) \right]$$

$$\text{and } h_m^T(\phi) = \frac{\pi}{\sin\phi} \left[ \sin(m\phi) \sum_{n=0}^m I_n^T(\phi) \cos(n\phi) + \cos(m\phi) \sum_{n=m+1}^{\infty} I_n^T(\phi) \sin(m\phi) \right] \quad (2-18)$$

For  $\phi=0$  and  $\phi=\pi$  these functions become indefinite and must be determined by means of l'Hospital's rule, viz:

$$h_m^A(\phi)_{\phi=0} = \left[ m \sum_{n=0}^m I_n^A(\phi)_{\phi=0} + \sum_{n=m+1}^{\infty} n I_n^A(\phi)_{\phi=0} \right]$$

and

$$h_m^T(\phi)_{\phi=\pi} = -\pi \cos(\pi m) \left[ m \sum_{n=0}^m I_n^A(\phi)_{\phi=\pi} \cdot \cos(\pi n) + \sum_{n=m+1}^{\infty} n I_n^A(\phi)_{\phi=\pi} \cdot \cos(\pi n) \right] \quad (2-19)$$

and likewise for  $h_m^T(\phi)_{\phi=0}$  and  $h_m^A(\phi)_{\phi=\pi}$ .

Substitution of equations 2-18 in the expressions for the induced velocities gives:

$$\left. \begin{aligned} \frac{U_A(\phi, \theta)}{V_A(\theta)} &= \frac{1}{1-x_h} \sum_{m=1}^{\infty} m G_m(\theta) h_m^A(\phi) \\ \text{and } \frac{U_T(\phi, \theta)}{V_A(\theta)} &= \frac{1}{1-x_h} \sum_{m=1}^{\infty} m G_m(\theta) h_m^T(\phi) \end{aligned} \right\} \quad (2-20)$$

In these equations, the values for  $U_A(\phi, \theta)$ ,  $U_T(\phi, \theta)$  and  $G_m(\phi)$  are

unknown so that it is necessary to have one more equation in these unknowns. Such a relation can be directly obtained from Fig. 6, viz:

$$\tan\beta_I(x, \theta) = \frac{\bar{V}_a(\theta) + U_A(x, \theta)}{\pi n D \bar{V}_t(x, \theta) - U_T(x, \theta)} \quad (2-21)$$

which can be written as:

$$\frac{V_A(\theta)}{\bar{V}_a(x, \theta)} \cdot \frac{U_A(x, \theta)}{V_A(\theta)} + \frac{V_A(\theta)}{\bar{V}_a(x, \theta)} \cdot \frac{U_T(x, \theta)}{V_A(\theta)} \tan\beta_I(x, \theta) = \frac{\tan\beta_I(x, \theta)}{\tan\beta(x, \theta)} - 1 \quad (2-22)$$

Substitutions of equations 2-20 gives:

$$\frac{1}{1-x_h} \sum_{m=1}^{\infty} m G_m(\theta) \left[ h_m^A(\phi) + \tan\beta_I(\phi, \theta) h_m^T(\phi) \right] \frac{V_A(\theta)}{\bar{V}_a(\phi, \theta)} = \frac{\tan\beta_I(\phi, \theta)}{\tan\beta(\phi, \theta)} - 1 \quad (2-23)$$

from which the values of  $G_m(\theta)$  at the 9 radial stations can be directly determined, after which, by equations 2-20 the values of  $U_A(\phi, \theta)$  and  $U_T(\phi, \theta)$  at the 9 values for  $\phi$  are determined. Here it is assumed that  $G_m(\theta) = 0$  for  $m=1$  and  $m \geq 9$ .

The second value for  $\beta_I(x, \theta)$  is obtained by means of an equation which incorporates the effects of blade section geometry. With the definition of the dimensionless circulation  $G(x, \theta)$  as:

$$G(x, \theta) = \frac{\Gamma(x, \theta)}{\pi D V_A(\theta)} ; \quad (2-24)$$

in which 
$$\Gamma(x, \theta) = \frac{L(x, \theta)}{\rho V(x, \theta)} \quad (2-25)$$

where  $\Gamma(x, \theta)$  = non-dimensional circulation,  
 $L(x, \theta)$  = lift force of blade section,  
 $V(x, \theta)$  = resultant velocity at blade section,  
 and  $\rho$  = density of water;

and with  $L(x, \theta) = C_L(x, \theta) \frac{1}{2} \rho V^2(x, \theta) c(x)$ , (2-26)

in which  $c(x)$  = chord length of blade section,  
the relation for  $G(x, \theta)$  becomes:

$$G(x, \theta) = \frac{C_L(x, \theta) c(x) V(x, \theta)}{2\pi D V_A(\theta)} \tag{2-27}$$

From Fig. 6 it follows that the resultant velocity  $V(x, \theta)$  can be expressed in its components by means of:

$$V(x, \theta) = \frac{\bar{V}_a(x, \theta) + U_A(x, \theta)}{\sin \beta_I(x, \theta)} \tag{2-28}$$

On substituting equation 2-28 in 2-27, the non-dimensional circulation can be written as:

$$G(x, \theta) = \frac{C_L(x, \theta) c(x) \left[ \bar{V}_a(x, \theta) / V_A(\theta) + U_A(x, \theta) / V_A(\theta) \right]}{2\pi D \sin \beta_I(x, \theta)} \tag{2-29}$$

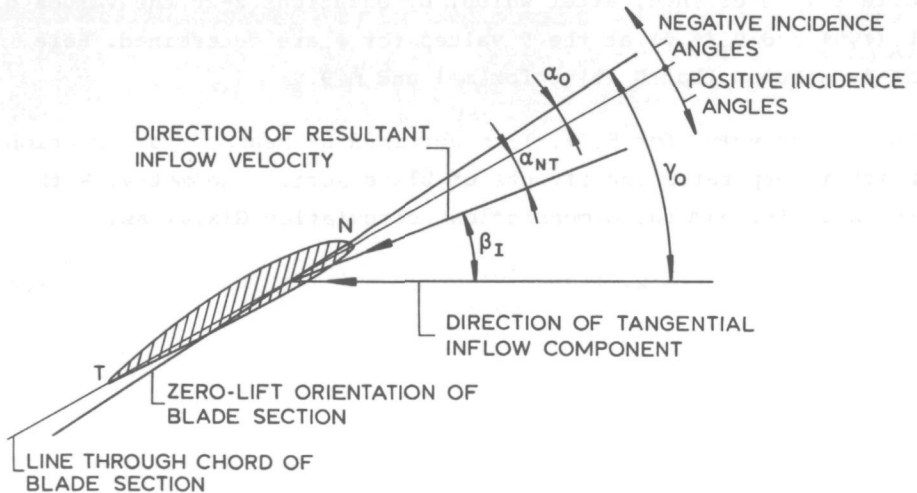


FIG. 8. DEFINITION OF ANGLES USED TO DERIVE THE RELATION BETWEEN GEOMETRIC ENTITIES.

The lift coefficient  $C_L(x, \theta)$  of the blade section is a function of the hydrodynamic pitch angle  $\beta_I(x, \theta)$  since the angle of attack of the incoming flow relative to the chord line of the blade section can be written as (see Fig 8):

$$\alpha_{NT}(x, \theta) = \gamma_0(x, \theta) + \alpha_0(x, \theta) - \beta_I(x, \theta) \quad (2-30)$$

where  $\alpha_{NT}(x, \theta)$  = angle of attack of flow relative to chord line of blade section,

$\gamma_0(x, \theta)$  = effective pitch of blade section as defined by equation 2-10,

and  $\alpha_0(x, \theta)$  = three-dimensional value of zero-lift angle in radians in real flow relative to chord line of blade section.

With equation 2-30 an expression for the lift coefficient  $C_L(x, \theta)$  can be derived in which the dependence on  $\beta_I(x, \theta)$  is explicitly given. This is necessary since equation 2-29 is to be used to determine a new value for  $\beta_I(x, \theta)$  with which the iteration process can be continued. The required expression for the lift coefficient can be obtained from the ratio of the two-dimensional lift-curve slope to the three-dimensional lift curve slope. A well-accepted value of this ratio is  $(dC_L/d\alpha_2)/K_C$  where  $dC_L/d\alpha_2$  is the two-dimensional lift curve-slope of the blade section in real flow and  $K_C$  represents the appropriate value of the lifting surface correction factor for camber.

It will be recalled that use of correction factors derived from lifting surface theory is necessary to account for finite blade width effects since in lifting line theory only three-dimensional spanwise effects are accounted for. The camber correction factor  $K_C$  accounts for the loss in lift due to the curvature of the distribution of the induced velocity along the chord. In the same way the ideal angle-of-attack correction factor  $K_\alpha$  accounts for the change in ideal angle-of-incidence from the two-dimensional value. The angle of attack correction factor for thickness  $K_t$  accounts for the main effect of blade thickness. Recently Morgan et al [2-5], Minsaas and Slattelid [2-37] and Cumming et al [2-38]



published accurate values for these correction factors in tabulated form as a function of the number of propeller blades  $Z$ , the expanded blade area ratio  $A_E/A_0$ , the induced advance coefficient  $\lambda_I = x \tan \beta_I$ , the radial coordinate  $x$  and the skew angle  $\theta_S$ . To facilitate their frequent application in numerical procedures, polynomials have been developed based on these tabulated values with which, for a specific combination of the independent variables, the required value of the 3 lifting surface correction factors can be obtained. These are presented and discussed in the appendix.

The three-dimensional lift curve coefficient of the blade section at  $(x, \theta)$  can therefore be written as:

$$C_L(x, \theta) = \frac{dC_L}{d\alpha_2} \int_{\beta_I(x, \theta)}^{\gamma_0(x, \theta)} \frac{d\beta_I}{K_C} \quad (2-31)$$

in which  $K_C$  is a function of the geometry of the propeller and  $\beta_I$ , and the two-dimensional lift-curve slope  $dC_L/d\alpha_2$  is considered constant for a given blade section geometry and Reynolds number as is shown in chapter 3.

In equation 2-31 the value of the three-dimensional zero-lift angle  $\alpha_0(x, \theta)$  is needed to find the value of the integrand  $\gamma_0(x, \theta)$  as defined in equation 2-10. This can be performed by means of the relation:

$$\alpha_0(x, \theta) = \alpha_{0_2}(x, \theta) + \alpha_{i_1}(x, \theta) - \alpha_{i_2}(x, \theta) \quad (2-32)$$

in which  $\alpha_{0_2}(x, \theta)$  = two-dimensional value of zero-lift angle,

$\alpha_{i_1}(x, \theta)$  = three-dimensional value of ideal angle of incidence,

and  $\alpha_{i_2}(x, \theta)$  = two-dimensional ideal angle of incidence,

The three-dimensional value of the ideal angle of incidence can be derived from the respective two-dimensional angle by means of:

$$\alpha_{i_1}(x, \theta) = K_\alpha \cdot \alpha_{i_2}(x, \theta) + K_t \cdot BTF_x \quad (2-33)$$

in which  $K_\alpha$  = lifting surface correction factor for ideal angle of attack.

$K_t$  = angle of attack lifting surface correction factor for thickness,

and  $BTF_x$  = blade thickness fraction based on maximum thickness of blade section at  $x$ .

Polynomials for  $K_\alpha$  and  $K_t$  are given in the appendix. The values for  $K_t$  on which the  $K_t$ -polynomials are based were obtained for a standard blade thickness fraction, based on a standard radial distribution of maximum thickness [2-5, 2-28]. To obtain the applicable angle of attack correction for thickness for other radial distributions of maximum thickness, it is necessary to substitute the thickness values of the actual propeller, viz:

$$BTF_x = \frac{[t_{\max}]_x / D - 0.003}{1-x} + 0.003 \quad (2-34)$$

in which  $[t_{\max}]_x$  = maximum thickness of blade section at  $x$ .

With equations 2-31 to 2-34 it is possible to determine an average value of the lift-curve slope according to:

$$\frac{\overline{dC_L}}{d\alpha}(x, \theta) = \frac{C_L(x, \theta)}{\gamma_0(x, \theta) - \beta_I(x, \theta)} \quad (2-35)$$

Using this equation, equation 2-29 can now be written as:

$$G(x, \theta) = \frac{\overline{dC_L}/d\alpha(x, \theta) [\gamma_0(x, \theta) - \beta_I(x, \theta)] \cdot c(x) [\bar{V}_a(x, \theta)/V_A(\theta) + U_A(x, \theta)/V_A(\theta)]}{2\pi D \sin \beta_I(x, \theta)} \quad (2-36)$$

$$\text{or} \quad \beta_I(x, \theta) = A - B \sin \beta_I(x, \theta) \quad (2-37)$$

where  $A = \gamma_0(x, \theta)$

$$\text{and } B = \frac{2\pi D G(x, \theta)}{\overline{dC_L}/d\alpha(x, \theta) \cdot c(x) [\bar{V}_a(x, \theta)/V_A(\theta) + U_A(x, \theta)/V_A(x, \theta)]}$$

Based on the first value of  $\beta_I$  according to equation 2-9 or 2-11, the value of the right-hand side of equation 2-37 can be determined and thereby a new value for  $\beta_I$ . With this new value for  $\beta_I$  the complete procedure described by equations 2-12 to 2-37 can be repeated whereby a third value for  $\beta_I$  results. This is continued until the difference between successive values is less than, say, 0.001 radians. This iteration procedure converges far more rapidly, however, if equation 2-37 is used as a reduction formula for the new  $\beta_I$ -value by repeatedly substituting the new  $\beta_I$ -value in the right-hand side of the equation until successive values differ by less than 0.001 radians, according to:

$$\beta_{I_n}(x, \theta) = A - B \sin \beta_{I_{n-1}} \quad (2-38)$$

in which A and B are considered constant.

The described iteration process is to be performed for the 9 radial stations  $x=0.2(0.1)1.0$  and for all angular positions of the lifting line. With the thus obtained final values for  $U_A(x, \theta)$ ,  $U_T(x, \theta)$ ,  $G(x, \theta)$ ,  $\alpha_0(x, \theta)$ ,  $C_L(x, \theta)$  and  $\beta_I(x, \theta)$  the resultant velocity at  $(x, \theta)$  can be found from:

$$V(x, \theta) = \sqrt{\left[ \bar{V}_a(x, \theta) + U_A(x, \theta) \right]^2 + \left[ x \pi n D - \bar{V}_t(x, \theta) - U_T(x, \theta) \right]^2} \quad (2-39)$$

and the cavitation number  $\sigma(x, \theta)$  from:

$$\sigma(x, \theta) = \frac{P_0 + x R g \cos \theta_x - P_V}{\frac{1}{2} \rho V^2(x, \theta)} \quad (2-40)$$

in which  $P_0$  = effective atmospheric pressure,

$P_V$  = vapour pressure at prevailing temperature,

$g$  = acceleration due to gravity,

and  $\theta_x$  = angular coordinate of radial stations on lifting line.

Also the radial distribution of thrust and torque can be determined by means of:

$$\left. \begin{aligned} \frac{dT}{dx}(x, \theta) &= \frac{1}{2} \rho C(x) V^2(x, \theta) [C_L(x, \theta) \cos \beta_I(x, \theta) - C_D(x, \theta) \sin \beta_I(x, \theta)] \\ \text{and} \\ \frac{dQ}{dx}(x, \theta) &= \frac{1}{2} \rho x R C(x) V^2(x, \theta) [C_L(x, \theta) \sin \beta_I(x, \theta) + C_D(x, \theta) \cos \beta_I(x, \theta)] \end{aligned} \right\} \quad (2-41)$$

It follows that the thrust and torque per blade as a function of angular blade position are:

$$\left. \begin{aligned} T(\theta) &= \int_{x_h}^1 \frac{1}{2} \rho C(x) V^2(x, \theta) [C_L(x, \theta) \cos \beta_I(x, \theta) - C_D(x, \theta) \sin \beta_I(x, \theta)] dx \\ Q(\theta) &= \int_{x_h}^1 \frac{1}{2} \rho x R C(x) V^2(x, \theta) [C_L(x, \theta) \sin \beta_I(x, \theta) + C_D(x, \theta) \cos \beta_I(x, \theta)] dx \end{aligned} \right\} \quad (2-42)$$

The thrust eccentricity per blade is defined as:

$$x_E(\theta) = \frac{1}{T(\theta)} \int_{x_h}^1 \frac{dT}{dx}(x, \theta) x dx \quad (2-43)$$

In equations 2-41 and 2-42,  $C_D(x, \theta)$  is the three-dimensional drag coefficient of the blade section, the determination of which is discussed in chapter 3. The total thrust and torque of the propeller is:

$$\left. \begin{aligned} T &= \frac{Z}{2\pi} \int_0^{2\pi} T(\theta) d\theta \\ \text{and } Q &= \frac{Z}{2\pi} \int_0^{2\pi} Q(\theta) d\theta \end{aligned} \right\} \quad (2-44)$$

If in addition the average value of the undisturbed axial inflow velocity is determined by:

$$\bar{V}_A = \frac{1}{2\pi} \int_0^{2\pi} V_A(\theta) d\theta, \quad (2-45)$$

then the thrust and torque coefficients, the advance ratio and the open-water efficiency can be determined by:

$$\left. \begin{aligned} K_T &= \frac{T}{\rho n^2 D^4} \\ K_Q &= \frac{Q}{\rho n^2 D^5} \\ J &= \frac{\bar{V}_A}{nD} \\ \text{and } \eta_0 &= \frac{K_T \cdot J}{2\pi K_Q} \end{aligned} \right\} \quad (2-46)$$

where  $K_T$  = thrust coefficient,  
 $K_Q$  = torque coefficient,  
 $J$  = advance ratio,  
and  $\eta_0$  = open-water efficiency.

### 2.2.2 Effect of Bound Vortices

When the lifting lines are symmetrically arranged and have the same radial circulation distribution, it can be shown that the vector sum of the induced velocities due to the vorticity of the bound vortex lines is zero, irrespective of whether the lifting lines have skew and rake or not. When the bound vortex lines representing the blades of the propeller have different circulation distributions as in the case of a circumferential varying propeller inflow, this is no longer true. In this case a net velocity is induced at a point P on one of the lifting lines due to the vorticity of the other lifting lines. These induced velocities can be determined by directly applying the Biot-Savart law as follows.

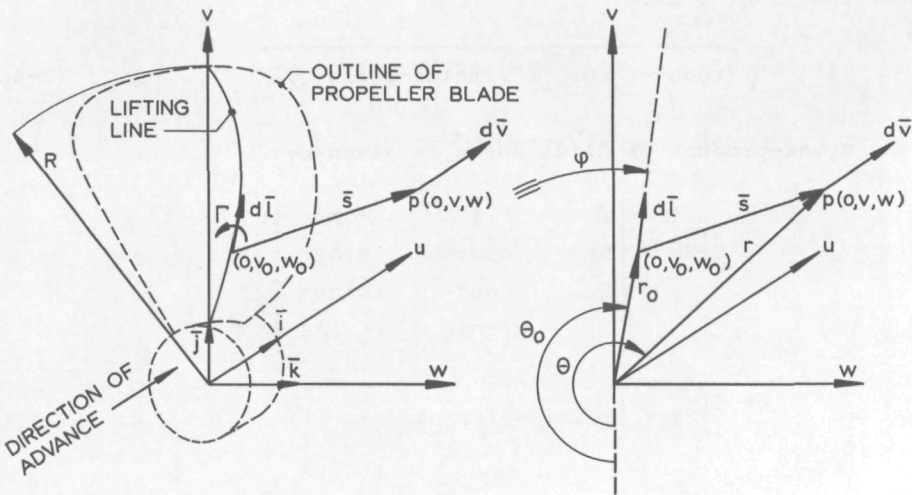


FIG. 9. THE SCHEME OF NOTATION FOR DETERMINING THE INDUCED VELOCITY AT P DUE TO LIFTING LINE ELEMENT  $d\vec{l}$ .

Using the cartesian coordinate system  $(u, v, w)$  and the cylindrical coordinate system  $(u, r, \theta)$  as shown in Fig.9, the Biot-Savart law in vector notation for the induced velocity at a point  $P(u, v, w)$  is:

$$d\vec{v} = \frac{\vec{\Gamma}}{4\pi} \left[ \frac{d\vec{l} \times \vec{s}}{|\vec{s}|^3} \right] \quad (2-47)$$

in which the velocity vector  $d\vec{v}$  is induced by a vortex element of strength  $\vec{\Gamma}$  and of length  $d\vec{l}$  of the lifting line at  $(u_0, v_0, w_0)$  as shown in Fig.9. The vector distance between the vortex element and the point P is  $\vec{s}$ . With the unit vectors  $\vec{i}$ ,  $\vec{j}$  and  $\vec{k}$  in the direction of the  $u$ ,  $v$  and  $w$  axes, the unit vector tangential to the lifting line at the vortex element, on disregarding rake, becomes:

$$\frac{d\vec{l}}{dl} = \cos\phi \cdot \vec{j} + \sin\phi \cdot \vec{k} \quad (2-48)$$

The vector  $\vec{s}$  is given by  $\vec{s} = (0, v-v_0, w-w_0)$ :

$$\text{i.e. } \vec{s} = (0, r\cos\theta - r_0\cos\theta_0, r\sin\theta - r_0\sin\theta_0) \quad (2-49)$$



the length of  $\vec{s}$  is:

$$|\vec{s}| = \sqrt{(r \cos \theta - r_0 \cos \theta_0)^2 + (r \sin \theta - r_0 \sin \theta_0)^2} \quad (2-50)$$

the cross-product of  $d\vec{l}/dl$  and  $\vec{s}$  is given by:

$$\frac{d\vec{l}}{dl} \times \vec{s} = \begin{vmatrix} \vec{i} & \vec{j} & \vec{k} \\ 0 & \cos \phi & \sin \phi \\ 0 & r \cos \theta - r_0 \cos \theta_0 & r \sin \theta - r_0 \sin \theta_0 \end{vmatrix}$$

$$\text{or } \frac{d\vec{l}}{dl} \times \vec{s} = [r \sin(\theta - \phi) + r_0 \sin(\phi - \theta_0)] \vec{i} \quad (2-51)$$

which is perpendicular to the plane through  $d\vec{l}$  and  $\vec{s}$ , in the direction of advance of the propeller.

The total velocity induced by the lifting line at P is obtained by integration along the lifting line according to:

$$\Delta U_A(r, \theta) = - \frac{1}{4\pi} \int_{l_{\text{hub}}}^{l_{\text{tip}}} \frac{\Gamma(r_0, \theta_0) [r \sin(\theta - \phi) + r_0 \sin(\phi - \theta_0)] dl}{[(r \cos \theta - r_0 \cos \theta_0)^2 + (r \sin \theta - r_0 \sin \theta_0)^2]^{3/2}} \quad (2-52)$$

and the total induced velocity at P(r, θ) due to all the lifting lines becomes:

$$\Delta U_A(r, \theta) = - \frac{1}{4\pi} \sum_{k=1}^{Z-1} \int_{l_{\text{hub}}}^{l_{\text{tip}}} \frac{\Gamma(r_0, \theta_0) [r \sin(\theta - \phi) + r_0 \sin(\phi - \theta_0)] dl}{[(r \cos \theta - r_0 \cos \theta_0)^2 + (r \sin \theta - r_0 \sin \theta_0)^2]^{3/2}} \quad (2-53)$$

The consideration of skew or of a curved lifting line in these equations is inconsistent with the theory of the previous section, since the free helical vortex sheets were considered to be shed from straight radial lifting lines. For a straight lifting line it follows from Fig.9 that  $\phi = \theta_0$ , and that  $dl$  becomes  $dr_0$ , by which equation 2-53 simplifies to:

$$\Delta U_A(r, \theta) = -\frac{1}{4\pi} \sum_{k=1}^{Z-1} \int_{r_h}^R \frac{\Gamma(r_0, \theta_0) r \sin(\theta - \theta_0) dr_0}{[(r \cos \theta - r_0 \cos \theta_0)^2 + (r \sin \theta - r_0 \sin \theta_0)^2]^{3/2}} \quad (2-54)$$

On using relation 2-24 and on introducing the variable  $x=r/R$  and  $x_0=r_0/R$ , equation 2-54 can be written as:

$$\frac{\Delta U_a(x, \theta)}{V_A(\theta)} = -\frac{1}{2} \sum_{k=1}^{Z-1} \int_{x_h}^1 \frac{G(x_0, \theta_0) \sin(\theta - \theta_0) x dx_0}{[(x \cos \theta - x_0 \cos \theta_0)^2 + (x \sin \theta - x_0 \sin \theta_0)^2]^{3/2}} \quad (2-55)$$

in which, for any one blade position  $\theta$  and radial station  $x$ , at which the induced velocity is to be calculated,  $\theta_0$  is constant.

The order of magnitude of this induced velocity is dependent on the order of magnitude of the variations in the value of the bound circulation  $G(x_0, \theta_0)$  at the various angular blade positions. The induced velocities caused by the free vortex sheets are generally considerably larger, however.

Proper consideration of the effect of these induced velocities on the pitch angle  $\beta_I$  can only be obtained when equation 2-55 is introduced into the iteration procedure described in the previous section. After the first step, a first value of the strength of the bound vortices is obtained with which the value of  $\Delta U_A(x, \theta)/V_A(\theta)$  can be determined, which value must then be added to the value of  $U_A(x, \theta)/V_A(\theta)$  in the respective equations (equations 2-22, 2-36 and 2-39).

### 2.3 Effect of Circumferentially-Varying Inflow

When a propeller blade rotates through a circumferentially-varying inflow, the angle of incidence continuously varies along the blade section. At every angular blade position the effect of such a variation of the undisturbed flow can be considered analogous to that of a rectilinear flow over a propeller blade of which the camber distribution at the various radial stations has been modified by an amount equal to the effective camber of the curved streamlines.

This is illustrated in Fig. 10 in which an attempt is made to show the equivalence of a curved flow over a flat plate and a rectilinear flow over a curved plate with a camber distribution equal to the curvature of the flow. The effect of the continuously changing effective camber of blade sections on the cavitation properties of propellers has been discussed by Van Manen [2-39] and Johnson et al [2-23]. A discussion of the effect on the lift of blade sections has been given by Kruppa [2-22]. Both of these effects are by no means small, and it is imperative when requiring accurate results to calculate the effective change in geometric camber at every blade position before proceeding to the calculation of geometry-dependent entities such as the pressure distribution and the lift and drag characteristics. Such a calculation procedure will now be discussed.

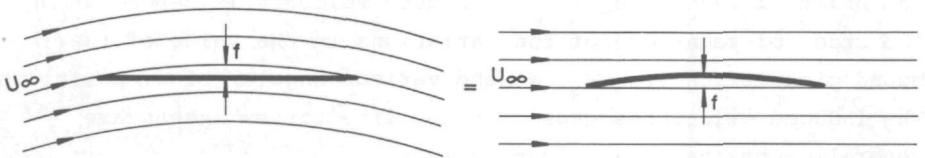


FIG.10. EQUIVALENCE OF CURVED FLOW ON FLAT PLATE AND RECTILINEAR FLOW ON CURVED PLATE WHEN CURVATURE DISTRIBUTIONS ARE EQUAL.

For every angular blade position, the value of the advance angle  $\beta$  along the chord can be determined by means of the relation:

$$\beta_k(x, \theta_k) = \arctan \left[ \frac{V_a(x, \theta_k)}{x\pi nD - V_t(x, \theta_k)} \right] \quad (2-56)$$

$$\text{in which } \theta_k = \arctan \left[ \frac{L_e(x) - c(x)k/N}{xR} \right] + \theta \quad (2-57)$$

where  $V_a(x, \theta_k), V_t(x, \theta_k)$  = axial and tangential inflow components at  $(x, \theta_k)$ ,

$L_e(x)$  = distance of leading edge to generator line,

$N$  = number of chordwise points at which effective camber is to be calculated

and  $k = 0, 1, 2, \dots, N$ .

The expression for the incidence of the undisturbed flow over the blade section relative to the orientation of the nose-tail line is then obtained from:

$$\alpha_{g_k}(x, \theta_k) = \arctan \left[ \frac{P(x)}{x\pi D} \right] + \alpha_{NT}(x) - \beta_k(x, \theta_k) \quad (2-58)$$

The variation of this incidence angle,  $\Delta\alpha_g$ , with respect to the average value between the leading and trailing edge (which value is used in the lifting line calculations discussed in the previous section) is found from:

$$\Delta\alpha_g(x, \theta_k) = \alpha_{g_k}(x, \theta_k) - \bar{\alpha}_g(x, \theta) \quad (2-59)$$

$$\text{where } \bar{\alpha}_g = \arctan \left[ \frac{P(x)}{x\pi D} \right] + \alpha_{NT}(x) - \beta(x, \theta) \quad (2-60)$$

in which  $\beta(x, \theta)$  follows from equation 2-7. The variation of the geometric incidence angle along the blade section is then in fact:

$$\Delta\alpha_{g_k}(x, \theta_k) = \arctan \left[ \frac{V_a(x, \theta_k)}{x\pi nD - V_t(x, \theta_k)} \right] - \arctan \left[ \frac{\bar{V}_a(x, \theta)}{x\pi nD - \bar{V}_t(x, \theta)} \right]$$

The tangent of  $\Delta\alpha_{g_k}(x, \theta_k)$  represents the gradient of the curved streamlines at  $(x, \theta_k)$ . This can be written as:

$$\frac{d(\Delta f_{g_k}(x, \theta_k))}{d\theta} = \tan \left[ \Delta\alpha_{g_k}(x, \theta_k) \right] \quad (2-61)$$

in which  $\Delta f_{g_k}$  equals the change in geometric camber at  $(x, \theta_k)$  due to the curvature of the inflow streamlines. It then follows that the change in geometric camber can be determined from:

$$\Delta f_{g_k}(x, \theta_k) = \int_0^{\theta_k} \tan \left[ \Delta\alpha_{g_k}(x, \theta_k) \right] d\theta \quad (2-62)$$

Due to the fact that the variation of the incidence angle  $\Delta\alpha_{g_k}$

was calculated with respect to the average value over the chord, it follows that:

$$\int_0^{\theta_n} \tan \Delta \alpha_{g_k}(x, \theta_k) d\theta = 0 \quad (2-63)$$

The effective camber distribution of the blade sections can then be found from:

$$f_k(x, \theta_k) = f_{g_k}(x, \theta_k) - \Delta f_{g_k}(x, \theta_k) \quad (2-64)$$

in which  $f_k(x, \theta_k)$  = coordinates of effective camber distribution,

and  $f_{g_k}(x, \theta_k)$  = coordinates of geometric camber distribution.

To obtain a smooth distribution of effective camber, it is necessary to fair the distribution of  $\Delta f_{g_k}(x, \theta_k)$  across the chord. A fairing procedure which works satisfactorily in this regard is a least squares method applied to the coefficients of a third degree polynomial, viz:

$$\Delta f_{g_k}(x, \theta_k) = A + B\theta_k + C\theta_k^2 + D\theta_k^3 \quad (2-65)$$

On identifying the angular coordinate  $\theta_k$  with the corresponding position on the chord of the blade section relative to the leading edge  $x_{c_k}$ , for a specific angular blade position, it follows that:

$$\Delta f_{g_k}(x, x_{c_k}) = A + Bx_{c_k} + Cx_{c_k}^2 + Dx_{c_k}^3 \quad (2-66)$$

in which  $\Delta f_{g_k}(x, x_{c_k}) = 0$  for  $x_c = 0$  and for  $x_c = c$

Accordingly:

$$\left. \begin{aligned} A &= 0 \\ \text{and } B &= -Cc - Dc^2 \end{aligned} \right\} \quad (2-67)$$

$$\text{i.e. } \Delta f_{g_k}(x, \theta_k) = Cx_{c_k} \left[ x_{c_k} - c \right] + Dx_{c_k} \left[ x_{c_k}^2 - c^2 \right] \quad (2-68)$$

in which the values of C and D are determined by the least squares method. Such a procedure leads to:

$$\left. \begin{aligned}
 D &= \frac{C_1 A_2 - C_2 A_1}{B_1 A_2 - B_2 A_1} \\
 \text{and } C &= \frac{C_1 - D B_1}{A_1} \\
 \text{where } A_1 &= \sum_{i=1}^{N-1} x_{C_k}^2 \left[ x_{C_k}^2 - c \right]^2 \\
 A_2 = B_1 &= \sum_{i=1}^{N-1} x_{C_k}^2 \left[ x_{C_k}^2 - c^2 \right] \left[ x_{C_k} - c \right] \\
 B_2 &= \sum_{i=1}^{N-1} x_{C_k}^2 \left[ x_{C_k}^2 - c^2 \right]^2 \\
 C_1 &= \sum_{i=1}^{N-1} \Delta f_{g_k} \cdot x_{C_k} \left[ x_{C_k} - c \right] \\
 C_2 &= \sum_{i=1}^{N-1} \Delta f_{g_k} \cdot x_{C_k} \left[ x_{C_k}^2 - c^2 \right]
 \end{aligned} \right\} \begin{array}{l} (2-69) \\ (2-70) \end{array}$$

2.4 Calculation of Chordwise Load (Pressure) Distribution.

2.4.1 Description of Theoretical Procedure

The calculation of the chordwise load or pressure distribution on propeller blades has been dealt with by several workers in various ways. The classical approach always assumes validity of the first inviscid approximation as defined by Twaites [2-40]. This approach presupposes that the body itself may be taken to constitute the boundary of the potential flow, which is a reasonable assumption



in the absence of flow separation. This constitutes the case of so-called unmixed boundary conditions in which the velocity normal to the boundary is zero.

When the flow separates (the imminent possibility of which is much greater than often presupposed by workers in the field of marine propulsion), or when cavitation is present on the body, the potential flow solution for the first inviscid approximation is bounded partly by the body and partly by some streamline representing the edge of the separated or cavitating region. Here the boundary conditions are mixed, necessitating a completely different analytical treatment. For example, the classical case of so-called Kirchoff flow arises when the velocity along this free streamline is considered constant. The required type of analytical approach for the case a cavity is situated on a two-dimensional body, has been given by Geurst [2-41] and others. For the general three-dimensional case of a propeller blade, however, the analytical difficulties are severe and, for the time being, must be left out of consideration. This requires that for the determination of the pressure distribution on a blade section of a cavitating propeller, another procedure must be used. Such an (approximate) procedure is used and discussed in chapter 4.

The exact theory for the calculation of the two-dimensional pressure distribution in potential flow was developed by Theodorsen [2-42]. This theory is based on a conformal mapping procedure which transforms the two-dimensional profile into a circle (cylinder) around which the potential flow is known. Due to the cumbersome calculation of the implicit Poisson integral for the conjugate function, this procedure is now rarely used. The Algol statements given by Krakowiak, Bindel and Brard [2-43] for this theory incorporates the original "Theodorsen" determination of the conjugate function which must be very carefully computed. Often this procedure gives computed points with a fair amount of scatter. Very adequate approximate procedures have been devised which avoid this difficulty. One of these is Goldstein's third approximation to Theodorsen's theory [2-44]. This approximation assumes that when the profile in the  $z$ -plane is transformed by means of the transformation:

$$z = \zeta + a^2 \zeta^{-1}, \quad (2-71)$$

the resulting figure in the  $\zeta$ -plane hardly differs from a circle. This pseudo-circle, which can be written as:

$$\zeta = ae^{\psi(\phi) + i\phi} \quad (2-72)$$

can then be transformed to a real circle in the  $\zeta_1$ -plane, by means of:

$$\zeta_1 = ae^{\psi_0 + i(\phi + \varepsilon(\phi))} \quad (2-73)$$

such that in the resulting equation for the velocity distribution, the powers of  $\varepsilon(\phi)$  and products of  $\varepsilon(\phi)$  and  $\psi(\phi)$  can be neglected. In addition, Goldstein assumes that the parametric coordinates of the profile  $(\psi, \phi)$ , which can be derived from equations 2-71 and 2-72 to be:

$$\left. \begin{aligned} 2\sin^2\theta &= p + \sqrt{p^2 + (y/a)^2} \\ 2\sin^2\psi &= -p + \sqrt{p^2 + (y/a)^2} \end{aligned} \right\} \quad (2-74)$$

where  $p = 1 - (x_c/2a)^2 - (y/2a)^2$

can be reduced to:

$$\left. \begin{aligned} \cos\phi &= 1 - 2x_c/c \\ \psi(\phi) &= \frac{2y}{c\sin\phi} \end{aligned} \right\} \quad (2-75)$$

in which for  $\sin\phi=0$  (at the leading and trailing edges), the value of  $\psi(\phi)$  is determined from

$$\left. \begin{aligned} \psi_l &= \sqrt{2\rho_l/c} \\ \text{and } \psi_t &= \sqrt{2\rho_t/c} \end{aligned} \right\} \quad (2-76)$$

in which  $\rho_1, \rho_t$  = radii of curvature of leading and trailing edges.

In equations 2-74 and 2-75,  $(x_c, y)$  are the coordinates of the profile, where  $0 \leq x_c \leq c$ . The conjugate function  $\varepsilon(\phi)$  of  $\psi(\phi)$  is now explicitly determined from Poisson's integral:

$$\varepsilon(\phi) = \frac{1}{2\pi} P \int_0^{2\pi} \psi(t) \cot \frac{1}{2}(\phi-t) dt \quad (2-77)$$

in which P indicates that the Cauchy principal value must be taken at the singularity  $t = \phi$  in the integration. The value of  $\psi_0$ , which together with  $\varepsilon(\phi)$  determines the final transformation to the real circle, is determined from:

$$\psi_0 = \frac{1}{2\pi} \int_0^{2\pi} \psi(\phi) d\phi \quad (2-78)$$

The expression for the velocity distribution becomes:

$$\frac{v}{U} = \frac{e^{\psi_0} \left[ 1 + \frac{d\varepsilon}{d\phi} \right]}{\sqrt{\psi^2(\phi) + \sin^2 \frac{\phi}{2}}} \left| \cos(\alpha+\beta) \cdot \sin(\phi+\varepsilon(\phi)-\beta) \right. \\ \left. + \sin(\alpha+\beta) \cdot \cos(\phi+\varepsilon(\phi)-\beta) + \sin(\alpha+\beta) \right| \quad (2-79)$$

In potential flow the zero-lift angle of attack  $\beta$  is equal to  $-\varepsilon(\phi)$  when  $\phi=\pi$ . The expression for the lift coefficient in potential flow is:

$$C_{L \frac{2}{p}} = 2\pi e^{\psi_0} \sin(\alpha+\beta) \quad (2-80)$$

from which it follows that the lift curve slope in potential flow is:

$$\frac{dC_L}{d\alpha \frac{2}{p}} = e^{\psi_0} \approx 1 + t/c \quad (2-81)$$

Numerical evaluation of equation 2-77 can be accurately performed by means of a method given by Watson [2-45] in which the value of  $\psi(\phi)$  is considered specified at  $2N$  equally-spaced values of  $\phi$ , such that:

$$\psi(\phi) = A_0 + \sum_{r=1}^{N-1} (A_r \cos r\phi + B_r \sin r\phi) + A_N \cos N\phi \quad (2-82)$$

with which the Fourier conjugate  $\epsilon(\phi)$  becomes:

$$\epsilon(\phi) = \sum_{r=1}^{N-1} (A_r \sin r\phi - B_r \cos r\phi) + A_N \sin N\phi \quad (2-83)$$

Watson then deduced that:

$$\epsilon(\phi_m) = - \sum_{p=1}^{N-1} \frac{1}{N} \cot \left[ \frac{p\pi}{2N} \right] \left[ \psi_{m+p} - \psi_{m-p} \right]$$

$$\text{and } \frac{d\epsilon}{d\phi_m} = \frac{1}{2N} \psi_m - \sum_{p=1}^{N-1} \frac{1}{2N} \operatorname{cosec}^2 \left[ \frac{p\pi}{2N} \right] \left[ \psi_{m+p} + \psi_{m-p} \right] \quad (2-84)$$

$$+ \begin{cases} +0 & \text{if } N \text{ is even} \\ - \frac{\psi_{m+N}}{2N} & \text{if } N \text{ is odd} \end{cases}$$

When  $N=20$  (for 40 points around the profile), the coefficients of the  $\psi_m$ -terms in these equations are given in Table 1.

It should be noted that in order to derive the  $\psi$ -values at 40 equally spaced  $\psi$ -values around the profile, an interpolation procedure must be used since the coordinates of the profile are usually given at specific percentages of the chord. In that case more accurate results are obtained if the given profile coordinates are first transformed to  $\psi$  and  $\phi$ -values, before the required  $\psi$ -values at the 40 equally spaced  $\phi$ -values, given by  $\phi_m = m\pi/N$ , where  $m=0,1,2,\dots,2N-1$ , are determined by interpolation. Likewise it is recommended that the velocity distribution at the given profile stations, if required, is calculated directly from equation 2-79 rather than by interpolation from the values for the

velocity at the 40 equally spaced positions. This necessitates that the required  $\varepsilon(\phi)$  and  $d\varepsilon/d\phi$ -values for the positions at which the profile coordinates are given, are obtained by interpolation from the calculated values at the 40 equally spaced positions.

Before continuing this discussion of how this method can be used to derive approximate three-dimensional pressure distributions for propeller blades, it is appropriate to demonstrate the accuracy of this calculation method. Table 2 gives the results of equation 2-79 and the values from Abbott and Von Doenhoff [2-46] for the NACA 0012 section at zero incidence and the NACA 64-012 section at 4 degrees incidence in potential flow.

p	$\varepsilon(\phi_m)$	$\frac{d\varepsilon}{d\phi_m}$
0	0	10
1	-0.6353102	-4.061191
2	0	0
3	-0.2082650	-0.458743
4	0	0
5	-0.1207107	-0.170711
6	0	0
7	-0.0815926	-0.091573
8	0	0
9	-0.0585425	-0.059272
10	0	0
11	-0.0427040	-0.043236
12	0	0
13	-0.0306400	-0.034388
14	0	0
15	-0.0207107	-0.029289
16	0	0
17	-0.0120039	-0.026441
18	0	0
19	-0.0039351	-0.025155
20	0	0

Table 1. Coefficients of  $\psi_{m+p}$  for N=20 in equation 2-84

NACA 0012 at zero incidence:			NACA 64 <sub>1</sub> -012 at 4 degrees incidence				
$x_c$	Values from [2-46]	Values from equation 2-79	$x_c$	Values from [2-46]		Values from equation 2-79	
	v/U	v/U		back v/U	face v/U	back v/U	face v/U
0	0	0	0	1.136	1.136	1.168	1.168
0.005	0.800	0.811	0.005	1.660	0.072	1.687	0.082
0.0125	1.005	0.994	0.0125	1.617	0.403	1.605	0.424
0.025	1.114	1.113	0.025	1.513	0.613	1.492	0.616
0.050	1.174	1.164	0.050	1.524	0.770	1.412	0.771
0.075	1.184	1.178	0.075	1.381	0.847	1.372	0.846
0.100	1.188	1.185	0.100	1.354	0.894	1.347	0.893
0.150	1.188	1.183	0.150	1.324	0.954	1.318	0.953
0.200	1.183	1.176	0.200	1.306	0.992	1.299	0.990
0.250	1.174	1.166	0.250	1.290	1.022	1.287	1.020
0.300	1.162	1.155	0.300	1.280	1.044	1.277	1.041
0.400	1.135	1.130	0.400	1.266	1.076	1.258	1.070
0.500	1.108	1.105	0.500	1.211	1.061	1.206	1.058
0.600	1.080	1.079	0.600	1.151	1.035	1.148	1.032
0.700	1.053	1.053	0.700	1.086	1.000	1.086	0.998
0.800	1.022	1.024	0.800	1.020	0.960	1.019	0.957
0.900	0.978	0.982	0.900	0.956	0.914	0.951	0.911
0.950	0.952	0.940	0.950	0.921	0.895	0.915	0.889
1.000	0	0	1.000	0.880*	0.880*	0.974*	0.974*

\*These values are unequal to zero due to the cusped trailing edge for which  $\rho_t=0$

Table 2. Comparison of velocity distributions calculated by means of Goldsteins 3rd approximation and the values given by Abbott and Von Doenhoff [2-46].



#### 2.4.2 Application to Propeller Blades

For the ultimate purpose of calculating cavitation on propeller blades, the pressure distribution must be calculated in considerable detail, particularly in the region of maximum velocity. In non-uniform flow a blade section seldom ever works at its design (ideal) angle of attack. This implies that in most cases the minimum pressure is found to occur near the leading edge. It is advisable, therefore, to calculate the velocity distribution in some 25 to 30 points on both the back and the face of a blade section, of which some 6 or so points should be situated in the first 2% of the chord length. Good experience will be obtained with the array: 0, 0.125, 0.25, 0.5, 0.75, 1.25, 1.75, 2.5, 5, 7.5, 10, 15, 20, 25, 30, 35, 40, 45, 50, 55, 60, 65, 70, 75, 80, 85, 90, 95, 97.5 and 100 percent of the chord.

A standard procedure involving these points will often require the calculation of extra camber and thickness ordinates by interpolation. For standard-type camber lines and use of an adequate interpolation procedure, this should cause no problem. For extra thickness distribution ordinates, however, a straightforward interpolation procedure cannot be used due to the large variation in curvature of most thickness forms in the region of the leading edge. The calculation of extra thickness ordinates can be achieved by means of the ratio of the ordinates of the given thickness distribution to the ordinates of an elliptic thickness distribution. Here the maximum thickness of the elliptical thickness distribution must be chosen equal to the maximum thickness of the given thickness form. Then the thickness ratio has values equal to unity at the leading and trailing edge and also at  $x_c/c=0.5$  if the position of maximum thickness of the given thickness form is situated halfway along the chord. For all standard-types of thickness forms, the resulting values for this thickness ratio constitute a smooth curve from leading to trailing edge. The analytical expression for this ratio is:

$$t_R = y_g/y_e', \quad (2-85)$$

$$\text{where } y_e = \frac{t}{2} \sin \left[ \arccos(1-2x_c/c) \right], \quad (2-86)$$

in which  $t_R$  = ratio of given to elliptical thickness ordinates,  
 $y_g$  = ordinate of given thickness distribution,  
 $y_e$  = ordinate of elliptical thickness distribution,  
 $t$  = maximum thickness of blade section,  
 $x_c$  = coordinate along chord,  
 and  $c$  = chord length.

Extra values of  $y_g$  can now be obtained by determining the value of the thickness ratio  $t_R^1$  at the required position along the chord  $x_c^1$  by interpolation, from which:

$$y_g^1 = t_R^1 \cdot \frac{t}{2} \sin \left[ \arccos(1-2x_c^1/c) \right] \quad (2-87)$$

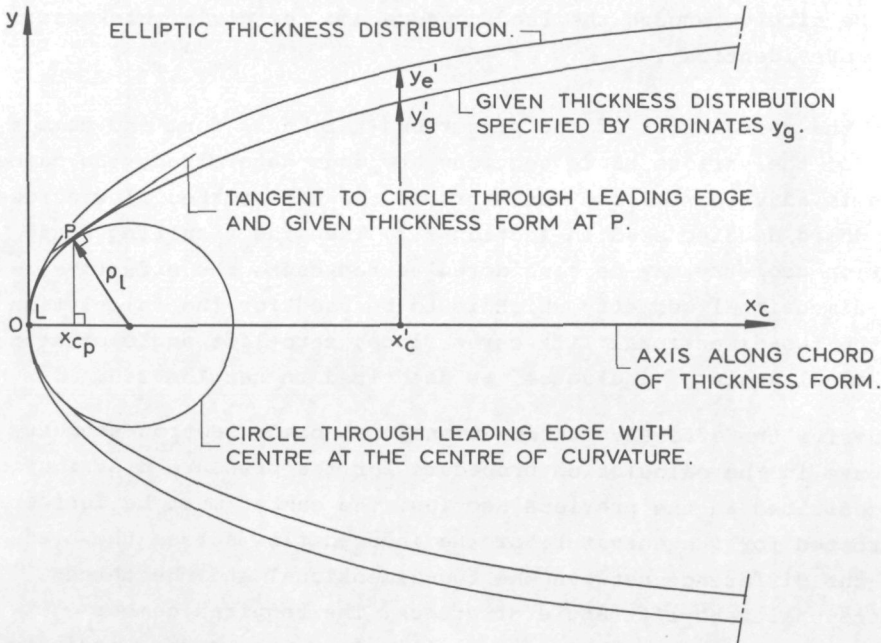


FIG. 11. SKETCH TO DEFINE USED GEOMETRIC CONCEPTS AT LEADING EDGE FOR CALCULATION OF ADDITIONAL ORDINATES OF THICKNESS FORM.

A difficulty is incurred at the leading edge when the given thickness form changes over into the circle passing through the leading edge with a radius equal to the radius of curvature of the leading edge. For points situated between the leading edge and  $x_{c_p}$ , as defined in Fig. 11, the ordinates of the given thickness distribution are equal to the ordinates of this circle. The value of the thickness ratio in this region is:

$$t_R = \frac{\rho_1^2 - (x_c - \rho_1)^2}{\frac{t}{2} \sin [\arccos(1 - 2x_c/c)]} \quad (2-88)$$

$x_c < x_{c_p}$

in which  $\rho_1$  = radius of curvature of leading edge.

To determine the value of  $x_{c_p}$ , i.e. the location of the point P (see Fig. 11), use can be made of the fact that at P the tangents to the circle through the leading edge and the given thickness form are identical.

When the coordinates of the prescribed thickness form and camber line of the various blade sections are thus determined, the camber line is adjusted for the curvature of the undisturbed flow across the chord as discussed in section 2.3. Then the resulting blade section geometry may be considered to represent the effective two-dimensional geometry which is to be used for the calculation of the two-dimensional lift-curve slope, zero-lift angle of attack and ideal angle of incidence, as described in section 3.3.

To derive the effective three-dimensional blade section geometry for use in the calculation procedure for the pressure distribution as described in the previous section, the camber must be further corrected for the curvature of the induced flow across the blade and the difference between the two-dimensional and the three-dimensional zero-lift angle of attack. The required camber distribution can be obtained by multiplying each camber ordinate by the ratio of the actual three-dimensional lift coefficient, without the influence of viscosity, to the two-dimensional lift coefficient in potential flow, both at zero incidence (relative to the orientation of the nose-tail line of the blade section), viz:

Bibliotheek TU Delft  
Afdeling Leverantie  
Prometheusplein 1  
2600 MG Delft

Information or extending loan period: +31 15 27 85678

## COLLECTION TICKET FOR DOCUMENT REQUESTS

Requested on: 08/02/2008

Time: 11:15

Return before (see stamp):

7 APR 2008

Material requested: Oossanen, Pieter van / Calculation of performance and cavitation characteristics of propellers including effects of non-uniform flow and viscosity ; Wageningen : Veenman, 1974 ;

Barcode: 3814577

Call Num.: 24435125

Sub Library: CBMG

Item Status: loan

Requested For: ID: 4002088

Status: Medewerkers TU Delft

Ms. Li, Ziru  
Fac. 3ME / 7-1-107  
Mekelweg 2  
2628 CD Delft  
Rasbak 7

Pickup Location: Office address

Your request cannot be supplied for the following reason:

Material not available

Only for perusal in the library

Outstanding fine

Other namely:

You have too many books

Li, Ziru

08/02/2008

$$f_{x_c}(x, \theta) = \left[ f_{g_{x_c}}(x, \theta) - \Delta f_{g_{x_c}}(x, \theta) \right] \frac{\alpha_0(x, \theta)}{\beta \cdot K_c(x, \theta)} \quad (2-89)$$

where  $f_{x_c}(x, \theta)$  = effective camber coordinate at  $x_c$  along the chord for the blade section at  $x$  at the angular blade position given by  $\theta$ ,

$f_{g_{x_c}}(x, \theta)$  = geometric camber at  $x_c$ ,

$\Delta f_{g_{x_c}}(x, \theta)$  = change in geometric camber at  $x_c$  due to curvature of undisturbed streamlines,

$\alpha_0(x, \theta)$  = three-dimensional zero-lift angle of incidence given by equation 2-32,

$\beta$  = zero-lift angle of incidence following from conformal transformation procedure (used in equation 2-80) or equation 3-24,

and  $K_c(x, \theta)$  = propeller lifting surface correction for camber.

The blade section geometry thus determined constitutes the effective geometry for the three-dimensional velocity distribution calculation. The effective angle of attack for this calculation can be derived from the assumption that the potential flow approximation for the three-dimensional case must result in a value of the lift coefficient equal to the value resulting from propeller theory (section 2.2.1) but without viscous losses, viz:

$$C_{L_p}(x, \theta) = C_L(x, \theta) + \Delta C_L(x, \theta) \quad (2-90)$$

where:

$$\Delta C_L(x, \theta) = \frac{2\pi e^{\psi_0} \sin[\alpha(x, \theta) - \alpha_0(x, \theta)] - 2\pi K_s(x, \theta) [\alpha(x, \theta) - \alpha_0(x, \theta)]}{K_c(x, \theta)}$$

$$\text{or } \Delta C_L(x, \theta) \approx \frac{C_L(x, \theta) \left[ 1 + \frac{t}{c}(x) - K_s(x, \theta) \right]}{K_s(x, \theta)} \quad (2-91)$$

where  $K_s(x, \theta)$  = three-dimensional lift-curve slope factor discussed in section 3.3.1.

It follows that in potential flow:

$$C_L(x, \theta) + \Delta C_L(x, \theta) = 2\pi e^{\psi_0} \sin[\alpha_{\text{eff}}(x, \theta) - \alpha_0(x, \theta)] \quad (2-92)$$

where  $\alpha_{\text{eff}}(x, \theta)$  = effective angle of attack for pressure distribution calculation.

Solving for  $\alpha_{\text{eff}}(x, \theta)$  gives:

$$\alpha_{\text{eff}}(x, \theta) = \arcsin \left[ \frac{C_L(x, \theta) + \Delta C_L(x, \theta)}{2\pi e^{\psi_0}} \right] + \alpha_0(x, \theta) \quad (2-93)$$



## CHAPTER 3

### ASSESSMENT OF VISCOSITY EFFECTS ON PROPELLER-BLADE SECTION CHARACTERISTICS AND LOADING DISTRIBUTIONS

#### 3.1 Introductory Remarks

The use of accurate values for the lift and drag of propeller blade sections in the theory of the previous chapter is essential. The error in the values of the hydrodynamic pitch angle and the radial load distribution is directly proportional to the errors in the used lift and drag data of the profiles of which the propeller blades are composed.

At present, no universal procedure for the calculation of two-dimensional lift and drag data is available. With the assumption of potential flow the calculation of the lift of a given profile is a simple matter and can be performed exactly as shown by Theodorsen in 1931 [3-1]. Yet the influence of viscosity, generally resulting in a decrease in lift (sometimes of the order of 30 percent or more) necessitates the application of corrections which are deduced from systematic force measurements in wind or water tunnels. A large compilation of results of such measurements is available in the form of books by Riegels [3-2] and by Abbott and Von Doenhoff [3-3]. Two-dimensional calculation procedures for the drag are also available in the absence of flow separation. Here, however, the differences with experimental values can sometimes be appreciable. This state of affairs does not mean that attempts at finding general relations between profile geometry and lift and drag data have not been performed in the past. Endeavours in this regard have been undertaken by Burrill [3-4], Hill [3-5] and recently by Van Oossanen [3-6]. The obtained results, however, should be considered valid only for the profiles from which these relations were derived and should not be applied in a general design or calculation procedure. For example, the lift correction factors derived by Burrill and used by O'Brien [3-7], Sontvedt [3-8], Glover [3-9] and many others, predict a lift decrease with increase of blade section thickness approximately according to the formula:

$$K_s = 0.947 - 9.76(t/c)^3, \quad (3-1)$$

in which  $K_s$  is the lift-curve slope correction factor with which the theoretical flat-plate value of  $2\pi$  is to be multiplied to obtain the actual two-dimensional lift-curve slope. Here  $t/c$  is the ratio of maximum thickness to chord length. This is only a reasonable assumption for super-critical values of the Reynolds number for profiles with the position of maximum thickness at about 30 percent of the chord. With this formula, erroneous results are obtained, for example, for the NACA 63, 64, 65 and 66-series thickness distributions. The same holds for Burrill's relation for the effect of viscosity on the theoretical angle of zero-lift. This relation can be approximately represented by means of the formula:

$$K_{\alpha_0} = 0.972 - 0.169(t/c) - 2.78(t/c)^2 + 21.0(f_x/c)(t/c)^2 - (f_x/c)^2 \left[ 0.320 + 278(t/c)^3 \right] - (f_x/c)^3 \left[ 28.7(t/c)^2 - 335((t/c)^3) \right] \quad (3-2)$$

in which  $K_{\alpha_0}$  is the factor with which the theoretical two-dimensional value is to be multiplied to obtain the experimental two-dimensional value,  $f/c$  is the ratio of maximum camber to chord length and  $f_x/c$  is the ratio of the position of maximum camber to chord length. This relation fails to discern between the different effects of viscosity, for example, on profiles with the NACA  $a=0.8$  and  $a=1.0$  camber lines. The effect of viscosity on profiles of small thickness having the first-mentioned camber line can be expressed in terms of a value of  $K_{\alpha_0}$  larger than unity, while in the latter case this factor is about  $0.75$ . Equation 3-2 gives the same value in both cases.

It is necessary, therefore, either to persist in using appropriate experimental lift and drag data from available literature, or to use a different approach to the problem of finding general relations between profile form and the lift and drag characteristics, an approach necessarily involving knowledge

of boundary layer characteristics on the profile. The first-mentioned possibility compels the use of standard aerofoil sections in propeller design. In the present study this is a drawback, since it is necessary to effectively distort blade section camber to account for the curvature of the undisturbed incoming flow over a blade section by which non-standard camber lines are obtained (see chapter 2). Furthermore, most of the available aerofoil data is limited to a minimum thickness of 6 percent of the chord length, while the thickness of propeller blade sections near the tip are often appreciably thinner. It was, therefore, considered necessary to find an improved method by which appropriate lift and drag data of propeller blade sections can be ascertained. This is the subject of section 3 and 4 of this chapter. The described method for the effect of viscosity on lift-curve slope and angle of zero-lift (section 3) incorporates boundary-layer theory which is first presented in section 2.

An improvement of the first inviscid approximation to the chordwise pressure distribution for the unmixed boundary case (no flow separation and no cavitation) is obtained if the boundary of the inviscid region is taken to be at a distance from the surface equal to the displacement thickness of the boundary layer. The new boundary then extends to infinity downstream to take into account the thickness of the wake. The value of the displacement thickness is given by the first boundary-layer approximation. With this new boundary, a revised velocity distribution can be calculated with which the boundary-layer calculation can be repeated. In this way an iteration procedure is started, the result of which is termed the second inviscid approximation. This procedure allows the calculation of the effect of Reynolds number on the pressure distribution which is the cause of an important scale effect on propeller cavitation properties. The analytical solution, however, requires a great deal of work, the results of which for a propeller blade are dubious due to possible errors in the result of the first inviscid approximation. This is why the second inviscid approximation has not yet been attempted. Here also, such a fundamental method for the effect of viscosity on the pressure distribution will not be employed. Instead a

relatively simple viscosity correction is used, which is described in section 5 of this chapter.

### 3.2 Two-Dimensional Boundary Layer Calculations

#### 3.2.1 The Laminar Boundary Layer and Laminar Separation

For the calculation of the laminar boundary layer characteristics use was made of the approximate method of Twaites [3-10]. This method only requires knowledge of the pressure distribution along the two-dimensional body at the edge of the boundary layer.

The momentum thickness is obtained from the equation:

$$\frac{v_{x_s}^2}{\nu} = \frac{0.45}{\nu^5} \int_0^{x_s} v_{x_s}^5 dx_s \quad (3-3)$$

- where  $\theta$  = momentum thickness at  $x_s$ ,  
 $v_{x_s}$  = velocity at  $x_s$  just outside the boundary layer,  
 $x_s$  = arc length along the surface of the body from beginning of boundary layer,  
 and  $\nu$  = kinematic viscosity.

This equation is an average result of a number of exact solutions. With this relation for the momentum thickness, a parameter  $m$  can be calculated according to:

$$m = - \frac{dv_{x_s}}{dx_s} \theta^2 / \nu \quad (3-4)$$

The displacement thickness of the boundary layer and the skin friction can be determined from this parameter by means of given numerical values connecting the value of  $m$  with the form parameter  $H(m)$  and the function  $l(m)$  for the calculation of the skin friction. The form parameter is defined as:

$$H(m) = \delta^* / \theta \quad (3-5)$$

where  $\delta^*$  is the displacement thickness of the boundary layer. The wall shear stress  $\tau_w$  is determined from:

$$\frac{\tau_w}{\rho v^2 x_s} = \frac{l(m) \nu}{v x_s \theta} \quad (3-6)$$

The relation between  $m$ ,  $H(m)$  and  $l(m)$ , as modified by Curl and Skan [3-11] is given in Table 3. Separation of the laminar boundary layer occurs when  $m=0.09$  or when  $l(m)=0$

$m$	$l(m)$	$H(m)$	$m$	$l(m)$	$H(m)$
-0.250	0.500	2.00	0.040	0.153	2.81
-0.200	0.463	2.07	0.048	0.138	2.87
-0.140	0.404	2.18	0.056	0.122	2.94
-0.120	0.382	2.23	0.060	0.113	2.99
-0.100	0.359	2.28	0.064	0.104	3.04
-0.080	0.333	2.34	0.068	0.095	3.09
-0.064	0.313	2.39	0.072	0.085	3.16
-0.048	0.291	2.44	0.076	0.072	3.24
-0.032	0.268	2.49	0.080	0.056	3.35
-0.016	0.244	2.55	0.084	0.038	3.47
0.000	0.220	2.61	0.086	0.027	3.54
0.016	0.195	2.67	0.088	0.015	3.62
0.032	0.168	2.75	0.090	0.000	3.70

Table 3. Functions for the calculation of  $\delta^*$  and  $\tau_w$  from the parameter  $m$ .

### 3.2.2 Estimation of Laminar-Turbulent Transition

The method adopted for the approximate calculation of the point of transition is that of Michel [3-12] as modified by Smith [3-13]. This method is simple, and comparisons with experimental results have shown it to be reasonably reliable for pressure profiles with a peaked minimum. For flat pressure profiles the method is less accurate.

The method consists of determining a critical value of the Reynolds number based on the momentum thickness. Michel found that experimental transition data could be correlated well by means of a plot of the transition Reynolds number based on momentum thickness,  $R_{\theta_{tr}}$ , versus the conventional Reynolds number based on the distance  $x$  along the body,  $R_{x_{tr}}$ . Smith later showed that this correlation can be explained by boundary-layer stability theory and that Michel's line is in fact the locus of a specific amplification of a Tollmien-Schlichting disturbance in the boundary layer. Smith's version of Michel's criterion is:

$$R_{\theta_{tr}} = 1.174 R_{x_{tr}}^{0.46} \quad (3-7)$$

where  $R_{\theta} = v_{x_c} \cdot \theta / \nu$  (3-8)

and  $R_{x} = x_s \cdot U / \nu$  (3-9)

in which  $U$  is the free-stream velocity. The validity of this criterion is for a value of  $R_{x_{tr}}$  between  $3 \times 10^5$  and  $2 \times 10^7$ , but may be used for reasonably reliable estimations of the point of transition for a value of  $R_{x_{tr}}$  between  $10^5$  and  $10^8$ .

### 3.2.3 The Turbulent Boundary Layer and Turbulent Separation

A simple and accurate method for the calculation of turbulent boundary layers has been developed by Nash and Macdonald [3-14] for the case that the pressure is steadily increasing along the body from the origin of the turbulent boundary layer. This method can be applied to most standard types of profiles at moderate



incidence angles since the pressure-decreasing part of the leading-edge suction peak is often laminar. The treatment of boundary layers for which the pressure-gradient is steadily increasing is relatively simple because the shape of the main velocity profile is principally a function of the local pressure gradient and only the thickness of the layer significantly reflects the influence of upstream history. In this case, turbulent boundary layers are characterized by a particular constant value of the pressure-gradient parameter  $\Pi$  and a corresponding constant value of the shape factor  $G$  along the body. The pressure-gradient parameter  $\Pi$  is defined as:

$$\Pi = \frac{\delta^*}{\tau_w} \cdot \frac{dp}{dx_s} \quad (3-10)$$

where  $\delta^*$  = displacement thickness of turbulent boundary layer,  
 $\tau_w$  = wall shear stress,  
and  $\frac{dp}{dx_s}$  = pressure gradient at edge of boundary layer.

The shape factor  $G$  in incompressible flow is defined as:

$$G = \sqrt{\rho v_{x_s}^2 / \tau_w} [1 - 1/H] \quad (3-11)$$

where  $v_{x_s}$  = velocity at edge of boundary layer

$$\text{and } H = \delta^* / \theta \quad (3-12)$$

in which  $\theta$  = momentum thickness of turbulent boundary layer.

It is shown by Nash [3-15] that for all turbulent boundary layers of this type, a good empirical fit to the unique function  $G(\Pi)$ , as determined from experiments, is:

$$G = 6.1 \sqrt{\Pi + 1.81}^{-1.7} \quad (3-13)$$

which relation constitutes a locus of all such boundary layers.

The growth of a turbulent boundary layer in two dimensions can be obtained by integrating the momentum-integral equation:

$$\frac{d}{dx_s}(\rho v_{x_s}^2 \theta) = \tau_w(1+\Pi) \quad (3-14)$$

$$\text{or } \frac{d\theta}{dx_s} = -(H+2)\theta/v_{x_s} \cdot dv_{x_s}/dx_s + \tau_w/\rho v_{x_s}^2 \quad (3-15)$$

The skin-friction law used, developed by Nash [3-16], for incompressible flow is:

$$\frac{\tau_w}{\rho v_{x_s}^2} = \left[ 2.4711 \ln(v_{x_s} \cdot \theta/v) + 475 + 1.5G + \frac{1724}{G^2 + 200} - 16.87 \right]^{-2} \quad (3-16)$$

If only the momentum thickness is required, Nash and Macdonald give as an approximation to the equations above the following relation:

$$\begin{aligned} \frac{d\theta}{dx_s} = & \left[ 2.4711 \ln(v_{x_s} \cdot \theta/v) + 4.75 \right]^{-2} - 3\theta/v_{x_s} \cdot dv_{x_s}/dx_s \\ & + 120(\theta/v_{x_s} \cdot dv_{x_s}/dx_s)^2 - 25000(\theta/v_{x_s} \cdot dv_{x_s}/dx_s)^3 \end{aligned} \quad (3-17)$$

The actual calculations are performed assuming continuity of momentum thickness at the point of transition as long as  $v_{x_s} \theta/v$  is greater than 320. If this is not the case then  $\theta$  is increased to make  $v_{x_s} \theta/v = 320$ . An iteration is then performed at the transition point, involving  $\theta$ ,  $\Pi$ ,  $G$ ,  $\tau_w$  and  $H$ . The first value of  $G$  is assumed to be 6.5. With these values of  $\theta$  and  $G$ , the values of  $\tau_w$ ,  $H$  and  $\Pi$  can be determined with which a second value of  $G$  can be calculated from equation 3-13. On convergence, the value of  $d\theta/dx_s$  is calculated according to equation 3-15.

At the following points this procedure can be repeated when it is assumed that a first value of  $\theta$  can be obtained from:

$$\theta_{i_1} = \theta_{i-1} + \left[ \frac{d\theta}{dx_s} \right]_{i-1} \Delta x_s \quad (3-18)$$

An adequate, first value of  $G$  can be the final value at the previous position on the profile. The iteration procedure must now involve  $d\theta/dx_s$  and the value for the momentum thickness according to:

$$\theta_i = \theta_{i-1} + \left[ \frac{d\theta}{dx_{s_{i-1}}} + \frac{d\theta}{dx_{s_i}} \right] \frac{\Delta x_s}{2} \quad (3-19)$$

This procedure necessarily requires that points at which these calculations are to be performed, are situated close together. If the value of  $\Pi$  during the iterations becomes smaller than -1.5, the value of  $\Pi$  is put equal to -1.5.

This solution procedure assumes precise local equilibrium corresponding to an exact correlation between the  $G^v\Pi$  trajectory and the equilibrium locus as given by equation 3-13. The derivative  $d\theta/dx_s$  is roughly a linear function of  $-(\theta/v_{x_s})dv_{x_s}$ , and over a limited range of Reynolds numbers the effect of variations of  $v_{x_s}^{\theta/\nu}$  is approximately independent of the pressure gradient.

Turbulent separation is predicted when  $\tau_w/\rho v_{x_s}$  becomes less than 0.0001.

Table 4 gives the results of laminar and turbulent boundary layer calculations for the NACA 64<sub>1</sub>-012 profile at zero incidence at a Reynolds number of  $7 \times 10^5$ . The profile is assumed to be 1 meter in length. Transition (and the origin of the turbulent boundary layer) was calculated to occur at  $x_c/c=0.4808$  and laminar separation at  $x_c/c=0.51$ . Turbulent separation was calculated to occur at  $x_c/c=0.947$ .

### 3.3 Effect of Viscosity on Lift-Curve Slope and Angle of Zero-Lift

#### 3.3.1 Lift-Curve Slope

Experimental values of the sectional lift-curve slope,  $dC_L/d\alpha_2$ , and angle of zero-lift,  $\alpha_{0_2}$ , of a large number of aerofoils have been

Laminar Boundary Layer Characteristics

x-coord.	pressure coefficient	momentum thickness	laminar separation parameter	Reynolds number based on $\theta$	Smith's transition Reynolds number
$x_c$	$C_p$	$\theta$	$m$		
$+1.000 \times 10^{-10}$	$+9.999 \times 10^{-1}$	0	0	0	$+1.000 \times 10^{-4}$
$+5.000 \times 10^{-3}$	$+2.138 \times 10^{-1}$	$+6.362 \times 10^{-5}$	$+2.171 \times 10^{-1}$	$+3.884 \times 10^{+1}$	$+7.142 \times 10^{+1}$
$+7.500 \times 10^{-3}$	$+8.391 \times 10^{-2}$	$+6.634 \times 10^{-5}$	$+6.894 \times 10^{-2}$	$+4.371 \times 10^{+1}$	$+8.035 \times 10^{+1}$
$+1.250 \times 10^{-2}$	$-3.347 \times 10^{-2}$	$+7.974 \times 10^{-5}$	$+4.120 \times 10^{-2}$	$+5.581 \times 10^{+1}$	$+9.427 \times 10^{+1}$
$+2.500 \times 10^{-2}$	$-1.165 \times 10^{-1}$	$+1.128 \times 10^{-4}$	$+2.311 \times 10^{-2}$	$+8.210 \times 10^{+1}$	$+1.196 \times 10^{+2}$
$+5.000 \times 10^{-2}$	$-1.968 \times 10^{-1}$	$+1.572 \times 10^{-4}$	$+1.881 \times 10^{-2}$	$+1.184 \times 10^{+2}$	$+1.558 \times 10^{+2}$
$+7.500 \times 10^{-2}$	$-2.363 \times 10^{-1}$	$+1.921 \times 10^{-4}$	$+1.470 \times 10^{-2}$	$+1.471 \times 10^{+2}$	$+1.836 \times 10^{+2}$
$+1.000 \times 10^{-1}$	$-2.609 \times 10^{-1}$	$+2.219 \times 10^{-4}$	$+1.331 \times 10^{-2}$	$+1.716 \times 10^{+2}$	$+2.070 \times 10^{+2}$
$+1.500 \times 10^{-1}$	$-2.945 \times 10^{-1}$	$+2.713 \times 10^{-4}$	$+1.231 \times 10^{-2}$	$+2.126 \times 10^{+2}$	$+2.460 \times 10^{+2}$
$+2.000 \times 10^{-1}$	$-3.161 \times 10^{-1}$	$+3.133 \times 10^{-4}$	$+1.189 \times 10^{-2}$	$+2.474 \times 10^{+2}$	$+2.786 \times 10^{+2}$
$+2.500 \times 10^{-1}$	$-3.349 \times 10^{-1}$	$+3.492 \times 10^{-4}$	$+1.210 \times 10^{-2}$	$+2.778 \times 10^{+2}$	$+3.072 \times 10^{+2}$
$+3.000 \times 10^{-1}$	$-3.493 \times 10^{-1}$	$+3.819 \times 10^{-4}$	$+1.006 \times 10^{-2}$	$+3.054 \times 10^{+2}$	$+3.330 \times 10^{+2}$
$+3.500 \times 10^{-1}$	$-3.582 \times 10^{-1}$	$+4.133 \times 10^{-4}$	$+6.120 \times 10^{-3}$	$+3.316 \times 10^{+2}$	$+3.565 \times 10^{+2}$
$+4.000 \times 10^{-1}$	$-3.614 \times 10^{-1}$	$+4.445 \times 10^{-4}$	$-1.278 \times 10^{-2}$	$+3.570 \times 10^{+2}$	$+3.784 \times 10^{+2}$
$+4.500 \times 10^{-1}$	$-3.364 \times 10^{-1}$	$+4.877 \times 10^{-4}$	$-5.198 \times 10^{-2}$	$+3.881 \times 10^{+2}$	$+3.989 \times 10^{+2}$
$+5.000 \times 10^{-1}$	$-2.884 \times 10^{-1}$	$+5.437 \times 10^{-4}$	$-8.446 \times 10^{-2}$	$+4.249 \times 10^{+2}$	$+4.182 \times 10^{+2}$
$+5.500 \times 10^{-1}$	$-2.421 \times 10^{-1}$	$+6.006 \times 10^{-4}$	$-1.056 \times 10^{-1}$	$+4.609 \times 10^{+2}$	$+4.366 \times 10^{+2}$
$+6.000 \times 10^{-1}$	$-1.936 \times 10^{-1}$	$+6.619 \times 10^{-4}$	$-1.372 \times 10^{-1}$	$+4.979 \times 10^{+2}$	$+4.541 \times 10^{+2}$

+6.500x10 <sup>-1</sup>	-1.428x10 <sup>-1</sup>	+7.292x10 <sup>-4</sup>	-1.766x10 <sup>-1</sup>	+5.367x10 <sup>+2</sup>	+4.709x10 <sup>+2</sup>
+7.000x10 <sup>-1</sup>	-9.060x10 <sup>-2</sup>	+8.034x10 <sup>-4</sup>	-2.270x10 <sup>-1</sup>	+5.776x10 <sup>+2</sup>	+4.871x10 <sup>+2</sup>
+7.500x10 <sup>-1</sup>	-3.625x10 <sup>-2</sup>	+8.871x10 <sup>-4</sup>	-2.934x10 <sup>-1</sup>	+6.217x10 <sup>+2</sup>	+5.026x10 <sup>+2</sup>
+8.000x10 <sup>-1</sup>	+1.955x10 <sup>-2</sup>	+9.823x10 <sup>-4</sup>	-3.721x10 <sup>-1</sup>	+6.697x10 <sup>+2</sup>	+5.176x10 <sup>+2</sup>
+8.500x10 <sup>-1</sup>	+7.463x10 <sup>-2</sup>	+1.088x10 <sup>-3</sup>	-4.640x10 <sup>-1</sup>	+7.208x10 <sup>+2</sup>	+5.321x10 <sup>+2</sup>
+9.000x10 <sup>-1</sup>	+1.289x10 <sup>-1</sup>	+1.207x10 <sup>-3</sup>	-5.853x10 <sup>-1</sup>	+7.760x10 <sup>+2</sup>	+5.462x10 <sup>+2</sup>
+9.500x10 <sup>-1</sup>	+1.833x10 <sup>-1</sup>	+1.345x10 <sup>-3</sup>	-5.375x10 <sup>0</sup>	+8.369x10 <sup>+2</sup>	+5.598x10 <sup>+2</sup>
+1.000x10 <sup>0</sup>	+7.290x10 <sup>-1</sup>	+2.369x10 <sup>-3</sup>	-1.667x10 <sup>+1</sup>	+1.223x10 <sup>+3</sup>	+5.729x10 <sup>+2</sup>

Turbulent Boundary Layer Characteristics

x-coord. x <sub>c</sub>	momentum thickness $\theta$	$\Pi$	G	H	$\tau_w / \rho V_{x_s}^2$
+5.000x10 <sup>-1</sup>	+5.832x10 <sup>-4</sup>	+1.312x10 <sup>-1</sup>	+6.798x10 <sup>0</sup>	+1.507x10 <sup>0</sup>	+2.448x10 <sup>-3</sup>
+5.500x10 <sup>-1</sup>	+7.458x10 <sup>-4</sup>	+1.858x10 <sup>-1</sup>	+6.917x10 <sup>0</sup>	+1.494x10 <sup>0</sup>	+2.288x10 <sup>-3</sup>
+6.000x10 <sup>-1</sup>	+9.159x10 <sup>-4</sup>	+2.637x10 <sup>-1</sup>	+7.084x10 <sup>0</sup>	+1.489x10 <sup>0</sup>	+2.154x10 <sup>-3</sup>
+6.500x10 <sup>-1</sup>	+1.098x10 <sup>-3</sup>	+3.629x10 <sup>-1</sup>	+7.292x10 <sup>0</sup>	+1.490x10 <sup>0</sup>	+2.034x10 <sup>-3</sup>
+7.000x10 <sup>-1</sup>	+1.297x10 <sup>-3</sup>	+4.943x10 <sup>-1</sup>	+7.559x10 <sup>0</sup>	+1.495x10 <sup>0</sup>	+1.919x10 <sup>-3</sup>
+7.500x10 <sup>-1</sup>	+1.518x10 <sup>-3</sup>	+6.743x10 <sup>-1</sup>	+7.914x10 <sup>0</sup>	+1.506x10 <sup>0</sup>	+1.804x10 <sup>-3</sup>
+8.000x10 <sup>-1</sup>	+1.767x10 <sup>-3</sup>	+8.995x10 <sup>-1</sup>	+8.340x10 <sup>0</sup>	+1.522x10 <sup>0</sup>	+1.691x10 <sup>-3</sup>
+8.500x10 <sup>-1</sup>	+2.046x10 <sup>-3</sup>	+1.182x10 <sup>0</sup>	+8.852x10 <sup>0</sup>	+1.542x10 <sup>0</sup>	+1.578x10 <sup>-3</sup>
+9.000x10 <sup>-1</sup>	+2.363x10 <sup>-3</sup>	+1.598x10 <sup>0</sup>	+9.562x10 <sup>0</sup>	+1.573x10 <sup>0</sup>	+1.452x10 <sup>-3</sup>
+9.500x10 <sup>-1</sup>	+6.264x10 <sup>-3</sup>	+2.524x10 <sup>+8</sup>	+9.692x10 <sup>+4</sup>	+2.999x10 <sup>0</sup>	+3.529x10 <sup>-10</sup>
+1.000x10 <sup>0</sup>	+3.486x10 <sup>-2</sup>	+2.184x10 <sup>+24</sup>	+9.015x10 <sup>+12</sup>	+3.000x10 <sup>0</sup>	+2.728x10 <sup>-25</sup>

Table 4. Results of laminar and turbulent boundary layer calculation for NACA 64<sub>1</sub>-012 profile

tabulated by Riegels [3-2]. For these aerofoils, boundary layer calculations were performed as described in the previous section for angles of incidence corresponding to the theoretical ideal angle in potential flow  $\alpha_{i_2 p}$ ,  $\alpha_{i_2 p} + 4^\circ$  and  $\alpha_{i_2 p} + 8^\circ$ . The required velocity distributions on suction and pressure sides were calculated by the method outlined in section 2.4.1. The only allowance for viscosity on the velocity distributions was that the velocity at the trailing edge was set equal to 0.75 of the free-stream velocity. The Reynolds number values of the boundary layer calculations for each aerofoil were the same as the values for which the  $dC_L/d\alpha_2$  and  $\alpha_{0_2}$ -values are given. Coordinates of the aerofoils were obtained from Abbott and Von Doenhoff [3-3]. In all cases the origin of the laminar boundary layer was taken to be at  $x_c/c=0$ , at which the local velocity was specified to be zero. The origin of the turbulent boundary layer was taken to be at the point of transition as calculated according to section 3.2. If transition was calculated to occur downstream of the position of laminar separation, which was often the case (particularly on the pressure side at Reynolds numbers below  $10^6$ ), the calculation of the turbulent boundary layer was not attempted since accurate information regarding re-attachment of the separated boundary layer and the length of separation bubbles is still lacking. In some cases transition was calculated to occur a small distance upstream of the position of laminar separation particularly when the pressure distribution was relatively flat. An example is the case of the NACA 64<sub>1</sub>-012 aerofoil at zero incidence, the results of which are presented in Table 4. When this occurred laminar separation was nevertheless suspected since it is known that the used transition criterium gives an early prediction of transition in such cases (a general discussion of this transition criterium is given by Hall and Gibbings [3-17]). A good correlation was obtained between the experimental lift-curve slope and the sum of aerofoil thickness and displacement thickness at the position of turbulent separation in the cases in which laminar separation does not occur. As shown in Fig. 12, this thickness, denoted as  $t_s$ , may be thought of as being an effective wake thickness of the aerofoil, viz:



$$t_s = y_{s_s} + \delta_{s_s}^* + y_{s_p} + \delta_{s_p}^* \quad (3-20)$$

in which  $t_s$  = effective wake thickness,  
 $y_{s_s}, y_{s_p}$  = coordinates of suction and pressure side at the position of turbulent separation,  
 and  $\delta_{s_s}^*, \delta_{s_p}^*$  = displacement thickness of turbulent boundary layer on suction and pressure side at the position of turbulent separation.

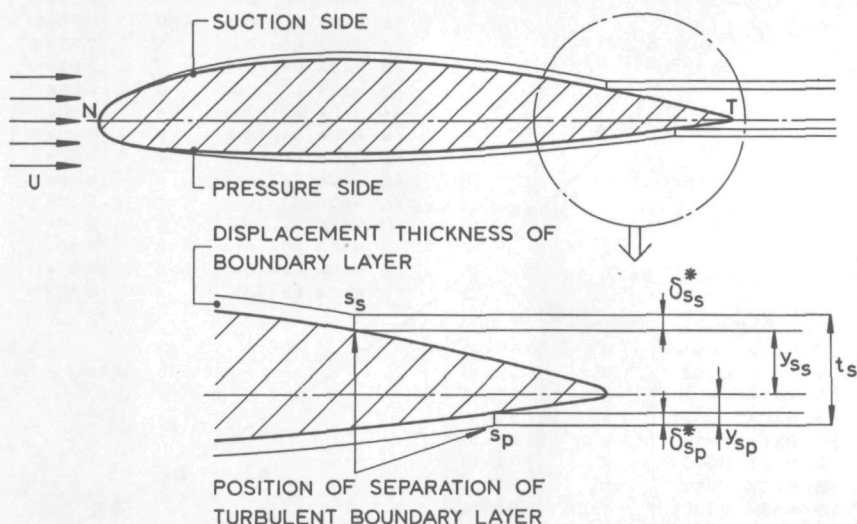


FIG. 12. SKETCH TO DEFINE VARIABLES FOR CORRELATION OF EXPERIMENTAL LIFT - CURVE SLOPE AND BOUNDARY LAYER CHARACTERISTICS

Fig. 13 gives the results for 28 aerofoils at various Reynolds number and incidence values. The correlation is surprisingly good when considering the possible inaccuracies in the boundary layer calculations and the fact that the value of  $dC_L/d\alpha_2$  given by Riegels is an average over an unspecified incidence range. The drawn curve through the spots in this figure represents the best fit. An analytical form of this curve is:

$$\frac{dC_L}{d\alpha_2} = 7.462 - \sqrt{135.2t_s/c - 2.899} \quad (3-21)$$

With this relation, the lift-curve slope factor  $K_S$ , as used by Burrill [3-4], becomes:

$$K_S = 1.188 - \sqrt{3.425t_s/c - 0.073} \quad (3-22)$$

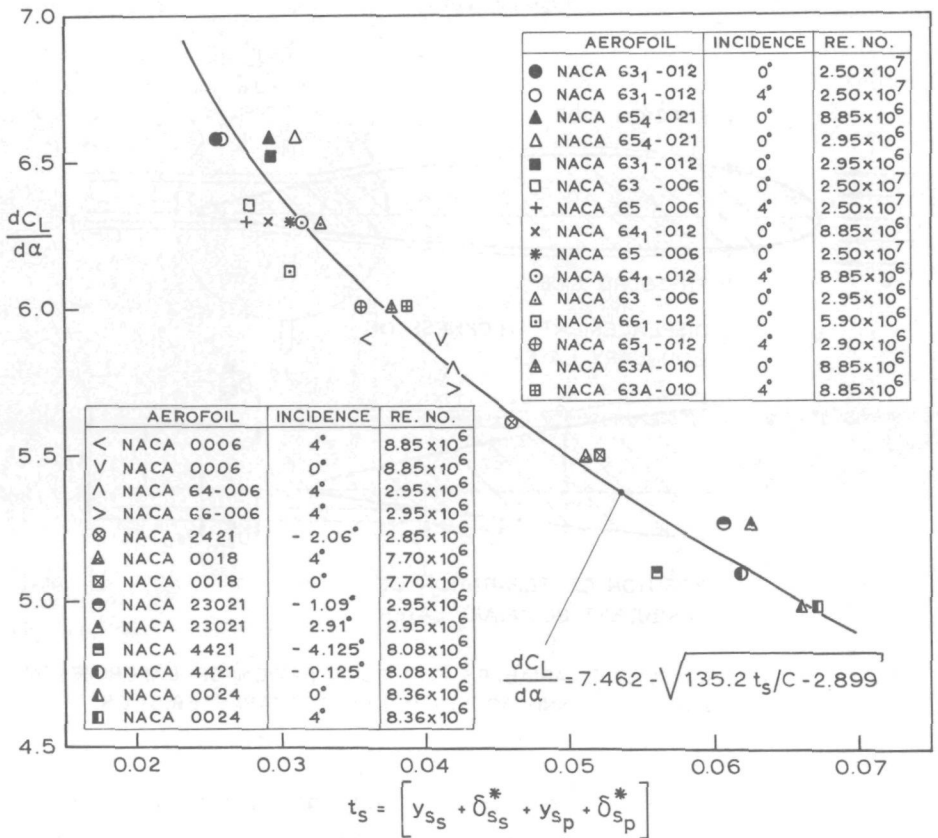


FIG. 13. CORRELATION BETWEEN EXPERIMENTAL LIFT - CURVE SLOPE AND SUM OF PROFILE AND DISPLACEMENT THICKNESS AT POSITION OF TURBULENT SEPARATION.

Some aerofoils have an appreciable variation in lift-curve slope with angle of attack. "Round back" or ogival sections, for example, are known to have this property. The explanation of this feature in the light of the results presented in Fig. 13, lies in the fact that these aerofoils tend to exhibit a forward movement of the location of turbulent separation with increasing (moderate) incidence of the flow. Hereby the value of  $t_s$  becomes larger, particularly due to the larger values of the aerofoil thickness at the point of separation. Whereas this property of a forward movement of the location of turbulent separation is quite general of all aerofoils, it was found that foils which have a relatively large slope in the region between  $x_c/c=0.9$  and the trailing edge, (i.e. a relatively large value of  $dy/dx_c$ ) display this property more extremely. In the design of lifting surfaces it is therefore important to adopt thickness distributions which not only have thin trailing edges but also small values for  $dy/dx_c$  in the region downstream of  $x_c/c=0.9$ .

To apply equation 3-21 or 3-22 to propeller-blade sections, it is recommended to calculate  $t_s$  at three (moderate) angles of incidence to determine whether the lift-curve slope appreciably varies with incidence. If so, it is advisable to adopt a formula of the type:

$$\frac{dC_L}{d\alpha_2} = A(1-B\alpha) \quad (3-23)$$

in which A and B are constants which can be determined from the calculated values for  $dC_L/d\alpha_2$  as a function of  $t_s/c$ .

The effect of roughness on  $dC_L/d\alpha_2$  can be assessed by the procedure outlined above by specifying that transition from laminar to turbulent flow occurs at the leading edge. Some calculations in this regard have shown that the momentum thickness at the location of turbulent boundary layer separation is larger and that this location moves forward. When roughness is introduced these characteristics lead to an appreciably larger effective wake thickness  $t_s$ . Here also, good agreement with experimental values was obtained on using equation 3-21 to calculate  $dC_L/d\alpha_2$  from the determined value of  $t_s/c$ .

### 3.3.2 Angle of Zero-lift

General rules for the effect of viscosity on the two-dimensional angle of zero-lift,  $\alpha_{0_2}$ , have been very difficult to ascertain in the past. It is known that in comparison to the theoretical value in potential flow,  $\alpha_{0_2p}$ , viscosity can lead to lower and higher values. A good example, already quoted, is the ratio of measured to theoretical zero-lift angle of about 0.75 for thin profiles having a NACA a=1.0 camber line and about 1.04 for thin profiles incorporating a NACA a=0.8 camber line. This case is illustrative of, probably, the only general rule which is discernable, viz, that the ratio  $\alpha_{0_2}/\alpha_{0_2p}$  increases with increasing ideal angle of incidence, which angle is a measure of the asymmetry of the camber distribution. The NACA a=1.0 camber line, which is symmetrical about the mid-chord position, has a zero-angle of ideal incidence while the NACA a=0.8 camber line, giving rise to a higher loading on the first half of the chord, has an ideal angle of incidence of  $1.4^\circ$  when the ideal lift coefficient equals 1.0. The NACA 230-series wing sections, with relatively high angles of ideal incidence, have a ratio of  $\alpha_{0_2}/\alpha_{0_2p}$  of about 1.08. The calculation of the angle of zero-lift and of the ideal angle of incidence of camber lines can be performed by means of two-dimensional thin wing theory. The resulting expressions for these quantities, according to Abbott and Von Doenhoff [3-2], are:

$$\alpha_{0_2p} = \int_{x_c/c=0}^1 \frac{y}{c} f_1 \left( \frac{x_c}{c} \right) \frac{dx_c}{c} \quad (3-24)$$

$$\text{and } \alpha_{i_2p} = \int_{x_c/c=0}^1 \frac{y}{c} f_3 \left( \frac{x_c}{c} \right) \frac{dx_c}{c} \quad (3-25)$$

$$\text{in which } f_1 \left( \frac{x_c}{c} \right) = \frac{1}{\pi [1-(x_c/c)] \sqrt{(x_c/c) [1-(x_c/c)]}} \quad (3-26)$$

$$\text{and } f_3\left(\frac{x_c}{c}\right) = \frac{1-(2x_c/c)}{2\pi \left[ (x_c/c) [1-(x_c/c)] \right]^{3/2}} \quad (3-27)$$

The functions  $f_1$  and  $f_3$  become infinite at both leading and trailing edges. Difficulties in this regard are avoided when the following formulas for evaluation of equations 3-24 and 3-25 are used, viz:

$$\alpha_{0_{2p}} = -\frac{1}{c} \sum_i k_{i1} \cdot f_{x_{c_i}} \quad (3-28)$$

$$\alpha_{i_{2p}} = \frac{1}{c} \sum_i k_{i3} \cdot f_{x_{c_i}} \quad (3-29)$$

The coefficients in these last equations,  $k_{i1}$  and  $k_{i3}$ , for specific values of  $x_c/c$ , are given in Table 5.

The described tendency in the value of  $\alpha_{0_{2p}}/\alpha_{0_{2p}}$  with increasing ideal angle of incidence points to the importance of having little or no camber near the trailing edge. A possible explanation for this trend is that turbulent boundary layer separation can then occur at almost equal positions on suction and pressure side of the foil, thereby leading to approximately equal wake thicknesses on suction and pressure sides at the trailing edge. It is clear that when the wake on the suction side at the trailing edge is importantly thicker than on the pressure side, and the effective trailing edge were taken to be at the midpoint of the wake, an effective reduction in camber and thus in zero-lift angle would result. Accordingly, an attempt was made to correlate the ratio of experimental to theoretical zero-lift angle with the ratio of effective wake thickness on the suction side to the effective wake thickness on the pressure side. The pressure distributions were calculated as before, but now only for the ideal angle of incidence. The results, for the cases that laminar separation does not occur, are given in Fig. 14.

i	coefficients for $\alpha_{0_2 P}$		coefficients for $\alpha_{i_2 P}$	
	$x_c/c$	$k_{i_1}$	$x_c/c$	$k_{i_3}$
1	0.05	5.040	0.0125	188.58
2	0.10	3.380	0.0250	53.017
3	0.15	3.010	0.0500	38.925
4	0.20	2.870	0.0750	20.821
5	0.25	2.920	1.1000	12.283
6	0.30	2.840	0.1500	16.313
7	0.35	2.810	0.2000	4.9750
8	0.40	3.090	0.2500	6.5330
9	0.45	3.320	0.3000	3.3100
10	0.50	3.640	0.4000	3.6130
11	0.55	4.070	0.6000	-3.6130
12	0.60	4.640	0.7000	-3.3190
13	0.65	5.440	0.7500	-6.5330
14	0.70	6.650	0.8000	-5.2830
15	0.75	8.590	0.8500	-13.763
16	0.80	11.40	0.9000	-26.529
17	0.85	17.05	0.9500	-41.642
18	0.90	35.40	0.9750	-130.50
19	0.95	186.2		

Table 5. Coefficients  $k_{i_1}$  and  $k_{i_3}$  in equations 3-28 and 3-29 for evaluation of angle of zero-lift and ideal angle of incidence in potential flow.



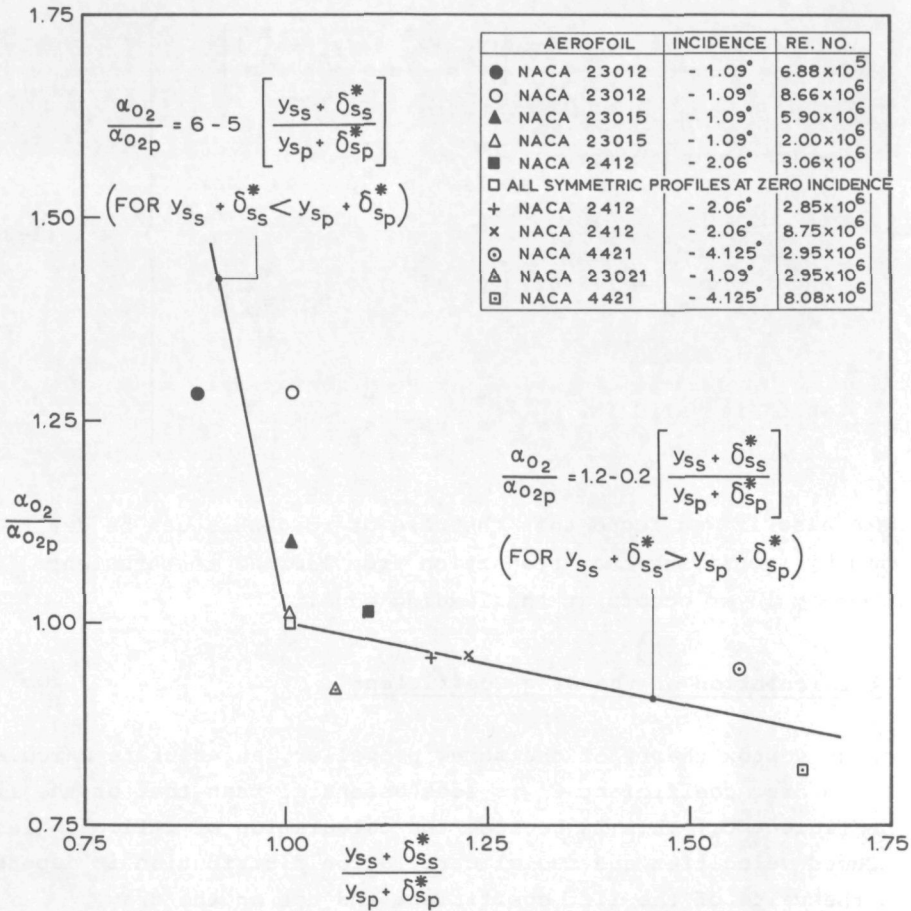


FIG. 14. CORRELATION BETWEEN RATIO OF EXPERIMENTAL TO THEORETICAL ANGLE OF ZERO-LIFT AND RATIO OF WAKE THICKNESS OF SUCTION TO PRESSURE SIDE.

It is clear that the results are significant, even though the scatter is somewhat larger than in the correlation of the lift-curve slope. It is probable that this is due to the fact that the demand on the accuracy of the boundary-layer calculations are higher when differentiating between the values for the two sides. Analytical expressions for the curves which fits the shown points best are:

$$\alpha_{0_2} / \alpha_{0_2p} = 6-5 \left[ (y_{s_s} + \delta_{s_s}^*) / (y_{s_p} + \delta_{s_p}^*) \right]$$

which is valid for  $y_{s_s} + \delta_{s_s}^* < y_{s_p} + \delta_{s_p}^*$

and  $\alpha_{0_2} / \alpha_{0_2p} = 1.2-0.2 \left[ (y_{s_s} + \delta_{s_s}^*) / (y_{s_p} + \delta_{s_p}^*) \right]$

which is valid for  $y_{s_s} + \delta_{s_s}^* > y_{s_p} + \delta_{s_p}^*$

(3-30)

Here also it was found that the case of roughness can be dealt with by specifying that transition from laminar to turbulent boundary layer occurs at the leading edge.

### 3.4 Calculation of the Drag Coefficient

In the vortex theory of the screw propeller, an accurate calculation of the drag coefficient  $C_D$  is less essential than that of the lift coefficient  $C_L$ . This is because the calculation of inflow angles, induced velocities and radial circulation distribution is dependent on the value of the lift coefficient and not on the drag coefficient. The drag characteristics of the blade sections are only required for the calculation of the thrust and torque characteristics (see equations 2-41 and 2-42). To obtain reliable values over a sizeable range of advance ratio's, reasonably accurate values of the drag coefficient are nevertheless required. This has been demonstrated by Johnsson [3-18] and Cummings [3-19], who have calculated the variation in the thrust and torque coefficients caused by a variation in the drag coefficient.

The calculation of the two-dimensional drag coefficient from basic boundary layer considerations at a given Reynolds number and angle of attack is still a difficult matter. Steady progress is being made for non-separated flows. It has become clear

that a reliable calculation of the point of transition from laminar to turbulent flow, and of the momentum thickness near the trailing edge, is indispensable. The recent method proposed by Cebeci and Smith [3-20] is representative for the state of the art of this topic.

In the case of a propeller blade an additional difficulty is incurred. This is the assessment of three-dimensional effects, of which only the part associated with so-called cascade effects is determinable. This situation necessitates, and warrants, a less fundamental approach to the problem.

In deriving the polynomial representation of the open-water characteristics of the Wageningen B-series propellers, Oosterveld and Van Oossanen [3-21, 3-22] used the "equivalent profile" method developed by Lerbs [3-23]. This method consists of replacing the propeller by one of its blade sections - the so-called equivalent profile or blade section - of which the lift and drag properties can be directly obtained from the thrust and torque coefficients of the propeller. Lerbs shows that the equivalent profile is the blade section at  $x=0.75$ . With this method the thrust and torque characteristics at various values of the advance ratio  $J$  can be corrected for Reynolds number effects from the known properties of this profile. Such was carried out for all the open-water results of the 120 model propellers constituting the Wageningen B-series to obtain consistent values of the thrust and torque for the derivation of the published  $K_T$  and  $K_Q$  polynomials. By means of this process more than 4000 values for the drag and lift coefficients were derived, each for a specific combination of blade number, expanded blade area ratio, pitch-diameter ratio and angle of attack.

A study of these drag coefficient values revealed an important increase in the minimum  $C_D$ -value below a specific value of the blade area-blade number ratio. For a pitch-diameter ratio of 1.0 this is shown in Fig.15. Each point in this figure represents a specific propeller of the B-series. More precisely, this increase was found to occur when:

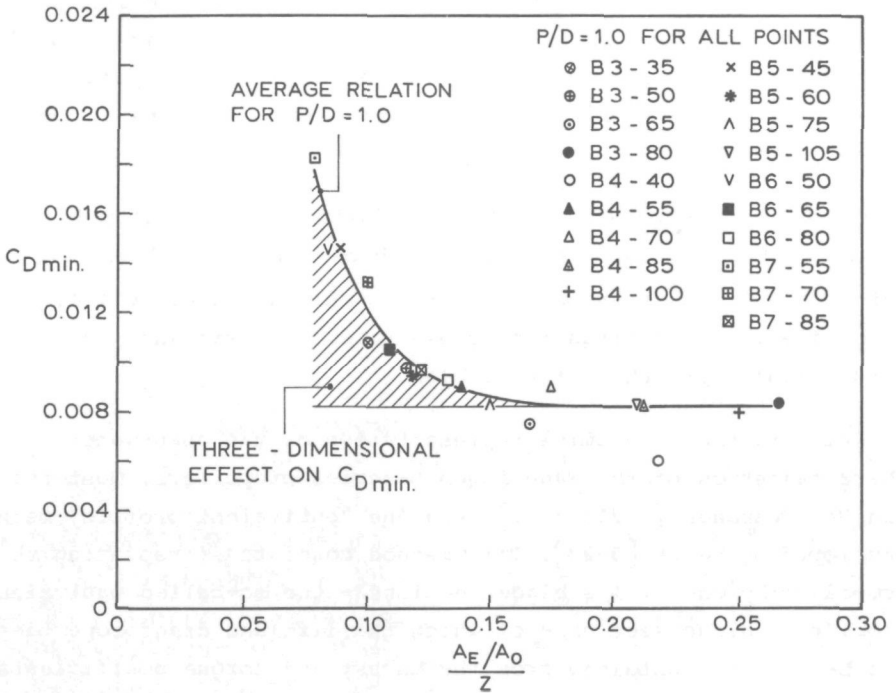


FIG. 15 THREE - DIMENSIONAL EFFECT ON MINIMUM DRAG COEFFICIENT OF EQUIVALENT PROFILE OF WAGENINGEN B-SERIES PROPELLERS.

$$\frac{A_E/A_O}{Z} < \frac{2.75 + 1.934P(x)/D}{17.785 + 13.515P(x)/D} \quad (3-31)$$

in which  $A_E/A_O$  equals the value of the expanded blade area ratio, and  $P(x)/D$  the pitch-diameter ratio at  $x$ . The minimum value of the drag coefficient was (accordingly) formulated to be:

$$C_{D \min} = 2C_f \left[ 1 + 2\left(\frac{t}{c}\right) + 60\left(\frac{t}{c}\right)^4 \right] + C_{D_3} \quad (3-32)$$

$$\text{where } C_f = \frac{0.075}{\left[ 0.434291 \ln(R_n(x) - 2) \right]^2} \quad (3-33)$$

$$C_{D_3} = \left[ (0.15)^2 - \left( \frac{A_E/A_O}{Z} \right)^2 \right] \left[ 1.375 + 0.967 \left( \frac{P(x)}{D} \right)^2 \right] - \left[ (0.15)^3 - \left( \frac{A_E/A_O}{Z} \right)^3 \right] \left[ 5.928 + 4.505 \left( \frac{P(x)}{D} \right)^2 \right] \quad (3-34)$$

and  $R_n(x) = \frac{V \cdot c(x)}{v} \quad (3-35)$

in which  $\left(\frac{t}{c}\right)$  = thickness-chord length ratio at  $x$ ,  
 $v$  = resultant velocity at  $x$ ,  
 and  $c(x)$  = chord length.

In equation 3-32,  $C_{D_3} = 0$  when the blade area-blade number ratio is less than 0.15. The two-dimensional part of this formula was taken from Hoerner [3-24]. The drag coefficient at other angles of attack was obtained from the knowledge that the minimum drag coefficient generally occurs at the ideal angle of incidence, so that:

$$C_D = \int_{\alpha_i}^{\alpha} \frac{dC_D}{d\alpha} d\alpha + C_{D_{min}} \quad (3-36)$$

The derivative of the drag coefficient with respect to the angle of attack was determined, and expressed as a polynomial by means of the multiple regression analysis procedure developed by Effroymsen [3-25]. This polynomial can be written as:

$$\left(\frac{dC_D}{d\alpha}\right)_{BS} = \sum_i k_i Z^{a_i} \left(\frac{A_E}{A_O}\right)^{b_i} \left(\frac{P(x)}{D}\right)^{c_i} \alpha^{d_i} \quad (3-37)$$

where the values of  $k_i$ ,  $a_i$ ,  $b_i$ ,  $c_i$  and  $d_i$  are given in Table 6. The subscript BS points to the fact that this polynomial is only valid for Wageningen B-series propellers for  $x=0.75$ . A typical result of the  $C_L$  and  $C_D$  calculations for the Wageningen B-series

i	Coefficient $k_i$	Power of Z $a_i$	Power of $A_E/A_O$ $b_i$	Power of P(x)/D $c_i$	Power of $\alpha$ $d_i$
1	$-8.515 \times 10^{-1}$	0	0	2	0
2	$1.886 \times 10^0$	0	1	1	0
3	$-3.398 \times 10^{-1}$	1	1	1	0
4	$2.167 \times 10^0$	0	0	3	0
5	$-1.536 \times 10^0$	0	2	1	0
6	$1.685 \times 10^{-1}$	1	0	3	0
7	$-2.573 \times 10^{-2}$	1	0	6	0
8	$2.354 \times 10^{-1}$	1	2	1	0
9	$1.247 \times 10^{-2}$	2	0	0	0
10	$-1.743 \times 10^{-2}$	2	0	1	0
11	$-5.944 \times 10^{-2}$	2	2	1	0
12	$1.585 \times 10^{-1}$	2	2	2	0
13	$-1.045 \times 10^{-1}$	2	2	3	0
14	$8.391 \times 10^{-3}$	2	2	6	0
15	$8.777 \times 10^0$	0	0	0	1
16	$-1.531 \times 10^0$	1	0	1	1
17	$-1.141 \times 10^0$	1	1	0	1
18	$6.981 \times 10^{-1}$	0	0	3	1
19	$5.631 \times 10^0$	0	2	1	1
20	$1.643 \times 10^{-2}$	2	0	6	1
21	$2.814 \times 10^{-1}$	2	1	0	1
22	$-2.170 \times 10^{-2}$	2	1	6	1
23	$1.271 \times 10^1$	0	0	1	2
24	$-2.127 \times 10^0$	1	0	3	2
25	$-2.568 \times 10^1$	1	2	0	2
26	$1.562 \times 10^1$	1	2	1	2
27	$9.580 \times 10^0$	2	0	1	2
28	$-1.620 \times 10^1$	2	0	2	2
29	$7.852 \times 10^0$	2	0	3	2
30	$-3.249 \times 10^{-1}$	2	0	6	2

Valid for:  $3 \leq Z \leq 7$ ;  $0.35 \leq A_E/A_O \leq 1.05$ ;  $0.5 \leq P(x)/D \leq 1.4$  and  $-0.04 \leq \alpha \leq 0.2$   
 (but not greater than the value for  $J=0$  where  $\alpha$  is in radians)

Table 6 Coefficients and powers of polynomial for  $dC_D/d\alpha$  as derived from Wageningen B-series propellers for  $x=0.75$ .



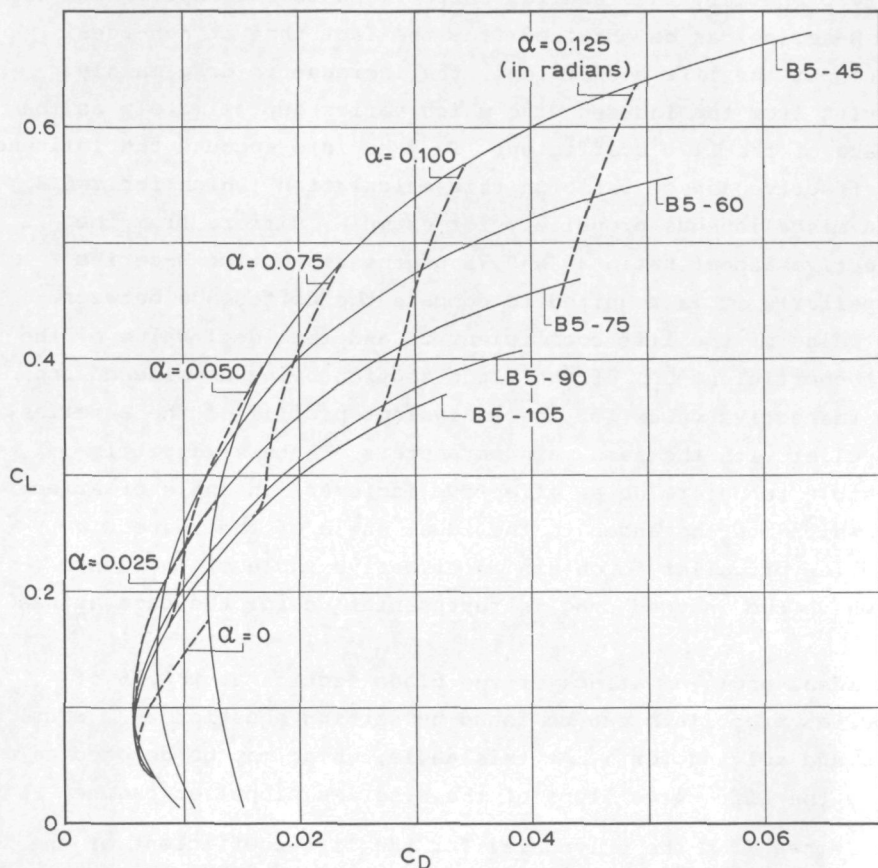


FIG.16. POLAR CURVES OF EQUIVALENT PROFILES OF 5 - BLADED B - SERIES PROPELLERS FOR  $P/D = 1.0$  AT A REYNOLDS NUMBER OF  $2 \times 10^7$

propellers is shown in Fig.16. The polar curves ( $C_L$ - $C_D$ -curves) of the 5-bladed B-series propellers for  $P/D=1.0$  at a Reynolds number of  $2 \times 10^7$  are given.

To derive the value of the drag coefficient of the blade sections of miscellaneous propellers, use can be made of the B-series propeller results when differences in blade section geometry and in effective aspect ratio are accounted for.

On assuming that the expression for the minimum drag coefficient given by equation 3-32 is appropriate for all blade sections of

every propeller, the required corrections to the expressions for the B-series can be obtained from the fact that at non-ideal values of the lift coefficient, the increase in drag mainly results from the induced drag which varies approximately as the square of the lift coefficient. To take into account the influence of effective aspect ratio in this calculation (which for  $x=0.2$  of a miscellaneous propeller, for example, differs from the effective aspect ratio at  $x=0.75$  of the respective B-series propeller), it is required to compare the difference between the value of the lift coefficient  $C_L$  and the ideal value of the lift coefficient  $C_{L_i}$  of the blade section being considered and the respective value  $C_{L_i}$  for the equivalent profile of the B-series propeller with the same main parameters. In this way it is possible to determine an effective increment in angle of attack  $\Delta\alpha$ , which must be added to the ideal angle of the respective B-series propeller to obtain an effective angle of incidence at which the induced drag is representative for the case at hand.

The ideal angle of attack of the blade section at  $x=0.75$  of B-series propellers can be found by setting equation 3-37 equal to zero and solving for  $\alpha$ . At this angle, which may be denoted as  $\alpha_{iBS}$ , the lift-curve slope of the B-series propeller can be determined from the polynomial for the lift coefficient of the B-series. This polynomial, obtained in the same manner as the polynomial for the derivative of the drag coefficient with respect to angle of incidence (expression 3-37), can be written as:

$$C_{L_{BS}} = \sum_i l_i z_i e^{i \left( \frac{A_E}{A_O} \right) f_i} \left( \frac{P(x)}{D} \right)^{g_i} \alpha^{h_i} \quad (3-38)$$

where the values of  $l_i, e_i, f_i, g_i$  and  $h_i$  are given in Table 7. The required increment in angle of attack,  $\Delta\alpha$ , then follows from:

$$\Delta\alpha = (C_L - C_{L_i}) / \left[ \frac{dC_L}{d\alpha} (\alpha_{iBS}) \right]_{BS} \quad (3-39)$$

in which  $C_L$  = lift coefficient of blade section in question,  
 $C_{L_i}$  = lift coefficient at ideal incidence of blade  
 section in question,  
 and  $\left[ \frac{dC_L}{d\alpha}(\alpha_{i_{BS}}) \right]$  = lift-curve slope at ideal incidence of equivalent  
 BS B-series propeller from equation 3-38.

The values of  $C_L$  and  $C_{L_i}$  of the blade section for which the  $C_D$  is to be calculated follows from the calculations described in sections 2.2.1 and 3.3.

The method described above is primarily for the effects of differences in blade section thickness and effective aspect ratio. A final correction is required for the difference in blade section camber. This is necessary since the limits of integration given in equation 3-36 assume an ideal angle of incidence equal to that of the B-series at  $x=0.75$ . It follows that the correction for camber consists of a shift of the obtained  $dC_D/d\alpha$  curve such that the minimum value of  $C_D$  (the value for which  $dC_D/d\alpha=0$ ) is situated at the ideal angle of incidence of the blade section in question. The final value of the drag coefficient then follows from:

$$C_D = \int_{\alpha_{i_{BS}}}^{\alpha_{i_{BS}} + \Delta\alpha} \frac{dC_D}{d\alpha} d\alpha + C_{D_{min}} \quad (3-40)$$

To recapitulate, the calculation of the drag coefficient at any radial station of an arbitrary propeller with main parameters within the wide range of B-series propellers is performed by first evaluating  $C_{D_{min}}$  from equation 3-32, then the appropriate value for  $\Delta\alpha$  from relation 3-39, and finally by integration the  $C_D$ -value from equation 3-40. This procedure necessitates previously calculated values of the lift coefficient and the ideal angle of incidence of the blade section in question together with the ideal angle of incidence and the lift-curve slope at the ideal angle of incidence for the respective B-series propeller at

i	Coefficient $l_i$	Power of $z$ $e_i$	Power of $A_E/A_O$ $f_i$	Power of $P(x)/D$ $g_i$	Power of $\alpha$ $h_i$
1.	$2.862 \times 10^{-1}_0$	0	0	0	0
2.	$5.072 \times 10^1$	0	0	0	1
3.	$1.447 \times 10^0$	0	0	1	2
4.	$-7.0015 \times 10^0$	0	0	2	2
5.	$-1.1132 \times 10^0$	0	1	0	0
6.	$-3.1261 \times 10^1$	0	1	0	1
7.	$3.568 \times 10^{-1}_1$	0	1	1	2
8.	$1.078 \times 10^1$	1	0	0	0
9.	$-1.042 \times 10^1$	1	0	0	2
10.	$-1.087 \times 10^1$	1	0	1	1
11.	$-3.566 \times 10^0$	0	1	2	3
12.	$-7.2492 \times 10^{-1}$	0	1	3	2
13.	$1.751 \times 10^{-1}$	0	1	6	1
14.	$9.141 \times 10^1$	0	2	0	0
15.	$4.089 \times 10^2$	0	2	0	2
16.	$-7.155 \times 10^1$	0	2	0	3
17.	$6.011 \times 10^0$	0	2	1	2
18.	$6.2696 \times 10^1$	0	2	6	3
19.	$1.218 \times 10^1$	1	0	0	3
20.	$2.419 \times 10^1$	1	1	1	3
21.	$-1.313 \times 10^{-1}_1$	1	2	0	0
22.	$-1.695 \times 10^2$	1	2	1	2
23.	$1.980 \times 10^{-1}_1$	1	2	1	3
24.	$-5.797 \times 10^1$	1	2	2	1
25.	$-7.709 \times 10^{-2}$	1	2	2	3
26.	$-1.292 \times 10^{-1}$	2	0	0	0
27.	$1.256 \times 10^{-1}$	2	0	0	1
28.	$7.702 \times 10^{-3}$	2	0	0	2
29.	$-3.759 \times 10^{-2}$	2	0	1	0
30.	$-2.126 \times 10^{-3}$	2	0	2	1
31.	$2.168 \times 10^{-2}$	2	0	3	0
32.	$1.506 \times 10^{-2}$	2	1	0	0

32.	$1.506 \times 10^{-2}$	2	1	0	0
33.	$-1.256 \times 10^{-1}$	2	1	0	1
34.	$-1.002 \times 10^1$	2	1	0	3
35.	$6.773 \times 10^{-1}$	2	1	1	2
36.	$-3.563 \times 10^{-3}$	2	1	2	0
37.	$-1.589 \times 10^{-4}$	2	1	6	0
38.	$6.105 \times 10^{-3}$	2	2	1	0
39.	$1.196 \times 10^{-1}$	2	2	1	1
40.	$1.529 \times 10^{-2}$	2	2	3	1

Valid for:  $3 \leq Z \leq 7$ ;  $0.35 \leq A_E/A_O \leq 1.05$ ;  $0.5 \leq P(x)/D \leq 1.4$  and  $-0.04 \leq \alpha \leq 0.2$   
(but not greater than the  $\alpha$ -value for  $J=0$ , where  $\alpha$  is in radians)

Table 7. Coefficients and powers of polynomial for  $C_L$  for the Wageningen B-series propellers for  $x=0.75$ .

$x=0.75$ . These last values are found from the polynomials given in Tables 6 and 7. The numerical values of  $dC_D/d\alpha$ , required for the integration in equation 3-40, are also derived from Table 6. All angles of attack are with respect to the chord line of the blade sections.

### 3.5 Effect of Viscosity on Chordwise Pressure Distribution

A simple viscosity allowance on the velocity distribution can be derived by assuming, after Pinkerton [3-26], that in the theory outlined in section 2.4.1.

$$C_L = 2\pi e^{\psi_0} \sin(\alpha + \beta_\alpha) \quad (3-41)$$

where  $C_L$  = experimental value of lift coefficient,  
and  $\beta_\alpha$  = corrected value of the zero-lift angle of attack  
to give experimental lift coefficient

Solving for  $\beta_\alpha$  gives:

$$\beta_\alpha = \arcsin(C_L / 2\pi e^{\psi_0}) \quad (3-42)$$

$$\varepsilon_{\alpha}(\phi) = \varepsilon(\phi) + \frac{\Delta\beta}{2}(1 - \cos\phi) \quad (3-43)$$

where  $\Delta\beta$  is the increment of  $\varepsilon$  required to give zero velocity at  $\phi = \pi$ , viz:

$$\Delta\beta = \beta_{\alpha} - \beta \quad (3-44)$$

The new value for  $d\varepsilon/d\phi$  then becomes:

$$\frac{d\varepsilon_{\alpha}}{d\phi} = \frac{d\varepsilon}{d\phi} + \frac{\Delta\beta}{2} \sin\phi \quad (3-45)$$

The relation for the velocity distribution is then:

$$\frac{v}{U} = \frac{e^{\psi_0 \left(1 + \frac{d\varepsilon}{d\phi} + \frac{\Delta\beta}{2} \sin\phi\right)}}{\sqrt{\psi^2(\phi) + \sin^2\phi}} \left| \cos(\alpha + \beta_{\alpha}) \sin \left[ \phi + \varepsilon(\phi) + \frac{\Delta\beta}{2}(1 - \cos\phi) - \beta_{\alpha} \right] \right. \\ \left. + \sin(\alpha + \beta_{\alpha}) \cos \left[ \phi + \varepsilon(\phi) + \frac{\Delta\beta}{2}(1 - \cos\phi) - \beta_{\alpha} \right] + \sin(\alpha + \beta_{\alpha}) \right| \quad (3-46)$$

In section 2.4.2, where this theory is applied to propeller blades, the effect of viscosity on the velocity distribution in the three-dimensional case can be determined by means of:

$$\beta_{\alpha_{\text{eff}}}(x, \theta) = \arcsin(C_L(x, \theta) / 2\pi e^{\psi_0}) - \alpha_{\text{eff}}(x, \theta) \quad (3-47)$$

$$\text{and } \varepsilon_{\alpha_{\text{eff}}}(\theta) = \varepsilon_{\text{eff}}(\theta) + \frac{\Delta\beta_{\text{eff}}(x, \theta)}{2}(1 - \cos\theta) \quad (3-48)$$

$$\text{where } \Delta\beta_{\text{eff}} = \beta_{\alpha_{\text{eff}}}(x, \theta) - \beta(x, \theta) \quad (3-49)$$

$\beta_{\alpha_{\text{eff}}}$  = corrected value of effective three-dimensional zero-lift angle of attack,

and  $\alpha_{\text{eff}}$  = effective angle of attack for three-dimensional pressure distribution calculation (from equation 2-93)



which values are now used in equation 3-46 in lieu of the values for the two-dimensional case. The pressure distribution is obtained from the velocity distribution by means of the Bernoulli relation, viz:

$$C_{p_{x_c}}(x, \theta) = 1 - \left[ v_{x_c}(x, \theta) / V(x, \theta) \right]^2 \quad (3-50)$$

where  $C_{p_{x_c}}$  = pressure coefficient at  $x_c$ ,

and  $V$  = resultant velocity at the blade section given by equation 2-39.

CHAPTER 4

CALCULATION OF CAVITATION PERFORMANCE OF PROPELLERS

4.1 General Remarks on Types of Cavitation Occurring on Propeller Blades.

There are two methods by which vapour- and gas filled bubbles become visible in a fluid and grow: when the fluid is heated under constant pressure and when the pressure in the fluid is reduced at constant temperature. The formation of such bubbles is called boiling when caused by temperature increase and cavitation when caused by the reduction of pressure.

It is possible to define two physically different types of cavitation. Firstly, cavity can form and grow by vaporization of the fluid. This type of cavitation is called vaporous cavitation and occurs when the dynamic pressure change is such that the local pressure somewhere in the fluid falls below the prevailing vapour pressure. Secondly, a cavity or bubble in a fluid can occur and grow due to diffusion of dissolved gases into the bubble or simply by expansion of the gas content in the liquid when the pressure decreases. This type of cavitation is called gaseous cavitation. The inception pressure of the gaseous cavitation form is often higher than the critical inception pressure of the vaporous cavitation form. Normally, however, the time between the formation and collapse of a vaporous cavity is too short to allow gas diffusion into the cavity. This is the reason that hydrodynamic cavitation processes are mainly of the vaporous type.

When a cavitation bubble moves into an area of higher pressure the bubble will collapse. Vapour-filled cavities collapse violently and cavities with a high gas content collapse relatively slowly and calmly. The violent collapse of a vapour-filled cavity is in fact an implosion and is caused by the sudden condensation of the vapour. The slower and more continuous process of a gas going into solution causes the slower rate of collapse of a gas-filled cavity.

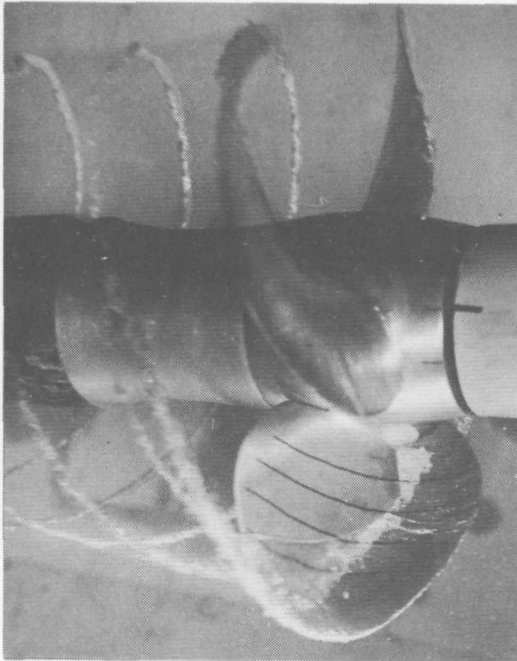


FIG.17 STABLE SHEET CAVITATION.

The mechanism of cavitation inception has held a large number of research workers occupied a very long time, and even now there is no universal agreement. The problem is that, even though cavitation experiments prove that inception occurs in the proximity of the vapour pressure, appreciable deviations keep eventuating - even for the same fluid. In addition, it has been shown that liquids can withstand very high tensions, i.e. negative pressures. Various hypotheses have been formulated on the mechanism of cavitation inception. Each tries to take into account the mentioned discrepancies. It seems that this behaviour of a fluid can only be explained by assuming the existence of weak spots in the liquid. It is nowadays considered probable that the amounts of undissolved gas and uncondensed vapour act as weak spots. Due to the fact that not only water but nearly all liquids can be made to cavitate, demonstrating the existence of weak spots or "holes" (as they are sometimes called), it is very likely that in particular undissolved gases act as such.

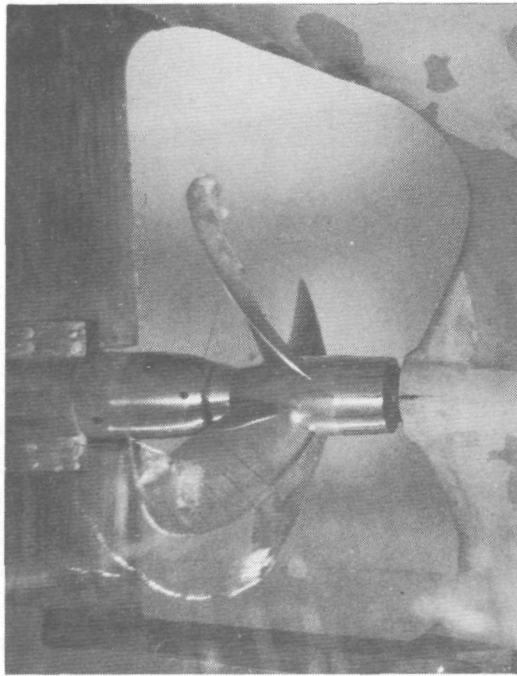


FIG.18 BUBBLE CAVITATION.

It has been pointed out that, if undissolved gases or uncondensed vapour are to be permanently present in the fluid, some stabilization process, preventing these small bubbles from dissolving or rising to the surface (if a free surface is present), must exist. Various hypotheses have been devised to account for such a stabilization process. In general, it may be said that all hypotheses show that undissolved gas can exist, either in the free stream, called stream nuclei, or in the form of pockets in microscopic cracks in solid boundaries, called wall or surface nuclei, or in both. In this way plausible theories have been put forward to show how a nucleus or weak spot can exist and cause cavitation. The most accepted theory is one put forward by Harvey et al [4-1]. He showed that the surface tension of the fluid can effectively decrease the pressure in the liquid surrounding a gas and vapour-filled nucleus in a crack or crevice of a solid boundary.

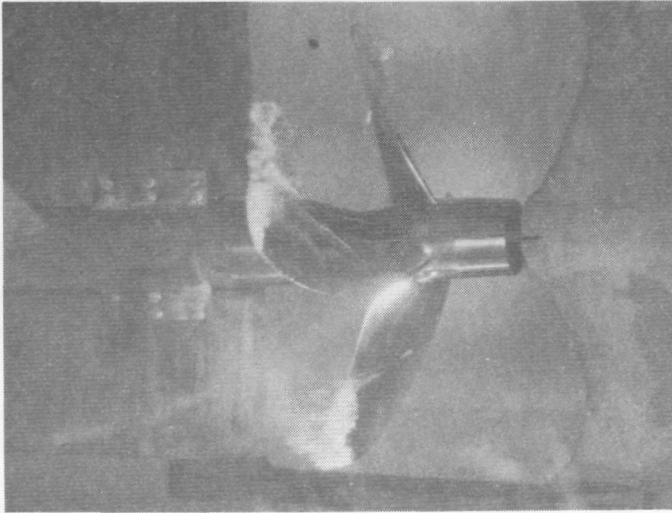


FIG.19 CLOUD CAVITATION BEHIND SHEET CAVITY.

Knapp etal [4-2] classify hydrodynamic cavitation, in general, into the following categories:

- travelling cavitation,
- fixed cavitation,
- vortex cavitation, and
- vibratory cavitation.

The travelling cavitation type occurs in the free stream and consists of individual bubbles moving with the flow. Fixed cavitation occurs on boundaries of immersed bodies. It is fixed in the sense that cavitation is attached to the body, as such being inherent to the body and not to the flow. A vortex occurs in a high shear flow. To balance centrifugal forces the pressure in the flow near the vortex must decrease continuously as the vortex is approached. These low pressures cause cavitation. Vibratory cavitation is caused by pressure pulsations in the

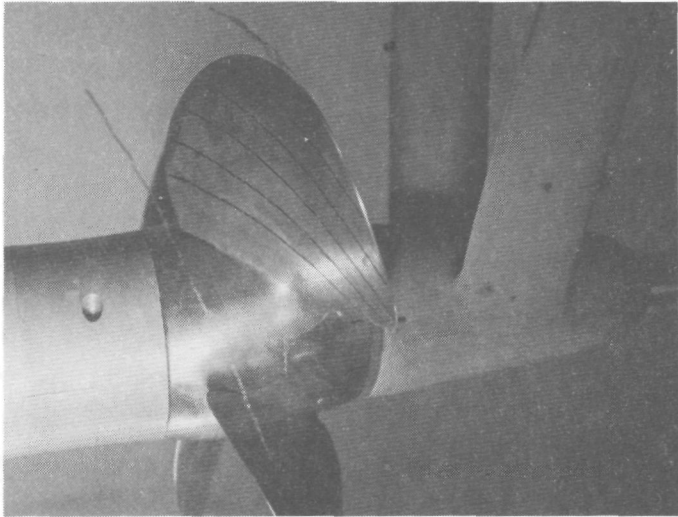


FIG.20 UNATTACHED TIP VORTEX CAVITATION.

liquid. Usually these pressure pulsations are due to a submerged object vibrating normal to its face, thus producing pressure waves. Cavitation is caused when these pressure variations are large enough to cause the pressure in the liquid to reach, and fall below, the vapour pressure.

Cavitation forms on marine propellers are mainly of the fixed and vortex type. These types can be subdivided either according to the position on the propeller where the cavitation occurs, or according to the physical nature of the cavitation. Classifying propeller cavitation according to the latter method, it is possible to specify the following types:

- sheet cavitation,
- bubble cavitation,
- cloud cavitation,
- tip vortex cavitation, and
- hub vortex cavitation.



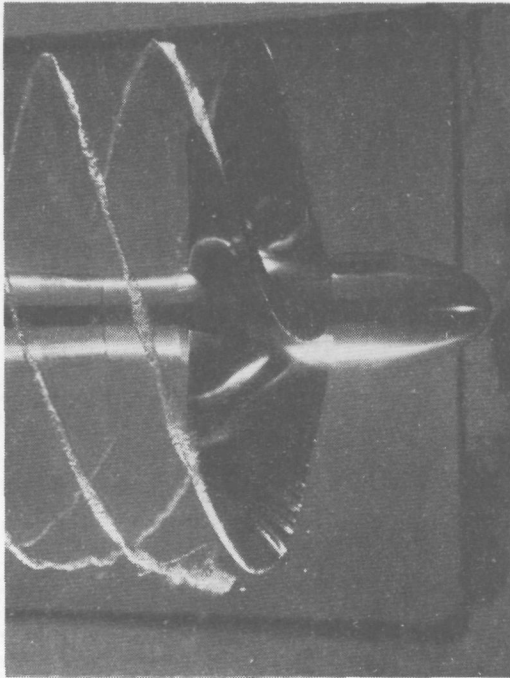


FIG.21 ATTACHED (DEVELOPED) TIP VORTEX CAVITATION.

Sheet cavitation first occurs at the leading edge of propeller blades on the suction side when the blade sections work under positive angles of attack, and on the pressure side when the blade sections work under negative angles of attack. This is due to the fact that these non-shock-free angles of attack cause large pressure gradients in this region. This cavitation form may develop to cover the complete suction side of a blade, spreading inward from the leading edge in the form of a sheet, in which case it will often have a very stable character as shown in Fig. 17. When working in a wake, however, this cavitation type often has a very unstable character.

Bubble cavitation first occurs at the midchord or at the position of maximum thickness of the blade sections, at shock-free entry of the flow. As such it occurs in non-separated flows. This cavitation type appears as large individual bubbles, growing and contracting rapidly; see Fig.18.

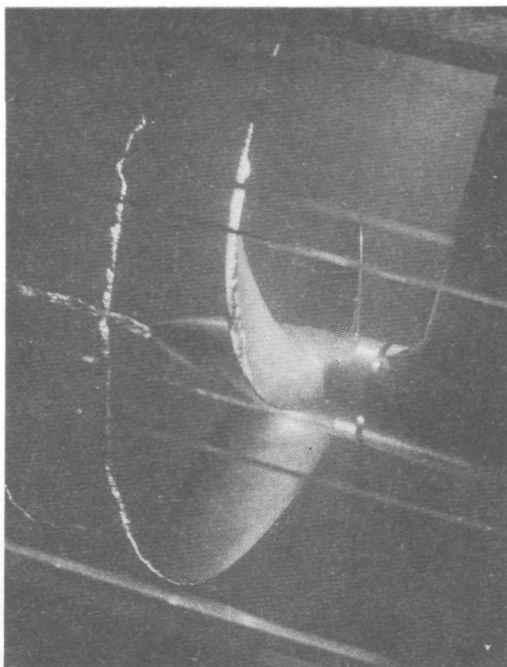


FIG.22 HUB AND TIP VORTEX CAVITATION.

Cloud cavitation often occurs behind strongly developed sheet cavities and, in general, in moderately separated flows in which many small vortices form kernels for many small cavities. Cloud cavitation appears as a mist or a "cloud" of very small bubbles as shown in Fig.19.

The vortex type of cavitation occurs at the tip and hub of the propeller. The flow around the end of the blades from the pressure to the suction side causes an unstable vortex which is shed from the tip and the hub into the flow in the same way as an aerofoil of finite aspect ratio generates a vortex at each end. The pressure is least in the centre of the vortex, and it is this vortex core which cavitates. Tip vortex cavitation usually starts somewhat behind the tip of propeller blades due to the fact that the maximum strength of the vortex occurs at that point where the flow around the blade tip is complete. In this early stage, the cavitation is therefore unattached to the tip as shown in Fig.20.

When the vortex becomes stronger, or the liquid pressure is reduced, the cavitating tip vortex becomes attached as shown in Fig. 21.

The hub vortex is formed by the combined vortices from the blades at the blade root, which by themselves are usually too weak to cavitate. With a converging hub fairwater form this hub vortex can, however, become very strong and cavitate readily. The resulting vortex cavitation is very stable and appears as a thick "rope" with strands corresponding to the number of blades as shown in Fig. 22.

#### 4.2 Method for Assessing Cavitation Inception.

An important step forward in the study of cavitation inception and related scale effects was made when it was found that the onset of cavitation can occur in the region of laminar boundary layer separation. The recent study performed by Arakeri [4-3] has shown that the value of the pressure coefficient at the location of laminar separation is closely correlated with the magnitude of the cavitation index at the onset of cavitation. Prior to this work, Alexander [4-4] and Bailey [4-5] had suggested that such a correlation existed. Besides the correlation with laminar boundary separation, Arakeri also found experimental evidence that the intense disturbances at the site of turbulent reattachment or of laminar-turbulent transition on bodies not possessing laminar separation can also be responsible for cavitation inception. He obtained excellent agreement between the negative value of the pressure coefficient at the calculated position of transition and the desinent cavitation number for a two-inch 1.5 calibre ogive determined by Parkin and Hall [4-6]. He suggests, however, that further verification of this result is required since the calculation of laminar-turbulent transition is only approximate. Because it is important to have an explanation for viscous scale effects on bodies which do not exhibit laminar separation (most bodies at high Reynolds numbers), it was deemed essential to obtain certainty regarding whether or not the onset

of cavitation occurs at, or near, the point of transition. The necessary study in this regard requires a comparison of the results of experimental studies on cavitation inception with the characteristics of the boundary layer.

A source of inaccuracies in boundary layer calculations is avoided when experimentally obtained pressure distributions are used. The only profile of which both cavitation inception characteristics and the pressure distributions have been measured is the NACA 4412 aerofoil. On this profile Pinkerton [4-7] performed pressure distribution measurements and Daily [4-8] and Kermeen [4-9] carried out cavitation experiments. The Reynolds number of the tests in the cavitation tunnel ranged between  $0.55 \times 10^6$  to  $1.5 \times 10^6$  while the tests performed by Pinkerton in the wind tunnel were at a Reynolds number of about  $3 \times 10^6$ . Bailey [4-5] rightly warns about the difficulty of making comparisons between the cavitation behaviour and the pressure distribution from these tests. Not only is there a difference in Reynolds number but also the turbulence level of the water tunnel probably differed from that in the wind tunnel. The results from these tests, however, will certainly suffice for the purpose of investigating the possible existence of a relationship between cavitation inception and laminar-turbulent transition.

Calculations were performed to determine the value of the Reynolds number based on momentum thickness and local velocity and the Reynolds number based on free-stream velocity at the position on the foil at which the negative value of the pressure coefficient equals the value of the cavitation index for the inception condition. The results are presented in Table 8 and Fig.23. Included also are some values for the NACA 66<sub>1</sub>-012 aerofoil for which the information on cavitation inception was taken from Kermeen [4-10] and the pertinent pressure distributions, valid for potential flow, from Bailey [4-5]. Contrary to what was supposed by Alexander [4-4] and Bailey, the boundary layer calculation did not exhibit laminar separation in the region of cavitation inception at the Reynolds numbers of the cavitation

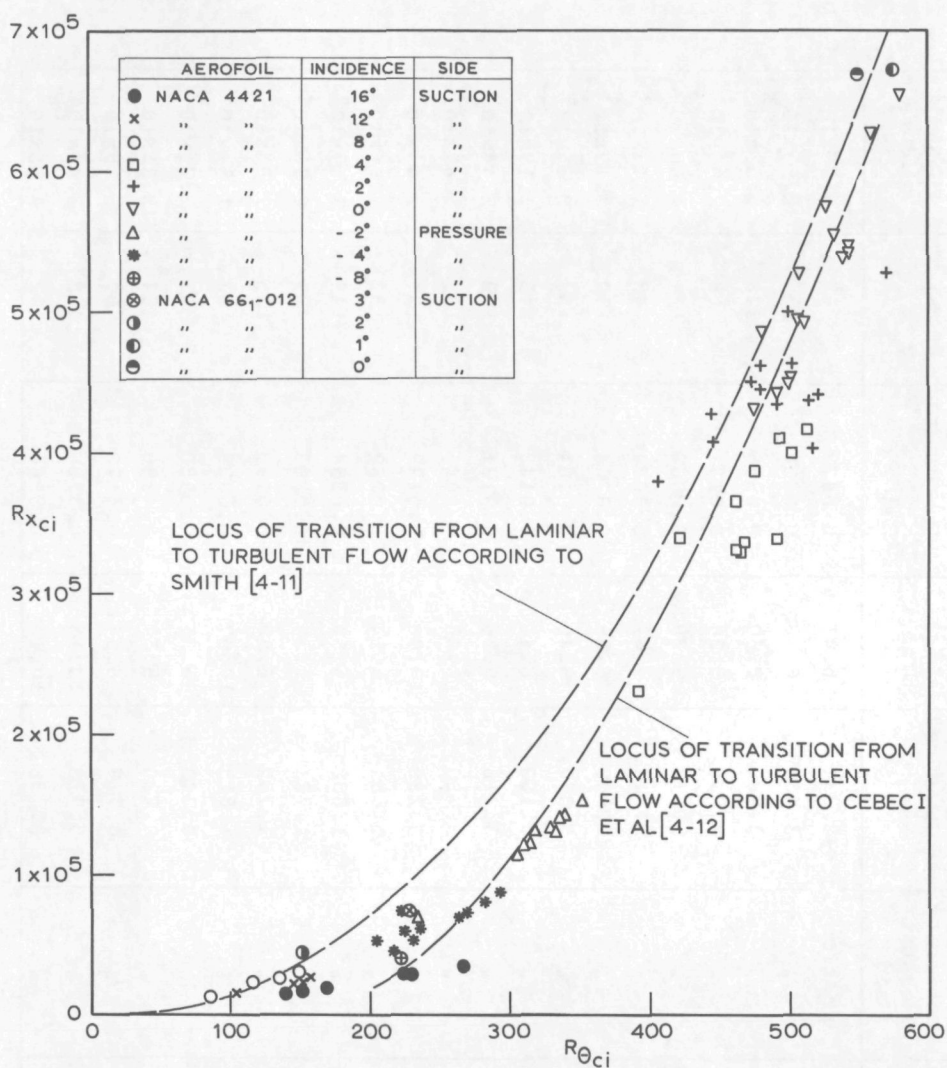


FIG. 23 CAVITATION INCEPTION DATA OF NACA 4412 AND NACA 66<sub>1</sub>-012 PROFILES.

experiments. All cavitation inception points, as set out in Fig. 23, lie essentially on one curve. The nature of this curve is very similar to a laminar-turbulent transition curve. To demonstrate this, the transition locus given by Smith [4-11] and used in the previous chapter is included. Also the relation used by Cebeci et al [4-12] is shown. It is seen that this last relation

Aerofoil	Incidence	suction or pressure side	$\sigma_i$ measured	U (m/sec)	$x_c/c$ where $-c_p = \sigma_i$	RE.NO. $v_{x_c} \theta / \nu$	RE.NO. $x_s \cdot cU / \nu$
NACA 4412	16°	suction	3.231	6.41	0.0472	267	3.77x10 <sup>4</sup>
"	"	"	3.589	6.38	0.0328	231	2.95x10 <sup>4</sup>
"	"	"	3.985	8.30	0.0245	226	3.03x10 <sup>4</sup>
"	"	"	4.808	8.20	0.0131	168	2.00x10 <sup>4</sup>
"	"	"	5.674	9.70	0.0064	141	1.60x10 <sup>4</sup>
"	"	"	5.514	9.62	0.0074	148	1.71x10 <sup>4</sup>
"	12°	"	2.900	6.56	0.0204	150	2.12x10 <sup>4</sup>
"	"	"	3.077	8.40	0.0164	153	2.36x10 <sup>4</sup>
"	"	"	3.162	8.45	0.0143	145	2.19x10 <sup>4</sup>
"	"	"	3.216	9.96	0.0131	152	2.44x10 <sup>4</sup>
"	"	"	3.730	12.00	0.0045	105	1.67x10 <sup>4</sup>
"	"	"	3.226	10.00	0.0129	151	2.43x10 <sup>4</sup>
"	8°	"	1.651	6.54	0.0289	133	2.68x10 <sup>4</sup>
"	"	"	1.608	6.54	0.0364	149	3.17x10 <sup>4</sup>
"	"	"	1.721	8.56	0.0203	129	2.75x10 <sup>4</sup>
"	"	"	1.752	8.58	0.0160	116	2.37x10 <sup>4</sup>
"	"	"	1.815	10.07	0.0055	82	1.54x10 <sup>4</sup>
"	4°	"	0.733	6.36	0.3980	391	2.31x10 <sup>5</sup>
"	"	"	0.720	8.57	0.4130	464	3.22x10 <sup>5</sup>
"	"	"	0.717	8.58	0.4170	467	3.25x10 <sup>5</sup>
"	"	"	0.773	10.13	0.3700	468	3.44x10 <sup>5</sup>
"	"	"	0.736	10.14	0.3960	492	3.66x10 <sup>5</sup>



NACA 4412	4°	suction	0.792	12.24	0.3580	502	4.03x10 <sup>5</sup>
"	"	"	0.857	13.29	0.2960	462	3.67x10 <sup>5</sup>
"	"	"	0.839	13.29	0.3110	477	3.84x10 <sup>5</sup>
"	"	"	0.920	15.70	0.2260	421	3.40x10 <sup>5</sup>
"	"	"	0.846	14.64	0.3040	493	4.14x10 <sup>5</sup>
"	"	"	0.770	12.21	0.3720	516	4.16x10 <sup>5</sup>
"	2°	"	0.483	8.39	0.5350	518	4.03x10 <sup>5</sup>
"	"	"	0.573	10.19	0.4810	521	4.42x10 <sup>5</sup>
"	"	"	0.570	12.11	0.4820	570	5.27x10 <sup>5</sup>
"	"	"	0.653	13.33	0.3810	503	4.65x10 <sup>5</sup>
"	"	"	0.686	13.32	0.3570	477	4.37x10 <sup>5</sup>
"	"	"	0.700	14.69	0.3370	481	4.57x10 <sup>5</sup>
"	"	"	0.721	14.64	0.3000	446	4.10x10 <sup>5</sup>
"	"	"	0.711	15.40	0.3170	474	4.53x10 <sup>5</sup>
"	"	"	0.714	17.20	0.3120	496	4.98x10 <sup>5</sup>
"	"	"	0.743	16.96	0.2680	445	4.28x10 <sup>5</sup>
"	"	"	0.757	19.09	0.2120	405	3.90x10 <sup>5</sup>
"	0°	"	0.439	10.09	0.5030	499	4.56x10 <sup>5</sup>
"	"	"	0.459	9.93	0.4970	490	4.44x10 <sup>5</sup>
"	"	"	0.493	10.07	0.4780	476	4.34x10 <sup>5</sup>
"	"	"	0.465	12.14	0.4940	539	5.40x10 <sup>5</sup>
"	"	"	0.451	12.10	0.5000	544	5.44x10 <sup>5</sup>
"	"	"	0.473	11.18	0.4900	514	4.94x10 <sup>5</sup>
"	"	"	0.502	11.74	0.4700	506	4.98x10 <sup>5</sup>

NACA 4412	0°	suction	0.541	13.33	0.4010	480	4.87x10 <sup>5</sup>
"	"	"	0.507	13.26	0.4640	532	5.56x10 <sup>5</sup>
"	"	"	0.523	13.25	0.4400	509	5.28x10 <sup>5</sup>
"	"	"	0.541	14.88	0.4010	507	5.44x10 <sup>5</sup>
"	"	"	0.518	15.43	0.4500	558	6.28x10 <sup>5</sup>
"	"	"	0.438	10.04	0.5040	499	4.55x10 <sup>5</sup>
"	-2°	pressure	0.533	8.39	0.0902	237	7.05x10 <sup>4</sup>
"	"	"	0.453	11.77	0.1133	318	1.22x10 <sup>5</sup>
"	"	"	0.433	11.80	0.1194	328	1.28x10 <sup>5</sup>
"	"	"	0.446	13.22	0.1154	340	1.39x10 <sup>5</sup>
"	"	"	0.460	13.11	0.1112	332	1.34x10 <sup>5</sup>
"	"	"	0.565	15.55	0.0815	306	1.19x10 <sup>5</sup>
"	"	"	0.517	15.45	0.0948	330	1.36x10 <sup>5</sup>
"	"	"	0.537	17.17	0.0891	337	1.43x10 <sup>5</sup>
"	"	"	0.583	17.00	0.0769	310	1.24x10 <sup>5</sup>
"	"	"	0.534	18.69	0.0900	353	1.57x10 <sup>5</sup>
"	"	"	0.598	18.93	0.0734	319	1.32x10 <sup>5</sup>
"	"	"	0.417	9.94	0.1245	308	1.12x10 <sup>5</sup>
"	-4°	"	0.937	8.36	0.0650	231	5.23x10 <sup>4</sup>
"	"	"	0.921	8.32	0.0669	234	5.33x10 <sup>4</sup>
"	"	"	0.869	6.45	0.0735	217	4.50x10 <sup>4</sup>
"	"	"	1.007	9.81	0.0578	233	5.52x10 <sup>4</sup>
"	"	"	0.939	11.70	0.0648	272	7.29x10 <sup>4</sup>
"	"	"	0.968	11.72	0.0617	265	6.99x10 <sup>4</sup>
"	"	"	0.912	13.03	0.0680	295	8.47x10 <sup>4</sup>

NACA 4412	-4°	pressure	0.956	13.09	0.0629	283	7.95x10 <sup>4</sup>
"	"	"	1.217	15.24	0.0402	236	6.28x10 <sup>4</sup>
"	"	"	1.228	15.46	0.0394	235	6.25x10 <sup>4</sup>
"	"	"	1.314	16.93	0.0333	224	5.96x10 <sup>4</sup>
"	"	"	1.456	18.60	0.0265	205	5.42x10 <sup>4</sup>
"	"	"	1.355	19.03	0.0307	227	6.27x10 <sup>4</sup>
"	-8°	"	2.750	15.00	0.0233	223	3.95x10 <sup>4</sup>
NACA 66 <sub>1</sub> -012	+3°	suction	0.571	12.50	0.0556	226	7.47x10 <sup>4</sup>
"	+2°	"	0.460	12.19	0.0326	152	4.57x10 <sup>4</sup>
"	+1°	"	0.370	12.19	0.5802	576	6.74x10 <sup>5</sup>
"	+0°	"	0.345	12.19	0.5780	552	6.71x10 <sup>5</sup>

Table 8 Results of analysis of inception data given by Kermeen [4-9, 4-10] for the NACA 4412 and NACA 66<sub>1</sub>-012 profiles.

agrees quite well with the obtained points. In this regard it is important to note that the relation derived by Cebeci et al is an approximation incorporating Smith's relation only for Reynolds numbers (based on  $x_s$ ) above  $7 \times 10^6$ . For Reynolds number below  $7 \times 10^6$  Smith's relation was altered to obtain an improved correlation with experimentally obtained transition data.

To obtain a diagram better suited for correlation with transition loci, a logarithmic plot of the transformed cavitation inception data was made. The result is shown in Fig. 24. The experimental data used by Smith [4-11] for high Reynolds numbers are included. It is seen that the formula derived by Cebeci et al [4-12] fits the combined data very well. It is suggested, therefore, that the formula:

$$R_{\theta_{tr}} = 1.174(1+22400/R_{x_{c_{tr}}})R_{x_{c_{tr}}}^{0.46} \quad (4-1)$$

could well be used to determine the location of cavitation inception. The range of applicability of this locus is:

$$1 \times 10^5 < R_{x_{c_{tr}}} < 6 \times 10^7 \quad (4-2)$$

For values of the  $x_s$ -Reynolds number below  $1 \times 10^5$  this relation does not hold. To obtain a formula for this region, a straight line can be drawn through the data of Fig. 24 in the  $x_s$ -Reynolds number range below  $7 \times 10^5$ . The equation of this line and its range of validity is:

$$R_{\theta_{ci}} = 4.048 R_{x_{ci}}^{0.368} \quad (4-3)$$

$$1 \times 10^4 < R_{x_{ci}} < 7 \times 10^5$$

in which  $R_{\theta_{ci}}$  = Reynolds number based on local velocity and momentum thickness at position of cavitation inception,

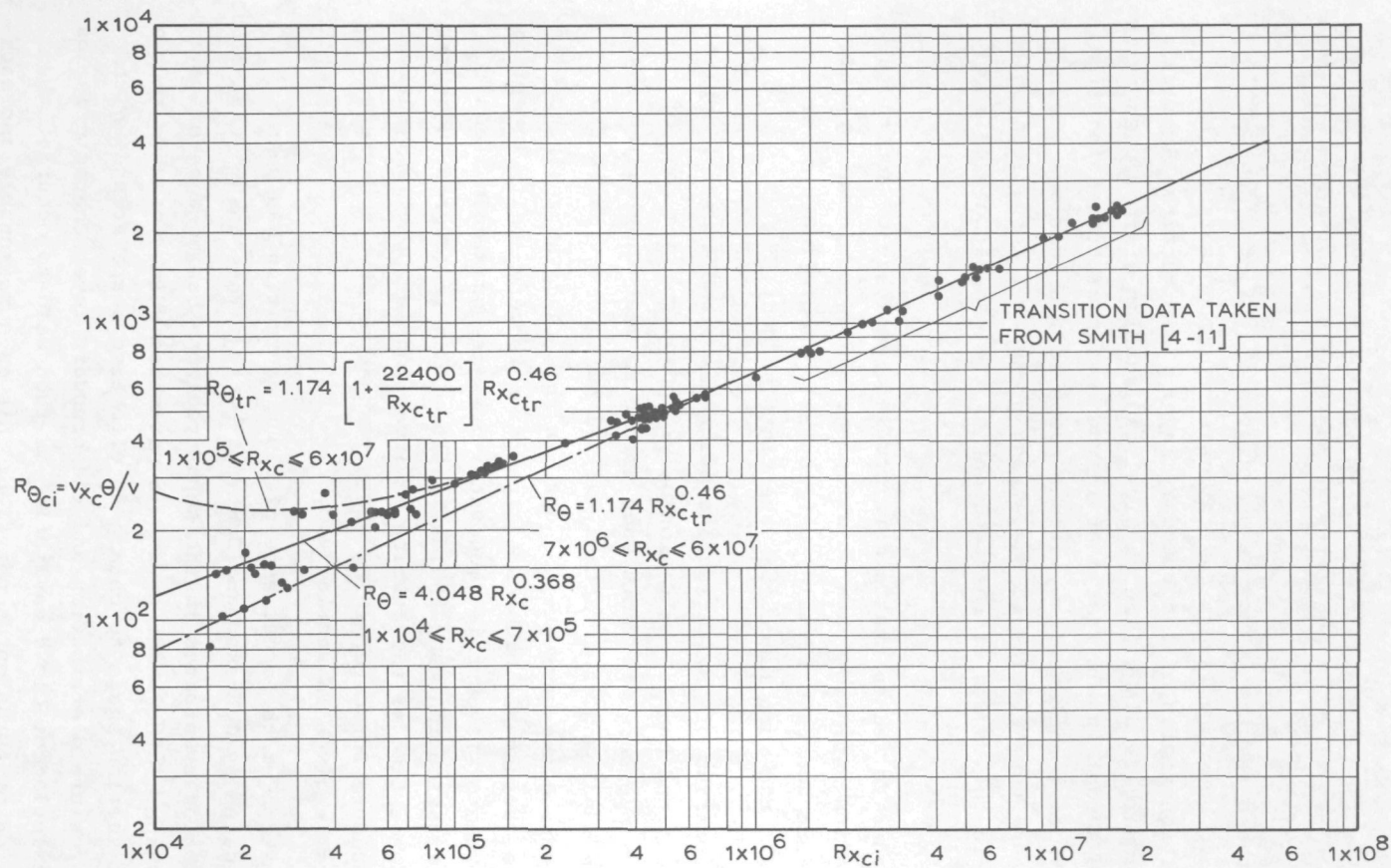


FIG. 24 LOGARITHMIC PLOT OF CAVITATION INCEPTION DATA OF NACA 4412 PROFILE TOGETHER WITH RELATIONS FOR LAMINAR - TURBULENT TRANSITION.

$R_{x_{ci}}$  = Reynolds number based on distance along surface from leading edge and free-stream velocity at position of cavitation inception.

From these results it may be postulated that in the case of attached boundary layers cavitation inception occurs in the transition region of the boundary layer. This confirms Arakeri's preliminary findings. The physical explanation of this phenomenon may be sought in the fact that in the region of transition from laminar to turbulent flow, strong pressure fluctuations occur which are very similar to the strong pressure fluctuations which occur in the region of reattachment of the separated free shear layer.

It stands to reason that a more complete analysis of additional cavitation inception data on different bodies could well result in a more accurate formula, particularly when effects of pressure gradient and turbulence are taken into account.

The mechanism of cavitation inception described thus far applies to sheet and bubble cavitation only. Inception in a zone of adverse pressure gradients such as occurs near the leading edge at non-ideal angles of attack, will lead to sheet cavitation on lowering the cavitation index. In this case the residence time of the macroscopic bubbles at inception is very small. Inception in a zone of favourable (moderate) pressure gradients leads to bubble cavitation when the cavitation index is lowered. Here the residence time of the bubbles at inception is appreciably larger. A procedure for determining whether sheet or bubble cavitation occurs is given in section 4.3.

Estimation of the occurrence of cloud cavitation has been considered by Johnsson and Sntvedt [4-13]. They assume that cloud cavitation eventuates in the separated zone behind a sheet cavity. The shape of the sheet cavity is estimated which is added to the blade section shape to obtain an effective shape around which the pressure distribution and the boundary layer characteristics are calculated. Cloud cavitation is then said to occur at the location of turbulent separation. This is a reasonable approach



since it agrees with experimental observations of the occurrence of cloud cavitation described by Van Manen [4-14]. The weakness of this approach, however, lies in the calculation of the shape of the cavity which can only be assessed approximately. This calculation procedure can be improved when the pressure distribution for the cavitating condition can be determined with acceptable accuracy. This topic is considered in section 4.4 in connection with the calculation of propeller performance for cavitating conditions.

The analytical assessment of the occurrence of vortex cavitation will not be attempted here. An accurate understanding of the mechanism of vortices behind lifting surfaces is still lacking. A "rough and ready" calculation procedure is given by Johnsson and Sjøntvedt [4-13].

Apart from viscous scale effects on cavitation inception, mention should also be made of scale effects due to roughness and air or gas content of the fluid. It is known that both roughness and a large air content give rise to cavitation inception at higher values of the cavitation index. In a recent paper by Brown [4-15] it is shown that air content effects are appreciable. Further study of this topic is required, particularly in regard to the relationship between total air content and bubble size and their effect on cavitation inception. Some very interesting findings in this context are given by Keller [4-16]. Effects of roughness on cavitation inception have been assessed by Holl [4-17].

#### 4.3 Calculation of Type and Extent of Cavitation.

Differences occur in the cavitation index at the onset of cavitation (incipient cavitation) and at the disappearance of cavitation (desinent cavitation). This phenomenon is called cavitation hysteresis. In the calculation of the extent of cavitation, it is necessary to take this phenomenon into account insofar that it is required to deal with the differences in time delay for the onset of cavitation and the disappearance of cavitation.

Although the phenomenon of time delay and hysteresis is not completely understood, it is clear that time is required for the growth of a nucleus to a visible cavity and for its decline. The duration of growth and decline is dependent on the effective liquid tension and the population and characteristics of gas or air nuclei entrained in the liquid. If it were assumed that the requirements for the growth of a nucleus to a macroscopic cavity are equal to those for the decline of the cavity, there would essentially be no hysteresis. If the requirements and characteristics for the onset of cavitation are known it would be possible to predict when and where the cavity will collapse.

In assessing the extent of cavitation, the effect of time delay on both the onset and disappearance of cavitation can be roughly determined if the pressure distribution of the non-cavitating body is known and a scaling relation for cavitation from nuclei on smooth surfaces can be found. Such a relation is Knapp's dynamic similarity parameter [4-18] for spherical cavities, which was deduced from Rayleigh's equation for bubble growth or collapse [4-19], viz:

$$R = kt\sqrt{\Delta p/\rho} \quad (4-4)$$

in which  $R$  = maximum radius of bubble,

$k$  = a constant,

$t$  = time of growth to  $R$ ,

$p$  = effective liquid tension causing growth or decline of the cavity,

and  $\rho$  = density of fluid.

Consider the flow past an immersed body having a pressure distribution with a peaked minimum for the non-cavitating condition as shown in Fig. 25. The cavitation index at inception is  $\sigma_1$ . On reducing the cavitation index to some value  $\sigma$ , the cavity will grow to some finite length  $l_{cav}$ , and terminate at some position given by  $x_{C_3}/c$ . Then the effective liquid tension responsible for the growth of the cavity of length  $l_{cav}$  can be written as:

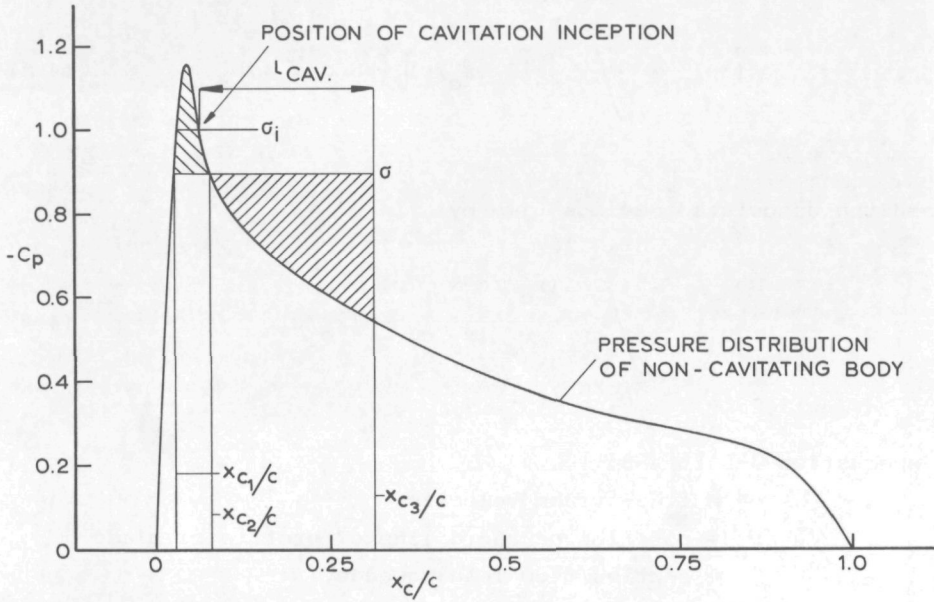


FIG. 25 SKETCH TO DEFINE VARIABLES USED IN THE RELATION FOR CALCULATION OF EXTENT OF CAVITATION.

$$(\Delta p)_G = \int_{x_{c_1}/c}^{x_{c_2}/c} -[\sigma + C_p(x_c/c)] \cdot \frac{1}{2} \rho U^2 d(x_c/c) \quad (4-5)$$

The associated growth time can be written as:

$$t_G = c \int_{x_{c_1}/c}^{x_{c_2}/c} \frac{(x_{c_2}/c - x_{c_1}/c)^2}{v_{x_c}(x_c/c)} d(x_c/c) \quad (4-6)$$

Likewise, the effective liquid tension working to decline the cavity is:

$$(\Delta p)_D = \int_{x_{c_2}/c}^{x_{c_3}/c} [\sigma + C_p(x_c/c)] \cdot \frac{1}{2} \rho U^2 d(x_c/c) \quad (4-7)$$

and the associated decline time by:

$$t_D = c \int_{x_{c_2}/c}^{x_{c_3}/c} \frac{(x_{c_3}/c - x_{c_2}/c)}{v_{x_c}(x_c/c)} d(x_c/c) \quad (4-8)$$

In equation 4-5 to 4-8:

$U$  = free-stream velocity,

$x_c$  = position on chord line of profile or blade section from leading edge,

$v_{x_c}$  = local velocity at  $x_c/c$ ,

and  $c$  = chord length of profile or blade section

With these equations, it is possible to determine the ratio of the value of Knapp's similarity parameter for decline and for growth of the cavity, if the cavity length and the pressure distribution of the non-cavitating body are known. Defining this ratio as  $K$ , we write:

$$K = t_d \sqrt{\frac{(\Delta p)_D}{\rho}} / t_G \sqrt{\frac{(\Delta p)_G}{\rho}} \quad (4-9)$$

which can be written as:

$$K = \frac{\int_{x_{c_2}/c}^{x_{c_3}/c} \frac{(x_{c_3}/c - x_{c_2}/c)}{v_{x_c}(x_c/c)} d(x_c/c) \sqrt{\int_{x_{c_2}/c}^{x_{c_3}/c} [\sigma + C_p(x_c/c)] d(x_c/c)}}{\int_{x_{c_1}/c}^{x_{c_2}/c} \frac{(x_{c_2}/c - x_{c_1}/c)}{v_{x_c}(x_c/c)} d(x_c/c) \sqrt{\int_{x_{c_1}/c}^{x_{c_2}/c} [-\sigma + C_p(x_c/c)] d(x_c/c)}} \quad (4-10)$$

It follows that if the position of  $x_{c_3}/c$  (specifying the cavity length) were not known then this could be determined if the value of  $K$  were known. In the general case, the value of  $K$  will depend on the type of pressure distribution, the value of the ratio  $\sigma/\sigma_i$ , the free-stream velocity, the size of the body, and the characteristics of the air or gas nuclei. An attempt to find such a general relation for  $K$  was undertaken by calculating  $K$  for the results of the cavitation measurements on the NACA 4412 profile already referred to [4-8, 4-9]. The results are shown in Fig. 26. In this figure the value of  $K$  is set out as a function of  $\sigma/\sigma_i$  for the pressure distributions on the suction side at angles of attack of  $+16^\circ$ ,  $+12^\circ$ ,  $+8^\circ$ ,  $+4^\circ$ ,  $+2^\circ$  and  $0^\circ$ , and for the pressure side at  $-2^\circ$  and  $-4^\circ$ . The effect of air content is not included since the NACA 4412 tests were performed at a constant value of the air content ratio. The cavity lengths, necessary to specify the value of  $x_{c_3}/c$  in each case, were obtained by interpolation from Fig. 20 of Reference 4-9. It follows from Fig. 26 that when cavitation inception occurs near the midchord position (for angles of attack of  $+4^\circ$ ,  $+2^\circ$  and  $0^\circ$ ), the value of  $K$  for a prescribed  $\sigma/\sigma_i$ -ratio is essentially the same. All other points are for sheet cavitation occurring near the leading edge. Here a large increase in  $K$  occurs just after inception (which occurs for  $\sigma = \sigma_i$ ), indicating that a much larger value of  $t \sqrt{\Delta p/\rho}$  is required for decline of the cavity than for the growth thereof. At about  $\sigma/\sigma_i = 0.25$  and lower, the value of  $K$  seems to become independent of the type of pressure distribution. In this region the various curves converge to essentially one relationship for  $K$  as a function of

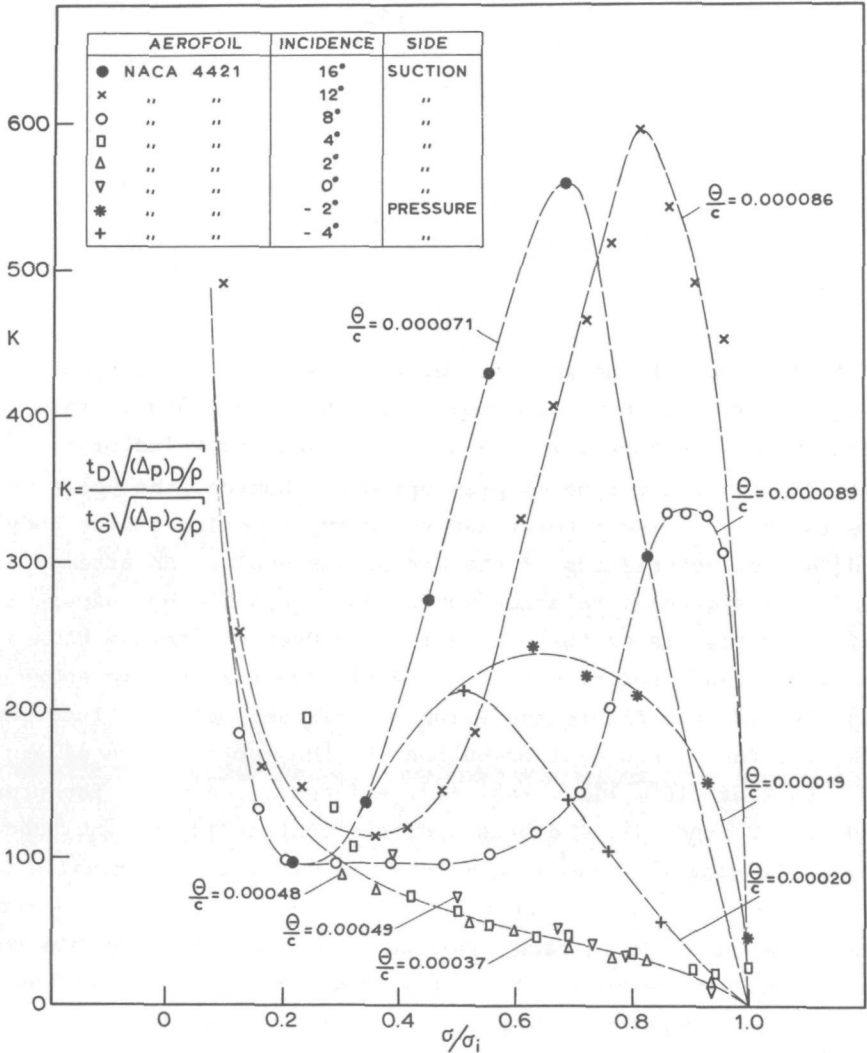


FIG. 26 RATIO OF VALUE OF KNAPP'S SIMILARITY PARAMETER FOR DECLINE TO VALUE FOR GROWTH AS DETERMINED FROM NACA 4412 MEASUREMENTS.

$\sigma/\sigma_i$ , which goes to infinity when  $\sigma/\sigma_i$  approaches zero. This situation probably arises because of the extreme cavity lengths at such low cavitation numbers (super cavitation). It should be noted that for the calculation of  $K$  when the cavity length exceeds the chord length, the value of  $C_p(x_c/c)$  in equation 4-10 is put equal to zero.



To have some measure for the large variation in K at constant  $\sigma/\sigma_i$ , particularly for the occurrence of sheet cavitation near the leading edge, a correlation was sought between K and a characteristic property of the pressure distribution and other parameters which influence K such as the position of cavitation inception. It was found that the momentum thickness of the boundary layer at the inception location afforded such a correlation. This is quite realistic since the value of the momentum thickness at a specific position on the body significantly reflects the upstream pressure history and absolute value of the velocity.

The final correlation, as obtained from the NACA 4412 profile is shown in Fig.27. To facilitate the determination of an analytical function for K, the logarithm to the base 10 is shown as a function of the ratio  $\sigma/\sigma_i$  and as a function of  $\log (\theta_{inc}/c)$  where  $\theta_{inc}$  is the momentum thickness of the laminar boundary layer at the cavitation inception location and c the chord length. The drawn curves represent the formula:

$$\log K = 1.852 + 23.85 \sigma/\sigma_i - 93.90 (\sigma/\sigma_i)^2 + 68.77 (\sigma/\sigma_i)^3 + \frac{0.0450}{\sigma/\sigma_i} + \log \left[ \frac{\theta_{inc}}{c} \right] \left[ -0.4110 + 9.951 (\sigma/\sigma_i) - 33.75 (\sigma/\sigma_i)^2 + 24.29 (\sigma/\sigma_i)^3 \right] \quad (4-11)$$

which was obtained by means of a multiple regression procedure. For calculation purposes it is suggested that for  $\theta_{inc}/c$  greater than approximately 0.0003 bubble cavitation occurs, and for smaller values sheet cavitation. At a specific value of  $\theta_{inc}/c$  and  $\sigma/\sigma_i$  the length of the cavity can be assessed from equation 4-10 when K is determined by means of equation 4-11. To solve equation 4-10 an iteration procedure is required to determine  $x_c/c$ . The beginning of the cavity is assumed to be situated at the point of inception as calculated by the method outlined in section 4.2.

Scale effect on the extent of cavitation exists if at the location of cavitation inception the value of  $\theta_{inc}/c$  varies between full-scale and model scale. This is particularly the case for values of  $\theta_{inc}/c$  smaller than about 0.0003, since then the value of  $K$  appreciably varies with  $\theta_{inc}/c$ . Since this range of  $\theta_{inc}/c$ -values seems to be associated with sheet cavitation on either the suction or pressure side, it may be concluded that a scale effect in the extent of sheet cavitation is very likely to occur. This does not mean that there is no scale effect on the extent of bubble cavitation. Differences in the calculation of  $\sigma_i$ , from the inception considerations of the previous section, will also result in a scale effect in the extent of cavitation.

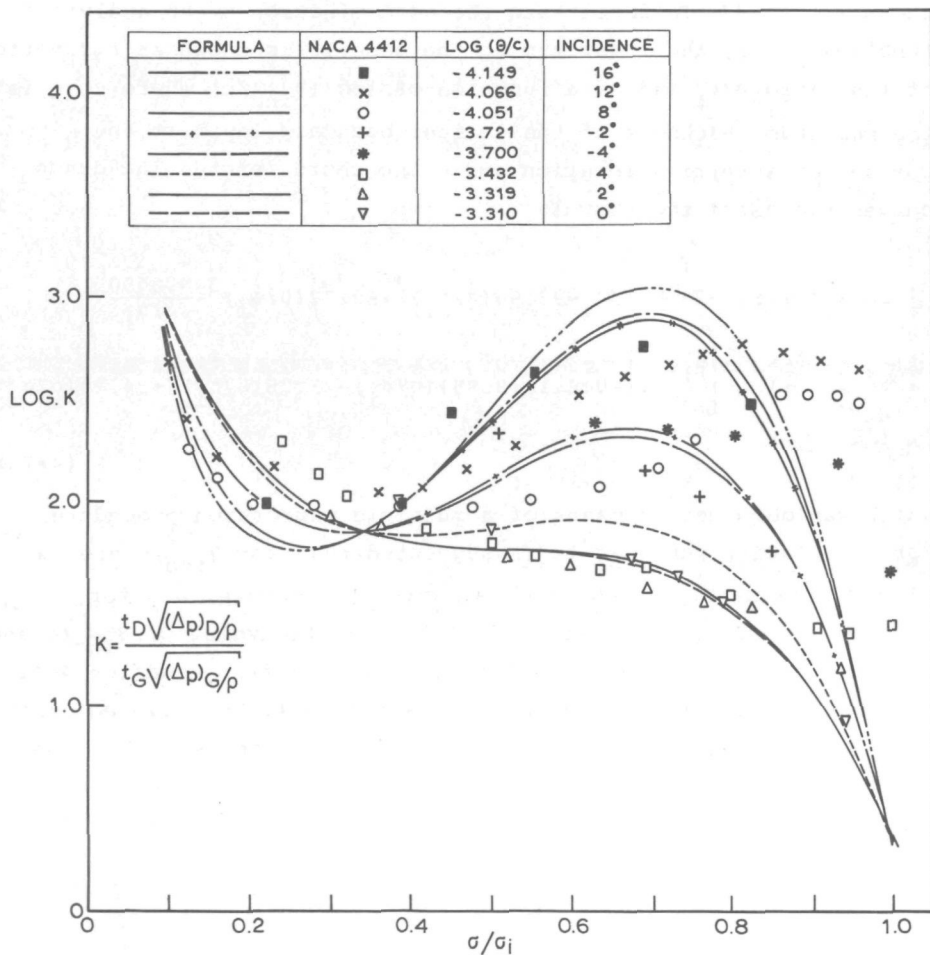
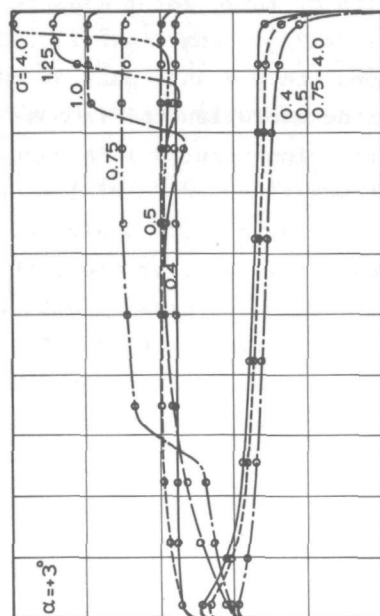
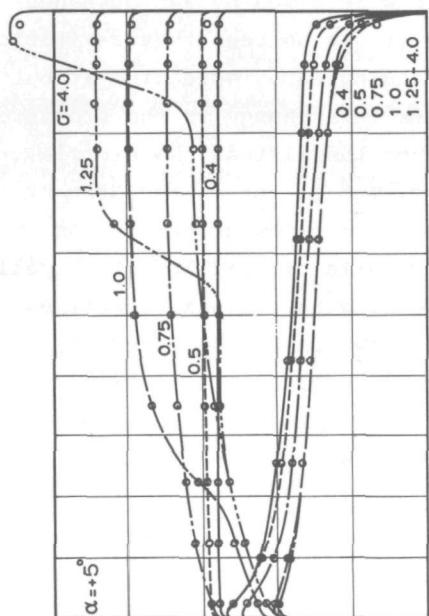
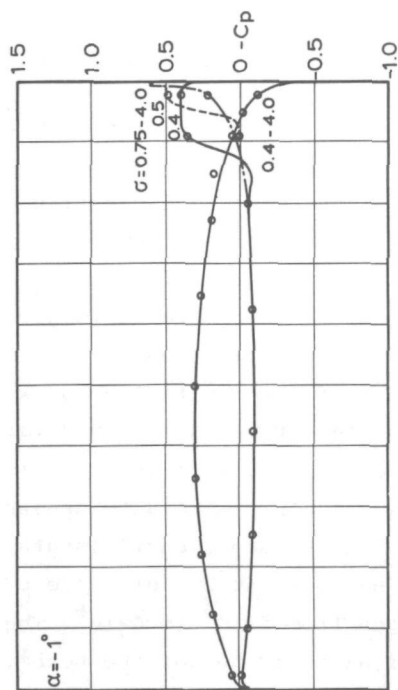
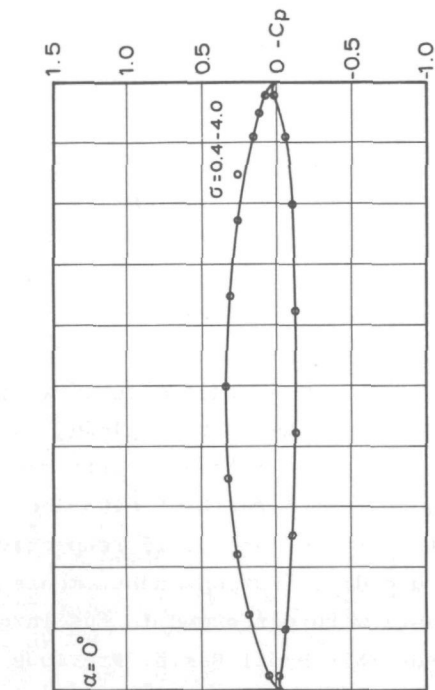


FIG. 27 CORRELATION OF DERIVED FORMULA FOR K AND NACA 4412 DATA

#### 4.4 Effect of Cavitation on Propeller Performance.

The effect of cavitation on propeller performance can be determined if the change in the value of the lift and drag coefficients, after the onset of cavitation, can be assessed. This change in the lift and drag forces on a profile is caused by the change in the flow over the lifting surface whereby the pressure distribution is modified. An example is given in Figs. 28 and 29 in which measure pressure distributions at various angles of attack and for different values of the cavitation index are given. The hydrofoils on which these measurements were made are of the Walchner type [4-20] (not to be confused with the ogival type on which Walchner performed measurements), with a thickness-chord length ratio of 0.03 and 0.06 and a camber-chord length ratio of 0.03 and 0.015 respectively. The Reynolds number of these pressure distribution measurements ranged from  $2 \times 10^6$  to  $6 \times 10^6$ . The tests were performed in the large cavitation tunnel of the Netherlands Ship Model Basin. Previous measurements of this type were reported on by Balhan [4-21]. Results of these later measurements were given by Van Oossanen [4-22, 4-23]. From Figs. 28 and 29 it can be seen that cavitation reduces the pressure peak at the leading edge, spreading it out over the chord length. In most cases this change in the pressure distribution results in a decrease of the lift on the profile, sometimes after an initial increase. The effect on the drag of the profile is quite analogous, but lags somewhat behind. As such, the effectiveness, or the lift-drag ratio of profiles or propeller blade sections decreases with increasing cavitation, sometimes after an initial increase. This is shown in Figs. 30 and 31, in which the lift coefficient, the drag coefficient and the  $C_D/C_L$ -values for the 2 Walchner profiles as a function of cavitation number and angle of attack are shown. The coordinates of these two profiles are given in Tables 9 and 10.

An example of how cavitation can influence the thrust, torque and efficiency of a propeller is given in Fig. 32, taken from Van Lammeren et al [4-24], which is valid for the Wageningen B5-75 propeller in uniform flow.



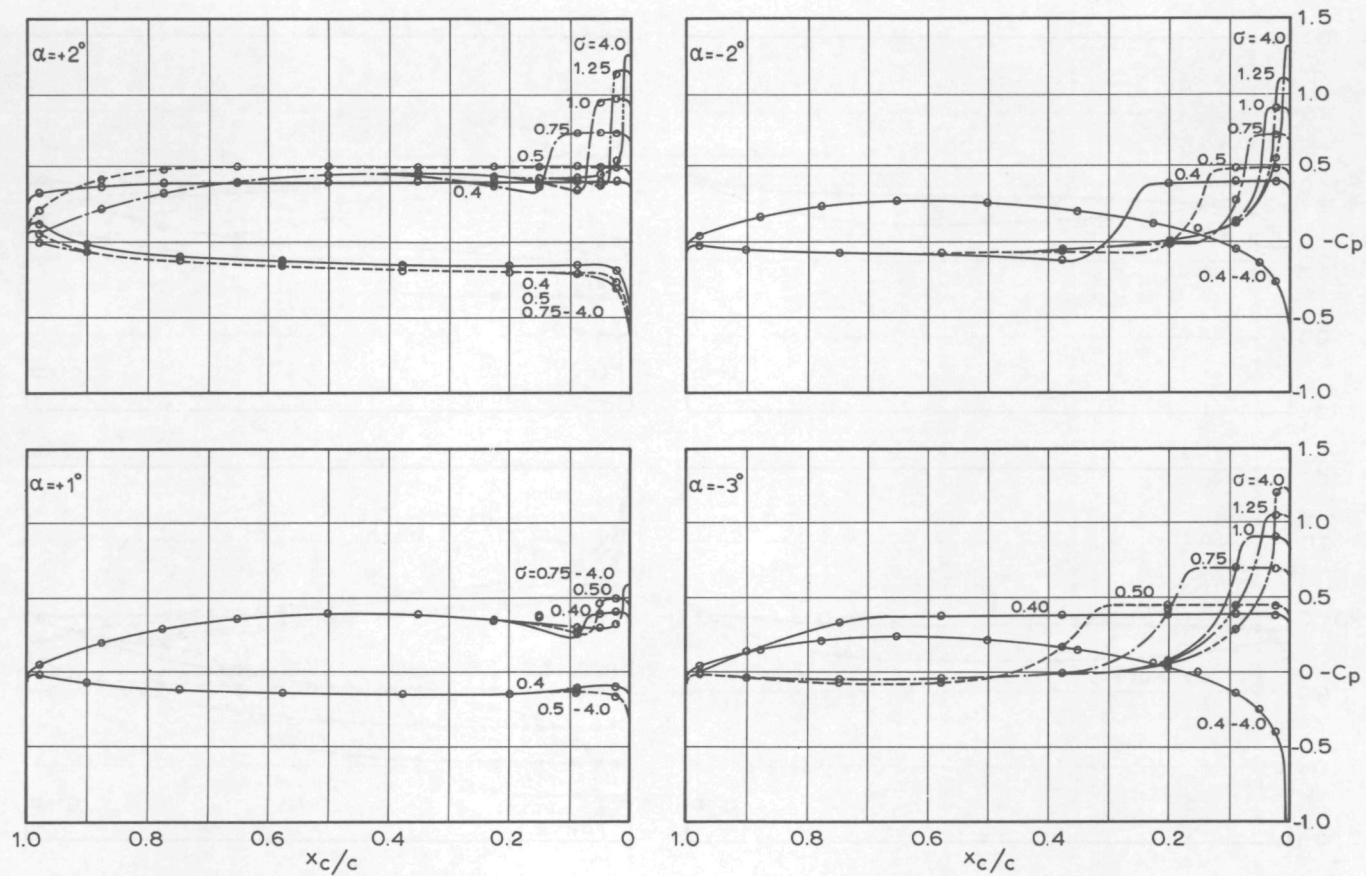
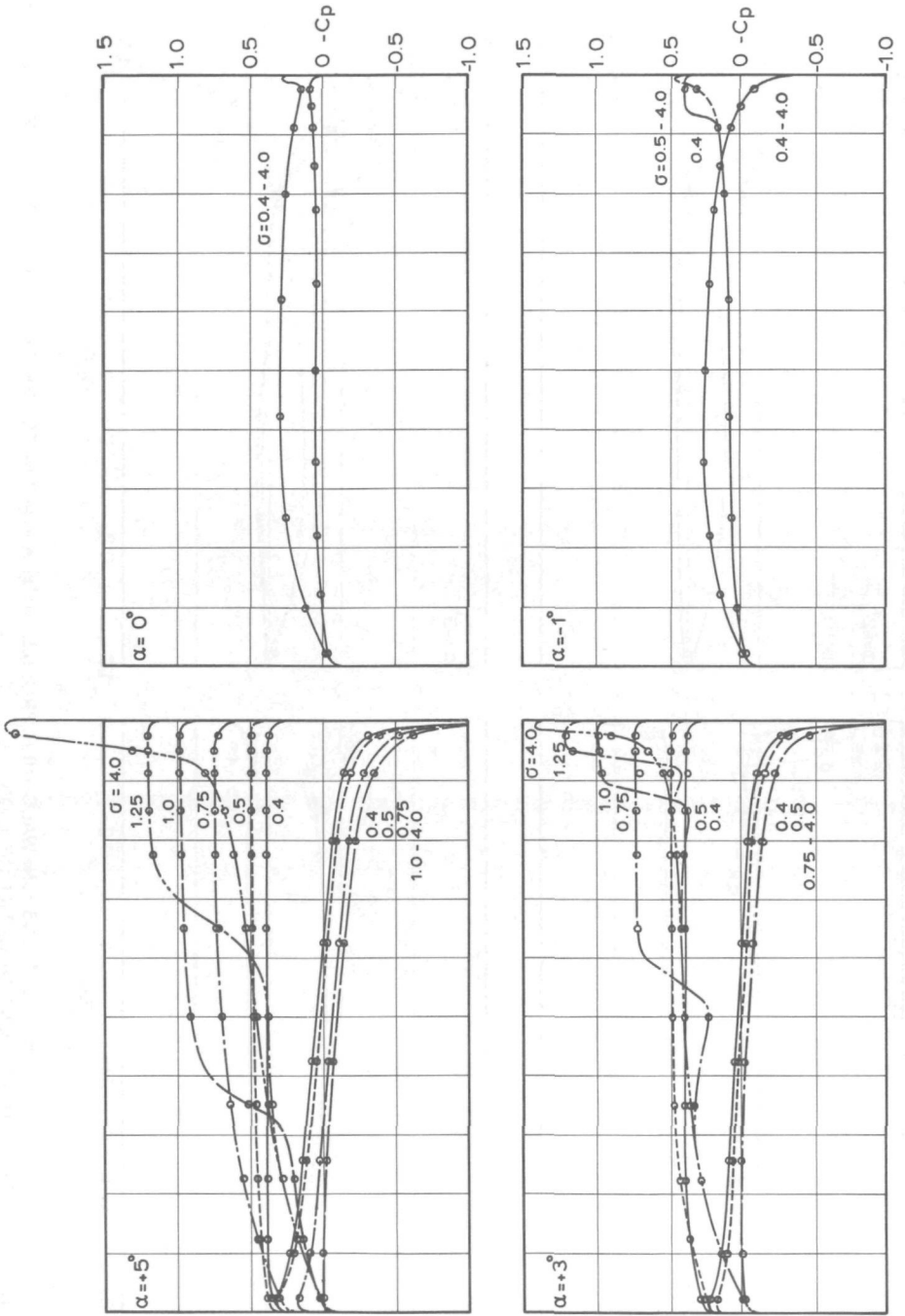


FIG.28. MEASURED PRESSURE DISTRIBUTIONS ON WALCHNER PROFILE WITH A THICKNESS - CHORD LENGTH RATIO OF 0.03 AND A CAMBER - CHORD LENGTH RATIO OF 0.03 .





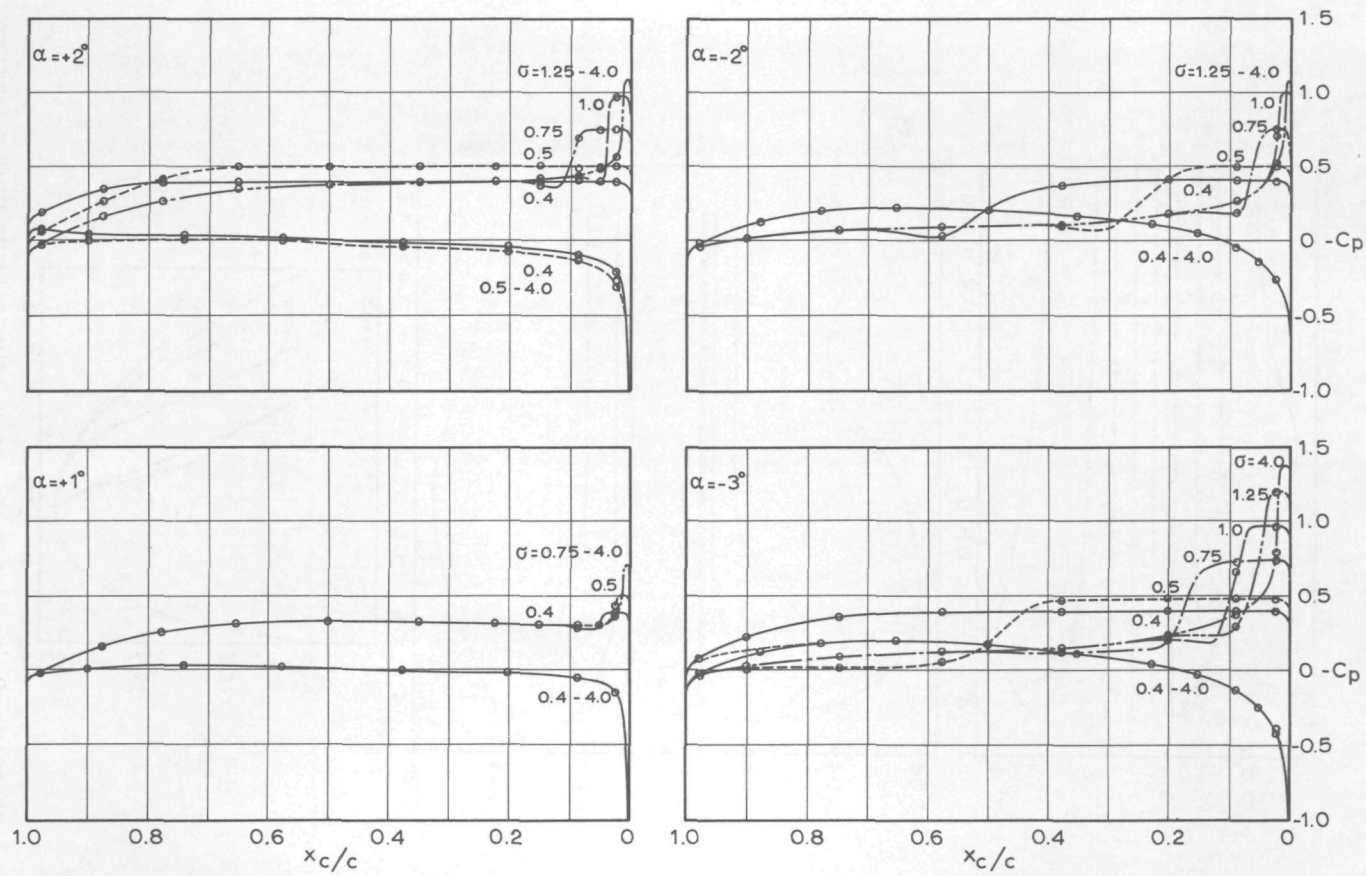


FIG.29. MEASURED PRESSURE DISTRIBUTIONS ON WALCHNER PROFILE WITH A THICKNESS - CHORD LENGTH RATIO OF 0.06 AND A CAMBER - CHORD LENGTH RATIO OF 0.015.

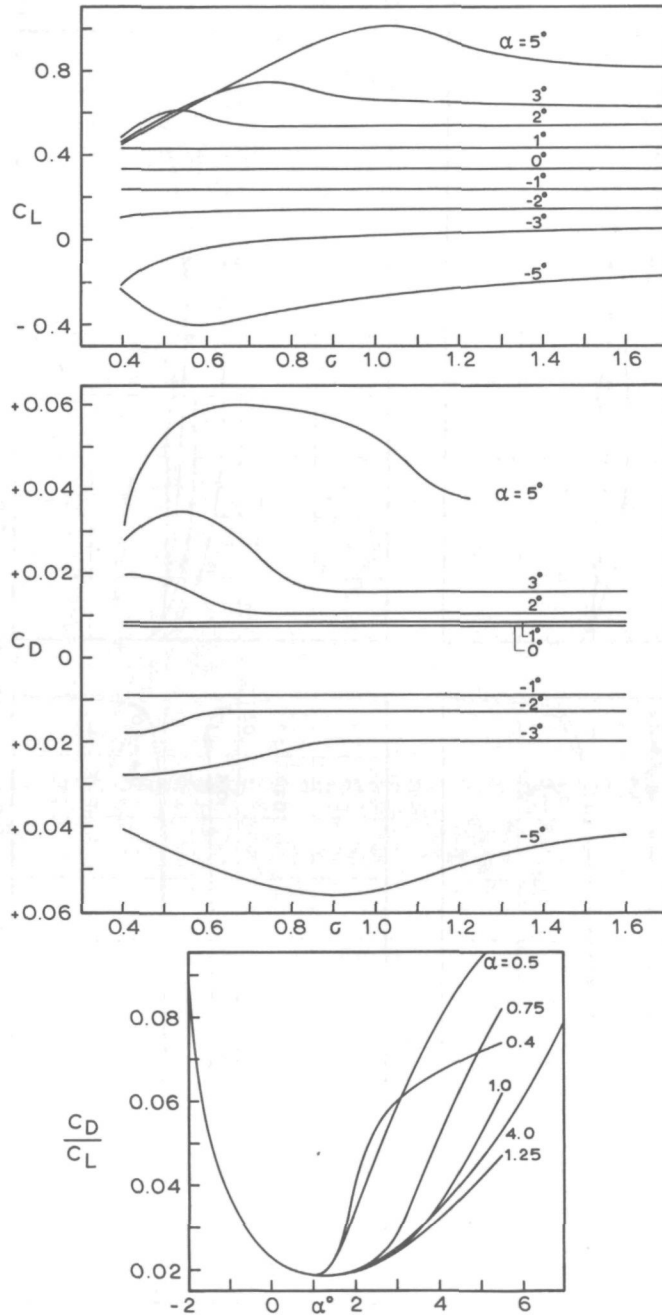


FIG.30 MEASURED  $C_L$ ,  $C_D$  AND  $C_D/C_L$  OF WALCHNER PROFILE AS A FUNCTION OF  $\sigma$  (SAME PROFILE FOR WHICH PRESSURE DISTRIBUTIONS ARE GIVEN IN FIG.28).

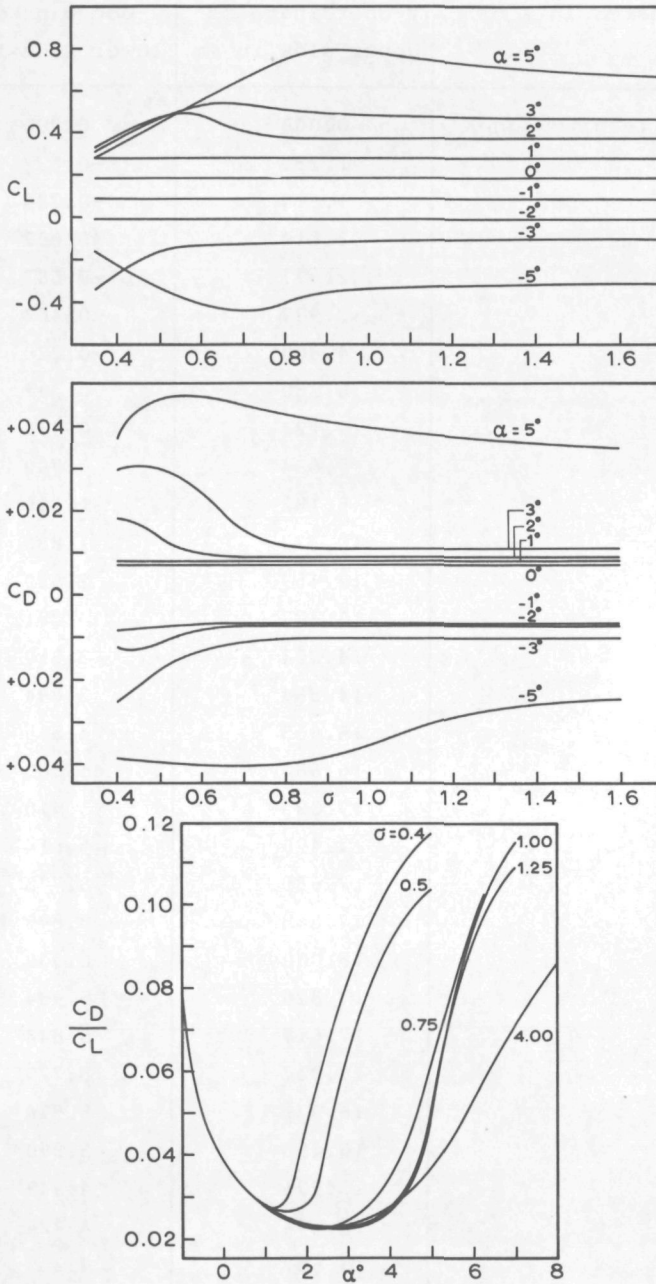


FIG. 31 MEASURED  $C_L$ ,  $C_D$  AND  $C_D/C_L$  OF WALCHNER PROFILE AS A FUNCTION OF  $\sigma$  (SAME PROFILE FOR WHICH PRESSURE DISTRIBUTIONS ARE GIVEN IN FIG. 29).

$x_c$ -coordinates in % of c	y-coordinate of upper side in mm	y-coordinate of lower side in mm
0.000 leading edge	0.000	0.000
0.625	1.235	-0.637
1.250	1.914	-0.726
2.250	2.814	-0.697
2.500	2.997	-0.687
3.750	3.937	-0.463
5.000	4.800	-0.228
7.500	6.380	0.297
8.750	7.123	0.559
10.000	7.834	0.790
12.500	9.182	1.339
15.000	10.372	1.888
20.000	12.459	2.920
22.500	13.377	3.381
25.000	14.204	3.810
25.500	14.364	3.894
30.000	15.605	4.565
35.000	16.683	5.163
37.500	17.093	5.410
40.000	17.429	5.614
42.500	17.685	5.775
45.000	17.865	5.895
50.000	18.000	6.000
55.000	17.826	5.934
57.500	17.617	5.844
60.000	17.317	5.725
62.500	16.931	5.574
65.000	16.456	5.390
70.000	15.221	4.949
74.500	13.844	4.424
75.000	13.657	4.359
77.500	12.747	4.011
80.000	11.745	3.633
85.000	9.460	2.800

87.500	8.180	2.341
90.000	6.814	1.846
91.250	6.091	1.591
92.500	5.350	1.326
95.000	3.798	0.774
96.250	2.974	0.500
97.500	2.129	0.218
97.750	1.954	0.124
98.750	1.248	-0.060
99.375	0.724	-0.116
100.000 trailing edge	0.000	0.000

Table 9. Coordinates of Walchner profile of which cavitation results are given in Figs.28 and 30. Length of profile is 400 mm . Radius of curvature of leading and trailing edges equals 0.35 mm.

x <sub>c</sub> -coordinate in % of c	y-coordinate of upper side in mm	y-coordinate of lower side in mm
0 leading edge	0.000	0.000
0.625	2.021	-1.723
1.250	2.937	-2.343
2.250	4.000	-2.951
2.500	4.423	-3.062
3.750	5.268	-3.533
5.000	6.169	-3.887
7.500	7.749	-4.417
8.750	8.481	-4.647
10.000	9.169	-4.847
12.500	10.369	-5.217
15.000	11.545	-5.423
20.000	13.380	-5.698
22.500	14.182	-5.810
25.000	14.896	-5.893
25.500	15.920	-5.901
30.000	16.081	-5.999
35.000	16.980	-6.060
37.500	17.308	-6.058
40.000	17.575	-6.055
42.500	17.775	-6.045
45.000	17.910	-6.030
50.000	18.000	-6.000
55.000	17.832	-5.952
57.500	17.638	-5.908
60.000	17.352	-5.832
62.500	16.983	-5.731
65.000	16.527	-5.606
70.000	15.313	-5.231
74.500	13.959	-4.841
75.000	13.798	-4.797
77.500	12.922	-4.550
80.000	11.953	-4.271
85.000	9.721	-3.599



87.000	8.465	-3.213
90.000	7.129	-2.807
91.250	6.417	-2.583
92.500	5.690	-2.357
95.000	4.165	-1.883
96.250	3.342	-1.607
97.500	2.452	-1.280
97.750	2.274	-1.186
98.750	1.420	-0.827
99.375	0.789	-0.508
100.000 trailing edge	0.000	0.000

Table 10. Coordinates of Walchner profile of which cavitation results are given in Figs.29 and 31. Length of profile is 400 mm. Radius of curvature of leading and trailing edges equals 0.35 mm.

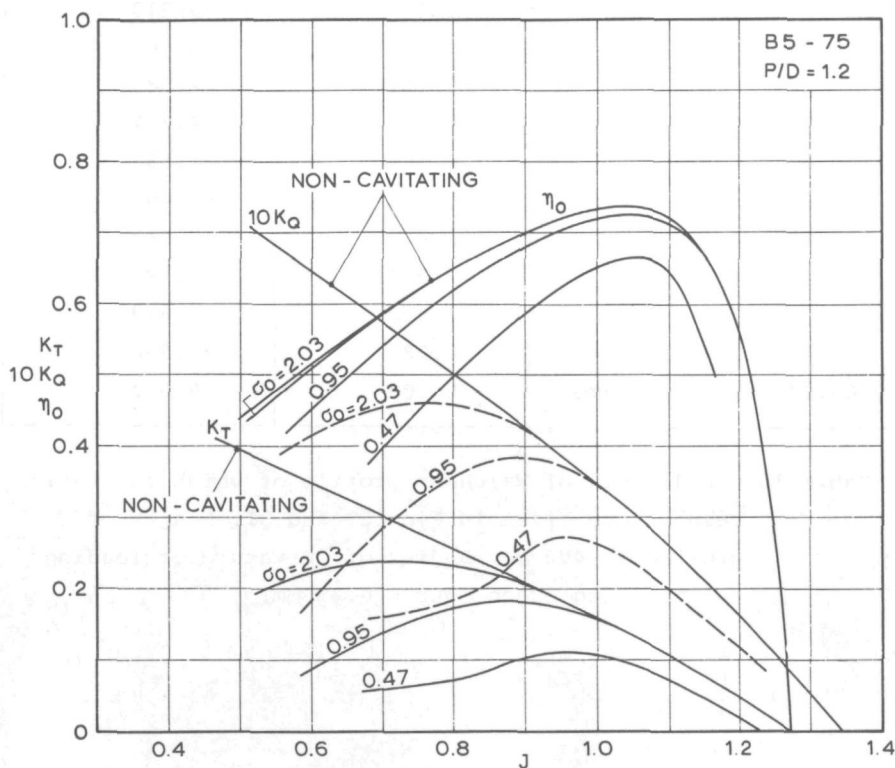


FIG. 32 EXAMPLE OF DECREASE IN THRUST, TORQUE AND EFFICIENCY OF PROPELLER DUE TO CAVITATION.

The analytical determination of the change in lift and drag properties due to cavitation has been considered extensively in the literature. For super-cavitation a number of satisfactorily accurate formulas are available for the lift and drag coefficients as functions of the cavitation index and relative properties of the cavity shape. A summary of these are given by Knapp et al [4-27]. For sub-cavitating cases, in which the cavity lengths are of the order of the chord length or less, only a few results are available. Geurst [4-25], and Hanaoka [4-26] among others, have applied a linearized approach and obtained results which could be used in specific cases. Gutsche [4-27, 4-28], also in an attempt to derive the propeller performance in cavitating conditions, gives a set of formulas which work reasonably well if the propeller blades are composed of ogival blade sections

(Gutsche uses Walchner's results [4-29] for deriving cavity lengths). None of these formulas account for the increase in lift and drag which can occur for cavity lengths less than the chord length. The graphs given by Van Oossanen [4-23] for the change in lift, drag and moment properties due to cavitation do account for this phenomenon. These, however, should only be considered valid for the profile types studied.

To derive a satisfactory method for the change in lift and drag, some reference will have to be given to the change in the pressure distribution of the non-cavitating body when cavitation occurs. From the results presented in Figs. 28 and 29 it can be seen that the distance along which the pressure distribution of the cavitating body is affected by cavitation is about twice the length of the cavity. The flat part of the pressure distribution corresponds to the position of the actual cavity. The pressure distribution on the cavitating body becomes equal to that of the non-cavitating body, downstream of the cavity, after bridging a region possessing a relatively steep pressure gradient. The length of this region is approximately equal to the length of the cavity. This is illustrated in Fig. 33. This fact leads to the possibility of determining the lift coefficient (or change in lift coefficient) by integrating the pressure distribution constructed in this way. This can only be carried out when the cavity length is smaller than half a chord length, since then the pressure distribution on the other side of the profile is unaffected. The required knowledge of the cavity length to determine if this is the case can be assessed by means of the equations of the previous section.

When the cavity extends onto the downstream half of the profile or blade section, there is a loss in lift caused by the change in pressure distribution on the non-cavitating side. As soon as lift loss occurs good use can be made of a formula given by Radar [4-30], to determine the change in lift due to cavitation, viz:

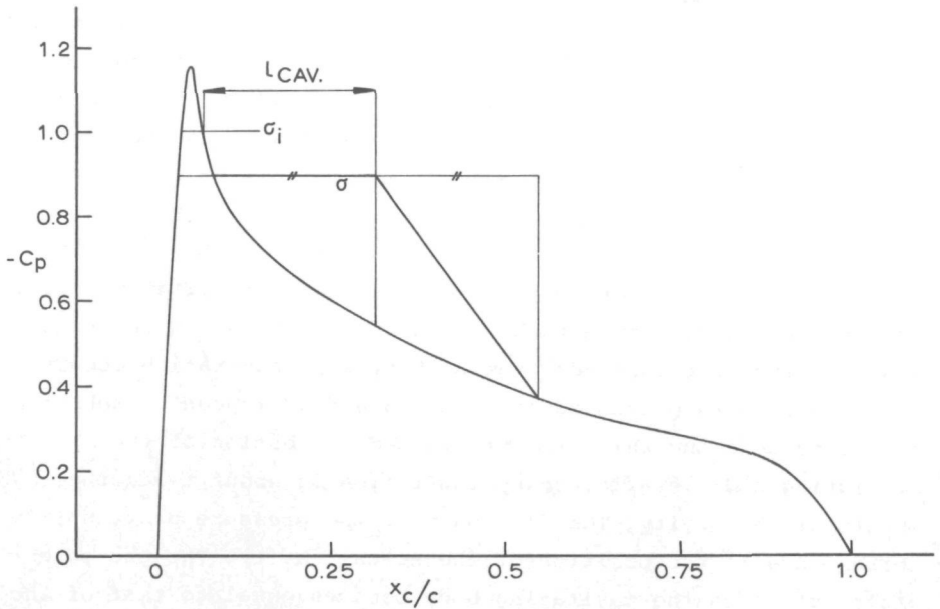


FIG. 33 CONSTRUCTION OF APPROXIMATE PRESSURE DISTRIBUTION ON CAVITATING BODY WHEN CAVITY LENGTH IS LESS THAN HALF THE CHORD LENGTH.

$$\frac{C_L}{C_{L_\infty}} = \frac{C_{L_0}}{C_{L_\infty}} + \left[ 1 - \frac{C_{L_0}}{C_{L_\infty}} \right] \sin^2 \left[ \frac{\pi}{2} \cdot \frac{\sigma}{\sigma_{crit}} \right] \quad (4-12)$$

in which  $C_L$  = lift coefficient for any cavitation number,

$C_{L_0}$  = lift coefficient for  $\sigma=0$ ,

$C_{L_\infty}$  = lift coefficient for non-cavitating condition  
or for beginning of lift loss,

and  $\sigma_{crit}$  = cavitation number for beginning of lift loss.

A well-accepted value for the lift coefficient for zero cavitation number is:

$$C_{L_0} = \frac{\pi \alpha}{2} \quad (4-13)$$

where  $\alpha$  = angle of attack in radians.

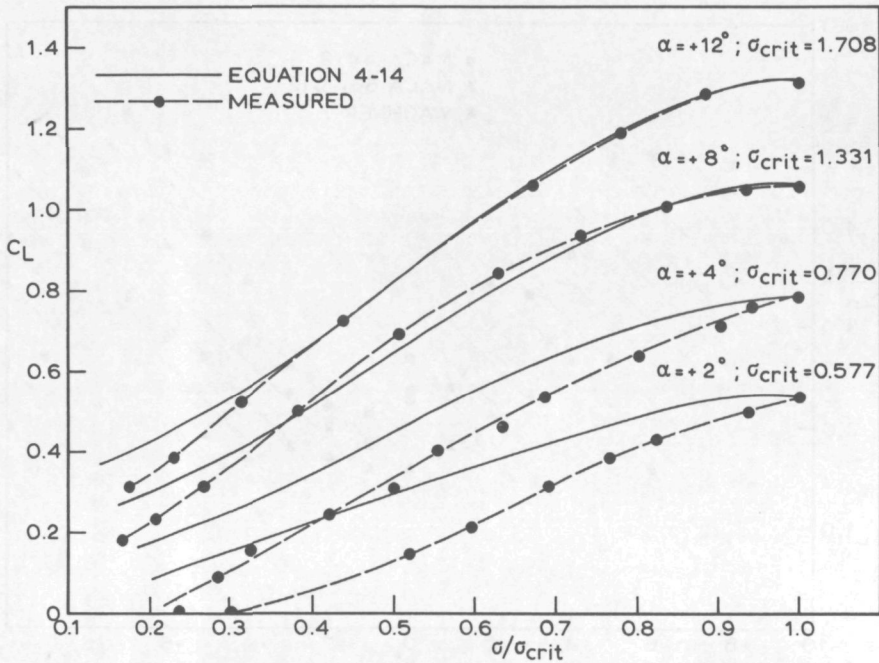


FIG. 34 CORRELATION OF NACA 4412 DATA AND RADAR'S FORMULA FOR EFFECT OF CAVITATION ON LIFT COEFFICIENT.

To use equation 4-12, the value of  $\sigma_{crit}$  and  $C_{L_\infty}$  must be determined at the beginning of lift loss. This may happen as soon as cavitation begins, or when the cavity develops beyond the midchord position. The trend in the value of the lift coefficient with the onset of cavitation can be determined by integration of the changed pressure distribution as constructed in Fig. 33.

Substitution of equation 4-13 in 4-12 gives:

$$\frac{C_L}{C_{L_\infty}} = \frac{\pi\alpha}{2C_{L_\infty}} + \left[ 1 - \frac{\pi\alpha}{2C_{L_\infty}} \right] \sin^2 \left[ \frac{\pi}{2} \cdot \frac{\sigma}{\sigma_{crit}} \right] \quad (4-14)$$

A comparison of the lift measurements on the cavitating NACA 4412 hydrofoil and this equation is shown in Fig. 34.

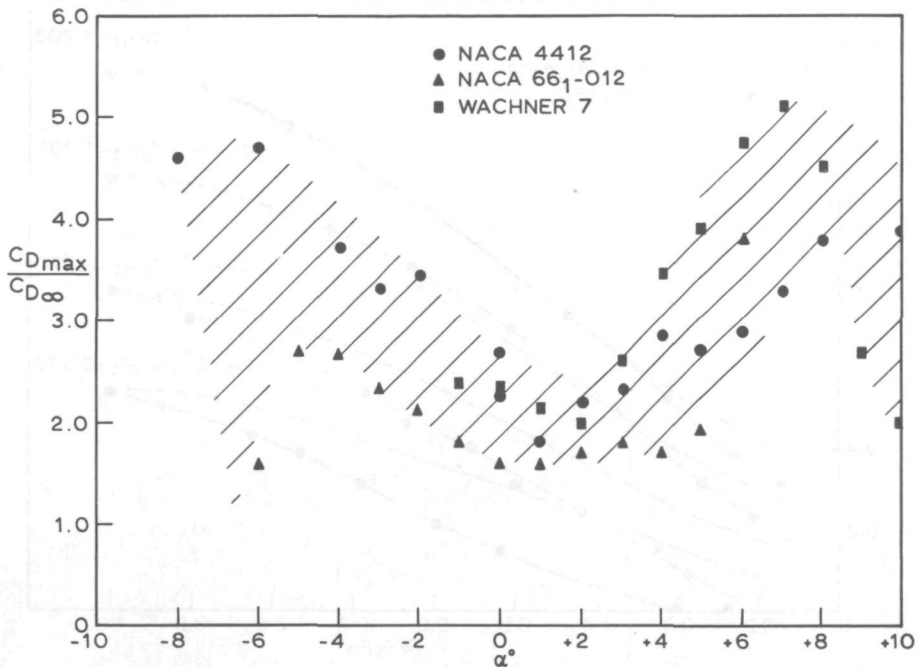


FIG.35 PLOT OF RATIO OF MAXIMUM DRAG COEFFICIENT (WHEN CAVITATION LENGTH EQUALS CHORD LENGTH) TO VALUE IN NON-CAVITATING FLOW AS A FUNCTION OF ANGLE OF INCIDENCE.

The increase in lift after the onset of cavitation may or may not occur. The tendency is that it will occur when the non-cavitating body has a very high and narrow pressure peak near the leading edge. The reason for this is that the eventuating sheet cavitation, just after inception, almost immediately has an appreciable length due to the large value of the factor  $K$ , as described in the previous section. The increase in drag after the onset of cavitation, however, always appears. To assess its value in cavitating flows, good use can be made of the fact that the maximum increase in  $C_D$  always occurs when the trailing edge of the cavity coincides with the trailing edge of the profile or propeller blade section. Fig. 35 shows the ratio of this maximum value of the drag coefficient to the value of the drag coefficient in non-cavitating flow as a function of the angle of attack for the NACA 4412, NACA 66<sub>1</sub>-012 and Walchner 7 profiles measured by Kermeen [4-9, 4-10]. It is seen that at approximately the ideal



angle of attack the value of this ratio is equal to about 2. This ratio increases to about 4 at angles of incidence equal to about  $\alpha_{i-}+6^\circ$ , beyond which a decrease occurs. If it is assumed that this trend is typical of all profiles used in propeller design, we write:

$$\frac{C_{D_{\max}}}{C_{D_\infty}} \approx 2 + \frac{(\alpha - \alpha_{i-})^2}{9} - \frac{(\alpha - \alpha_{i-})^4}{648} \quad (4-15)$$

which is approximately valid for:

$$-8^\circ \leq \alpha - \alpha_{i-} \leq +8^\circ$$

If it is, furthermore, assumed that the change in  $C_D$  occurs as does the change in  $C_L$ , we write, analogously to Radar's formula for the change in lift:

$$\frac{C_D}{C_{D_\infty}} = \frac{C_{D_0}}{C_{D_\infty}} + \left[ 1 - \frac{C_{D_0}}{C_{D_\infty}} \right] \sin^2 \left[ \frac{\pi}{2} \frac{\sigma}{\Delta\sigma} \right] \quad (4-16)$$

in which  $C_D$  = drag coefficient at any cavitation number,  
 $C_{D_\infty}$  = drag coefficient of non-cavitating profile when the trailing edge of the cavity is situated upstream of the profile trailing edge, and equal to  $C_{D_{\max}}$  when the trailing edge of the cavity is situated downstream of the profile trailing edge,  
 and  $C_{D_0}$  = drag coefficient equal to  $C_{D_{\max}}$  for determining  $C_D$  when the trailing edge of the cavity is situated upstream of the profile trailing edge, and equal to the value for  $\sigma=0$  when the trailing edge of the cavity is situated downstream of the profile trailing edge.

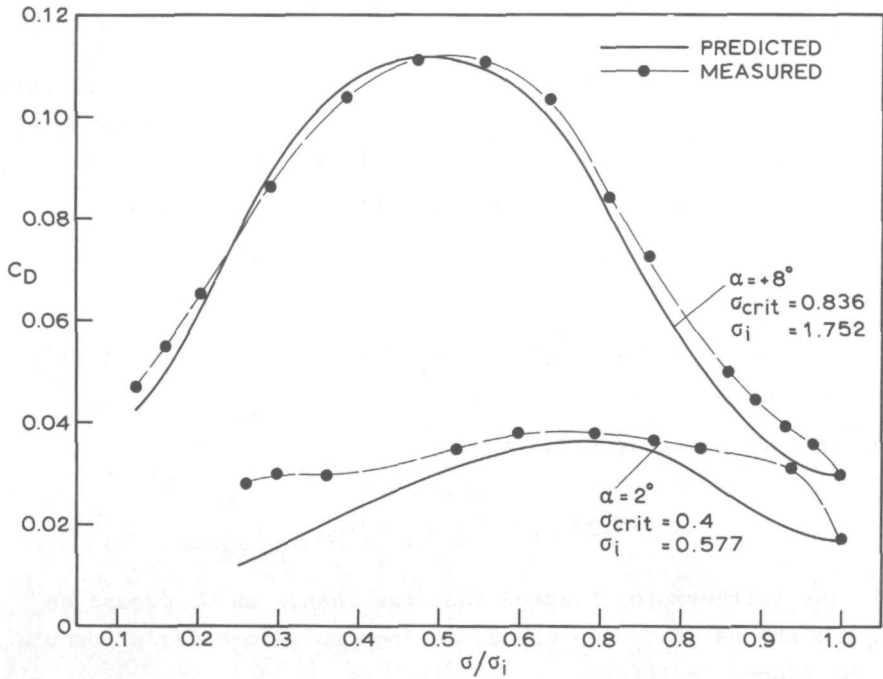


FIG.36 COMPARISON OF PREDICTED AND MEASURED DRAG COEFFICIENT OF CAVITATING NACA 4412 PROFILE FOR TWO ANGLES OF ATTACK.

The value of  $C_D$  at  $\sigma=0$  is considered to be:

$$C_{D_0} = \frac{\pi\alpha^2}{2} \tag{4-17}$$

where  $\alpha$  is in radians. Hence, when the trailing edge of the cavity is situated upstream of the profile trailing edge:

$$\frac{C_D}{C_{D_\infty}} = \frac{C_{D_{max}}}{C_{D_\infty}} + \left[ 1 - \frac{C_{D_{max}}}{C_{D_\infty}} \right] \sin^2 \left[ \frac{\pi}{2} \left( \frac{\sigma_{crit} - \sigma}{\sigma_{crit} - \sigma_i} \right) \right] \tag{4-18}$$

and when the trailing edge of the cavity is situated downstream of the profile trailing edge:

$$\frac{C_D}{C_{D_{max}}} = \frac{\pi\alpha^2}{2C_{D_{max}}} + \left[ 1 - \frac{\pi\alpha^2}{2C_{D_{max}}} \right] \sin^2 \left[ \frac{\pi}{2} \frac{\sigma}{\sigma_{crit}} \right] \tag{4-19}$$

In equations 4-18 and 4-19,  $C_{D_{max}}$  follows from equation 4-15,  $\sigma_{crit}$  equals the value of the cavitation index for beginning of drag loss (which starts when the trailing edge of the cavity coincides with the trailing edge of the profile), and  $\sigma_i$  is equal to the value of the cavitation index for cavitation inception. Fig. 36 gives a comparison of the drag coefficient measured on the NACA 4412 hydrofoil and the results of equations 4-18 and 4-19.

The calculation of propeller thrust, torque and efficiency, when cavitation occurs, is analogous to the calculation procedure for the non-cavitating case. Use is made of equations 2-41 to 2-46 with the understanding that now the procedure described above is used for the determination of the lift and drag coefficients.

CHAPTER 5

RESULTS OF CALCULATIONS AND CORRELATION WITH EXPERIMENT

5.1 Open-Water Propeller Performance: Differences Between Model and Full Scale.

To assess the accuracy of the propeller theory developed in chapter 2, a number of performance calculations were made in uniform flow (open-water). These calculations were carried out for propellers of the Wageningen B-series to estimate the accuracy of the theory for various blade numbers and blade areas, and for the high skew propeller series developed at the Naval Ship Research and Development Center to assess the accuracy of predicting the influence of skew. Figures 37 to 41 present the results for the B-series propellers and Fig. 42 presents the results for the high skew propellers.

Table 11 gives the overall geometric properties of the original Wageningen B-series. The required coordinates of the profiles were calculated by means of formulas, analogous to the formulas given by Van Gent and Van Oossanen [5-2], viz:

$$\left. \begin{aligned} y_{\text{face}} &= V_1 (t_{\text{max}} - t_{\text{t.e.}}) \\ y_{\text{back}} &= (V_1 + V_2) (t_{\text{max}} - t_{\text{t.e.}}) + t_{\text{t.e.}} \end{aligned} \right\} \text{for } P \leq 0 \quad (5-1)$$

$$\text{and } \left. \begin{aligned} y_{\text{face}} &= V_1 (t_{\text{max}} - t_{\text{l.e.}}) \\ y_{\text{back}} &= (V_1 + V_2) (t_{\text{max}} - t_{\text{l.e.}}) + t_{\text{l.e.}} \end{aligned} \right\} \text{for } P > 0 \quad (5-2)$$

From Fig. 43 it follows that:

$y_{\text{face}}, y_{\text{back}}$  = vertical ordinate of a point on a blade section on the face and on the back with respect to the pitch line,

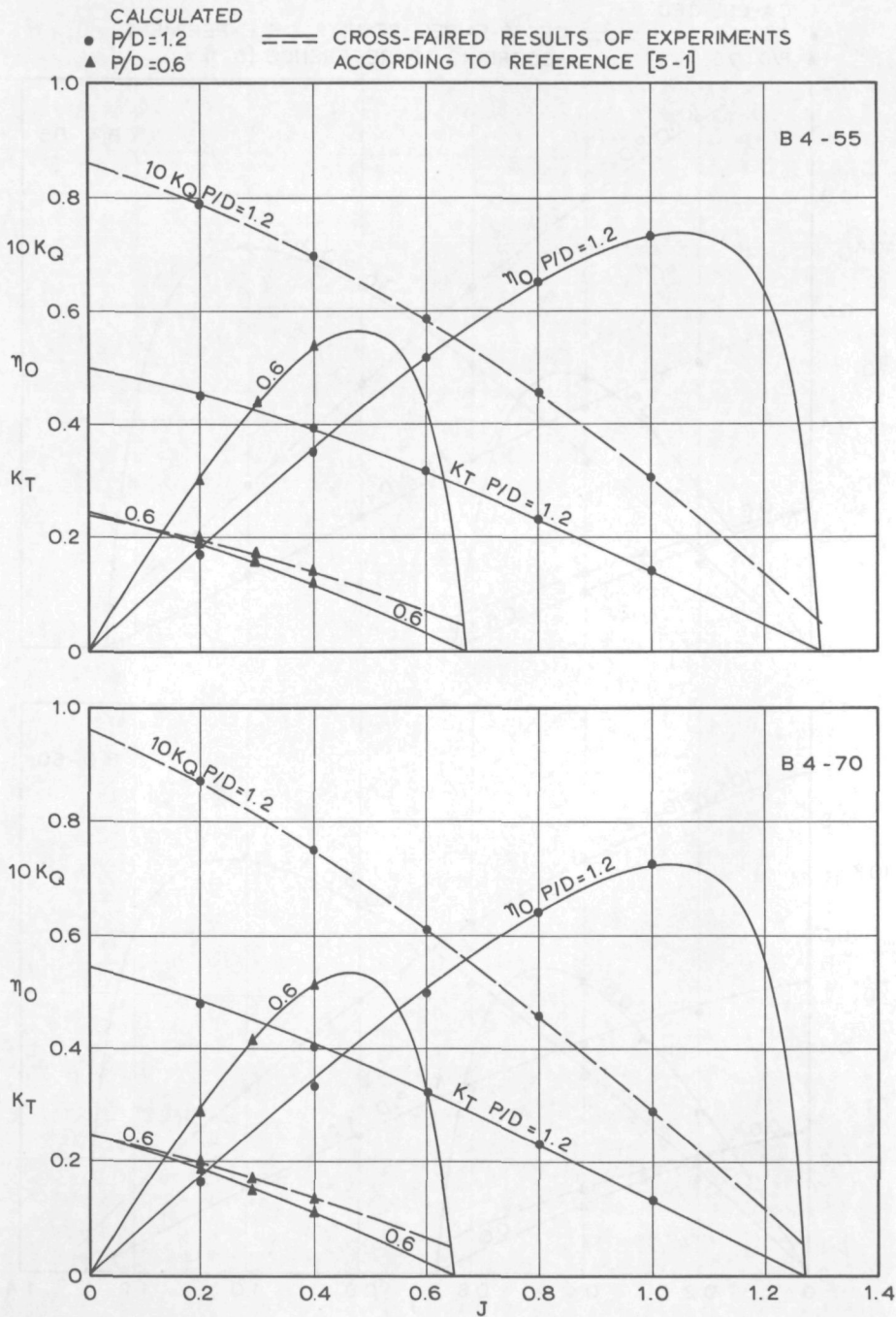


FIG. 37 RESULTS OF CALCULATION AND EXPERIMENTS FOR B-SERIES PROPELLERS

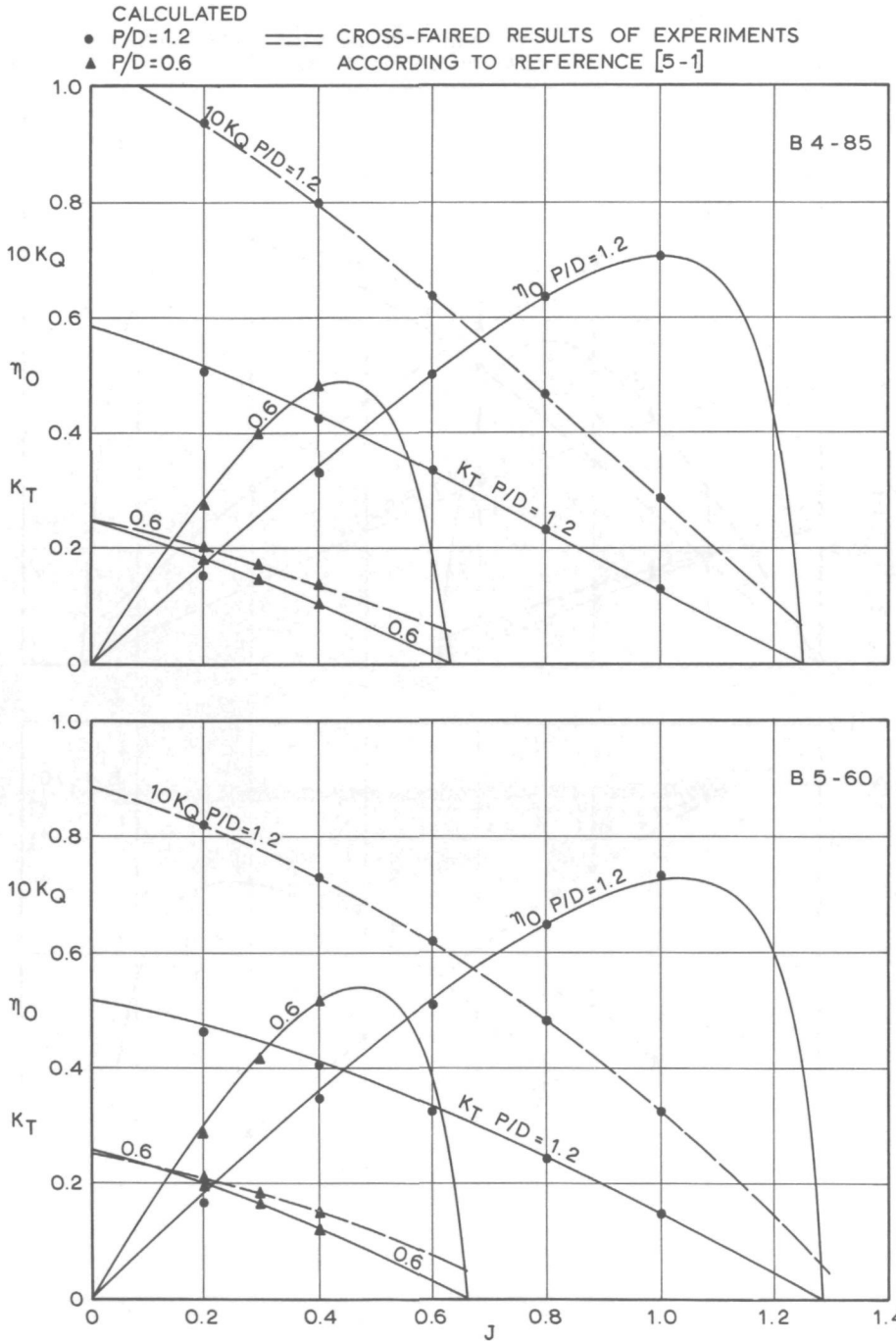


FIG.38 RESULTS OF CALCULATION AND EXPERIMENTS FOR B-SERIES PROPELLERS



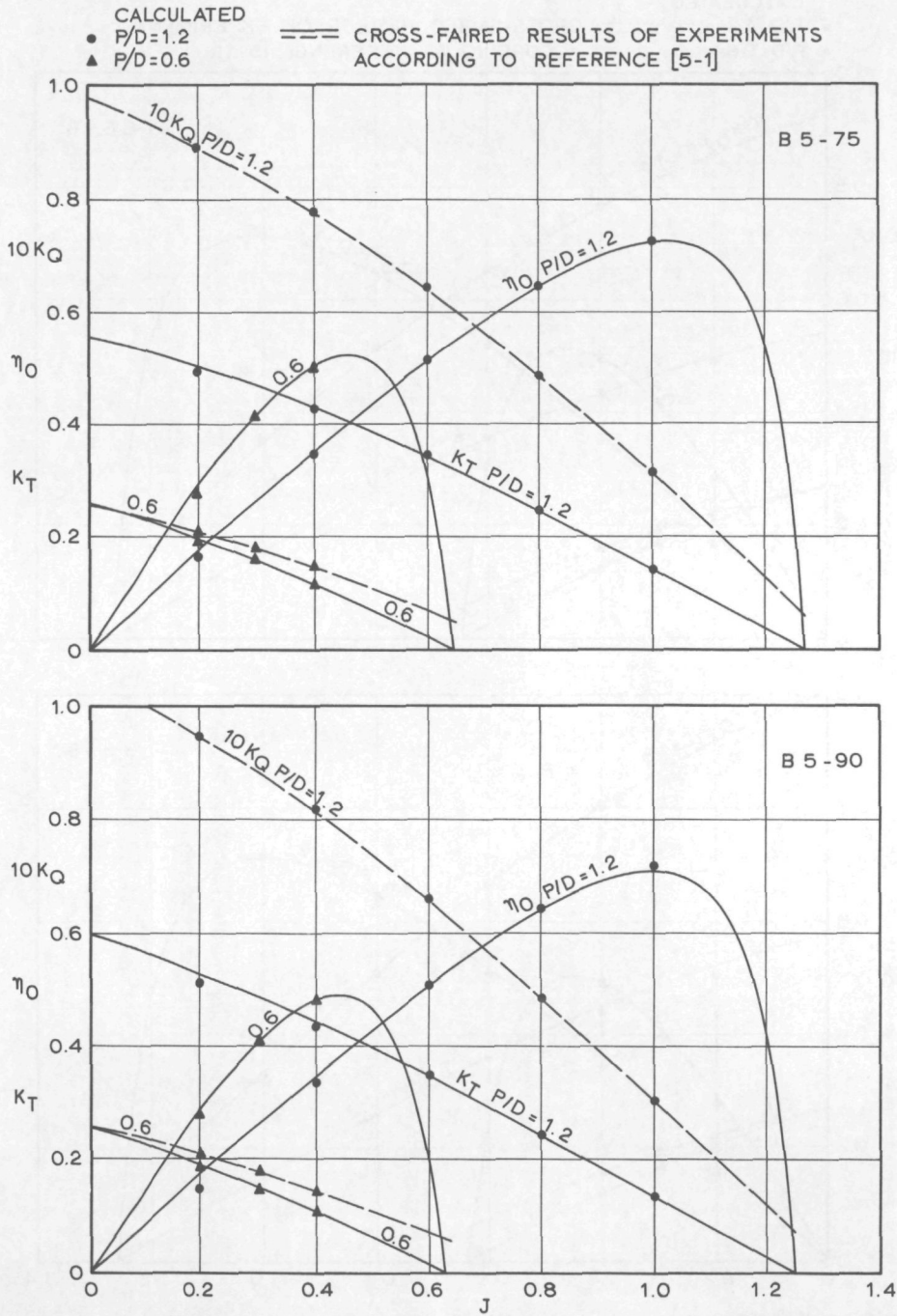


FIG.39 RESULTS OF CALCULATION AND EXPERIMENTS FOR B-SERIES PROPELLERS

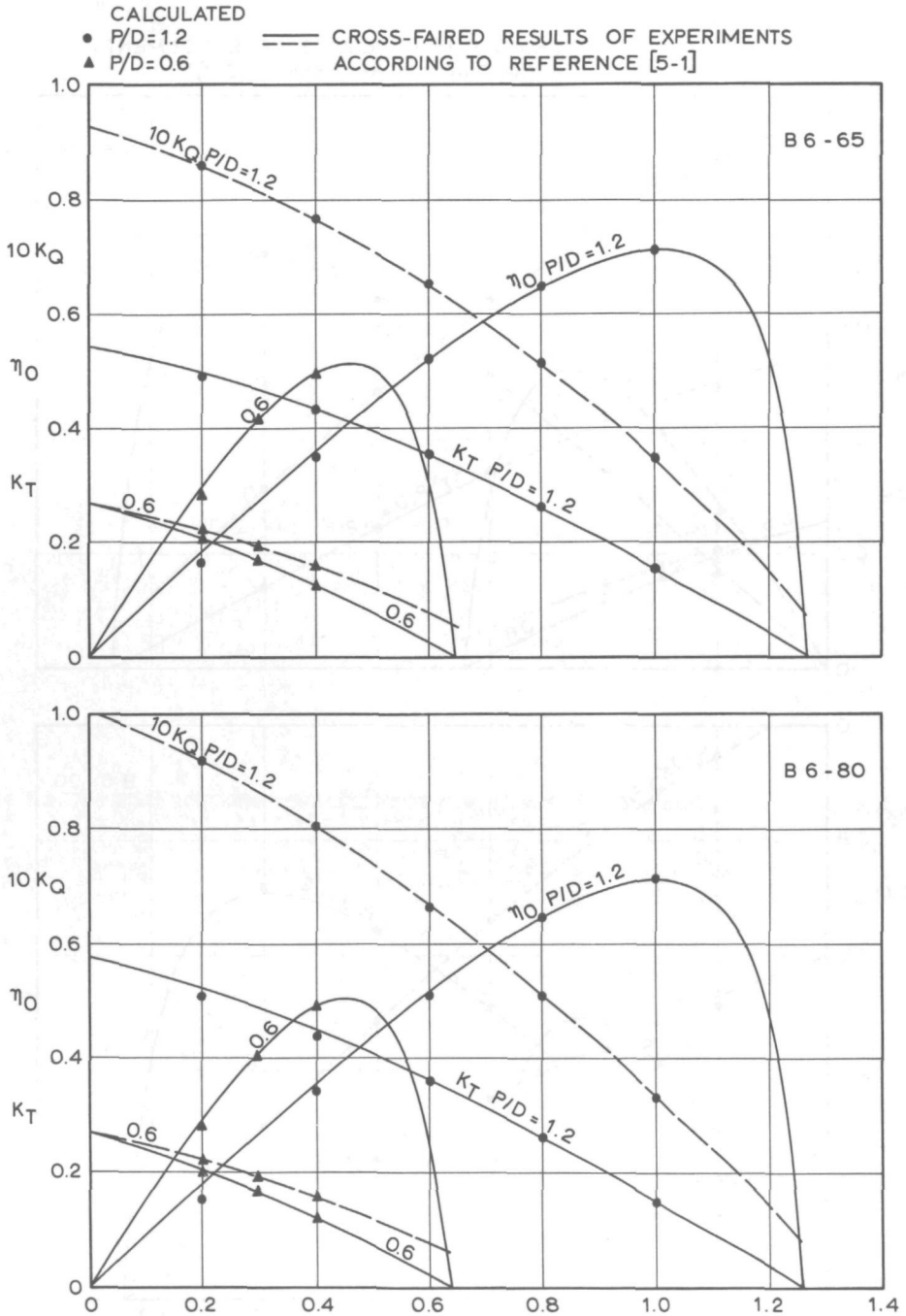


FIG.40 RESULTS OF CALCULATION AND EXPERIMENTS FOR B-SERIES PROPELLERS

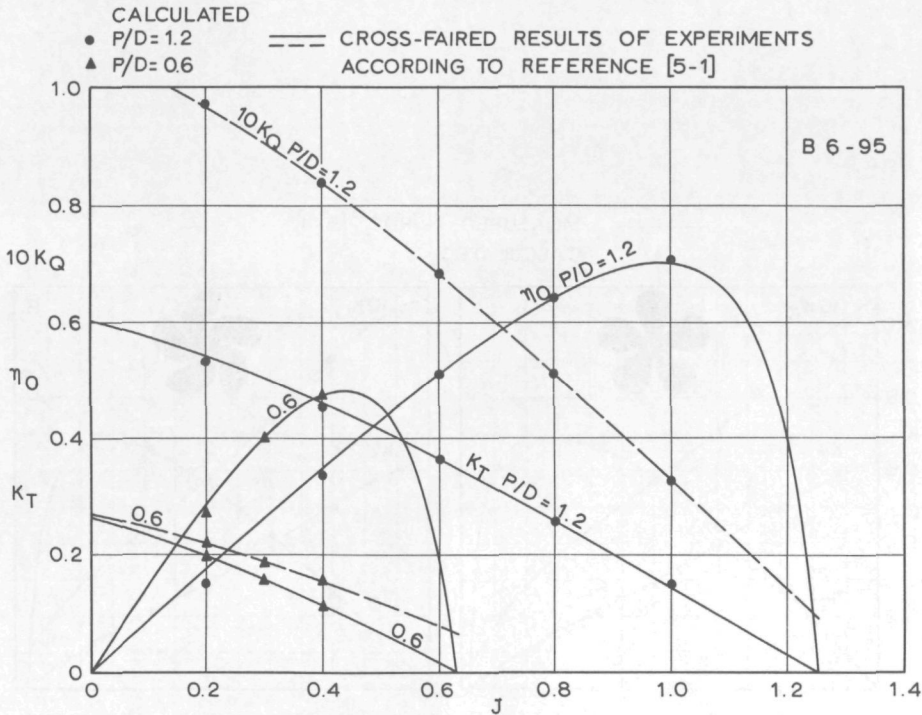


FIG.41 RESULTS OF CALCULATION AND EXPERIMENTS FOR B-SERIES PROPELLERS

$t_{max}$  = maximum thickness of blade section,  
 $t_{t.e.}, t_{l.e.}$  = extrapolated blade section thickness at  
 the trailing and leading edges,  
 $V_1, V_2$  = tabulated functions dependent on  $r/R$  and  $P$ ,  
 and  $P$  = non-dimensional coordinate along pitch line  
 from position of maximum thickness to  
 leading edge (where  $P=1$ ), and from position  
 of maximum thickness to trailing edge  
 (where  $P = -1$ ).

Values of  $V_1$  and  $V_2$  are given in Tables 12 and 13. The values of  $t_{l.e.}$  and  $t_{t.e.}$  are usually chosen in accordance with rules laid down by classification societies or in accordance with manufacturing requirements. In conjunction with the geometry of this propeller series, it is remarked that at the Netherlands Ship Model Basin, now modified B-series propellers are used and designed, which have a slightly wider blade contour near the blade tip. These

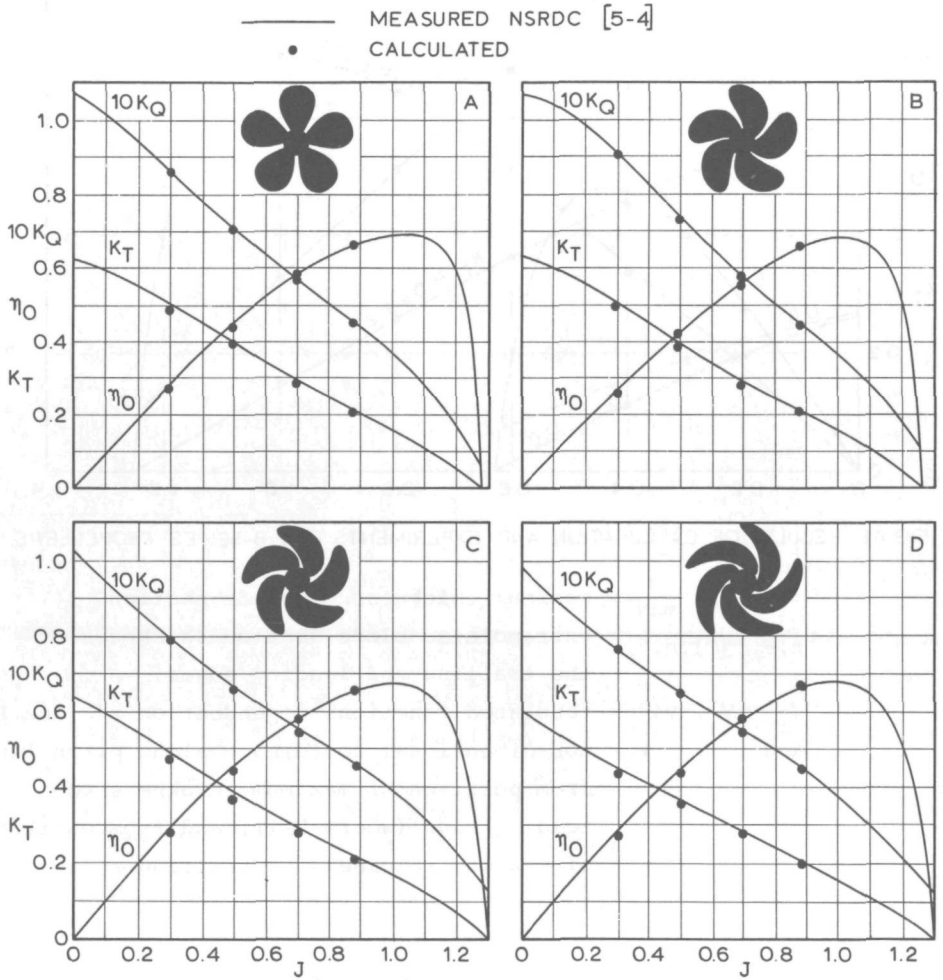


FIG.42 COMPARISON OF MEASUREMENTS AND CALCULATIONS FOR STEADY THRUST AND TORQUE OF HIGH SKEW PROPELLER SERIES OF REFENCE 5-4

Dimensions of four-, five-, six- and seven bladed B-screw series.

r/R	$\frac{c_r}{D} \cdot \frac{Z}{A_E/A_O}$	$a_r/c_r$	$b_r/c_r$	$s_r/D = A_r - B_r Z$	
				$A_r$	$B_r$
0.2	1.662	0.617	0.350	0.0526	0.0040
0.3	1.882	0.613	0.350	0.0464	0.0035
0.4	2.050	0.601	0.351	0.0402	0.0030
0.5	2.152	0.586	0.355	0.0340	0.0025
0.6	2.187	0.561	0.389	0.0278	0.0020
0.7	2.144	0.524	0.443	0.0216	0.0015
0.8	1.970	0.463	0.479	0.0154	0.0010
0.9	1.582	0.351	0.500	0.0092	0.0005
1.0	0.000	0.000	0.000	0.0030	0.000

Dimensions of three bladed B-screw series.

r/R	$\frac{c_r}{D} \cdot \frac{Z}{A_E/A_O}$	$a_r/c_r$	$b_r/c_r$	$s_r/D = A_r - B_r Z$	
				$A_r$	$B_r$
0.2	1.633	0.616	0.350	0.0526	0.0040
0.3	1.832	0.611	0.350	0.0464	0.0035
0.4	2.000	0.599	0.350	0.0402	0.0030
0.5	2.120	0.583	0.355	0.0340	0.0025
0.6	2.186	0.558	0.389	0.0278	0.0020
0.7	2.168	0.526	0.442	0.0216	0.0015
0.8	2.127	0.481	0.478	0.0154	0.0010
0.9	1.657	0.400	0.500	0.0092	0.0005
1.0	0.000	0.000	0.000	0.0030	0.0000

$A_r, B_r$  = constants in equation for  $s_r/D$

$a_r$  = distance between leading edge and generator line at r

$b_r$  = distance between leading edge and location of maximum thickness

$c_r$  = chord length of blade section at radius r

$s_r$  = maximum blade section thickness at radius r.

Table 11. Dimensions of Wageningen B-propeller series.

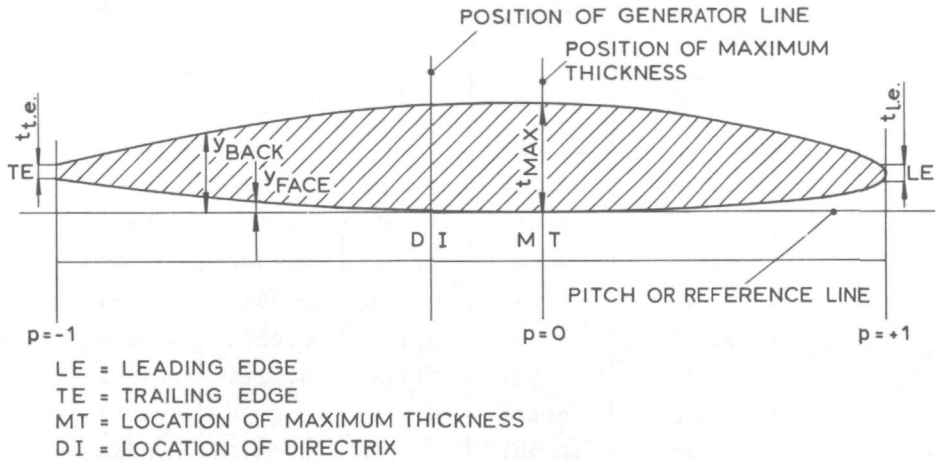


FIG. 43 DEFINITION OF GEOMETRIC BLADE SECTION PARAMETERS OF WAGENINGEN B AND BB SERIES PROPELLERS.

propellers are denoted as "BB" propellers. For the sake of completeness, Table 14 is included which gives the modified particulars of this series. The performance characteristics of these BB-series propellers may be considered identical with the original B-series propellers. The geometry of the high skew propellers were taken from Morgan et al [5-3] and Cumming et al [5-4].

From the results presented in Figs. 37 to 42, it may be concluded that the performance in uniform flow is predicted within experimental accuracy for moderate loadings. At low advance ratios (heavy loadings) the tendency to predict somewhat lower thrusts can be discerned. The experimental curves were taken from Oosterveld and Van Oossanen [5-1] for the B-series propellers and from Cumming et al [5-4] for the high skew series. The Reynolds number of the calculations was chosen to be  $2 \times 10^6$  which is an equivalent Reynolds number of the model tests on which the curves representing the measurements were based. In this regard it is noted that from the analysis performed by Oosterveld and Van Oossanen [5-1], it is clear that all open-water tests with model propellers suffer



$r/R \setminus P$	-1.0	-.95	-.9	-.8	-.7	-.6	-.5	-.4	-.2	0
.7-1.0	0	0	0	0	0	0	0	0	0	0
.6	0	0	0	0	0	0	0	0	0	0
.5	.0522	.0420	.0330	.0190	.0100	.0040	.0012	0	0	0
.4	.1467	.1200	.0972	.0630	.0395	.0214	.0116	.0044	0	0
.3	.2306	.2040	.1790	.1333	.0943	.0623	.0376	.0202	.0033	0
.25	.2598	.2372	.2115	.1651	.1246	.0899	.0579	.0350	.0084	0
.2	.2826	.2630	.2400	.1967	.1570	.1207	.0880	.0592	.0172	0
.15	.3000	.2824	.2650	.2300	.1950	.1610	.1280	.0955	.0365	0

$r/R \setminus P$	+1.0	+.95	+.9	+.85	+.8	+.7	+.6	+.5	+.4	+.2	0
.7-1.0	0	0	0	0	0	0	0	0	0	0	0
.6	.0382	.0169	.0067	.0022	.0006	0	0	0	0	0	0
.5	.1278	.0778	.0500	.0328	.0211	.0085	.0034	.0008	0	0	0
.4	.2181	.1467	.1088	.0833	.0637	.0357	.0189	.0090	.0033	0	0
.3	.2923	.2186	.1760	.1445	.1191	.0790	.0503	.0300	.0148	.0027	0
.25	.3256	.2513	.2068	.1747	.1465	.1008	.0669	.0417	.0224	.0031	0
.2	.3560	.2821	.2353	.2000	.1685	.1180	.0804	.0520	.0304	.0049	0
.15	.3860	.3150	.2642	.2230	.1870	.1320	.0920	.0615	.0384	.0096	0

Table 12. Values of  $V_1$  for use in equations 5-1 and 5-2.

$r/R \setminus P$	-1.0	-.95	-.9	-.8	-.7	-.6	-.5	-.4	-.2	0
.9-1.0	0	.0975	.19	.36	.51	.64	.75	.84	.96	1
.85	0	.0975	.19	.36	.51	.64	.75	.84	.96	1
.8	0	.0975	.19	.36	.51	.64	.75	.84	.96	1
.7	0	.0975	.19	.36	.51	.64	.75	.84	.96	1
.6	0	.0965	.1885	.3585	.5110	.6415	.7530	.8426	.9613	1
.5	0	.0950	.1865	.3569	.5140	.6439	.7580	.8456	.9639	1
.4	0	.0905	.1810	.3500	.5040	.6353	.7525	.8415	.9645	1
.3	0	.0800	.1670	.3360	.4885	.6195	.7335	.8265	.9583	1
.25	0	.0725	.1567	.3228	.4740	.6050	.7184	.8139	.9519	1
.2	0	.0640	.1455	.3060	.4535	.5842	.6995	.7984	.9446	1
.15	0	.0540	.1325	.2870	.4280	.5585	.6770	.7805	.9360	1

$r/R \setminus P$	+1.0	+.95	+.9	+.85	+.8	+.7	+.6	+.5	+.4	+.2	0
.9-1.0	0	.0975	.1900	.2775	.3600	.51	.6400	.75	.8400	.9600	1
.85	0	.1000	.1950	.2830	.3660	.5160	.6455	.7550	.8450	.9615	1
.8	0	.1050	.2028	.2925	.3765	.5265	.6545	.7635	.8520	.9635	1
.7	0	.1240	.2337	.3300	.4140	.5615	.6840	.7850	.8660	.9675	1
.6	0	.1485	.2720	.3775	.4620	.6060	.7200	.8090	.8790	.9690	1
.5	0	.1750	.3056	.4135	.5039	.6430	.7478	.8275	.8880	.9710	1
.4	0	.1935	.3235	.4335	.5220	.6590	.7593	.8345	.8933	.9725	1
.3	0	.1890	.3197	.4265	.5130	.6505	.7520	.8315	.8920	.9750	1
.25	0	.1758	.3042	.4108	.4982	.6359	.7415	.8259	.8899	.9751	1
.2	0	.1560	.2840	.3905	.4777	.6190	.7277	.8170	.8875	.9750	1
.15	0	.1300	.2600	.3665	.4520	.5995	.7105	.8055	.8825	.9760	1

Table 13. Values of  $V_2$  for use in equations 5-1 and 5-2.

$r/R$	$\frac{c_r \cdot z}{D \cdot A_E/A_O}$	$a_r/c_r$	$b_r/c_r$
0.200	1.600	0.581	0.350
0.300	1.832	0.584	0.350
0.400	2.023	0.580	0.351
0.500	2.163	0.570	0.355
0.600	2.243	0.552	0.389
0.700	2.247	0.524	0.443
0.800	2.132	0.480	0.486
0.850	2.005	0.448	0.498
0.900	1.798	0.402	0.500
0.950	1.434	0.318	0.500
0.975	1.122	0.227	0.500

<p><math>a_r</math> = distance between leading edge and generator line at <math>r</math></p> <p><math>b_r</math> = distance between leading edge and location of maximum thickness at <math>r</math></p> <p><math>c_r</math> = chord length at <math>r</math></p>
---

Table 14. Modified particulars of BB-series propellers

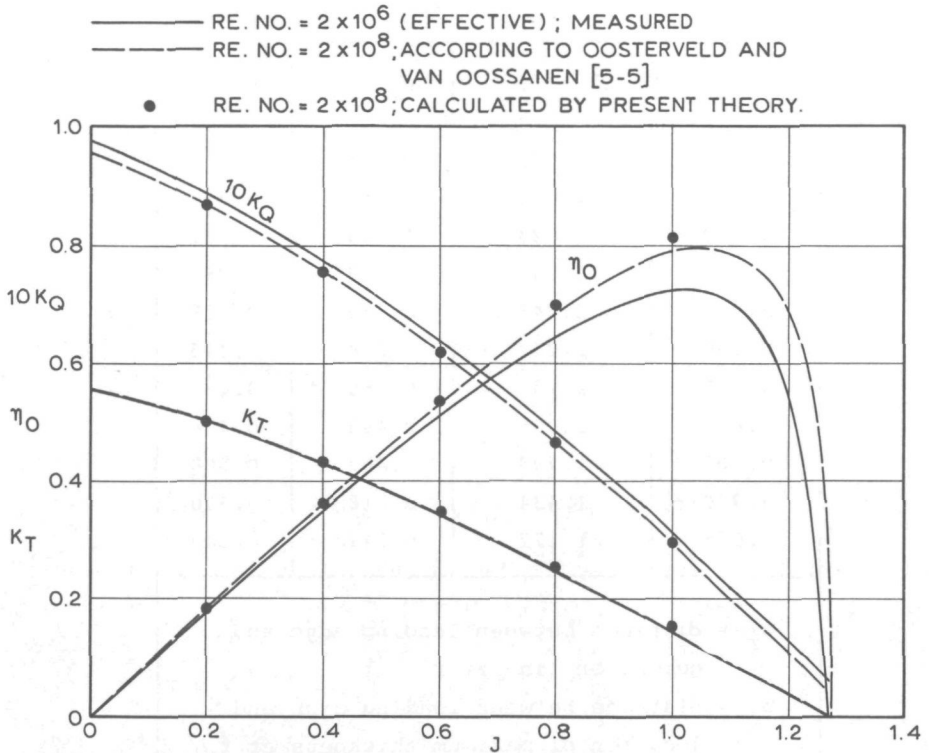


FIG. 44 COMPARISON OF "MEASURED" AND CALCULATED THRUST, TORQUE AND EFFICIENCY OF B5-75 PROPELLER WITH P/D = 1.2 FOR A REYNOLDS NUMBER OF  $2 \times 10^8$

in some degree from laminar flow over the blades (especially at the inner blade sections). The associated reduction in drag of the propeller blades can be accounted for by considering that the tests were performed at an effective Reynolds number of  $2 \times 10^6$  (when the Reynolds number is based on chord length at  $r/R = 0.75$ , as defined in reference [5-1]).

To obtain some indications of full-scale open-water performance, the characteristics of the B5-75 propeller was also calculated at a Reynolds number of  $2 \times 10^8$ . The results are shown in Fig. 44. The curves representing the "measured" values were taken from polynomials for Reynolds number scale effects on B-series propellers given by Oosterveld and Van Oossanen [5-5]. It is seen

that whereas the torque is satisfactorily predicted, the predicted thrust is somewhat higher. Since the polynomials for scale effect on thrust and torque were developed from an equivalent profile theory (discussed in section 3.5) which does not explicitly consider the influence of viscosity on lift, it is probable that the  $K_T$ -value at higher Reynolds numbers is better assessed by the present approach.

### 5.2 Type and Extent of Cavitation: Differences Between Model and Full Scale.

The type and extent of cavitation on propellers were calculated for three cases. For each of these, appropriate model test data was available. For one case, also the corresponding full-scale cavitation behaviour was known. With this information it is possible to obtain an indication of the accuracy of the calculated differences in type and extent of cavitation for both model and full scale. One of these three cases concerns a propeller of a single screw vessel and the remaining two involve the propellers of high speed twin-screw ships.

The calculations first carried out were for a medium size, single screw cargo-vessel. The cavitation properties of this propeller were obtained by performing tests in the cavitation tunnel. The results of the three-dimensional wake survey, performed with a 5-hole pitot-tube, of the simulated wakefield in the cavitation tunnel, is given in Table 15. This wakefield was also used for the calculations. The propeller has 4 blades, an expanded blade area ratio of 0.6, and a diameter of 4.85 meter. It was designed to absorb 9600 metric horsepower at 155.5 revolutions per minute when the ship speed is 15.8 knots. The effective static pressure at the propeller shaft is  $18000 \text{ kgf/m}^2$ . Particulars of the radial distribution of pitch, maximum camber and maximum thickness are given in Table 16. The blade design is of the composite type, incorporating sections with the position of maximum thickness at 0.3 of the chord length from the leading edge near the hub and Walchner-type sections near the tip. Particulars of this

angle in degrees	r/R = 0.27			r/R = 0.44			r/R = 0.62			r/R = 0.80		
	V <sub>a</sub> /V	V <sub>t</sub> /V	V <sub>r</sub> /V	V <sub>a</sub> /V	V <sub>t</sub> /V	V <sub>r</sub> /V	V <sub>a</sub> /V	V <sub>t</sub> /V	V <sub>r</sub> /V	V <sub>a</sub> /V	V <sub>t</sub> /V	V <sub>r</sub> /V
0	0.171	0.000	-0.003	0.257	0.000	-0.025	0.467	0.000	-0.049	0.638	0.000	-0.141
5	0.258	-0.035	-0.022	0.292	-0.040	-0.053	0.427	-0.080	-0.105	0.743	-0.048	-0.158
10	0.196	-0.064	-0.022	0.255	-0.072	-0.067	0.630	-0.099	-0.132	0.885	-0.059	-0.179
15	0.260	-0.087	-0.032	0.428	-0.090	-0.098	0.574	-0.079	-0.175	0.934	-0.033	-0.159
20	0.299	-0.102	-0.042	0.414	-0.092	-0.139	0.898	0.018	-0.210	0.971	0.022	-0.151
30	0.326	-0.110	-0.097	0.726	-0.043	-0.203	0.971	0.051	-0.180	0.968	0.067	-0.144
40	0.374	-0.075	-0.163	0.776	0.037	-0.194	0.949	0.098	-0.154	0.959	0.088	-0.135
60	0.509	0.004	-0.177	0.845	0.126	-0.164	0.968	0.125	-0.119	0.941	0.132	-0.119
80	0.448	0.066	-0.175	0.818	0.183	-0.130	0.945	0.180	-0.080	0.931	0.158	-0.078
100	0.386	0.089	-0.129	0.798	0.195	-0.077	0.935	0.210	-0.025	0.931	0.205	-0.036
120	0.295	0.069	-0.061	0.515	0.175	-0.048	0.759	0.203	-0.008	0.869	0.203	0.019
140	0.112	0.048	-0.030	0.351	0.115	-0.040	0.542	0.129	0.000	0.674	0.127	0.012
150	0.096	-0.005	-0.019	0.164	0.054	-0.004	0.321	0.058	-0.011	0.285	0.119	-0.011
160	0.093	-0.005	-0.018	0.081	0.030	0.010	0.139	0.044	0.000	0.192	0.067	-0.038
165	0.101	-0.009	-0.017	0.059	0.022	0.011	0.144	0.016	0.017	0.166	0.048	-0.020
170	0.081	-0.020	-0.021	0.054	-0.007	0.010	0.142	0.000	0.014	0.135	0.009	-0.012
175	0.066	-0.027	-0.017	0.040	-0.020	0.008	0.142	0.000	0.014	0.101	0.000	-0.010
180	0.060	0.000	-0.008	0.031	0.000	0.003	0.123	0.000	0.006	0.085	0.000	-0.010



angle in degrees	r/R = 0.89			r/R = 0.98			r/R = 1.07		
	$v_a/v$	$v_t/v$	$v_r/v$	$v_a/v$	$v_t/v$	$v_r/v$	$v_a/v$	$v_t/v$	$v_r/v$
0*	0.840	0.000	-0.124	1.049	0.000	-0.103	1.003	0.000	-0.132
5	0.843	-0.046	-0.142	0.980	-0.023	-0.093	0.992	-0.010	-0.134
10	0.982	-0.004	-0.143	0.961	0.005	-0.148	0.985	-0.005	-0.119
15	0.959	0.033	-0.148	0.970	0.028	-0.130	1.012	0.021	-0.119
20	0.971	0.044	-0.138	0.974	0.044	-0.135	0.994	0.038	-0.119
30	0.982	0.056	-0.131	0.958	0.063	-0.135	0.970	0.047	-0.121
40	0.951	0.077	-0.125	0.960	0.068	-0.123	0.951	0.074	-0.124
60	0.952	0.128	-0.110	0.936	0.109	-0.102	0.950	0.112	-0.106
80	0.949	0.165	-0.077	0.937	0.151	-0.068	0.942	0.152	-0.075
100	0.942	0.198	-0.021	0.927	0.187	-0.024	0.928	0.191	-0.034
120	0.878	0.224	0.039	0.894	0.226	0.038	0.922	0.222	0.025
140	0.745	0.180	0.032	0.690	0.174	0.040	0.757	0.194	0.059
150	0.467	0.131	0.016	0.465	0.137	0.015	0.521	0.166	0.032
160	0.173	0.075	-0.008	0.156	0.075	-0.034	0.412	0.101	-0.029
165	0.107	0.050	-0.030	0.106	0.049	-0.034	0.355	0.061	-0.021
170	0.073	0.029	-0.030	0.091	0.028	-0.044	0.282	0.033	-0.059
175	0.061	0.011	-0.021	0.068	0.009	-0.029	0.223	0.012	-0.031
180	0.093	0.000	-0.018	0.062	0.000	-0.014	0.201	0.000	-0.068

\*Angles are given with respect to the vertical downward blade position.

Table 15. Results of wake survey of simulated wakefield in cavitation tunnel (used in cavitation calculations, the results of which are given in Fig.45).

$x=r/R$	maximum thickness in meter	maximum camber in meter	pitch in meter	distance of leading edge to generator line in meter	distance of trailing edge to generator line in meter
0.200	0.247	0.055	3.500	0.650	0.532
0.250	0.230	0.052	3.557	0.673	0.571
0.300	0.212	0.049	3.613	0.693	0.607
0.400	0.177	0.044	3.714	0.722	0.681
0.500	0.144	0.039	3.802	0.741	0.756
0.600	0.117	0.035	3.869	0.740	0.831
0.700	0.092	0.031	3.912	0.701	0.906
0.800	0.067	0.029	3.929	0.605	0.965
0.850	0.055	0.028	3.925	0.521	0.970
0.900	0.042	0.025	3.919	0.400	0.940
0.950	0.030	0.021	3.905	0.223	0.853
0.975	0.023	0.016	3.895	0.072	0.763

Table 16. Geometric particulars of blades of propeller of which calculated and observed cavitation properties are shown in Fig.45.

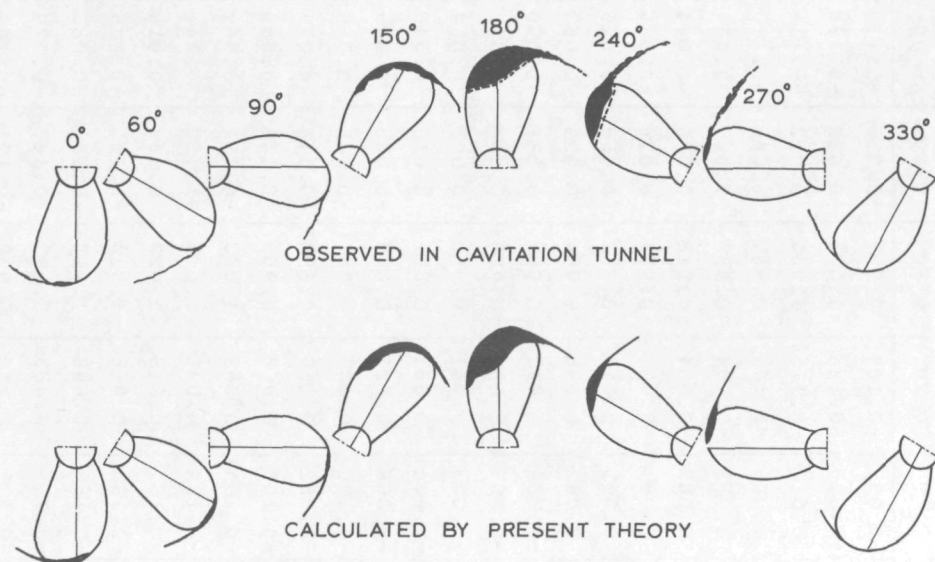


FIG. 45 OBSERVED AND CALCULATED CAVITATION ON SUCTION SIDE OF MODEL PROPELLER (1:22) EQUIVALENT SHIP SPEED =15.8 KNOTS,  $K_T=0.188$  AND  $C_n=2.181$ .

type of propeller-blade design are given in the appendix of reference [5-2]. The radial distribution of the distance of the leading edge to the generator line and of the trailing edge to the generator line are also given in Table 16. The ratio of hub diameter to propeller diameter is 0.18.

The results of the cavitation calculations are given in Fig. 45. Also shown are details of the observed cavitation behaviour in the cavitation tunnel. As can be seen, a good correlation between the calculated and observed cavitation characteristics are obtained. The calculations were carried out for the model propeller in the cavitation tunnel (the scale ratio was 1:22). The dominating type of cavitation on this propeller is sheet cavitation. In the top position, the blades show more cavitation on the back due to the low intake velocities in this region.

The second case for which calculations were performed was for the port propeller of a fast twin-screw ship. The cavitation

	r/R = 0.30			r/R = 0.50			r/R = 0.60			r/R = 0.70		
	V <sub>a</sub> /V	V <sub>t</sub> /V	V <sub>r</sub> /V	V <sub>a</sub> /V	V <sub>t</sub> /V	V <sub>r</sub> /V	V <sub>a</sub> /V	V <sub>t</sub> /V	V <sub>r</sub> /V	V <sub>a</sub> /V	V <sub>t</sub> /V	V <sub>r</sub> /V
0*	0.970	-0.073	-0.203	0.991	-0.062	-0.156	0.989	-0.057	-0.139	0.997	-0.055	-0.130
20	0.996	-0.031	-0.200	0.997	-0.029	-0.152	1.003	-0.020	-0.134	1.008	-0.020	-0.128
40	0.995	0.007	-0.193	1.000	0.010	-0.142	0.995	0.014	-0.125	1.000	0.012	-0.118
60	0.979	0.051	-0.179	0.983	0.043	-0.125	0.986	0.049	-0.109	0.987	0.046	-0.100
80	0.969	0.081	-0.158	0.969	0.067	-0.101	0.983	0.072	-0.084	0.986	0.067	-0.074
100	0.966	0.094	-0.139	0.966	0.079	-0.075	0.984	0.085	-0.054	0.918	0.080	-0.044
120	0.959	0.103	-0.124	0.962	0.076	-0.046	0.981	0.081	-0.021	0.984	0.078	-0.006
140	0.956	0.115	-0.138	0.960	0.053	-0.019	0.988	0.055	0.019	0.962	0.060	0.026
150	0.929	0.144	-0.137	0.981	0.065	-0.015	0.984	0.041	0.038	0.954	0.039	0.053
160	0.992	0.032	-0.120	0.979	-0.051	0.043	0.931	-0.004	0.047	0.967	0.081	0.050
170	0.921	0.011	-0.098	0.993	-0.002	0.034	0.966	-0.007	0.059	0.970	-0.008	0.070
180	0.895	0.024	-0.089	0.961	-0.005	0.024	0.961	-0.003	0.047	0.953	0.008	0.064
190	0.840	0.014	-0.083	0.926	-0.014	0.011	0.918	-0.024	0.033	0.897	-0.015	0.046
200	0.778	-0.029	-0.089	0.887	-0.051	0.005	0.882	-0.066	0.027	0.849	-0.065	0.045
210	0.787	-0.100	-0.099	0.887	-0.083	0.009	0.897	-0.108	0.040	0.881	-0.109	0.065
220	0.893	-0.123	-0.104	0.948	-0.087	0.026	0.950	-0.082	0.065	0.898	-0.114	0.079
230	0.782	-0.191	-0.094	0.951	-0.176	0.034	1.002	-0.168	0.068	0.955	-0.148	0.085
240	0.906	-0.187	-0.096	0.989	-0.157	0.042	1.010	-0.155	0.063	1.003	-0.152	0.069
250	0.954	-0.178	-0.072	1.020	-0.165	0.017	1.021	-0.164	0.038	1.015	-1.159	0.041
260	0.963	-0.183	-0.084	1.009	-0.170	-0.007	1.035	-0.167	0.015	1.028	-0.163	0.016
270	0.967	-0.186	-0.101	0.998	-0.171	-0.034	1.033	-0.168	-0.015	1.024	-0.163	-0.005
280	0.961	-0.187	-0.119	0.992	-0.172	-0.060	1.007	-0.166	-0.080	1.014	-0.161	-0.032
300	0.970	-0.175	-0.152	0.986	-0.156	-0.099	1.016	-0.153	-0.083	0.999	-0.147	-0.070
320	0.970	-0.150	-0.177	0.985	-0.133	-0.128	1.010	-0.129	-0.112	0.939	-0.121	-0.102

\*Angles are given with respect to the vertical downward blade position.

*	r/R = 0.80			r/R = 0.90			r/R = 1.00			r/R = 1.10		
	V <sub>a</sub> /V	V <sub>t</sub> /V	V <sub>r</sub> /V	V <sub>a</sub> /V	V <sub>t</sub> /V	V <sub>r</sub> /V	V <sub>a</sub> /V	V <sub>t</sub> /V	V <sub>r</sub> /V	V <sub>a</sub> /V	V <sub>t</sub> /V	V <sub>r</sub> /V
0	0.971	-0.050	-0.130	1.021	-0.069	-0.119	0.965	-0.045	-0.120	0.957	-0.041	-0.121
20	0.986	-0.018	-0.127	1.002	-0.116	-0.116	0.973	-0.010	-0.120	0.968	-0.011	-0.118
40	0.982	0.012	-0.117	1.002	0.010	-0.108	0.993	0.015	-0.117	0.953	0.032	-0.108
60	0.975	0.045	-0.099	0.983	0.042	-0.085	0.981	0.044	-0.102	0.941	0.061	-0.088
80	0.952	0.068	-0.083	0.981	0.066	-0.058	0.974	0.066	-0.078	0.942	0.079	-0.065
100	0.945	0.080	-0.057	0.982	0.079	-0.029	0.955	0.081	-0.044	0.933	0.085	-0.028
120	0.924	0.077	-0.028	0.955	0.074	-0.007	0.930	0.077	-0.035	0.917	0.081	-0.017
140	0.913	0.061	0.009	0.940	0.065	0.024	0.922	0.077	-0.009	0.921	0.096	0.007
150	0.900	0.046	0.031	0.921	0.055	0.052	0.893	0.064	0.038	0.901	0.085	0.036
160	0.960	0.052	0.077	0.874	0.045	0.061	0.871	0.054	0.067	0.862	0.063	0.068
170	0.967	-0.020	0.087	0.867	-0.039	0.071	0.824	-0.025	0.078	0.803	0.036	0.066
180	0.937	0.002	0.074	0.869	0.005	0.065	0.852	0.014	0.074	0.785	0.024	0.071
190	0.877	-0.014	0.055	0.817	-0.011	0.045	0.789	-0.004	0.060	0.737	0.003	0.068
200	0.835	-0.062	0.057	0.735	-0.064	0.054	0.725	-0.046	0.053	0.681	-0.025	0.061
210	0.840	-0.111	0.076	0.779	-0.110	0.071	0.723	-0.104	0.075	0.702	-0.092	0.077
220	0.858	-0.146	0.084	0.849	-0.164	0.073	0.811	-0.157	0.091	0.806	-0.137	0.078
230	0.924	-0.147	0.096	0.912	-0.142	0.073	0.876	-0.142	0.079	0.844	-0.136	0.077
240	0.999	-0.155	0.071	0.947	-0.157	0.046	0.928	-0.156	0.056	0.928	-0.149	0.077
250	0.976	-0.163	0.021	0.995	-0.161	0.036	0.959	-0.162	0.027	0.949	-0.161	0.030
260	1.026	-0.164	0.024	1.008	-0.162	0.014	0.981	-0.162	0.007	0.962	-0.161	0.005
270	1.033	-0.162	0.010	1.004	-0.160	-0.012	0.984	-0.158	-0.021	0.972	-0.154	-0.019
280	1.018	-0.158	-0.031	0.998	-0.156	-0.037	0.973	-0.155	-0.046	0.967	-0.151	-0.044
300	1.009	-0.145	-0.067	0.976	-0.138	-0.082	0.964	-0.137	-0.075	0.957	-0.132	-0.077
320	1.003	-0.119	-0.095	0.986	-0.110	-0.110	0.974	-0.112	-0.103	0.973	-0.106	-0.099

Table 17. Results of wake survey of simulated wakefield in cavitation tunnel (used in calculations of Fig. 46)

$x=r/R$	maximum thickness in meter	maximum camber in meter	pitch in meter	distance of leading edge to generator line in meter	distance of trailing edge to generator line in meter
0.30	0.198	0.000	5.250	0.400	0.575
0.40	0.132	0.024	5.254	0.596	0.766
0.50	0.099	0.029	5.246	0.757	0.949
0.60	0.074	0.029	5.204	0.853	1.067
0.70	0.055	0.028	5.111	0.851	1.112
0.80	0.040	0.024	4.960	0.722	1.082
0.90	0.026	0.018	4.750	0.452	0.931
0.95	0.019	0.014	4.628	0.256	0.755
1.00	0.012	0.000	4.490	0.000	0.000

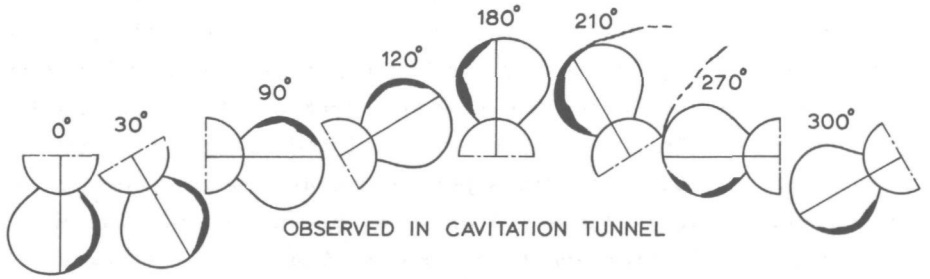
Table 18. Geometric particulars of blades of propeller of which calculated and observed cavitation properties are shown in Fig.46.



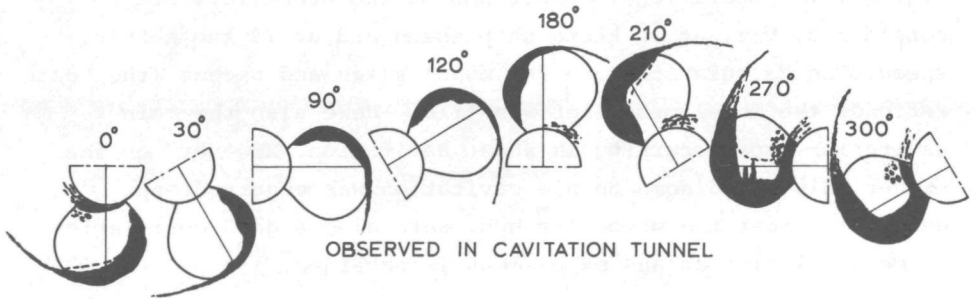
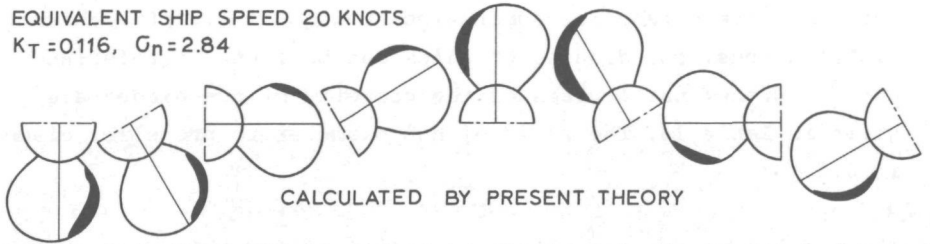
behaviour of this propeller was also determined from observations in the cavitation tunnel. Particulars of the simulated wake pattern at the location of the propeller in the tunnel are given in Table 17. Here, as before, the wake pattern was simulated by building into the tunnel the relevant portion of the afterbody of the vessel. The propellers were designed to absorb 14750 metric horsepower at 206 revolutions per minute at a ship speed of 28 knots. They have 4 blades, an expanded blade area of 0.64, a diameter of 4.2 meter and turn inboard. The effective static pressure at the propeller shafts is  $13750 \text{ kgf/m}^2$ . The blade sections have parabolic camber lines and quasi-elliptic thickness distributions, coordinates of which can be found in reference [5-7]. Further particulars of the geometry of the blades are given in Table 18. The ratio of hub diameter to propeller diameter is 0.33.

The results of the cavitation calculations for this case, together with the observed cavitation patterns are given in Fig. 46. Two operational conditions of the propellers are considered, viz: at 20 knots ship speed and at 28 knots ship speed. The calculations are for model sizes and speeds (the scale ratio of the model propeller was 1:16). Here also the main cavitation type occurring is sheet cavitation. However, at the higher ship speed some bubble cavitation was observed and calculated near the propeller hub. Here also a good correlation between calculation and experiment is obtained.

The final case for which cavitation calculations were made, again involved the port propeller of a fast twin-screw vessel. Here also the cavitation observations were performed in the cavitation tunnel. Particulars of the simulated wake pattern are given in Table 19. These propellers have 5-blades, an expanded blade area ratio of 0.8 and a diameter of 3.65 meter. Each propeller was designed to absorb 15500 metric horsepower at 230 revolutions per minute at a ship speed of 30 knots. These propellers turn outboard. The effective static pressure at the propeller shaft is  $14050 \text{ kgf/m}^2$ . Details of the blade design are given in Table 20. The ratio of hub diameter to propeller diameter is 0.185.



EQUIVALENT SHIP SPEED 20 KNOTS  
 $K_T=0.116$ ,  $C_n=2.84$



EQUIVALENT SHIP SPEED 28 KNOTS  
 $K_T=0.139$ ,  $C_n=1.27$

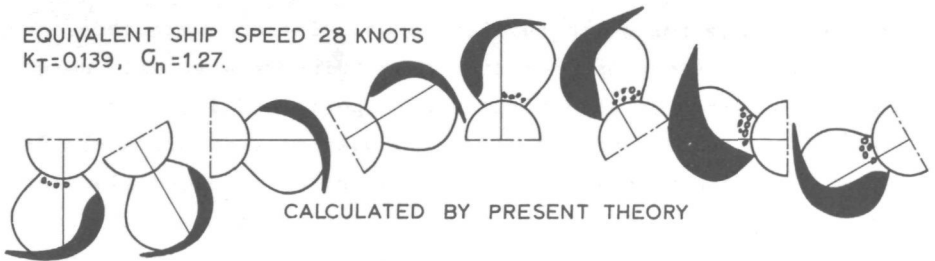


FIG.46 OBSERVED AND CALCULATED CAVITATION ON SUCTION SIDE OF MODEL PROPELLER (1:16).

The observed and calculated cavitation patterns for this case are given in Fig. 47. The equivalent ship speed to which these calculations and observed cavitation phenomena pertain is 24 knots. The calculations were performed for model size and speed (the scale ratio was 1:19). Again the correlation is satisfactory.

The corresponding full scale results are shown in Fig. 48. This case is particularly interesting since on the full scale propeller, sheet cavitation on the face of the blades was observed at the angular blade position shown. The calculation also shows the occurrence of sheet cavitation on the face in the same angular blade position. This was somewhat surprising since the wake particulars of the model ship were used. This demonstrates that a large scale effect in sheet cavitation is possible. Since on the model scale no sheet cavitation on the face was predicted or observed, it may be concluded that the explanation of this scale effect may be sought in the cavitation inception mechanism and not in the mechanism for the extent of cavitation. As described in section 4.2, when the cavitation number is equal to the magnitude of the pressure coefficient in the region of laminar separation or of laminar-turbulent transition, cavitation inception will occur. A small shift of this region, in the neighbourhood of a pressure peak, can result in a relatively large variation in the corresponding value of the pressure coefficient. It follows, therefore, that a relatively large scale effect on the inception value of the cavitation index will occur when the location of laminar-turbulent transition shifts.

### 5.3 Effect of Cavitation on Propeller Performance.

The results of section 4.4 were used for the calculation of the effect of cavitation on the thrust, torque and efficiency of the Wageningen B5-75 propeller with a pitch-diameter ratio of 1.2 in uniform flow. The cavitation number based on the speed of advance for which these calculations were made, was 0.94. The experimentally determined characteristics were taken from Van Lammeren et al [5-6]. The results are shown in Fig. 49. It is seen that a reasonable correlation is obtained.

Angle in degrees	$r/R = 0.415$			$r/R = 0.623$			$r/R = 0.831$		
	$Vx/V$	$Vt/V$	$Vr/V$	$Vx/V$	$Vt/V$	$Vr/V$	$Vx/V$	$Vt/V$	$Vr/V$
0*	1.036	-0.067	-0.152	1.027	-0.059	-0.136	0.997	-0.058	-0.139
20	1.070	-0.025	-0.148	1.067	-0.023	-0.128	1.065	-0.023	-0.128
40	1.052	0.080	-0.132	1.054	0.079	-0.112	1.041	0.078	-0.110
60	1.004	0.142	-0.108	1.030	0.124	-0.089	1.025	0.121	-0.086
80	1.020	0.170	-0.079	1.025	0.157	-0.053	1.016	0.153	-0.052
100	1.015	0.184	-0.045	0.966	0.176	-0.022	0.960	0.170	0.020
120	1.007	0.181	0.025	0.994	0.162	0.048	0.992	0.157	0.056
130	0.962	0.179	0.042	0.994	0.153	0.063	0.991	0.149	0.073
140	0.987	0.162	0.055	0.994	0.142	0.076	0.979	0.129	0.089
150	0.983	0.147	0.068	0.995	0.127	0.091	0.953	0.103	0.095
160	0.991	0.163	0.081	0.987	0.120	0.097	0.848	0.084	0.101
170	0.867	0.106	0.073	0.931	0.032	0.142	0.906	-0.035	0.162
180	0.924	0.054	0.064	0.963	0.030	0.148	0.923	0.026	0.169
190	0.909	-0.050	0.047	0.921	-0.049	0.118	0.894	-0.031	0.140
200	0.886	-0.101	0.049	0.873	-0.092	0.118	0.813	-0.072	0.126
210	0.877	-0.171	0.054	0.870	-0.167	0.093	0.751	-0.154	0.088
220	0.986	-0.180	0.067	0.887	-0.166	0.097	0.833	-0.142	0.101
230	0.989	-0.179	0.057	0.966	-0.169	0.084	0.922	-0.152	0.096
240	0.996	-0.190	0.045	0.990	-0.178	0.070	0.945	-0.166	0.082
260	1.010	-0.206	-0.027	1.007	-0.192	0.034	0.992	-0.184	0.044
280	0.985	-0.211	-0.065	1.014	-0.192	-0.030	0.981	-0.187	-0.037
300	1.009	-0.191	-0.100	0.986	-0.181	-0.080	1.007	-0.167	-0.073
320	1.009	-0.163	-0.128	1.010	-0.147	-0.109	1.065	-0.138	-0.101

\* Angles are given with respect to the vertical downward blade position

Angle in degrees	r/R = 0.934			r/R = 1.038			r/R = 1.142		
	Vx/V	Vt/V	Vr/V	Vx/V	Vt/V	Vr/V	Vx/V	Vt/V	Vr/V
	0*	1.016	-0.055	-0.127	1.018	-0.054	-0.120	1.006	-0.053
20	1.058	0.023	-0.118	1.065	0.021	-0.113	1.056	-0.021	-0.110
40	1.036	0.079	-0.103	1.039	0.075	-0.099	1.033	0.072	-0.095
60	1.022	0.121	-0.079	1.022	0.119	-0.073	1.018	0.118	-0.072
80	1.015	0.149	-0.045	0.961	0.157	-0.042	0.992	0.152	-0.039
100	0.967	0.170	0.028	1.002	0.161	0.032	1.003	0.163	0.034
120	0.991	0.158	0.064	0.995	0.158	0.072	0.997	0.165	0.078
130	0.982	0.149	0.084	0.971	0.147	0.088	0.979	0.151	0.091
140	0.952	0.125	0.096	0.935	0.119	0.098	0.943	0.113	0.096
150	0.925	0.092	0.099	0.812	0.081	0.104	0.811	0.080	0.097
160	0.823	0.058	0.087	0.857	0.046	0.075	0.870	0.065	0.074
170	0.868	-0.035	0.158	0.839	-0.025	0.141	0.854	-0.017	0.123
180	0.873	-0.019	0.169	0.829	-0.022	0.148	0.819	0.025	0.131
190	0.859	-0.032	0.147	0.803	-0.030	0.134	0.778	-0.017	0.122
200	0.808	-0.057	0.127	0.673	-0.055	0.141	0.595	-0.048	0.138
210	0.780	-0.140	0.086	0.733	-0.130	0.085	0.686	-0.122	0.094
220	0.871	-0.139	0.106	0.998	-0.135	0.117	0.771	-0.119	0.121
230	0.905	-0.150	0.104	0.861	-0.143	0.112	0.825	-0.126	0.112
240	0.940	-0.167	0.093	0.914	-0.163	0.102	0.852	-0.154	0.107
260	0.967	-0.187	0.053	0.976	-0.186	0.062	0.948	-0.189	0.069
280	1.002	-0.182	-0.028	1.005	-0.182	-0.023	1.000	-0.182	-0.021
300	1.010	-0.165	-0.068	1.011	-0.166	-0.059	1.008	-0.160	-0.058
320	1.016	-0.137	-0.097	1.017	-0.142	-0.087	1.014	-0.131	-0.088

Table 19. Results of wake survey of simulated wakefield in cavitation tunnel (used in cavitation calculations, the results of which are shown in Figs. 47 and 48)

$x=r/R$	maximum thickness in meter	maximum camber in meter	pitch in meter	distance of leading edge to generator line in meter	distance of trailing edge to generator line in meter
0.20	0.145	0.014	5.414	0.436	0.287
0.30	0.120	0.018	5.533	0.529	0.438
0.40	0.098	0.023	5.621	0.603	0.561
0.50	0.078	0.027	5.666	0.657	0.648
0.60	0.062	0.030	5.645	0.694	0.694
0.70	0.048	0.029	5.561	0.701	0.703
0.80	0.035	0.025	5.433	0.656	0.656
0.90	0.023	0.020	5.262	0.515	0.520
0.95	0.018	0.015	5.171	0.381	0.387
1.00	0.013	0.000	5.074	0.000	0.000

Table 20. Geometric particulars of blades of propeller of which calculated and observed cavitation properties are shown in Fig.47 and 48.



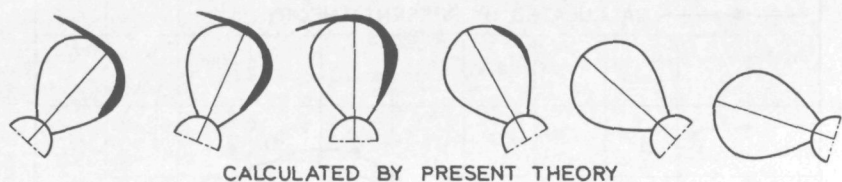
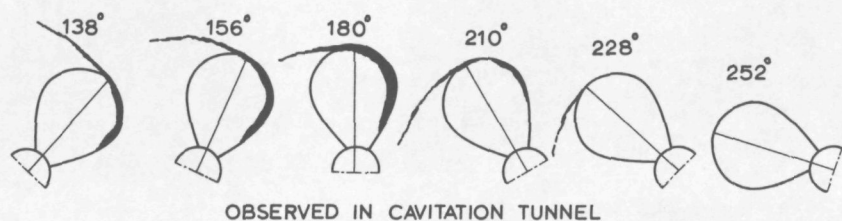
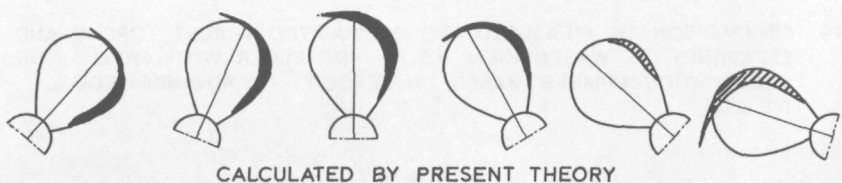
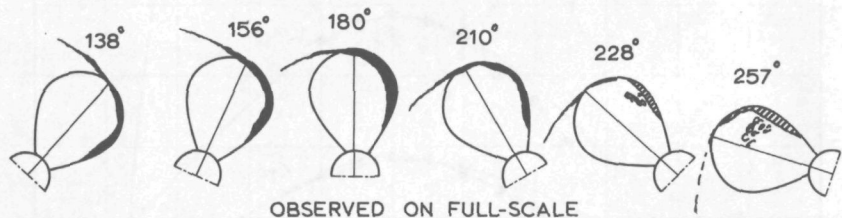


FIG. 47 OBSERVED AND CALCULATED CAVITATION ON MODEL PROPELLER (1:19)  
EQUIVALENT SHIP SPEED = 24 KNOTS,  $K_T=0.18$  AND  $G_o=2.013$ .




 SHEET CAVITATION  
ON PRESURE SIDE

FIG. 48 OBSERVED AND CALCULATED CAVITATION ON FULL-SCALE PROPELLER  
SHIP SPEED = 24 KNOTS,  $K_T=0.18$  AND  $G_o=2.013$ .

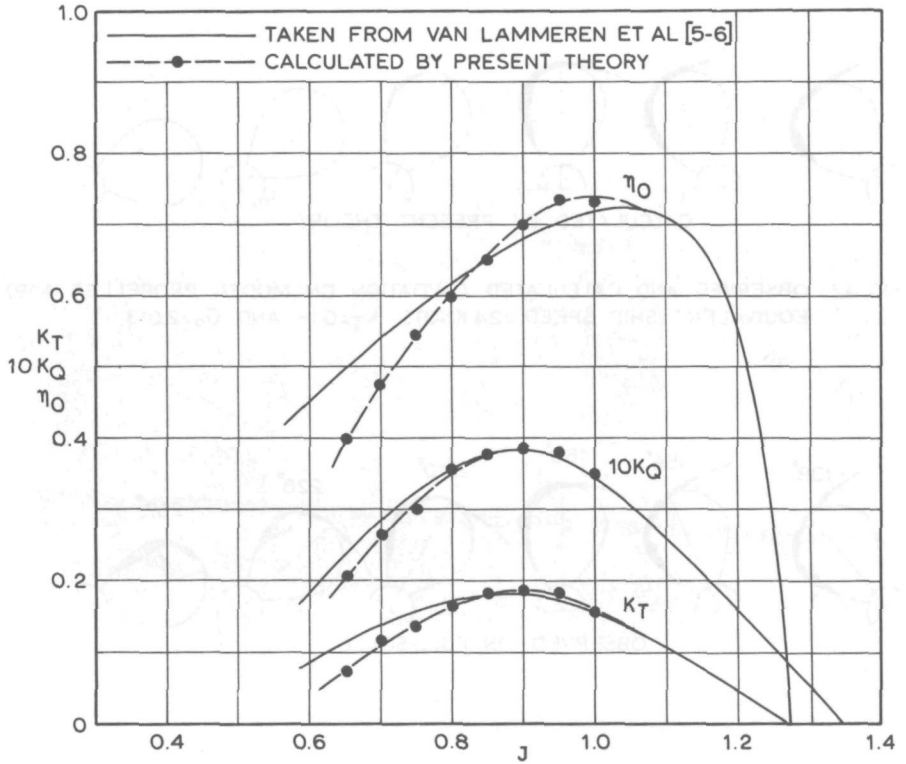


FIG.49 COMPARISON OF MEASURED AND CALCULATED THRUST, TORQUE AND EFFICIENCY OF WAGENINGEN B5-75 PROPELLER WITH  $P/D=1.2$  FOR A CAVITATION NUMBER (BASED ON VELOCITY OF ADVANCE) EQUAL TO 0.95.

CHAPTER 6

FINAL REMARKS AND CONCLUSIONS

The presented and discussed results in chapter 5 have demonstrated the validity of the theory outlined in chapter 2, 3 and 4. The described procedures for assessing effects of non-uniform flow and viscosity on propeller characteristics work satisfactorily. The developed methods for determining the onset and extent of cavitation function particularly well.

On turning to each part of the developed theoretical approach, it is possible to discern some major features and conclusions on which the overall result of the presented method is dependent. These can be reviewed as follows.

- The inverse of the Lerbs induction factor method for the moderately loaded propeller can form the successful starting-point of an approach for the calculation of the performance and cavitation characteristics of propellers.
- Adequate convergence of the Lerbs induction factor method applied in the inverse sense (hitherto unobtained), can be reached by introducing an extra iteration for the hydro-dynamic pitch angle.
- The main effects of non-uniform flow on the performance and cavitation characteristics of propellers can be adequately described by using a quasi-steady approach. At every blade position the average of the undisturbed inflow velocities over the blade section can be used to determine the advance angle, and the variation of the undisturbed inflow velocities over the blade section can be used to effectively distort the blade section camber.
- In a non-uniform flow the effect of bound vortices on the induced velocities should be included in a lifting line approach.

- The approximate calculation of the pressure distribution on propeller blades can be accomplished by using a two-dimensional approach when an effective angle of attack is used and the blade section camber is reduced to account for the smaller value of the three-dimensional angle of zero-lift.
- For the correct prediction of off-design propeller performance, it is necessary to account for viscous effects on the lift and drag properties of propeller blade sections.
- The prediction of viscous effects on the lift coefficient can only be adequately performed by incorporating boundary layer characteristics.
- The experimental value of the lift-curve slope of all profiles at all values of the Reynolds number can be satisfactorily correlated with the sum of profile and displacement thickness at the position of turbulent boundary layer separation in the absence of laminar boundary layer separation.
- The ratio of experimental to theoretical zero-lift angle of attack is dependent on the relative wake thickness of suction and pressure side of a profile.
- The effective wake thickness of a profile can be expressed as the sum of profile and displacement thickness at the position of turbulent boundary layer separation in the absence of laminar boundary layer separation.
- A calculation procedure for the drag coefficient of propeller blade sections can be derived from the results of an "equivalent profile" analysis of experimental characteristics of the Wageningen B-series propellers.
- The large scatter in cavitation inception data on smooth bodies, for constant characteristics and population of cavitation nuclei, can be mainly ascribed due to boundary layer effects.
- Inception of vaporous cavitation always occurs in the

laminar-turbulent transition region of the boundary layer.

- For a Reynolds number (based on free-stream velocity and the distance of the point of inception from the leading edge) above  $1 \times 10^5$  the approximate laminar-turbulent transition formula of Cebeci et al can be used to predict the value of the cavitation inception index at the location of cavitation inception.
- A criterium for the estimation of the extent of cavitation can be derived by means of a known value for growth and for decline of Knapp's dynamic similarity parameter for spherical cavities.
- The value of the momentum thickness of the laminar boundary layer divided by a length dimension of the body, at the location of cavitation inception, can be used to determine whether sheet or bubble cavitation will occur.
- From a study of measured pressure distributions on cavitating profiles it is possible to derive criteria for the approximate construction of the pressure distribution on cavitating bodies, when the cavity length is restricted to the first half of the body.
- An adequate calculation of the change in lift and drag due to cavitation can be obtained by use of radar's formula when the extent of cavitation at which the loss in lift and drag begins, is known.

The numerical method based on the present theory can be used with success in conjunction with propeller design studies in cases in which it is important to minimize the occurrence of cavitation on the propeller. The relative importance of many propeller parameters with regard to cavitation can be easily assessed.

Some preliminary calculations for model and full-scale propellers have shown that the numerical program can be used to estimate viscous scale effects. A more complete assessment of scale effects can be obtained if the effects of roughness and characteristics of cavitation nuclei can be accounted for.

APPENDIX

POLYNOMIAL REPRESENTATION OF PROPELLER LIFTING  
SURFACE CORRECTION FACTORS

The success of using lifting line theory for the design and performance analysis of broad-bladed screw propellers, depends to a large degree on the accuracy of the supplementary method used to predict three-dimensional chordwise effects. Lifting line theory is only satisfactory for dealing with three-dimensional effects in the direction of the span. In most cases use is made of correction factors derived from lifting surface theory. Recently, very comprehensive values were published by Morgan et al [A-1], Minsaas and Slattelid [A-2] and Cumming et al [A-3] based on the program developed by Cheng [A-4] for loading effects and on the program developed by Kerwin and Leopold [A-5] for thickness effects. From a study by Cox [A-6] of current propeller design methods in use at various research institutes, shipyards and propeller manufacturing companies, it can be concluded that these correction factors are used nearly universally. In comparison to the factors derived by others, these values cover a much larger variation in propeller geometry. The number of blades which are considered are 3, 4, 5 and 6. The covered expanded blade area ratio values are 0.35, 0.55, 0.75, 0.95 and 1.15. The examined values of the induced advance ratio are  $0.4/\pi$ ,  $0.8/\pi$ ,  $1.2/\pi$ ,  $1.6/\pi$  and  $2.0/\pi$ . The skew angle, considered as an independent variable for the first time, has values at the tip of the blades of  $0^\circ$ ,  $7^\circ$ ,  $14^\circ$ ,  $21^\circ$ ,  $180^\circ/Z$  and  $360^\circ/Z$ . The radial stations for which these values are given are 0.3, 0.4, 0.5, 0.6, 0.7, 0.8 and 0.9.

Important three-dimensional chordwise effects accounted for by these correction factors are the effects on camber and on the ideal angle of incidence due to loading and due to thickness. Other three-dimensional chordwise effects have been found to be comparatively small. The camber correction for loading is defined as the ratio of the maximum camber ordinate required to give a specific lift coefficient in three-dimensional flow to



the maximum two-dimensional camber ordinate that will give the same lift coefficient in two-dimensional flow. This factor is nearly always greater than unity due to the curvature of the induced flow along the blade section which effectively decreases the geometric camber. The ideal angle-of-attack correction factor for loading is defined as the ratio of the three-dimensional ideal angle of attack to the two-dimensional value for a lift coefficient equal to unity, times the actual value of the lift coefficient. The value for this factor is again always greater than unity except in the tip region for highly skewed propellers. This points to the fact that for a prescribed lift coefficient, the three-dimensional ideal angle of incidence is larger than the respective two-dimensional value. The angle-of-attack correction factor for thickness is defined as the ratio of the three-dimensional angle of attack induced by blade thickness to the blade thickness fraction. The values for this factor are mostly positive indicating that the effect of thickness requires an additional positive incidence angle to obtain a specified value of the lift coefficient. The propellers for which the lifting surface calculations were made have a hub diameter of 0.2 of the propeller diameter and a NACA 66 (mod.) thickness distribution and a NACA  $a=0.8$  camber distribution at all radii. The spanwise thickness of these propellers is given by:

$$\frac{t_{\max}(x)}{D} = (\text{BTF}-0.003) \cdot (1-x) + 0.003 \quad (\text{A-1})$$

where  $t_{\max}$  is the maximum thickness ordinate at  $x$ , and BTF the blade-thickness fraction. The blade outline is given by the formula:

$$c/D = \frac{k(x)}{z} \frac{A_E}{A_O} \quad (\text{A-2})$$

where  $k(x) = 1.6338, 1.8082, 1.9648, 2.0967, 2.1926, 2.232, 2.1719, 1.8931, 1.5362$  and  $0$  for  $x=0.2, 0.3, \dots, 1.0$  respectively.

The application of these correction factors to propellers with other, not to extremely differing, chordwise distributions of camber and thickness, other blade contours and other radial load distributions, is considered admissible.

A polynomial representation of these correction factors in a numerical program offers many advantages. One of these is the avoidance of a cumbersome interpolation procedure for the frequent case that the correction factors are required at intermediate values of the 5 independent variables. For the values calculated by Morgan et al [A-1] and Minsaas and Slattelid [A-2], polynomials were derived by means of the multiple regression method given by Effroymsen [A-7]. These polynomials can be written as:

$$K_c, K_q, K_t = \sum_i c_i z^{s_i} (\tan \theta_{s_x})^{t_i} \left(\frac{A_E}{A_O}\right)^{u_i} (\lambda_i)^{v_i} \quad (A-3)$$

The coefficient  $c_i$  and the powers  $s_i$ ,  $t_i$ ,  $u_i$  and  $v_i$  are given in Tables 21 to 47 for  $x = 0.2, 0.3, 0.4, \dots, 1.0$ . These 27 polynomials are valid for the following range of variables:

$$\left. \begin{aligned} 3 &\leq Z \leq 7 \\ 0 &\leq \tan \theta_{s_x} \leq 1.02556 - \sqrt{1.05177 - (x-0.2)^2} \\ 0.35 &\leq A_E/A_O \leq 1.15 \\ 0.4/\pi &\leq \lambda_i \leq 2/\pi \end{aligned} \right\} \quad (A-4)$$

The local skew angle  $\theta_{s_x}$ , shown in Fig.50, is defined as the angle between the radial line  $s_x$  passing through the effective skew line of the propeller blade at the radius considered and the radial line tangent to this skew line at the radius where the skew is least (i.e. at the radius where the angular polar coordinate - in the direction of rotation - is greatest). Even though no values are published for  $Z=7$ , it was found that all curves, when set out as a function of the number of blades, show regular tendencies which allow the extrapolation from  $Z=6$  to  $Z=7$ . A comparison of the values derived from the polynomials with other data for  $Z=7$

confirmed this supposition. The polynomials for  $x = 0.2$  and  $1.0$  were obtained by extrapolation and should only be used for fairing radial-varying entities near the hub and the tip. Figures 51 to 64 give a comparison of the values calculated by means of these polynomials with the original tabulated values.

The polynomials discussed thus far are for a moderate skew only, viz:  $0^\circ$  at  $x=0.2$ , about  $0.3^\circ$  at  $x=0.3$ ,  $1.2^\circ$  at  $x=0.4$ ,  $2.6^\circ$  at  $x=0.5$ ,  $4.7^\circ$  at  $x=0.6$ ,  $7.5^\circ$  at  $x=0.7$ ,  $11.2^\circ$  at  $x=0.8$ ,  $16^\circ$  at  $x=0.9$  and  $21^\circ$  at  $x=1$ . For high skews, use can be made of the data published by Cumming et al [A-3]. These values, however, are only given for the one value of the expanded blade area ratio of  $0.75$  and only for two values of the induced advance ratio  $0.8/\pi$  and  $1.2/\pi$ .

Using the same method, polynomials were derived for these values. These can be written as:

$$K_C, K_\alpha, K_t = \sum_i c_i x^{a_i} z^{b_i} (\theta_{s_x})^{d_i} \quad (A-5)$$

where  $\theta_{s_x}$  is the skew angle at  $x$  in radians. One set of polynomials is given for  $A_E/A_0=0.75$  and  $\lambda_i=0.8/\pi$  and one set for  $A_E/A_0=0.75$  and  $\lambda_i=1.2/\pi$ . These are given in Tables 48 to 53.

Approximate values of these correction factors at other blade areas and induced advance ratios can be determined from these polynomials by determining the total differential:

$$K = K_0 \left[ Z_0, \theta_{s_x}, \left( \frac{A_E}{A_0} \right)_0, (\lambda_i)_0 \right] + \left( \frac{\partial K}{\partial Z} \right)_0 \Delta Z + \left( \frac{\partial K}{\partial A_E/A_0} \right)_0 \Delta A_E/A_0 + \left( \frac{\partial K}{\partial \lambda_i} \right)_0 \Delta \lambda_i \quad (A-6)$$

where:  $(A_E/A_0)_0 = 0.75$ ,  
 $(\lambda_i)_0 = 0.8/\pi$  or  $1.2/\pi$ ,  
 and  $Z_0 = 4, 5$  or  $6$ .

Here the derivatives of  $K$  need to be determined with respect to the blade area ratio, the induced advance ratio and the number of blades. Approximate expressions for these derivatives can be obtained by differentiating the moderate skew polynomials (equation A-3).

Figure 65 demonstrates the accuracy of these high skew polynomials. The comparison with the original published values is shown.

i	Coefficient $C_i$	Power of Z $s_i$	Power of $\tan \theta_{s_x}$ $t_i$	Power of $A_E/A_O$ $u_i$	Power of $\lambda_i$ $v_i$
1	$8.74739 \times 10^0$	0	0	0	0
2	$1.76066 \times 10^0$	0	0	1	3
3	$-1.62981 \times 10^{-1}$	1	0	1	0
4	$8.95728 \times 10^0$	1	0	2	0
5	$2.05419 \times 10^0$	1	0	2	1
6	$3.76827 \times 10^0$	1	0	2	2
7	$-2.90623 \times 10^0$	1	0	2	3
8	$-7.94741 \times 10^{-2}$	2	0	2	0
9	$-3.31422 \times 10^{-1}$	2	0	2	1

Table 21. Coefficients and powers of  $K_c$ -polynomial for  $x=0.2$

$i$	Coefficient $C_i$	Power of Z $s_i$	Power of $\tan \theta_{s_x}$ $t_i$	Power of $A_E/A_0$ $u_i$	Power of $\lambda_i$ $v_i$
1	$-2.89350 \times 10^0$	0	0	0	0
2	$1.71122 \times 10^1$	0	0	1	0
3	$-8.22327 \times 10^0$	0	0	1	1
4	$1.90837 \times 10^0$	0	0	1	2
5	$-3.00176 \times 10^1$	0	0	2	1
6	$1.67447 \times 10^0$	1	0	0	0
7	$-5.37643 \times 10^0$	1	0	1	0
8	$1.09281 \times 10^0$	1	0	1	1
9	$1.13887 \times 10^1$	1	0	2	1
10	$-1.63820 \times 10^{-1}$	2	0	0	0
11	$4.59060 \times 10^{-1}$	2	0	1	0
12	$-1.07026 \times 10^0$	2	0	2	1

Table 22. Coefficients and powers of  $K_\alpha$  -polynomial for  $x=0.2$



$i$	Coefficient $C_i$	Power of $Z$ $s_i$	Power of $\tan \theta_{s_x}$ $t_i$	Power of $A_E/A_O$ $u_i$	Power of $\lambda_i$ $v_i$
1	$-1.78853 \times 10^{-1}$	0	0	0	0
2	$-1.01333 \times 10^0$	0	0	0	3
3	$-6.88780 \times 10^{-1}$	1	0	0	0
4	$2.86681 \times 10^0$	1	0	0	1
5	$-2.38539 \times 10^0$	1	0	0	2
6	$2.38679 \times 10^0$	1	0	1	0
7	$-9.18820 \times 10^0$	1	0	1	1
8	$6.34538 \times 10^0$	1	0	1	2
9	$2.98870 \times 10^0$	1	0	1	3
10	$-1.26860 \times 10^0$	1	0	2	0
11	$4.29288 \times 10^0$	1	0	2	1
12	$-5.26416 \times 10^0$	1	0	2	3
13	$-7.86711 \times 10^{-2}$	2	0	0	3
14	$6.78057 \times 10^{-2}$	2	0	1	0
15	$-3.03908 \times 10^{-2}$	2	0	2	0
16	$-2.19229 \times 10^{-1}$	2	0	2	2
17	$2.87881 \times 10^{-1}$	2	0	2	3

Table 23. Coefficients and powers of  $K_t$ -polynomial for  $x=0.2$

i	Coefficient $C_i$	Power of Z $s_i$	Power of $\tan \theta_{s_x}$ $t_i$	Power of $A_E/A_O$ $u_i$	Power of $\lambda_i$ $v_i$
1	$9.11810 \times 10^{-1}$	0	0	0	0
2	$1.93712 \times 10^0$	0	0	1	0
3	$1.85792 \times 10^0$	0	0	2	0
4	$-5.22595 \times 10^0$	0	0	2	1
5	$3.86139 \times 10^0$	0	0	2	2
6	$-3.68361 \times 10^{-1}$	1	0	1	0
7	$5.43644 \times 10^{-3}$	2	0	0	0
8	$-3.42316 \times 10^{-2}$	2	0	0	2
9	$6.38566 \times 10^{-2}$	2	0	1	1
10	$4.35558 \times 10^2$	0	2	0	0
11	$1.40849 \times 10^2$	0	1	1	0
12	$-2.26761 \times 10^2$	0	1	2	0
13	$-4.25085 \times 10^3$	0	1	2	3
14	$2.65433 \times 10^4$	0	2	0	1
15	$7.36106 \times 10^3$	0	2	2	0
16	$8.68561 \times 10^5$	0	2	2	3
17	$-1.23440 \times 10^2$	1	1	0	0
18	$6.54931 \times 10^1$	1	1	0	1
19	$4.87154 \times 10^1$	1	1	1	0
20	$2.16454 \times 10^3$	1	1	2	3
21	$-1.40637 \times 10^4$	1	2	0	2
22	$-4.14518 \times 10^5$	1	2	2	3
23	$7.65664 \times 10^0$	2	1	0	0
24	$-2.65005 \times 10^2$	2	1	2	3
25	$-5.77500 \times 10^2$	2	2	1	0
26	$4.85252 \times 10^4$	2	2	2	3

Table 25. Coefficients and powers of  $K_\alpha$ -polynomial for  $x=0.3$

$i$	Coefficient $C_i$	Power of $Z$ $s_i$	Power of $\tan \theta_{s_x}$ $t_i$	Power of $A_E/A_O$ $u_i$	Power of $\lambda_i$ $v_i$
1	$4.96670 \times 10^{-2}$	0	0	0	0
2	$-2.19523 \times 10^0$	0	0	0	3
3	$7.53685 \times 10^{-1}$	0	0	1	0
4	$-9.85501 \times 10^{-1}$	0	0	2	0
5	$3.95207 \times 10^0$	0	0	2	2
6	$-2.97105 \times 10^1$	0	0	2	3
7	$-2.92359 \times 10^4$	0	1	1	0
8	$-1.77704 \times 10^{-1}$	0	2	2	0
9	$-3.29894 \times 10^0$	1	0	0	0
10	$1.07918 \times 10^{-1}$	1	0	0	1
11	$-3.11179 \times 10^{-1}$	1	0	0	2
12	$6.49957 \times 10^{-1}$	1	0	1	0
13	$-2.95439 \times 10^0$	1	0	1	1
14	$3.56386 \times 10^0$	1	0	1	3
15	$9.31772 \times 10^{-1}$	1	0	2	1
16	$-2.07700 \times 10^1$	1	0	2	3
17	$1.54139 \times 10^3$	1	1	2	0
18	$5.87904 \times 10^{-3}$	1	2	1	0
19	$-9.10425 \times 10^4$	1	2	1	1
20	$1.07601 \times 10^{-1}$	1	2	2	1
21	$-1.09997 \times 10^{-2}$	2	0	0	3
22	$8.09697 \times 10^{-2}$	2	0	1	0
23	$-6.05111 \times 10^{-3}$	2	0	2	0
24	$-9.06378 \times 10^{-2}$	2	0	2	1
25	$6.53703 \times 10^0$	2	0	2	2
26	$2.36752 \times 10^2$	2	1	0	1
27	$-5.99557 \times 10^2$	2	2	1	1
28	$-3.44358 \times 10^0$	2	2	2	0
29	$-3.06082 \times 10^0$	2	1	1	0

Table 26. Coefficients and powers of  $K_t$ -polynomial for  $x=0.3$

i	Coefficient	Power of Z	Power of $\tan \theta_{s_x}$	Power of $A_E/A_O$	Power of $\lambda_i$
	$C_i$	$s_i$	$t_i$	$u_i$	$v_i$
1	$1.18394 \times 10^0$	0	0	0	0
2	$-1.01634 \times 10^0$	0	0	0	3
3	$3.53423 \times 10^0$	0	0	1	2
4	$8.78312 \times 10^{-1}$	0	0	2	1
5	$-3.29213 \times 10^1$	0	1	1	0
6	$2.98927 \times 10^3$	0	1	1	1
7	$1.85720 \times 10^3$	0	2	1	1
8	$4.59108 \times 10^3$	0	2	2	0
9	$-4.80612 \times 10^3$	0	2	2	1
10	$-7.81509 \times 10^3$	0	2	2	2
11	$-2.78747 \times 10^{-1}$	1	0	1	0
12	$-4.17348 \times 10^{-1}$	1	0	1	2
13	$4.00174 \times 10^{-1}$	1	0	2	0
14	$-2.93279 \times 10^{-1}$	1	0	2	1
15	$-4.67973 \times 10^0$	1	0	2	2
16	$4.77160 \times 10^1$	1	1	1	0
17	$-3.66287 \times 10^1$	1	1	1	3
18	$7.39813 \times 10^3$	1	1	2	3
19	$-1.20415 \times 10^3$	1	2	2	0
20	$2.49808 \times 10^3$	1	2	2	2
21	$1.25382 \times 10^{-2}$	2	0	0	0
22	$-5.48070 \times 10^{-2}$	2	0	0	1
23	$9.69427 \times 10^{-2}$	2	0	0	3
24	$-3.61895 \times 10^{-2}$	2	0	1	0
25	$2.99654 \times 10^{-1}$	2	0	1	1
26	$-2.98000 \times 10^{-1}$	2	0	1	2
27	$-1.73371 \times 10^{-1}$	2	0	2	1
28	$2.96699 \times 10^{-1}$	2	0	2	2
29	$-4.51589 \times 10^{-2}$	2	0	2	3
30	$-2.01416 \times 10^{-1}$	2	1	0	1
31	$-1.96830 \times 10^2$	2	1	2	3
32	$-1.83197 \times 10^2$	2	2	1	2

33	$8.09448 \times 10^1$	2	2	0	0
34	$1.60593 \times 10^2$	2	2	2	2
35	$1.00900 \times 10^1$	2	1	1	3

Table 27. Coefficients and powers of  $K_c$ -polynomial for  $x=0.4$

$i$	Coefficient $C_i$	Power of $Z$ $s_i$	Power of $\tan^{\theta} s_x$ $t_i$	Power of $A_E/A_O$ $u_i$	Power of $\lambda_i$ $v_i$
1	$1.42326 \times 10^0$	0	0	0	0
2	$9.93240 \times 10^{-1}$	0	0	1	0
3	$1.69788 \times 10^0$	0	0	2	0
4	$-2.20353 \times 10^0$	0	0	2	1
5	$7.22549 \times 10^1$	0	1	0	1
6	$1.28506 \times 10^2$	0	1	1	0
7	$-7.07529 \times 10^1$	0	1	2	0
8	$1.18022 \times 10^3$	0	2	0	0
9	$-1.94985 \times 10^{-1}$	1	0	0	0
10	$-3.42182 \times 10^{-1}$	1	0	1	0
11	$4.17149 \times 10^{-1}$	1	0	1	1
12	$-1.77888 \times 10^1$	1	1	2	1
13	$1.15400 \times 10^2$	1	1	2	3
14	$-5.26076 \times 10^2$	1	2	1	0
15	$-3.35487 \times 10^3$	1	2	1	3
16	$3.85190 \times 10^2$	1	2	2	0
17	$2.40312 \times 10^{-2}$	2	0	0	0
18	$5.12306 \times 10^{-2}$	2	0	0	3
19	$3.57173 \times 10^{-2}$	2	0	1	3
20	$9.07878 \times 10^{-1}$	2	1	2	0
21	$2.35274 \times 10^1$	2	1	2	3
22	$-7.44835 \times 10^0$	0	2	0	0
23	$-2.47954 \times 10^2$	2	2	0	3
24	$9.58773 \times 10^2$	2	2	1	3
25	$2.70421 \times 10^0$	2	1	1	2

Table 28. Coefficients and powers of  $K_\alpha$ -polynomial for  $x=0.4$



	Coefficient	Power of Z	Power of $\tan \theta_{s_x}$	Power of $A_E/A_0$	Power of $\lambda_i$
i	$C_i$	$s_i$	$t_i$	$u_i$	$v_i$
1	$8.89973 \times 10^{-2}$	0	0	0	0
2	$-1.10689 \times 10^{-1}$	0	0	1	0
3	$8.13371 \times 10^2$	0	2	0	3
4	$-2.39677 \times 10^3$	0	2	1	1
5	$-1.59699 \times 10^3$	0	2	2	0
6	$6.24729 \times 10^3$	0	2	2	1
7	$-4.71327 \times 10^3$	0	2	2	2
8	$-1.77191 \times 10^{-1}$	1	0	0	0
9	$7.54841 \times 10^{-1}$	1	0	0	1
10	$-1.00643 \times 10^0$	1	0	0	2
11	$2.87198 \times 10^{-1}$	1	0	0	3
12	$3.25166 \times 10^{-1}$	1	0	1	0
13	$-1.13399 \times 10^0$	1	0	1	1
14	$1.09346 \times 10^0$	1	0	1	2
15	$-9.53737 \times 10^1$	1	1	1	2
16	$1.35407 \times 10^3$	1	1	1	3
17	$3.56643 \times 10^3$	1	2	1	0
18	$2.83446 \times 10^{-2}$	2	0	1	0
19	$-1.23066 \times 10^{-2}$	2	0	2	0
20	$1.51268 \times 10^{-2}$	2	0	2	3
21	$-3.45097 \times 10^1$	2	2	1	0

Table 29. Coefficients and powers of  $K_t$ -polynomial for  $x=0.4$

$i$	Coefficient $C_i$	Power of $Z$ $s_i$	Power of $\tan^{\theta} s_x$ $t_i$	Power of $A_E/A_O$ $u_i$	Power of $\lambda_i$ $v_i$
1	$1.39766 \times 10^0$	0	0	0	0
2	$-9.75342 \times 10^{-1}$	0	0	0	1
3	$3.99593 \times 10^0$	0	0	1	1
4	$-1.56771 \times 10^0$	0	0	1	3
5	$5.29452 \times 10^0$	0	0	2	3
6	$-9.14154 \times 10^1$	0	1	1	0
7	$3.77834 \times 10^1$	0	1	1	3
8	$2.17865 \times 10^1$	0	1	2	2
9	$4.05793 \times 10^2$	0	2	1	0
10	$6.50533 \times 10^3$	0	2	2	0
11	$-3.96633 \times 10^{-2}$	0	2	2	2
12	$-3.64281 \times 10^{-1}$	1	0	0	0
13	$2.89802 \times 10^{-1}$	1	0	0	2
14	$-4.20753 \times 10^{-1}$	1	0	1	0
15	$-9.49219 \times 10^{-1}$	1	0	1	2
16	$4.13566 \times 10^{-1}$	1	0	2	0
17	$-4.83935 \times 10^0$	1	0	2	1
18	$-1.19324 \times 10^0$	1	0	2	3
19	$1.43645 \times 10^2$	1	1	1	0
20	$-1.10581 \times 10^2$	1	2	1	3
21	$-2.13400 \times 10^3$	1	2	2	0
22	$1.20197 \times 10^{-2}$	1	2	2	2
23	$1.26615 \times 10^{-2}$	2	0	0	0
24	$-3.64070 \times 10^{-2}$	2	0	0	1
25	$1.65124 \times 10^{-2}$	2	0	0	3
26	$1.14217 \times 10^{-1}$	2	0	1	1
27	$-2.30953 \times 10^{-2}$	2	0	2	0
28	$1.30607 \times 10^0$	2	0	2	3
29	$-2.84697 \times 10^1$	2	1	2	3
30	$1.64554 \times 10^1$	2	2	2	0
31	$-9.94599 \times 10^1$	2	2	2	2
32	$5.38213 \times 10^1$	2	2	2	3

Table 30. Coefficients and powers of  $K_c$ -polynomial for  $x=0.5$

$i$	Coefficient $C_i$	Power of $Z$ $s_i$	Power of $\tan \theta_{s_x}$ $t_i$	Power of $A_E/A_O$ $u_i$	Power of $\lambda_i$ $v_i$
1	$1.18796 \times 10^0$	0	0	0	0
2	$2.77035 \times 10^0$	0	0	1	1
3	$1.64842 \times 10^0$	0	0	2	0
4	$8.01762 \times 10^{-1}$	0	0	2	3
5	$2.76945 \times 10^1$	0	1	0	0
6	$4.86743 \times 10^1$	0	1	1	1
7	$-3.80382 \times 10^1$	0	1	2	1
8	$1.76834 \times 10^2$	0	2	1	0
9	$-2.08273 \times 10^3$	0	2	2	2
10	$-7.51441 \times 10^{-2}$	1	0	0	0
11	$1.39785 \times 10^{-1}$	1	0	0	1
12	$-3.36033 \times 10^{-1}$	1	0	0	2
13	$-2.32585 \times 10^{-1}$	1	0	1	0
14	$-9.98356 \times 10^{-1}$	1	0	2	1
15	$-3.11649 \times 10^0$	1	1	0	0
16	$5.99613 \times 10^0$	1	1	1	1
17	$1.77605 \times 10^1$	1	1	2	2
18	$3.50182 \times 10^2$	1	2	0	3
19	$-1.43481 \times 10^3$	1	2	1	3
20	$1.71742 \times 10^3$	1	2	2	3
21	$1.03624 \times 10^{-2}$	2	0	0	0
22	$1.07037 \times 10^{-1}$	2	0	2	1
23	$-2.47859 \times 10^0$	2	1	0	3
24	$-9.74822 \times 10^{-1}$	2	1	2	1
25	$-1.24621 \times 10^1$	2	1	2	3
26	$3.52732 \times 10^{-1}$	2	1	1	0
27	$1.00956 \times 10^1$	2	1	1	3

Table 31. Coefficients and powers of  $K_\alpha$ -polynomial for  $x=0.5$

i	Coefficient $C_i$	Power of Z $s_i$	Power of $\tan \theta_{s_x}$ $t_i$	Power of $A_E/A_O$ $u_i$	Power of $\lambda_i$ $v_i$
1	$5.13190 \times 10^{-2}$	0	0	0	0
2	$5.72406 \times 10^{-1}$	0	0	1	1
3	$-7.85738 \times 10^{-1}$	0	0	1	3
4	$-1.96120 \times 10^0$	0	0	2	0
5	$-5.26024 \times 10^1$	0	1	2	0
6	$-2.07049 \times 10^1$	0	2	2	0
7	$-7.05954 \times 10^{-2}$	1	0	1	0
8	$2.58128 \times 10^{-1}$	1	0	2	0
9	$-9.14025 \times 10^0$	1	0	2	1
10	$1.50529 \times 10^0$	1	0	2	2
11	$-8.12677 \times 10^{-1}$	1	0	2	3
12	$2.26890 \times 10^0$	1	1	2	0
13	$-1.19824 \times 10^0$	1	1	2	2
14	$2.46777 \times 10^1$	1	2	2	1
15	$-2.00759 \times 10^{-3}$	2	0	0	0
16	$-4.01033 \times 10^{-3}$	2	0	1	0
17	$1.97880 \times 10^{-1}$	2	0	1	1
18	$-3.73815 \times 10^{-1}$	2	0	1	2
19	$2.22945 \times 10^{-1}$	2	0	1	3
20	$-6.38862 \times 10^{-2}$	2	0	2	1
21	$6.25384 \times 10^{-2}$	2	0	2	2
22	$-2.22995 \times 10^{-1}$	2	1	2	0
23	$-6.94019 \times 10^{-1}$	2	2	2	0

Table 32. Coefficients and powers of  $K_t$ -polynomial for  $x=0.5$

$i$	Coefficient $C_i$	Power of $Z$ $s_i$	Power of $\tan \theta_{s_x}$ $t_i$	Power of $A_E/A_0$ $u_i$	Power of $\lambda_i$ $v_i$
1	$1.12317 \times 10^0$	0	0	0	0
2	$-5.39068 \times 10^{-1}$	0	0	0	3
3	$8.67821 \times 10^{-1}$	0	0	1	0
4	$1.55686 \times 10^0$	0	0	1	2
5	$3.19469 \times 10^{-1}$	0	0	2	0
6	$2.69341 \times 10^0$	0	0	2	1
7	$-4.80363 \times 10^0$	0	0	2	2
8	$7.99860 \times 10^0$	0	0	2	3
9	$-9.22357 \times 10^0$	0	1	2	3
10	$-4.44005 \times 10^{-1}$	1	0	1	0
11	$7.97250 \times 10^{-2}$	1	0	2	1
12	$-2.12053 \times 10^0$	1	0	2	3
13	$3.00384 \times 10^{-2}$	2	0	1	0
14	$1.07912 \times 10^{-2}$	2	0	1	1
15	$-2.15709 \times 10^{-2}$	2	0	2	1
16	$1.79629 \times 10^{-1}$	2	0	2	3
17	$9.82096 \times 10^{-1}$	2	2	1	1

Table 33. Coefficients and powers of  $K_C$ -polynomial for  $x=0.6$

i	Coefficient $C_i$	Power of Z $s_i$	Power of $\tan \theta_{s_x}$ $t_i$	Power of $A_E/A_O$ $u_i$	Power of $\lambda_i$ $v_i$
1	$2.55233 \times 10^0$	0	0	0	0
2	$-6.09552 \times 10^0$	0	0	0	1
3	$3.23416 \times 10^0$	0	0	0	3
4	$9.54750 \times 10^0$	0	0	1	1
5	$1.87190 \times 10^1$	0	1	0	1
6	$9.97576 \times 10^0$	0	1	1	0
7	$-5.58234 \times 10^1$	0	1	1	3
8	$-2.17616 \times 10^1$	0	1	2	1
9	$8.21871 \times 10^1$	0	1	2	3
10	$6.31802 \times 10^3$	0	2	0	0
11	$-1.35821 \times 10^3$	0	2	2	3
12	$-6.44559 \times 10^{-1}$	1	0	0	0
13	$2.68087 \times 10^0$	1	0	0	1
14	$-1.04657 \times 10^0$	1	0	0	2
15	$-3.03476 \times 10^0$	1	0	1	1
16	$-9.97800 \times 10^{-1}$	1	0	1	3
17	$-3.02846 \times 10^{-1}$	1	0	2	0
18	$-1.18227 \times 10^0$	1	1	0	1
19	$1.70184 \times 10^{-1}$	1	1	2	3
20	$3.15108 \times 10^2$	1	2	2	3
21	$7.76604 \times 10^{-2}$	2	0	0	0
22	$-2.71830 \times 10^{-1}$	2	0	0	1
23	$1.03732 \times 10^{-1}$	2	0	0	3
24	$6.38933 \times 10^{-2}$	2	0	1	0
25	$4.27747 \times 10^{-1}$	2	0	1	1
26	$-9.34772 \times 10^{-2}$	2	0	2	1
27	$7.73809 \times 10^{-2}$	2	0	2	3
28	$-6.63840 \times 10^0$	2	1	2	3
29	$-3.36131 \times 10^0$	2	2	0	1
30	$2.37964 \times 10^0$	2	1	1	2

Table 34. Coefficients and powers of  $K_\alpha$ -polynomial for  $x=0.6$



i	Coefficient $C_i$	Power of Z $s_i$	Power of $\tan \theta_{s_x}$ $t_i$	Power of $A_E/A_O$ $u_i$	Power of $\lambda_i$ $v_i$
1	$1.74390 \times 10^{-1}$	0	0	0	0
2	$-2.13885 \times 10^{-1}$	0	0	1	0
3	$-9.84378 \times 10^{-1}$	0	1	0	3
4	$-3.47821 \times 10^0$	0	2	2	0
5	$-7.55138 \times 10^{-3}$	1	0	0	0
6	$-2.33967 \times 10^{-1}$	1	0	0	1
7	$2.55268 \times 10^{-1}$	1	0	0	2
8	$-1.27981 \times 10^{-1}$	1	0	1	0
9	$1.04848 \times 10^0$	1	0	1	1
10	$-1.05163 \times 10^0$	1	0	1	2
11	$2.03059 \times 10^{-1}$	1	0	2	0
12	$-8.98430 \times 10^{-1}$	1	0	2	1
13	$8.49644 \times 10^{-1}$	1	0	2	2
14	$3.40908 \times 10^0$	1	2	1	1
15	$3.25330 \times 10^{-2}$	2	0	0	1
16	$-6.94331 \times 10^{-2}$	2	0	0	2
17	$4.68188 \times 10^{-2}$	2	0	0	3
18	$-3.43812 \times 10^{-2}$	2	1	1	1

Table 35. Coefficients and powers of  $K_t$ -polynomial for  $x=0.6$

i	Coefficient $C_i$	Power of Z $s_i$	Power of $\tan \theta_{s_x}$ $t_i$	Power of $A_E/A_0$ $u_i$	Power of $\lambda_i$ $v_i$
1	$1.14830 \times 10^0$	0	0	0	0
2	$1.52827 \times 10^0$	0	0	1	0
3	$6.68774 \times 10^{-1}$	0	0	1	3
4	$5.80186 \times 10^0$	0	0	2	1
5	$-3.72790 \times 10^0$	0	0	2	2
6	$1.50400 \times 10^0$	0	0	2	3
7	$-1.92169 \times 10^1$	0	1	1	1
8	$1.31887 \times 10^1$	0	1	2	2
9	$3.60576 \times 10^2$	0	2	2	1
10	$3.90539 \times 10^2$	0	2	2	2
11	$-7.62452 \times 10^{-2}$	1	0	0	0
12	$-4.34806 \times 10^1$	1	0	1	0
13	$1.07642 \times 10^0$	1	0	1	1
14	$-1.20723 \times 10^0$	1	0	2	1
15	$2.89690 \times 10^{-1}$	1	1	0	1
16	$9.26507 \times 10^1$	1	2	2	2
17	$9.61027 \times 10^{-3}$	2	0	0	0
18	$-1.52201 \times 10^{-2}$	2	0	0	3
19	$2.36964 \times 10^{-2}$	2	0	1	0
20	$1.02351 \times 10^{-1}$	2	0	2	1
21	$-5.66654 \times 10^{-1}$	2	1	2	2
22	$-2.97668 \times 10^0$	2	2	2	0
23	$-3.94694 \times 10^0$	2	2	2	2
24	$2.03666 \times 10^{-2}$	2	1	1	0

Table 36. Coefficients and powers of  $K_C$ -polynomial for  $x=0.7$

i	Coefficient	Power of z	Power of $\tan \theta_{s_x}$	Power of $A_E/A_O$	Power of $\lambda_i$
	$C_i$	$s_i$	$t_i$	$u_i$	$v_i$
1	$2.78074 \times 10^{-2}$	0	0	0	0
2	$3.79837 \times 10^0$	0	0	0	3
3	$3.45696 \times 10^0$	0	0	1	0
4	$2.87946 \times 10^0$	0	0	1	1
5	$4.03683 \times 10^{-1}$	0	0	2	0
6	$-4.65991 \times 10^0$	0	0	2	1
7	$-2.85455 \times 10^0$	0	1	2	0
8	$4.36673 \times 10^1$	0	2	0	0
9	$-5.98466 \times 10^1$	0	2	0	1
10	$3.06700 \times 10^2$	0	2	0	3
11	$-2.79628 \times 10^1$	0	2	1	0
12	$-3.17681 \times 10^2$	0	2	1	2
13	$6.15558 \times 10^1$	0	2	0	0
14	$2.10900 \times 10^1$	0	2	2	1
15	$1.87899 \times 10^2$	0	2	2	3
16	$3.52852 \times 10^{-1}$	1	0	0	0
17	$-2.33519 \times 10^0$	1	0	0	3
18	$-1.13230 \times 10^0$	1	0	1	0
19	$1.21624 \times 10^0$	1	0	2	1
20	$4.37569 \times 10^{-1}$	1	0	2	3
21	$7.59610 \times 10^{-1}$	1	1	1	0
22	$1.94198 \times 10^1$	1	1	1	2
23	$-3.17524 \times 10^1$	1	1	1	3
24	$6.81420 \times 10^0$	1	1	2	3
25	$-1.17677 \times 10^1$	1	2	2	0
26	$-2.03469 \times 10^{-2}$	2	0	0	0
27	$-3.91583 \times 10^{-2}$	2	0	0	1
28	$3.12484 \times 10^{-1}$	2	0	0	3
29	$6.72536 \times 10^{-2}$	2	0	1	0
30	$-1.79963 \times 10^{-1}$	2	0	2	2
31	$-1.18739 \times 10^0$	2	1	0	2
32	$2.37083 \times 10^0$	2	1	0	3

33	$1.01405 \times 10^{-1}$	2	1	2	0
34	$-7.71482 \times 10^{-1}$	2	1	2	1
35	$-2.35894 \times 10^{-1}$	2	2	0	0
36	$-6.56064 \times 10^0$	2	2	0	3
37	$5.98944 \times 10^0$	2	2	1	1

Table 37. Coefficients and powers of  $K_{\alpha}$ -polynomial for  $x=0.7$

	Coefficient	Power of Z	Power of $\tan \theta_{s_x}$	Power of $A_E/A_0$	Power of $\lambda_i$
i	$C_i$	$s_i$	$t_i$	$u_i$	$v_i$
1	$6.24487 \times 10^{-2}$	0	0	0	0
2	$3.13343 \times 10^{-1}$	0	0	1	1
3	$-4.47576 \times 10^{-1}$	0	0	2	1
4	$-9.07230 \times 10^{-1}$	0	1	0	3
5	$-2.47680 \times 10^{-2}$	1	0	0	2
6	$-8.40292 \times 10^{-2}$	1	0	1	0
7	$6.64169 \times 10^{-2}$	1	0	1	1
8	$8.14497 \times 10^{-2}$	1	0	2	0
9	$2.65926 \times 10^{-1}$	1	1	1	3
10	$-1.30269 \times 10^{-2}$	2	0	0	2
11	$2.44126 \times 10^{-2}$	2	0	0	3
12	$2.76463 \times 10^{-3}$	2	0	1	0
13	$3.56886 \times 10^{-2}$	2	0	1	1
14	$-6.43053 \times 10^{-2}$	2	0	1	3
15	$-2.23179 \times 10^{-2}$	2	2	0	1
16	$-2.43987 \times 10^{-2}$	2	0	2	1
17	$6.49649 \times 10^{-2}$	2	0	2	3
18	$3.31181 \times 10^{-2}$	2	2	1	0
19	$-1.92557 \times 10^{-2}$	2	1	1	1

Table 38. Coefficients and powers of  $K_t$ -polynomial for  $x=0.7$

i	Coefficient	Power of Z	Power of $\tan \theta_{s_x}$	Power of $A_E/A_O$	Power of $\lambda_i$
	$C_i$	$s_i$	$t_i$	$u_i$	$v_i$
1	$2.07742 \times 10^{-1}$	0	0	0	0
2	$-2.22127 \times 10^0$	0	0	0	2
3	$4.72883 \times 10^0$	0	0	1	0
4	$1.46060 \times 10^{-1}$	0	0	2	0
5	$-2.73109 \times 10^0$	0	0	2	1
6	$-4.21241 \times 10^0$	0	0	2	2
7	$9.42885 \times 10^0$	0	0	2	3
8	$-2.04250 \times 10^0$	0	1	0	1
9	$-5.63450 \times 10^{-1}$	0	1	2	0
10	$2.01121 \times 10^1$	0	2	2	0
11	$2.66213 \times 10^{-1}$	1	0	0	0
12	$1.16124 \times 10^{-1}$	1	0	0	1
13	$-1.47752 \times 10^0$	1	0	1	0
14	$1.94917 \times 10^0$	1	0	2	1
15	$-2.72823 \times 10^0$	1	0	2	3
16	$7.06644 \times 10^{-1}$	1	1	1	1
17	$2.80644 \times 10^0$	1	1	1	3
18	$1.22911 \times 10^0$	1	1	2	3
19	$5.35826 \times 10^1$	1	2	0	1
20	$-2.55614 \times 10^0$	1	2	1	3
21	$-7.31722 \times 10^0$	1	2	2	0
22	$-1.88847 \times 10^{-2}$	2	0	0	0
23	$-2.65593 \times 10^{-2}$	2	0	0	1
24	$1.08805 \times 10^{-1}$	2	0	1	0
25	$3.57113 \times 10^{-2}$	2	0	1	1
26	$-1.91507 \times 10^{-1}$	2	0	2	1
27	$2.52300 \times 10^{-1}$	2	0	2	3
28	$-9.06911 \times 10^{-1}$	2	1	2	3
29	$-2.86708 \times 10^0$	2	2	0	2
30	$3.70945 \times 10^0$	2	2	0	3
31	$7.42903 \times 10^1$	2	2	2	0
32	$-1.42384 \times 10^0$	2	2	2	1
33	$4.38710 \times 10^0$	2	2	2	2

Table 39. Coefficients and powers of  $K_c$ -polynomial for  $\kappa=0.8$



i	Coefficient $C_i$	Power of Z $s_i$	Power of $\tan \theta_{s_x}$ $t_i$	Power of $A_E/A_O$ $u_i$	Power of $\lambda_i$ $v_i$
1	$5.88189 \times 10^{-1}$	0	0	0	0
2	$4.34765 \times 10^0$	0	0	0	1
3	$2.00902 \times 10^0$	0	0	1	0
4	$-5.58331 \times 10^0$	0	0	1	2
5	$-9.72288 \times 10^{-1}$	0	0	2	0
6	$1.74641 \times 10^0$	0	0	2	1
7	$-2.19749 \times 10^0$	1	0	0	1
8	$1.22175 \times 10^0$	1	0	0	2
9	$1.89463 \times 10^{-1}$	1	0	1	0
10	$3.66149 \times 10^{-1}$	1	0	1	1
11	$6.66130 \times 10^{-1}$	1	0	2	2
12	$-1.65108 \times 10^{-1}$	1	0	2	3
13	$2.27292 \times 10^{-1}$	2	0	0	1
14	$-2.39706 \times 10^{-1}$	2	0	0	3
15	$-4.33732 \times 10^{-2}$	2	0	1	0
16	$-1.21061 \times 10^{-1}$	2	0	1	1
17	$2.69159 \times 10^{-1}$	2	0	1	3
18	$1.30770 \times 10^{-1}$	2	0	2	1
19	$-3.41882 \times 10^{-1}$	2	0	2	2
20	$1.14838 \times 10^{-1}$	2	0	2	3
21	$-3.70986 \times 10^1$	0	1	1	1
22	$2.54793 \times 10^1$	0	1	1	2
23	$1.63528 \times 10^1$	0	1	2	1
24	$2.04222 \times 10^1$	0	2	2	0
25	$-2.94409 \times 10^0$	1	1	0	3
26	$9.59024 \times 10^0$	1	1	1	3
27	$-1.00282 \times 10^1$	1	1	2	3
28	$1.91599 \times 10^0$	1	2	0	0
29	$-6.29038 \times 10^0$	1	2	2	0
30	$9.67031 \times 10^{-2}$	2	1	0	1
31	$3.44031 \times 10^{-1}$	2	2	2	0
32	$1.34795 \times 10^1$	2	2	2	2

Table 40. Coefficients and powers of  $K_\alpha$ -polynomial for  $x=0.8$

i	Coefficient $C_i$	Power of Z $s_i$	Power of $\tan \theta_{s_x}$ $t_i$	Power of $A_E/A_O$ $u_i$	Power of $\lambda_i$ $v_i$
1	$3.44724 \times 10^{-2}$	0	0	0	0
2	$1.57437 \times 10^{-1}$	0	0	0	3
3	$-1.24263 \times 10^{-1}$	0	0	1	3
4	$-8.00466 \times 10^{-2}$	0	0	2	1
5	$-9.41774 \times 10^{-3}$	1	0	0	0
6	$-2.86837 \times 10^{-2}$	1	0	0	2
7	$-1.46913 \times 10^{-2}$	1	0	1	0
8	$1.14895 \times 10^{-1}$	1	0	1	1
9	$-4.57533 \times 10^{-2}$	1	0	1	3
10	$1.77024 \times 10^{-1}$	1	0	2	0
11	$-1.16799 \times 10^{-1}$	1	0	2	2
12	$1.08940 \times 10^{-1}$	1	0	2	3
13	$1.28529 \times 10^{-3}$	2	0	0	0
14	$1.37762 \times 10^0$	0	2	1	0
15	$-7.40226 \times 10^0$	0	2	1	3
16	$-1.98478 \times 10^{-2}$	1	1	2	0
17	$1.13830 \times 10^{-1}$	1	2	0	0
18	$-6.50591 \times 10^{-1}$	1	2	1	0
19	$3.02109 \times 10^0$	1	2	2	3
20	$-1.36263 \times 10^{-2}$	2	1	0	3
21	$1.56943 \times 10^{-2}$	2	1	2	0
22	$-5.21823 \times 10^{-2}$	2	1	2	1
23	$4.69550 \times 10^{-2}$	2	2	2	0
24	$-2.07603 \times 10^{-1}$	2	2	2	3
25	$-1.02309 \times 10^{-2}$	2	1	1	0
26	$4.37783 \times 10^{-2}$	2	1	1	1

Table 41. Coefficients and powers of  $K_t$ -polynomial for  $x=0.8$

i	Coefficient $C_i$	Power of Z $s_i$	Power of $\tan \theta_{s_x}$ $t_i$	Power of $A_E/A_0$ $u_i$	Power of $\lambda_i$ $v_i$
1	$5.78921 \times 10^{-1}$	0	0	0	0
2	$5.48705 \times 10^0$	0	0	0	1
3	$4.72979 \times 10^0$	0	0	1	0
4	$-2.43459 \times 10^0$	0	0	1	1
5	$-6.86422 \times 10^{-1}$	1	0	1	0
6	$-5.32060 \times 10^0$	1	0	1	1
7	$1.43507 \times 10^0$	1	0	2	1
8	$4.22475 \times 10^{-2}$	2	0	1	0
9	$1.97703 \times 10^{-2}$	2	0	1	1
10	$-1.29499 \times 10^{-2}$	2	0	2	0
11	$-1.27207 \times 10^0$	2	0	2	1
12	$-7.60864 \times 10^1$	0	1	0	2
13	$-2.61404 \times 10^1$	0	1	1	3
14	$1.19140 \times 10^1$	0	2	0	0
15	$2.70101 \times 10^1$	0	2	0	2
16	$7.55210 \times 10^1$	0	2	2	1
17	$1.26025 \times 10^0$	1	1	1	3
18	$-4.06508 \times 10^1$	1	2	0	0
19	$-3.02806 \times 10^1$	1	2	2	1
20	$7.46118 \times 10^{-1}$	2	1	0	3
21	$3.65338 \times 10^0$	2	2	0	0
22	$-1.57938 \times 10^0$	2	2	0	3
23	$2.93711 \times 10^0$	2	2	2	1
24	$7.92343 \times 10^{-1}$	2	2	2	3
25	$-1.91686 \times 10^0$	2	1	1	3

Table 42. Coefficients and powers of  $K_C$ -polynomial for  $x=0.9$

i	Coefficient	Power of Z	Power of $\tan \theta_{s_x}$	Power of $A_E/A_O$	Power of $\lambda_i$
	$C_i$	$s_i$	$t_i$	$u_i$	$v_i$
1	$7.08338 \times 10^{-1}$	0	0	0	0
2	$5.18820 \times 10^0$	0	0	1	0
3	$-1.99554 \times 10^0$	0	0	1	2
4	$-4.75392 \times 10^{-1}$	1	0	0	1
5	$1.06284 \times 10^0$	1	0	0	2
6	$-8.43029 \times 10^{-1}$	1	0	1	0
7	$-1.25360 \times 10^{-1}$	1	0	2	2
8	$1.91512 \times 10^{-2}$	2	0	0	0
9	$-1.50032 \times 10^{-1}$	2	0	0	3
10	$1.92610 \times 10^{-2}$	2	0	1	0
11	$8.01379 \times 10^{-2}$	2	0	1	2
12	$1.16538 \times 10^{-2}$	2	0	2	0
13	$-4.84115 \times 10^0$	1	0	1	0
14	$-4.22219 \times 10^0$	0	1	1	0
15	$3.93820 \times 10^1$	0	1	1	1
16	$1.26584 \times 10^1$	0	1	1	3
17	$-1.82613 \times 10^2$	0	2	0	1
18	$-1.12818 \times 10^2$	0	2	1	1
19	$2.14891 \times 10^2$	0	2	1	2
20	$-1.32306 \times 10^2$	0	2	2	3
21	$-5.19123 \times 10^0$	1	1	0	2
22	$-1.73841 \times 10^1$	1	1	1	1
23	$5.62809 \times 10^{-1}$	1	1	2	0
24	$3.12705 \times 10^0$	1	2	0	0
25	$6.55534 \times 10^1$	1	2	0	1
26	$1.10477 \times 10^1$	1	2	2	1
27	$2.22179 \times 10^{-1}$	2	1	0	1
28	$-6.29968 \times 10^{-1}$	2	1	2	2
29	$-6.01973 \times 10^0$	2	2	2	1
30	$-4.72036 \times 10^{-1}$	2	2	1	0
31	$-1.37463 \times 10^0$	2	2	1	3
32	$1.16317 \times 10^0$	2	1	1	1
33	$1.16877 \times 10^0$	2	1	1	3

Table 43. Coefficients and powers of  $K_\alpha$ -polynomial for  $x=0.9$

i	Coefficient $C_i$	Power of Z $s_i$	Power of $\tan \theta_{s_x}$ $t_i$	Power of $A_E/A_O$ $u_i$	Power of $\lambda_i$ $v_i$
1	$4.82069 \times 10_0^{-2}$	0	0	0	0
2	$5.84711 \times 10_0$	0	0	0	3
3	$-4.75411 \times 10_0$	0	0	1	2
4	$-5.59450 \times 10_0^{-2}$	0	0	2	0
5	$5.49112 \times 10_0^{-1}$	0	0	2	1
6	$5.48893 \times 10_0^{-1}$	0	0	2	2
7	$-2.24794 \times 10_0$	1	0	0	3
8	$-9.50604 \times 10_0^{-2}$	1	0	1	0
9	$3.20695 \times 10_0^{-1}$	1	0	1	1
10	$1.40785 \times 10_0$	1	0	1	2
11	$9.17161 \times 10_0^{-2}$	1	0	2	0
12	$-3.76493 \times 10_0^{-1}$	1	0	2	1
13	$1.50713 \times 10_0^{-2}$	2	0	0	1
14	$-1.10186 \times 10_0^{-1}$	2	0	0	2
15	$3.57601 \times 10_0^{-1}$	2	0	0	3
16	$-2.51326 \times 10_0^{-1}$	2	0	1	3
17	$-3.67332 \times 10_0^{-2}$	2	0	2	2
18	$1.17211 \times 10_1^{-1}$	2	0	2	3
19	$-3.69784 \times 10_1$	0	1	0	3
20	$1.66122 \times 10_1$	0	1	1	3
21	$3.95173 \times 10_0$	0	1	2	2
22	$8.87010 \times 10_1$	0	2	0	3
23	$-4.20393 \times 10_1$	0	2	1	3
24	$2.91040 \times 10_0^{-2}$	1	1	0	0
25	$3.91848 \times 10_1^{-1}$	1	1	0	2
26	$1.17670 \times 10_1$	1	1	0	3
27	$-3.96703 \times 10_0$	1	1	2	2
28	$-1.36948 \times 10_1^{-1}$	1	2	0	0
29	$-2.91280 \times 10_1$	1	2	0	3
30	$5.79204 \times 10_0$	1	2	2	2
31	$-1.22679 \times 10_0$	2	1	0	3
32	$3.70134 \times 10_0^{-1}$	2	1	2	2

33	$2.89587 \times 10^0$	2	2	0	3
34	$-5.13705 \times 10^{-1}$	2	2	2	2

Table 44. Coefficients and powers of  $K_t$ -polynomial for  $x=0.9$



$i$	Coefficient $C_i$	Power of $Z$ $s_i$	Power of $\tan \theta_{s_x}$ $t_i$	Power of $A_E/A_0$ $u_i$	Power of $\lambda_i$ $v_i$
1	$8.58453 \times 10^{-1}$	0	0	0	0
2	$1.26484 \times 10^0$	0	0	1	1
3	$7.48262 \times 10^0$	0	0	1	2
4	$-6.39486 \times 10^0$	0	0	1	3
5	$1.86234 \times 10^0$	0	0	2	0
6	$-3.27633 \times 10^0$	0	0	2	1
7	$1.42478 \times 10^{-1}$	1	0	0	0
8	$-1.20680 \times 10^{-1}$	1	0	0	1
9	$-1.39817 \times 10^{-1}$	1	0	1	0
10	$-9.92650 \times 10^{-1}$	1	0	1	1
11	$1.27584 \times 10^0$	1	0	2	2
12	$-1.27089 \times 10^{-2}$	2	0	0	0
13	$1.44941 \times 10^{-1}$	2	0	1	1
14	$-1.69328 \times 10^{-1}$	2	0	2	2
15	$7.05701 \times 10^{-4}$	0	2	1	3
16	$5.26987 \times 10^{-1}$	1	1	0	3
17	$-3.40353 \times 10^{-4}$	1	2	1	3
18	$-3.42722 \times 10^{-1}$	2	1	2	3
19	$5.79771 \times 10^{-3}$	2	2	2	3
20	$1.26539 \times 10^{-1}$	2	1	1	3

Table 24. Coefficients and powers of  $K_C$ -polynomial for  $x=0.3$

i	Coefficient $C_i$	Power of Z $s_i$	Power of $\tan \theta_{s_x}$ $t_i$	Power of $A_E/A_O$ $u_i$	Power of $\lambda_i$ $v_i$
1	$-1.18795 \times 10^{-1}_0$	0	0	0	0
2	$2.01598 \times 10^0_0$	0	0	0	1
3	$6.87514 \times 10^0_1$	0	0	1	0
4	$-1.15131 \times 10^1_1$	0	0	1	1
5	$-7.13361 \times 10^{-1}_0$	0	0	2	0
6	$3.47574 \times 10^0_0$	0	0	2	1
7	$2.01846 \times 10^1_1$	1	0	1	2
8	$-3.03496 \times 10^{-2}_0$	2	0	1	0
9	$-2.35333 \times 10^{-1}_1$	2	0	1	3
10	$1.88149 \times 10^{-2}_1$	2	0	2	0
11	$-5.47917 \times 10^2_2$	0	1	0	2
12	$1.45517 \times 10^1_1$	0	2	0	1
13	$1.97521 \times 10^1_1$	0	2	2	3
14	$1.77607 \times 10^1_1$	1	1	0	2
15	$-5.13660 \times 10^1_1$	1	2	0	1
16	$-9.41584 \times 10^{-1}_0$	2	1	0	2
17	$2.81359 \times 10^{-1}_0$	2	1	2	2
18	$4.27159 \times 10^0_0$	2	2	0	1
19	$7.66821 \times 10^{-2}_0$	2	2	1	0
20	$-8.45623 \times 10^{-1}_0$	2	1	1	2

Table 45. Coefficients and powers of  $K_C$ -polynomial for  $x=1.0$

i	coefficient	Power of Z	Power of $\tan \theta_{s_x}$	Power of $A_E/A_0$	Power of $\lambda_i$
	$C_i$	$s_i$	$t_i$	$u_i$	$v_i$
1	$9.93376 \times 10^{-1}$	0	0	0	0
2	$3.12492 \times 10^0$	0	0	1	0
3	$-3.56192 \times 10^0$	0	0	1	1
4	$2.88875 \times 10^0$	0	0	2	0
5	$1.46103 \times 10^0$	1	0	0	3
6	$-5.02920 \times 10^{-1}$	1	0	1	1
7	$-4.11696 \times 10^{-1}$	1	0	2	0
8	$-2.88346 \times 10^{-1}$	2	0	0	3
9	$2.11808 \times 10^{-1}$	2	0	1	2
10	$-3.72276 \times 10^1$	0	1	0	0
11	$-1.16539 \times 10^2$	0	1	1	3
12	$-4.59246 \times 10^1$	0	1	2	0
13	$2.49071 \times 10^1$	0	1	2	1
14	$6.44461 \times 10^1$	0	1	2	3
15	$1.54087 \times 10^2$	0	2	1	0
16	$1.10554 \times 10^0$	0	2	2	2
17	$9.58574 \times 10^1$	1	1	0	0
18	$1.78395 \times 10^1$	1	1	0	3
19	$1.54661 \times 10^1$	1	1	2	0
20	$-1.29253 \times 10^1$	1	1	2	1
21	$-5.62147 \times 10^1$	1	2	1	0
22	$-4.42923 \times 10^1$	1	1	0	2
23	$-4.80448 \times 10^{-1}$	2	1	0	0
24	$-4.80640 \times 10^0$	2	1	0	2
25	$-6.70299 \times 10^{-1}$	2	1	2	0
26	$-3.12233 \times 10^0$	2	1	2	3
27	$6.39530 \times 10^{-1}$	2	2	0	1
28	$3.20161 \times 10^0$	2	2	0	2
29	$4.78984 \times 10^0$	2	2	1	0
30	$-8.21605 \times 10^{-1}$	2	1	1	0
31	$7.37340 \times 10^0$	2	1	1	2

Table 46. Coefficients and powers of  $K_\alpha$ -polynomial for  $x=1.0$

i	Coefficient $C_i$	Power of Z $s_i$	Power of $\tan \theta_{s_x}$ $t_i$	Power of $A_E/A_O$ $u_i$	Power of $\lambda_i$ $v_i$
1	$1.20038 \times 10^{-1}$	0	0	0	0
2	$-2.82693 \times 10^{-1}$	0	0	1	0
3	$4.71273 \times 10^{-1}$	0	0	1	1
4	$-5.21481 \times 10^{-1}$	0	0	1	3
5	$-3.20622 \times 10^{-1}$	1	0	0	2
6	$4.16623 \times 10^{-1}$	1	0	0	3
7	$3.72223 \times 10^{-2}$	1	0	2	0
8	$-2.98658 \times 10^{-2}$	2	0	1	0
9	$1.70393 \times 10^{-1}$	2	0	1	1
10	$-1.68435 \times 10^{-1}$	2	0	1	2
11	$2.67771 \times 10^{-2}$	2	0	2	0
12	$-1.49122 \times 10^{-1}$	2	0	2	1
13	$1.46661 \times 10^{-1}$	2	0	2	2
14	$7.96811 \times 10^{-1}$	0	1	0	2
15	$-7.98236 \times 10^{-1}$	0	2	0	0
16	$-2.38902 \times 10^{-1}$	1	1	1	1
17	$6.38107 \times 10^{-1}$	1	2	1	0
18	$-7.06930 \times 10^{-1}$	1	2	1	2
19	$6.90654 \times 10^{-3}$	2	1	2	0
20	$-1.13384 \times 10^{-1}$	2	2	2	0
21	$1.51088 \times 10^{-1}$	2	2	2	1

Table 47. Coefficients and powers of  $K_t$ -polynomial for  $x=1.0$

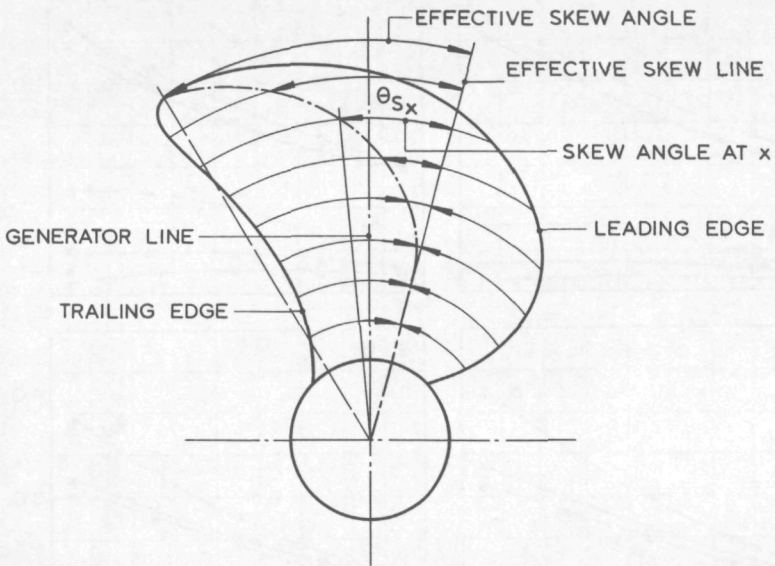


FIG.50 SKETCH TO DEFINE EFFECTIVE SKEW AND LOCAL SKEW ANGLES  $\theta_{Sx}$

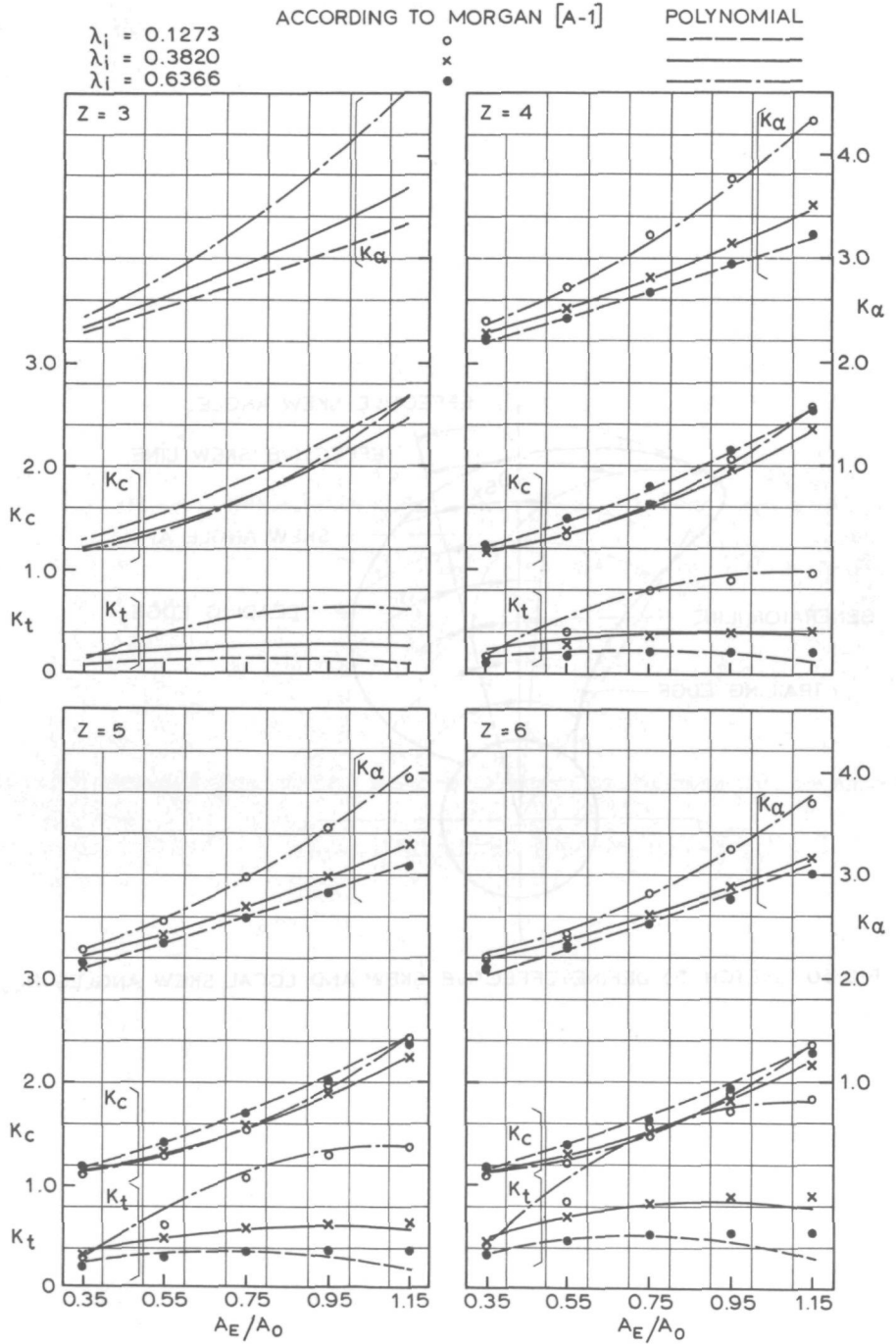


FIG.51 RESULTS OF POLYNOMIALS FOR LIFTING SURFACE CORRECTIONS FOR  $x = 0.3$  AND  $\theta_{Sx} = 0$ .



ACCORDING TO MORGAN [A-1]

POLYNOMIAL

$\lambda_i = 0.1273$   
 $\lambda_i = 0.3820$   
 $\lambda_i = 0.6366$

○  
 x  
 ●

---  
 ---  
 ---

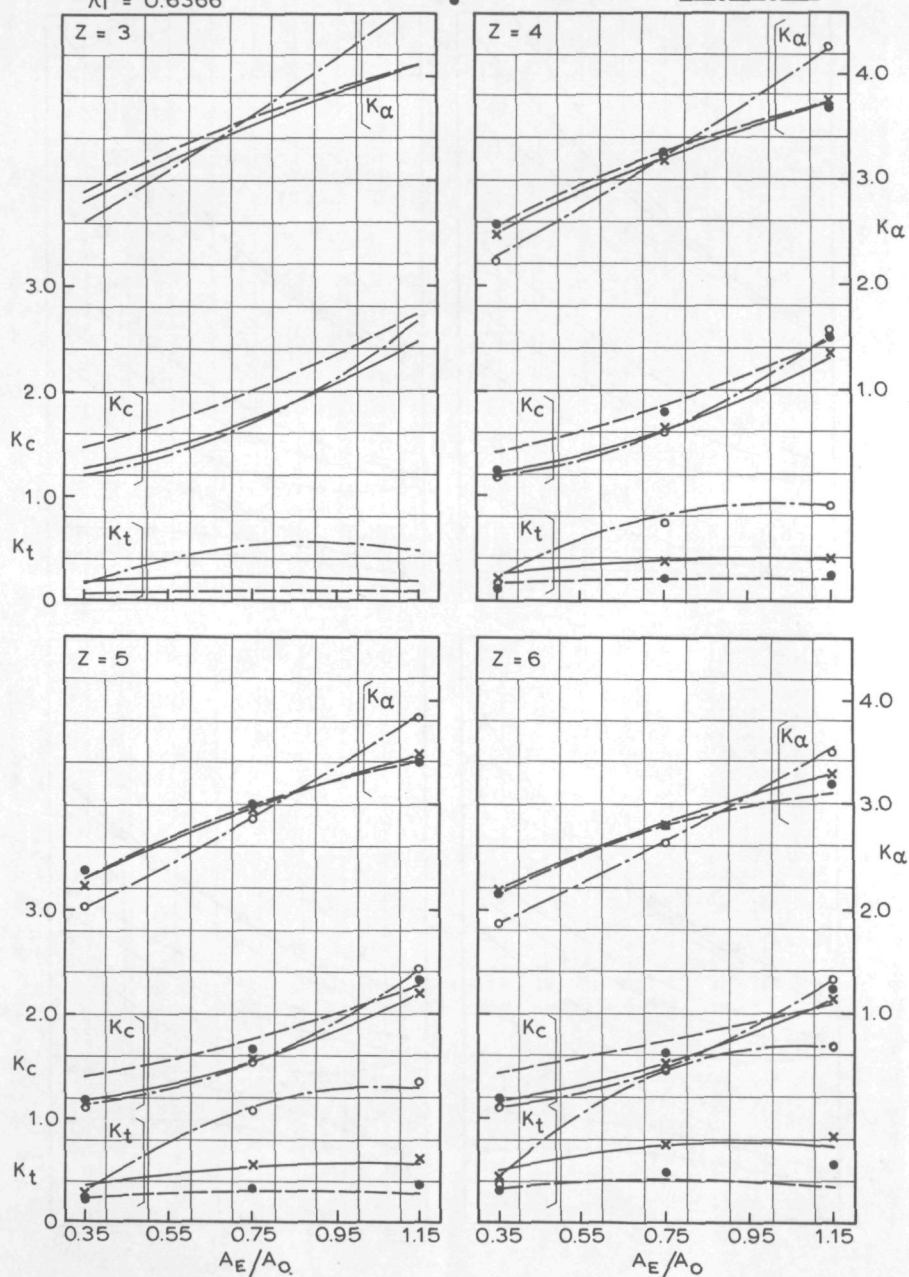


FIG.52 RESULTS OF POLYNOMIALS FOR LIFTING SURFACE CORRECTIONS FOR  $x = 0.3$  AND  $\theta_{Sx} = 0.0049$ .

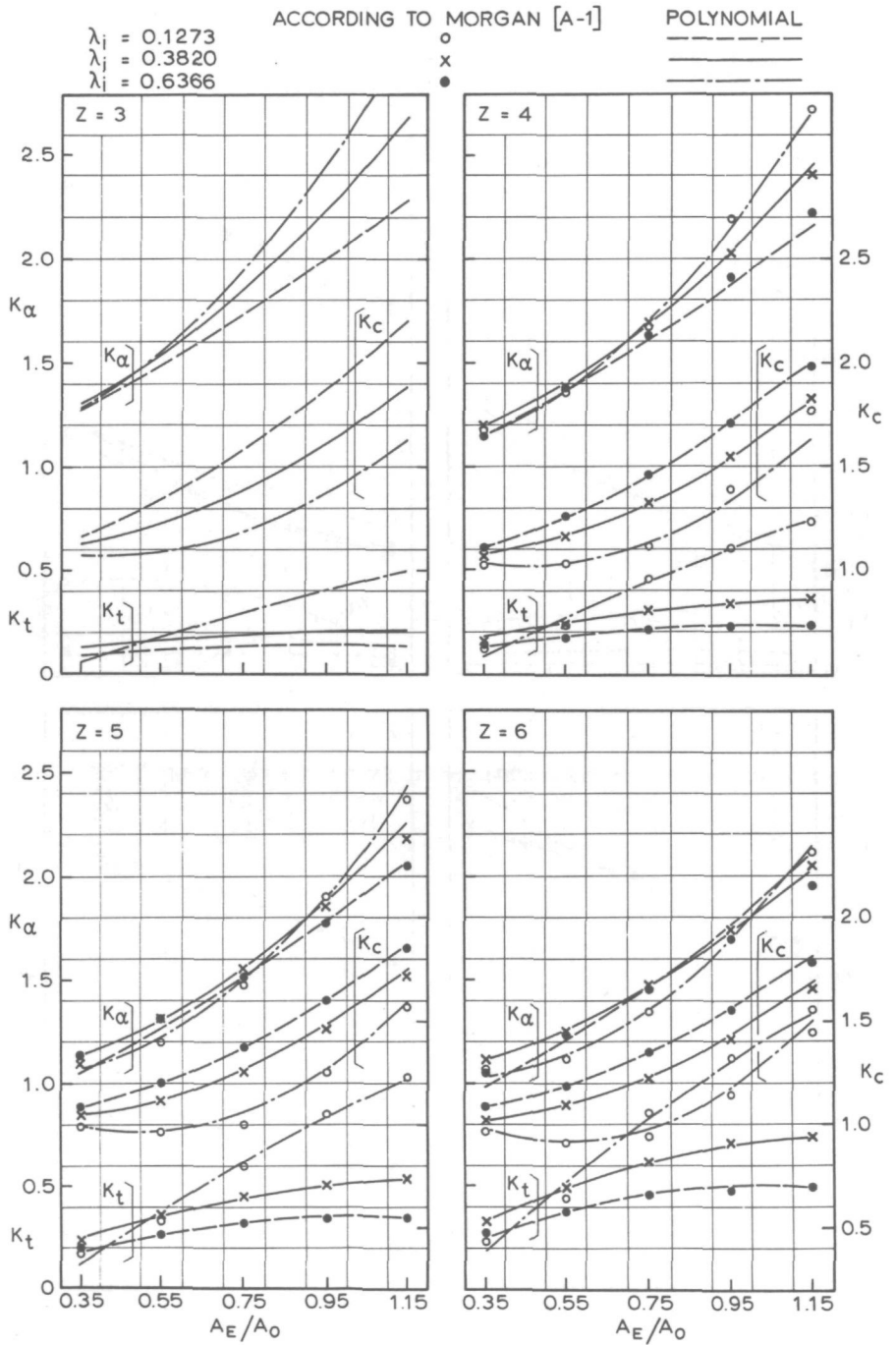


FIG.53 RESULTS OF POLYNOMIALS FOR LIFTING SURFACE CORRECTIONS FOR  $x = 0.4$  AND  $\theta_{Sx} = 0$ .

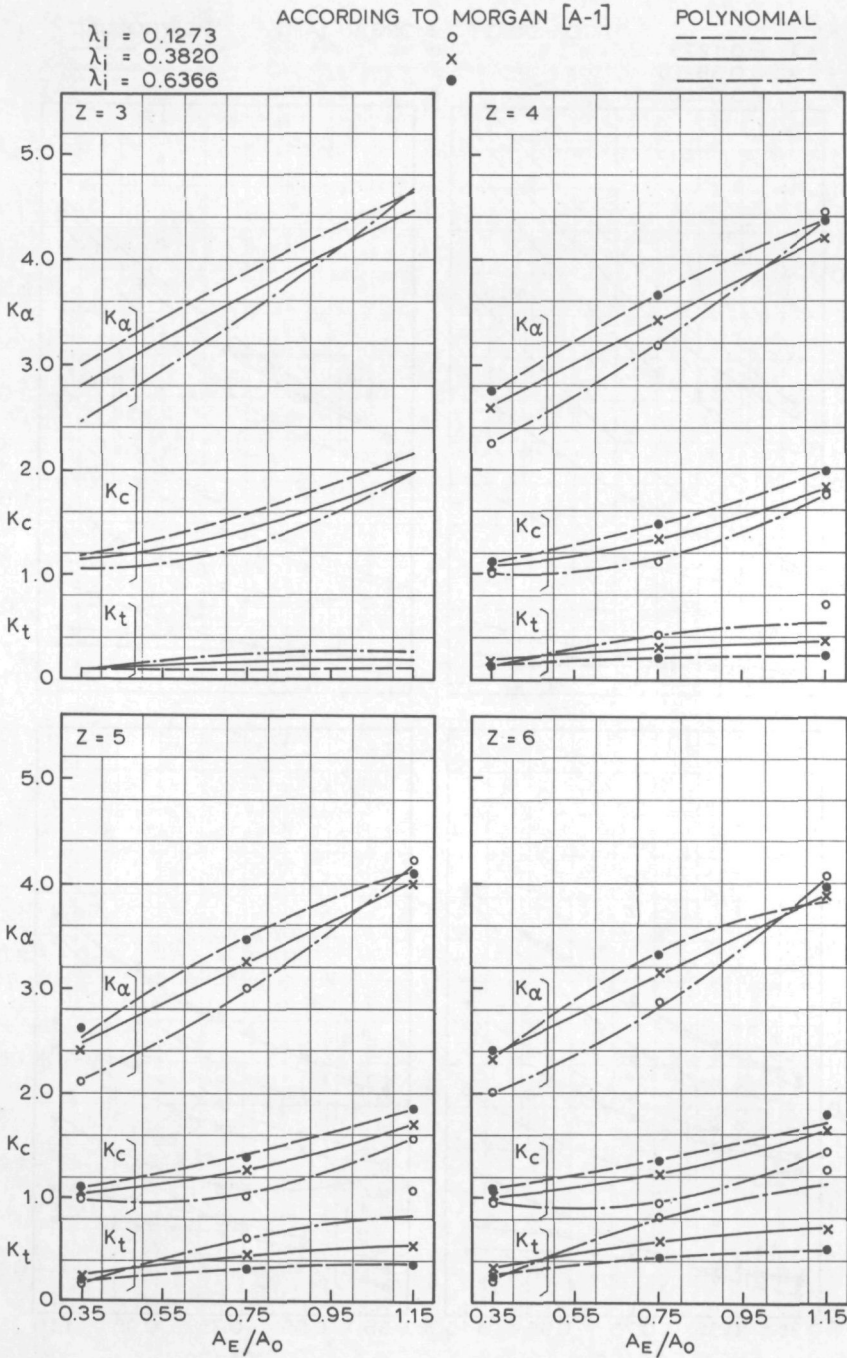


FIG.54 RESULTS OF POLYNOMIALS FOR LIFTING SURFACE CORRECTIONS FOR  $x = 0.4$  AND  $\theta_{Sx} = 0.0197$ .

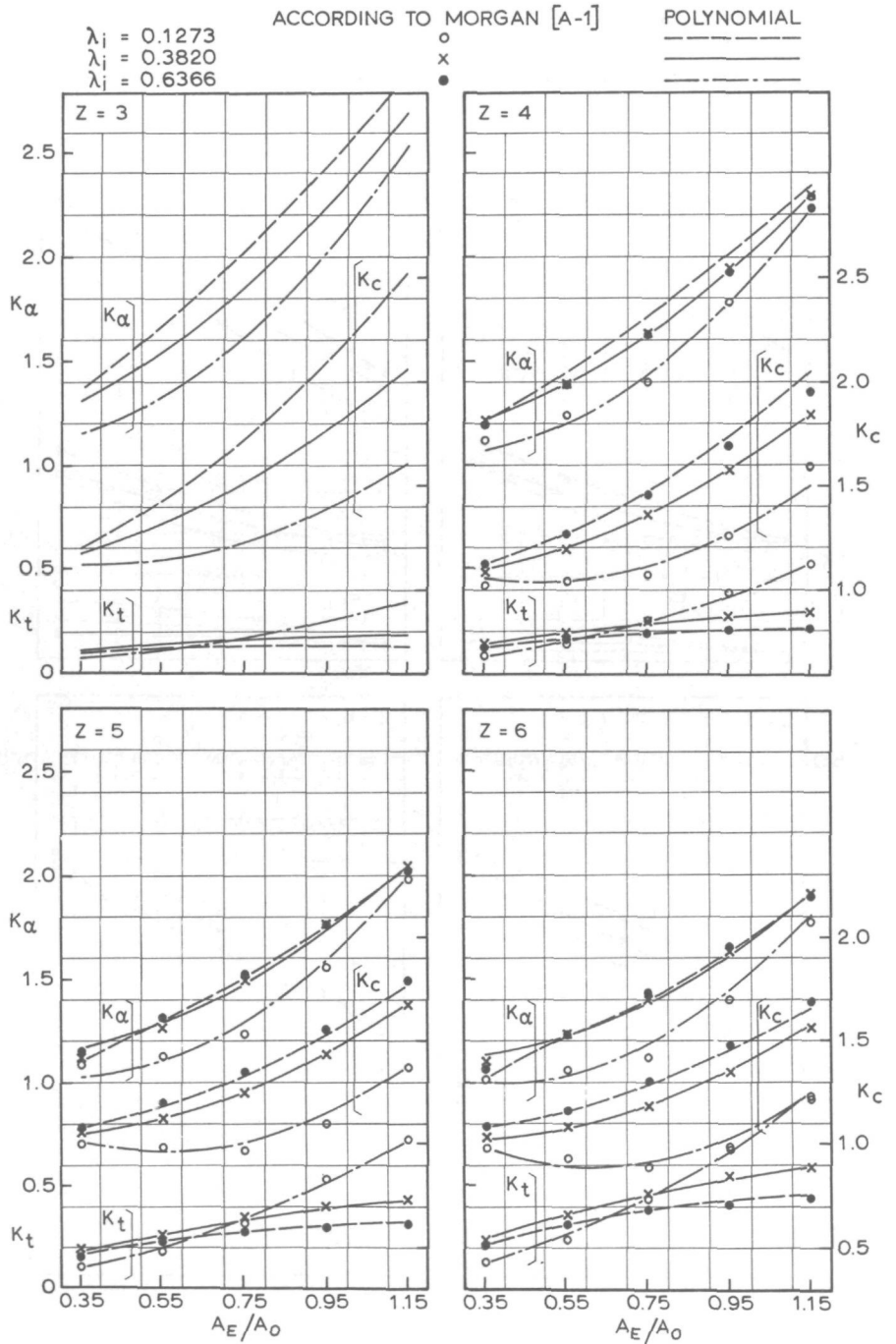


FIG.55 RESULTS OF POLYNOMIALS FOR LIFTING SURFACE CORRECTIONS FOR  $x = 0.5$  AND  $\theta_{Sx} = 0$ .

$\lambda_i = 0.1273$   
 $\lambda_j = 0.3820$   
 $\lambda_k = 0.6366$

ACCORDING TO MORGAN [A-1]

POLYNOMIAL

○  
 x  
 ●

-----  
 \_\_\_\_\_  
 - - - - -

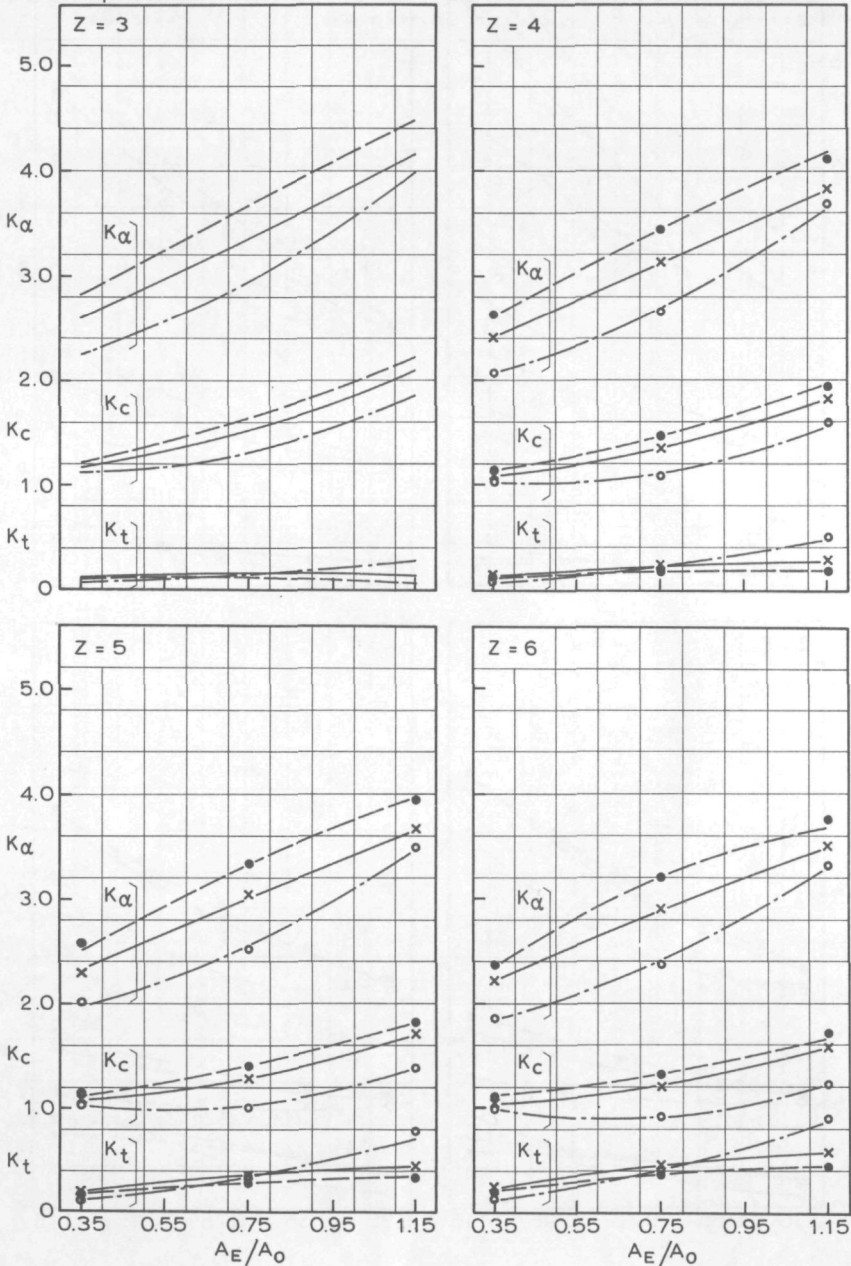


FIG.56 RESULTS OF POLYNOMIALS FOR LIFTING SURFACE CORRECTIONS FOR  $x = 0.5$  AND  $\theta_{Sx} = 0.0449$ .

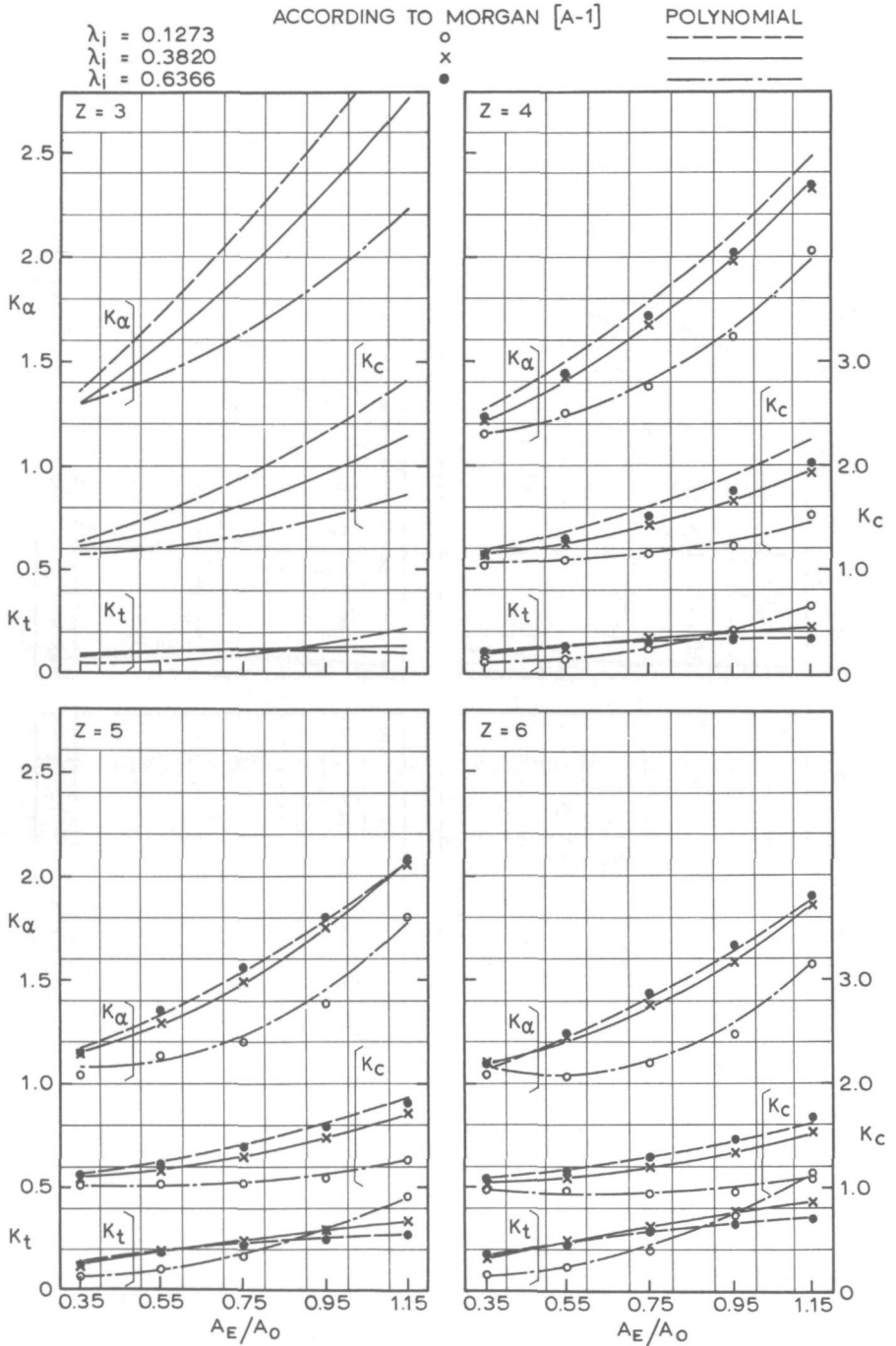


FIG.57 RESULTS OF POLYNOMIALS FOR LIFTING SURFACE CORRECTIONS FOR  $x = 0.6$  AND  $\theta_{Sx} = 0$ .



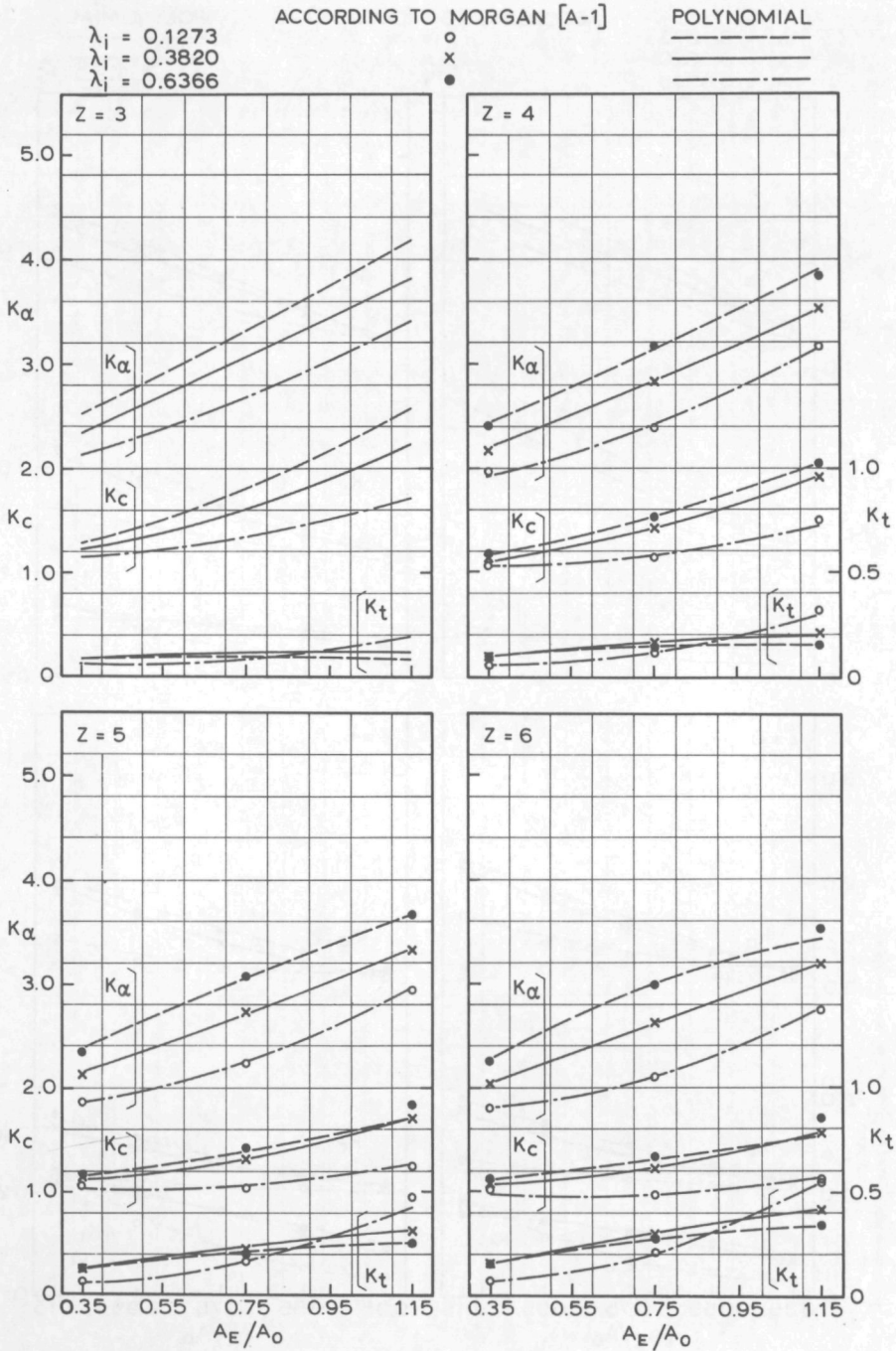


FIG.58 RESULTS OF POLYNOMIALS FOR LIFTING SURFACE CORRECTIONS FOR  $x = 0.6$  AND  $\theta_{Sx} = 0.0812$ .

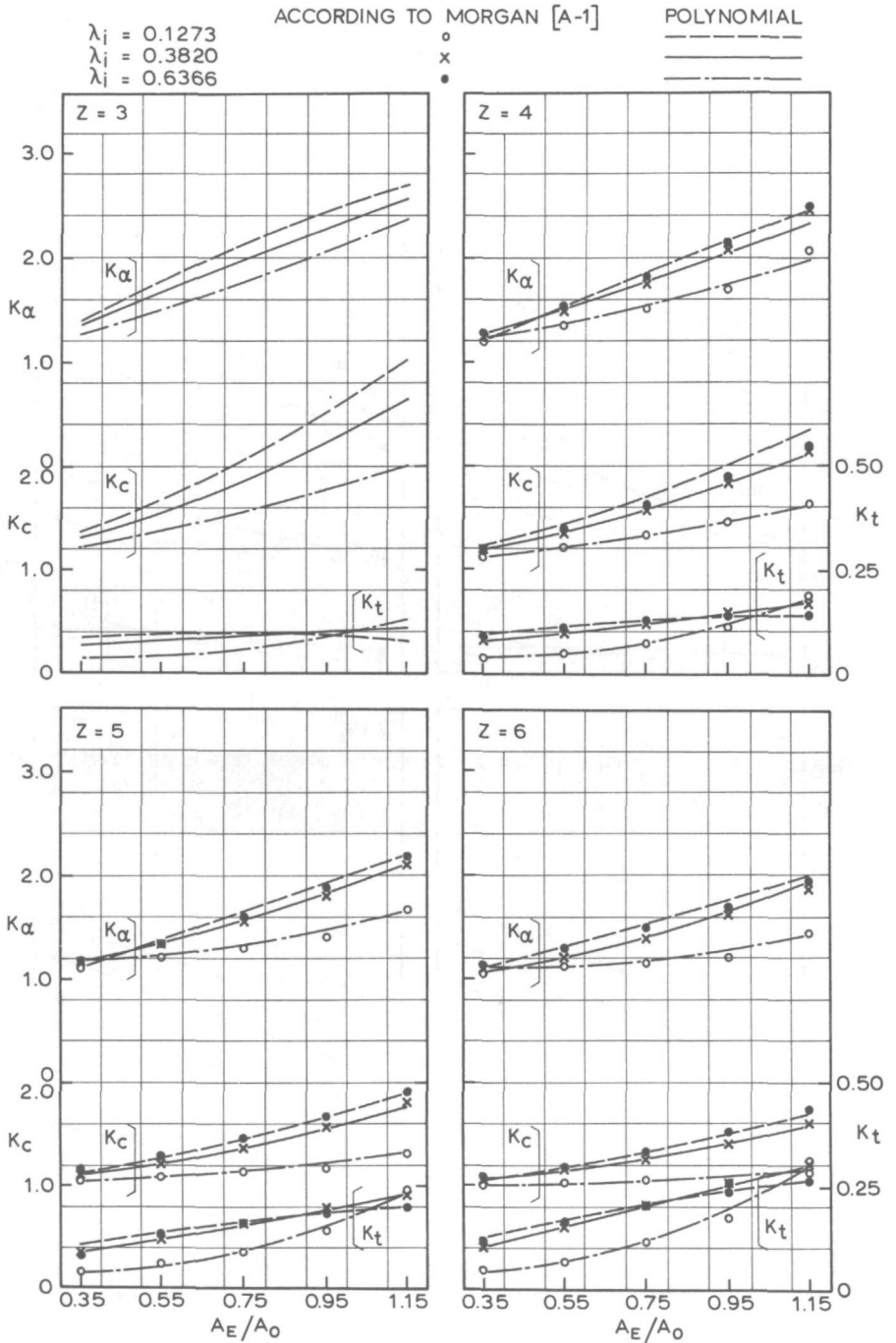


FIG.59 RESULTS OF POLYNOMIALS FOR LIFTING SURFACE CORRECTIONS FOR  $x = 0.7$  AND  $\theta_{SX} = 0$ .

$\lambda_i = 0.1273$   
 $\lambda_j = 0.3820$   
 $\lambda_k = 0.6366$

ACCORDING TO MORGAN [A-1]

○  
 x  
 ●

POLYNOMIAL

---  
 ---  
 ---

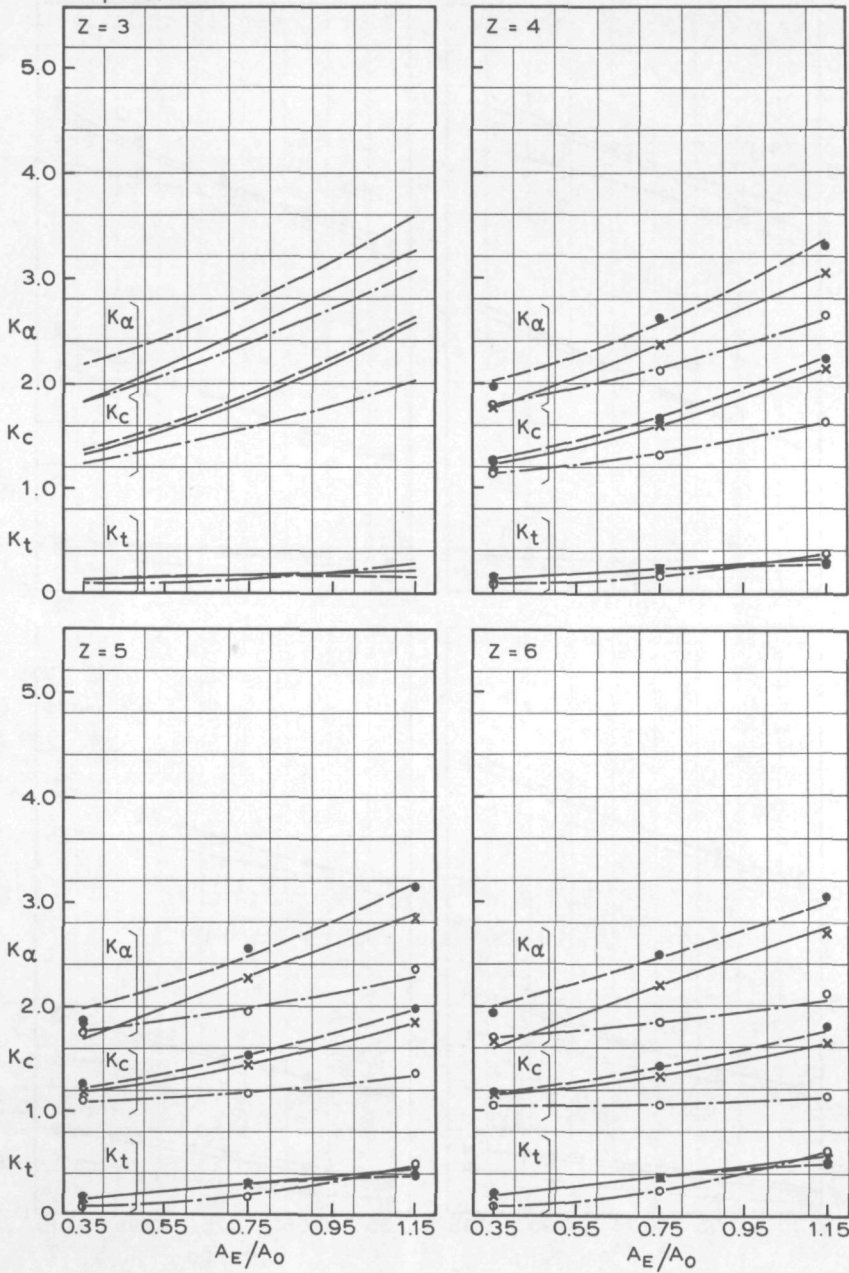


FIG.60 RESULTS OF POLYNOMIALS FOR LIFTING SURFACE CORRECTIONS FOR  $x = 0.7$  AND  $\theta_{Sx} = 0.1301$

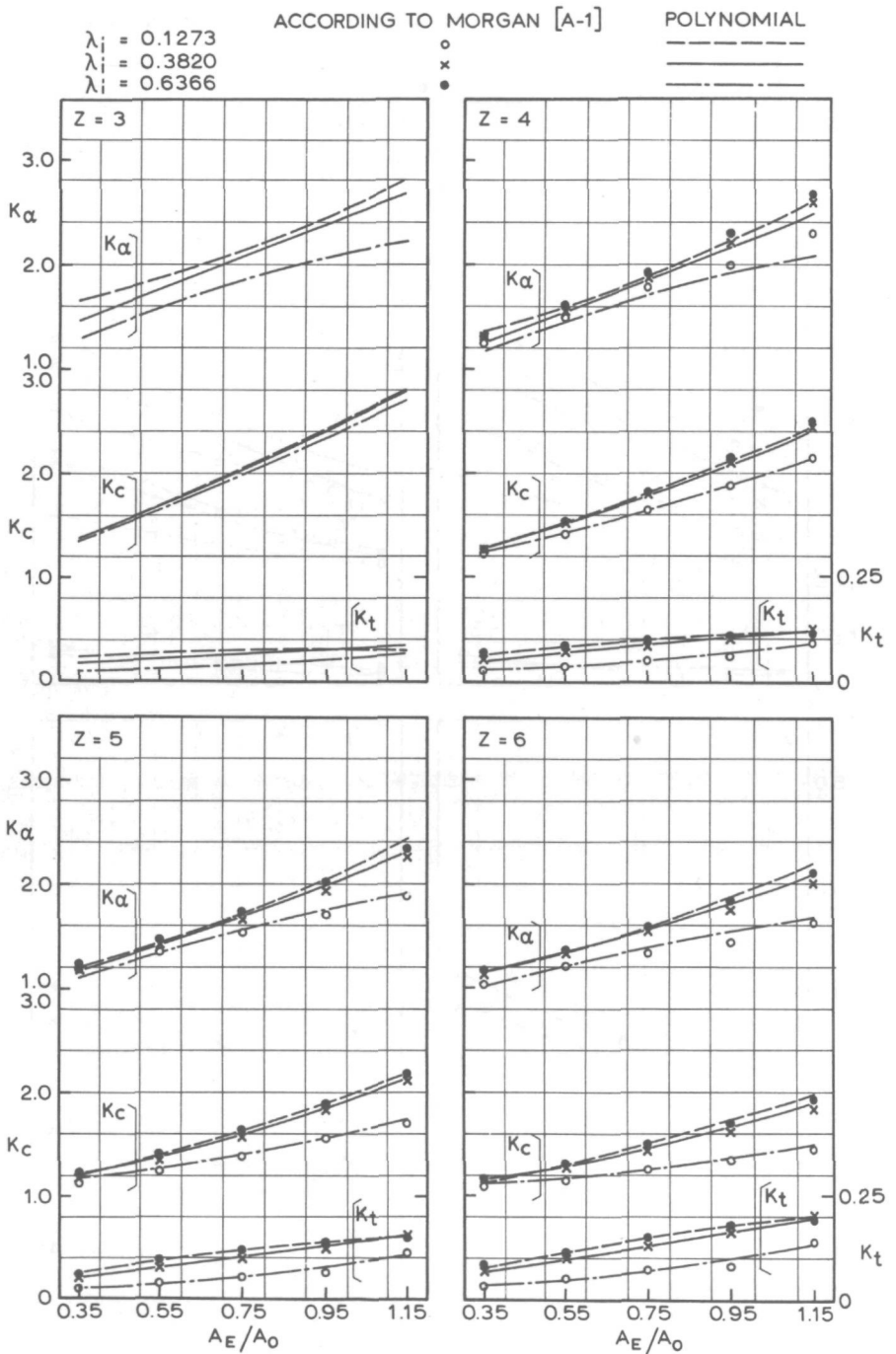


FIG.61 RESULTS OF POLYNOMIALS FOR LIFTING SURFACE CORRECTIONS FOR  $x = 0.8$  AND  $\theta_{Sx} = 0$ .

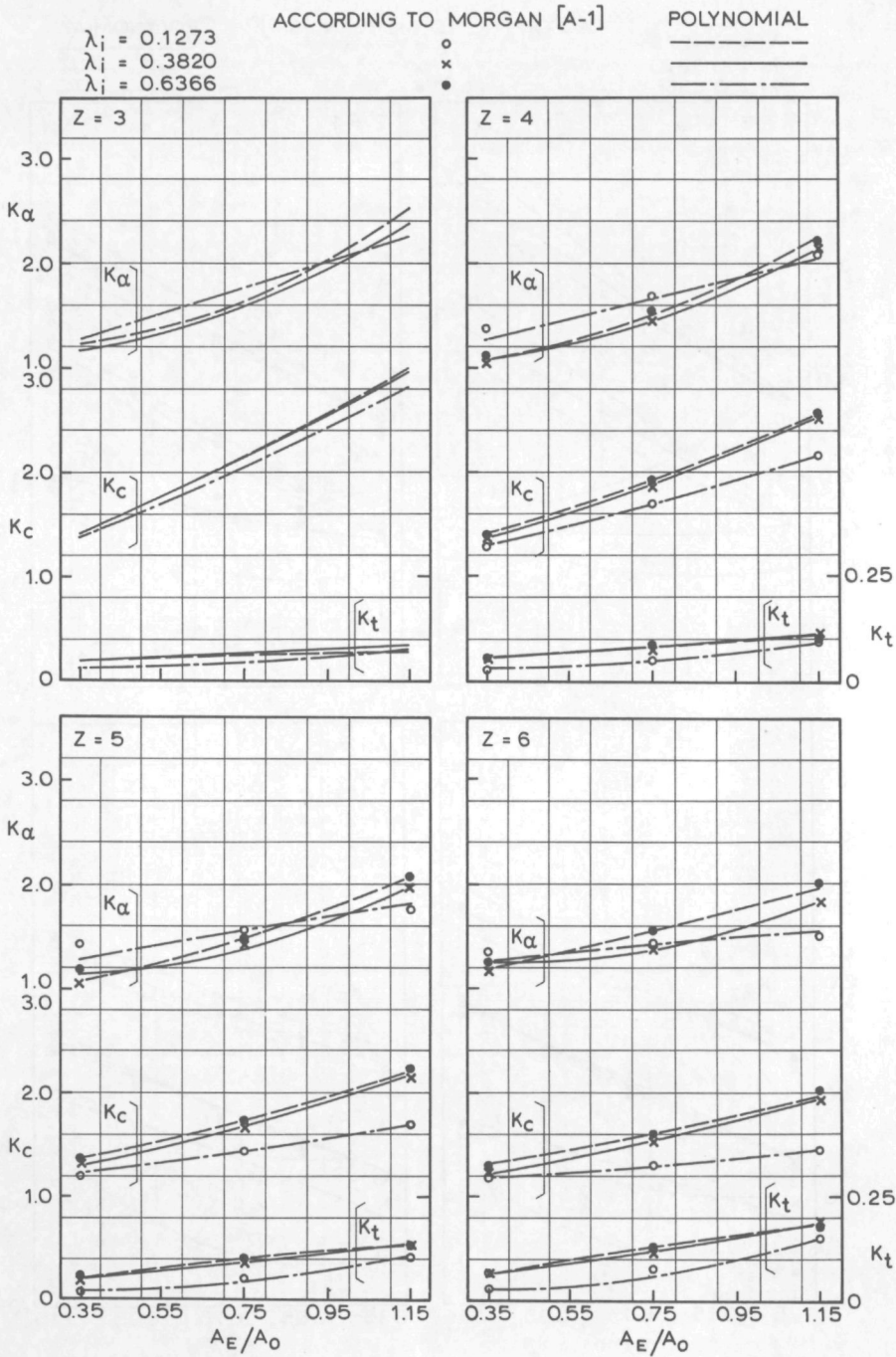


FIG.62 RESULTS OF POLYNOMIALS FOR LIFTING SURFACE CORRECTIONS FOR  $x = 0.8$  AND  $\theta_{Sx} = 0.1938$ .

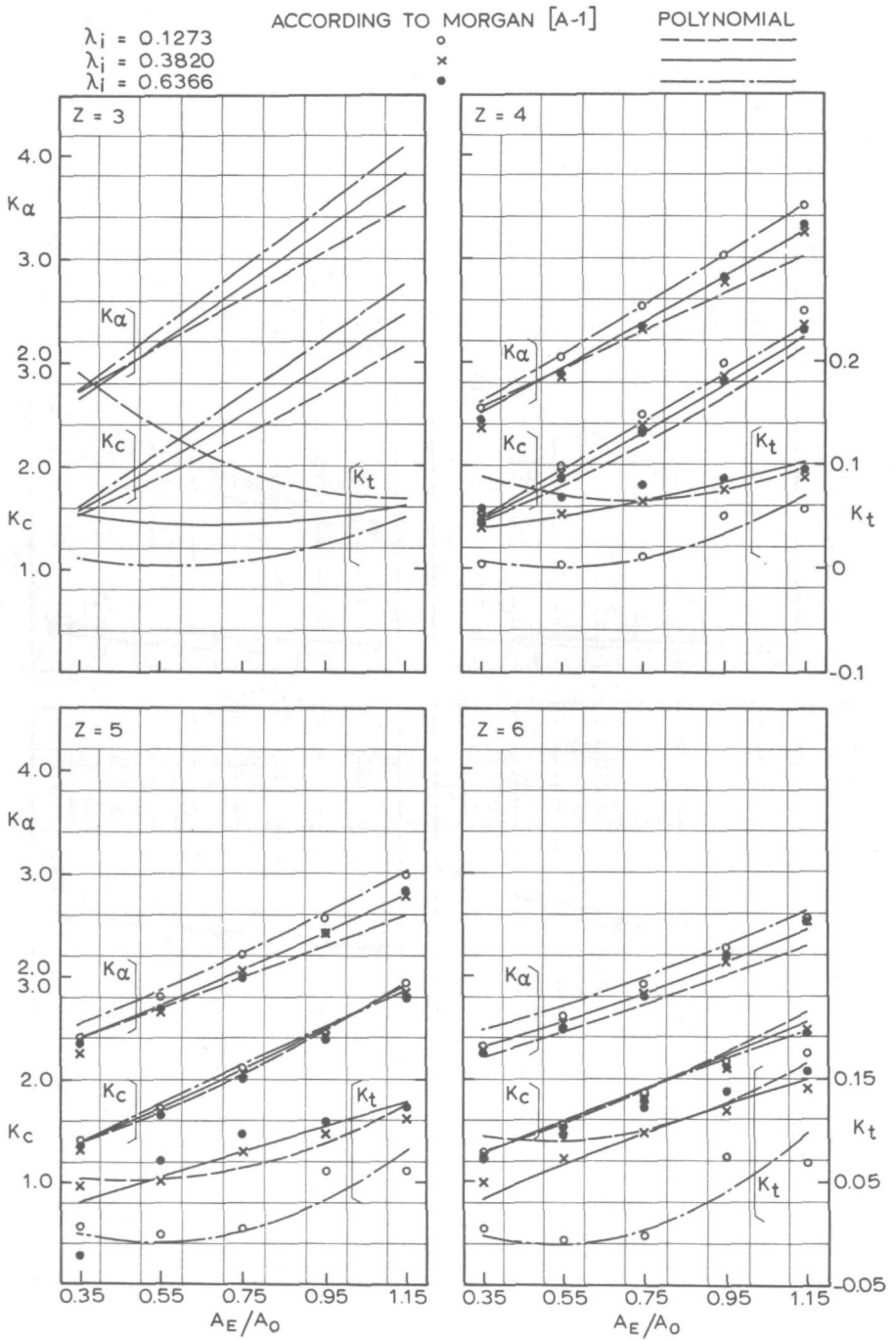


FIG.63 RESULTS OF POLYNOMIALS FOR LIFTING SURFACE CORRECTIONS FOR  $x = 0.9$  AND  $\theta_{Sx} = 0$ .



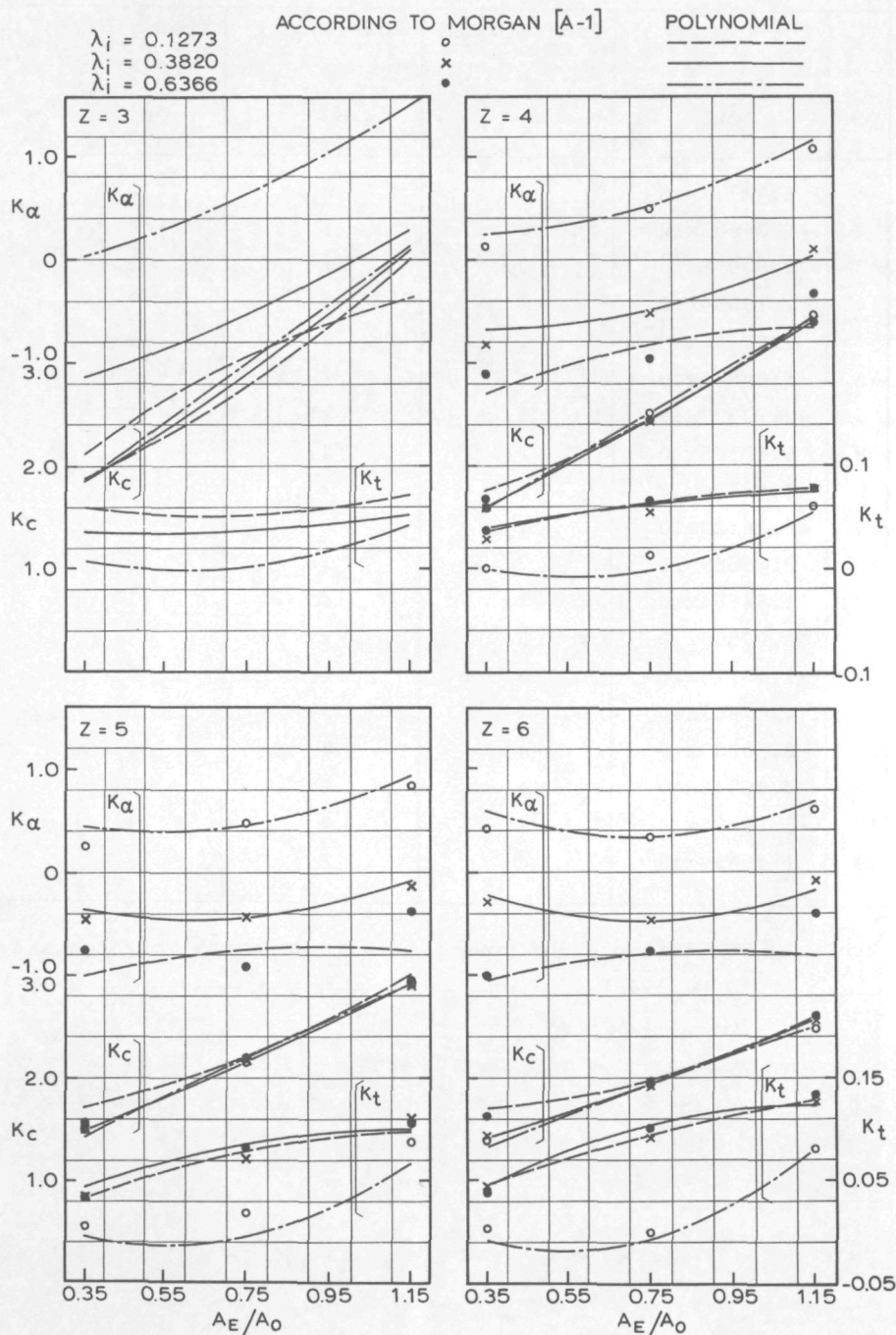


FIG.64 RESULTS OF POLYNOMIALS FOR LIFTING SURFACE CORRECTIONS FOR  $x = 0.9$  AND  $\theta_{Sx} = 0.276$ .

i	Coefficient $c_i$	Powers of x $a_i$	Powers of Z $b_i$	Powers of $(\theta_s)_x$ $d_i$
1	$2.02777 \times 10^0$	0	0	0
2	$1.24905 \times 10^0$	0	1	0
3	$9.82058 \times 10^{-1}$	0	1	1
4	$2.16554 \times 10^{-1}$	0	2	2
5	$7.62355 \times 10^{-1}$	1	0	2
6	$-1.00340 \times 10^1$	1	1	0
7	$-2.72320 \times 10^0$	1	1	1
8	$5.60305 \times 10^{-2}$	1	2	0
9	$-3.08334 \times 10^{-1}$	1	2	1
10	$-3.46120 \times 10^{-1}$	1	2	2
11	$2.45805 \times 10^1$	2	1	0
12	$1.84664 \times 10^0$	2	1	1
13	$6.00509 \times 10^{-1}$	2	2	1
14	$-2.73228 \times 10^1$	3	1	0
15	$4.07967 \times 10^0$	4	0	0
16	$-7.58383 \times 10^{-1}$	4	0	2
17	$1.06848 \times 10^1$	4	1	0
18	$-3.22825 \times 10^{-1}$	4	2	1
19	$1.49636 \times 10^{-1}$	4	2	2

Table 48. Coefficients and powers of  $K_c$ -polynomial for high skews  
( $\lambda_1 = 0.2546$ )

i	Coefficient $c_i$	Powers of x $a_i$	Powers of Z $b_i$	Powers of $(\theta_s)_x$ $d_i$
1	$1.12215 \times 10^1$	0	0	0
2	$1.97422 \times 10^2$	0	0	1
3	$-1.56434 \times 10^{-1}$	0	1	0
4	$-4.02815 \times 10^1$	1	0	0
5	$-8.35271 \times 10^2$	1	0	1
6	$4.75346 \times 10^1$	2	0	0
7	$1.21907 \times 10^3$	2	0	1
8	$-6.09326 \times 10^2$	3	0	1
9	$-1.63664 \times 10^1$	4	0	0
10	$7.36687 \times 10^{-2}$	4	2	2

Table 49. Coefficients and powers of  $K_\alpha$ -polynomial for high skews  
 $(\lambda_i = 0.2546)$

i	Coefficient	Powers of x	Powers of z	Powers of $(\theta_s)_x$
	$c_i$	$a_i$	$b_i$	$d_i$
1	$-2.92330 \times 10^{-1}$	0	0	0
2	$1.96293 \times 10^{-1}$	0	0	1
3	$2.25090 \times 10^{-1}$	0	1	0
4	$-9.74349 \times 10^{-2}$	0	1	2
5	$3.82143 \times 10^{-2}$	0	2	0
6	$-1.68137 \times 10^{-1}$	0	2	1
7	$2.85782 \times 10^{-1}$	0	2	2
8	$3.88645 \times 10^{-1}$	1	0	0
9	$-2.08159 \times 10^{-1}$	1	0	1
10	$-4.31435 \times 10^{-1}$	1	1	0
11	$-8.62862 \times 10^{-2}$	1	2	0
12	$6.44546 \times 10^{-1}$	1	2	1
13	$-8.99078 \times 10^{-1}$	1	2	2
14	$2.66389 \times 10^{-1}$	2	1	0
15	$-8.66308 \times 10^{-1}$	2	2	1
16	$8.57897 \times 10^{-1}$	2	2	2
17	$1.27725 \times 10^{-1}$	3	1	2
18	$9.44608 \times 10^{-2}$	3	2	0
19	$3.96425 \times 10^{-1}$	3	2	1
20	$-9.93084 \times 10^{-2}$	4	1	0
21	$-4.10845 \times 10^{-2}$	4	2	0
22	$-2.59281 \times 10^{-1}$	4	2	2

Table 50. Coefficients and powers of  $K_t$ -polynomial for high skews  
 $(\lambda_i = 0.2546)$

i	Coefficient $c_i$	Powers of x $a_i$	Powers of Z $b_i$	Powers of $(\theta_s)_x$ $d_i$
1	$8.65275 \times 10^0$	0	0	0
2	$9.68244 \times 10^0$	0	0	1
3	$9.49071 \times 10^{-1}$	0	1	2
4	$-2.42277 \times 10^{-2}$	0	2	1
5	$-8.73305 \times 10^{-2}$	0	2	2
6	$-5.14997 \times 10^1$	1	0	0
7	$-4.15264 \times 10^2$	1	0	1
8	$1.34613 \times 10^1$	2	0	0
9	$5.64964 \times 10^1$	2	0	1
10	$-6.72181 \times 10^{-1}$	2	1	0
11	$1.05575 \times 10^{-1}$	2	2	1
12	$-1.48957 \times 10^2$	3	0	0
13	$-2.47538 \times 10^1$	3	0	1
14	$-1.27825 \times 10^1$	3	0	2
15	$1.04036 \times 10^{-1}$	3	2	0
16	$-2.57815 \times 10^{-2}$	3	2	2
17	$6.47761 \times 10^1$	4	0	0
18	$1.14329 \times 10^1$	4	0	2
19	$-7.31471 \times 10^{-1}$	4	1	0
20	$-8.83453 \times 10^{-2}$	4	2	1

Table 51. Coefficients and powers of  $K_C$ -polynomial for high skews  
 $(\lambda_i = 0.382)$

i	Coefficient $c_i$	Powers of x $a_i$	Powers of Z $l_i$	Powers of $(\theta_s)_x$ $d_i$
1	$1.10606 \times 10^1$	0	0	0
2	$2.13273 \times 10^2$	0	0	1
3	$-1.33272 \times 10^{-1}$	0	1	0
4	$-4.06248 \times 10^1$	1	0	0
5	$-8.98589 \times 10^2$	1	0	1
6	$4.88940 \times 10^1$	2	0	0
7	$1.30557 \times 10^2$	2	0	1
8	$-6.49956 \times 10^2$	3	0	1
9	$-1.75252 \times 10^1$	4	0	0
10	$8.88577 \times 10^{-2}$	4	2	2

Table 52. Coefficients and powers of  $K_\alpha$ -polynomial for high skews  
 $(\lambda_i = 0.382)$



i	Coefficient $c_i$	Powers of x $a_i$	Powers of z $b_i$	Powers of $(\theta_s)_x$ $d_i$
1	$6.51655 \times 10^{-2}$	0	0	0
2	$3.56363 \times 10^{-2}$	0	2	0
3	$-7.02449 \times 10^{-2}$	0	2	1
4	$-5.16297 \times 10^{-2}$	1	2	0
5	$2.70219 \times 10^{-1}$	1	2	1
6	$-3.59651 \times 10^{-1}$	2	2	1
7	$1.61209 \times 10^{-1}$	3	2	1
8	$-5.58543 \times 10^{-2}$	4	0	0
9	$1.97056 \times 10^{-2}$	4	2	0

Table 53. Coefficients and powers of  $K_t$ -polynomial for high skews  
 $(\lambda_1 = 0.382)$

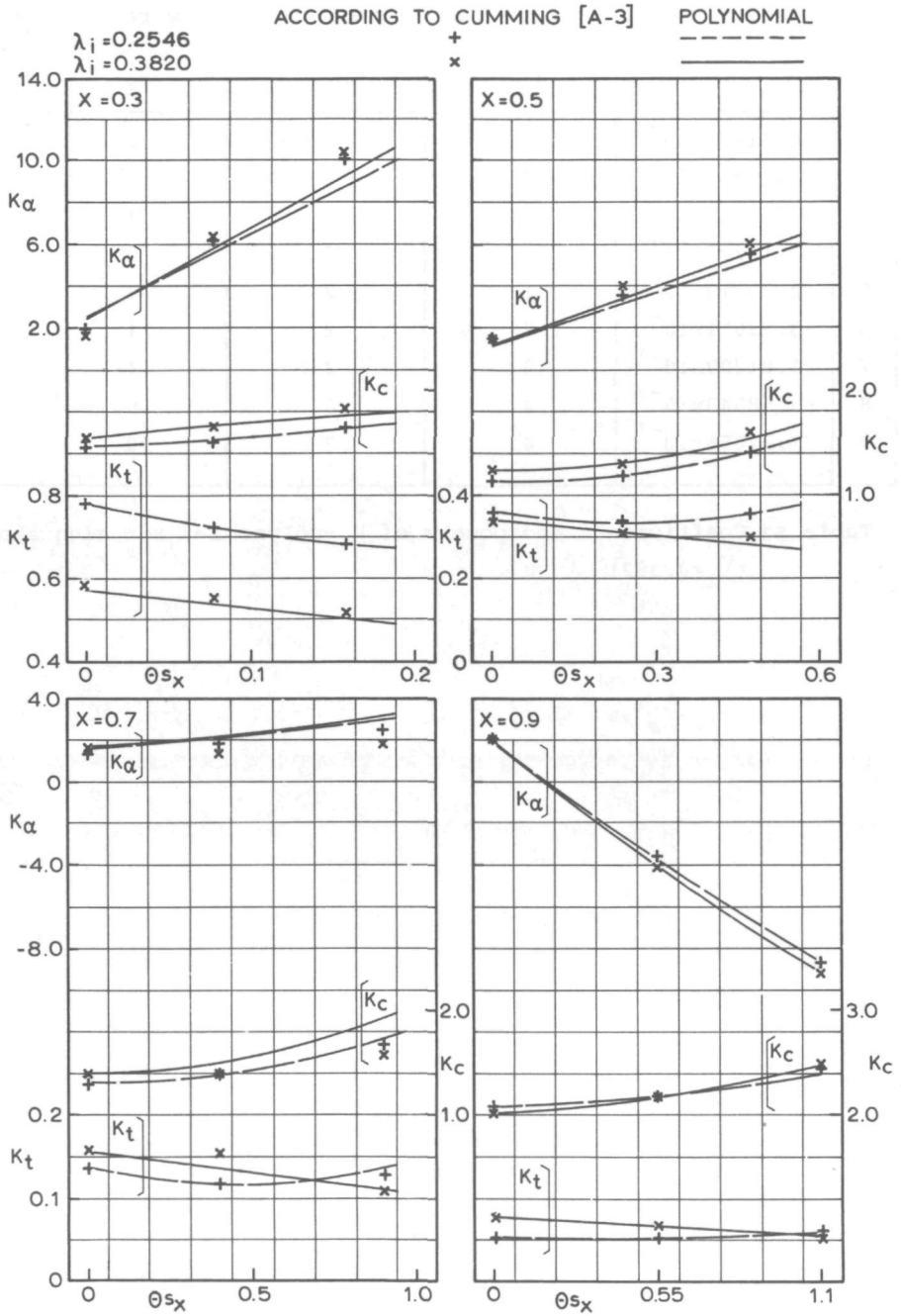


FIG.65 RESULTS OF HIGH SKEW POLYNOMIALS FOR LIFTING CORRECTIONS FOR  $Z=5$  AND  $A_E/A_0=0.75$ .

REFERENCES OF CHAPTER 1

- [1-1] L. Euler; "Théorie plus complète des Machines qui sont mises en mouvement par la réaction de l'eau": Histoire de l'Académie Royale des Sciences et Belles Lettres (Mém. de l'Acad. Tom. X), Berlin, 1754, pp. 277-295.
- [1-2] L.C. Burrill; "Sir Charles Parsons and Cavitation": Trans. of The Institute of Marine Engineers, Vol. LxIII, no. 8, 1951.
- [1-3] O. Reynolds; "The Causes of the Racing of the Engines of Screw Steamers Investigated Theoretically and by Experiment": Trans. Royal Institution of Naval Architects, 1873.
- [1-4] O. Reynolds; "On the Effect of Immersion on Screw Propellers": Trans. Royal Institution of Naval Architects, 1874.
- [1-5] J.I. Thornycroft and J.W. Barnaby; "Torpedo Boat Destroyers": Minute of Proc. of the Institution of Civil Engineers, Vol. 122, part IV, 1894-1895.
- [1-6] L.C. Burrill; "Developments in Propeller Design and Manufacture for Merchant Ships": Trans. of the Institute of Marine Engineers, 1943.
- [1-7] J. auf'm Keller; "Enige aspecten bij het ontwerpen van schepsschroeven": Schip en Werf, No. 24, 1966.
- [1-8] C.A. Parsons and S.S. Cook; "Investigations into the Causes of Corrosion or Erosion of Propellers": Trans. of the Institution of Naval Architects, Vol. 61, 1919.

- [1-9] P. Eisenberg, H.S. Preiser and A. Thiruvengadam; "On the Mechanics of Cavitation Damage and Methods of Protection": Trans. of the Society of Naval Architects and Marine Engineers, Vol. 73, 1965.
- [1-10] J.D. van Manen; "Bent Trailing Edges of Propeller Blades of High Powered Single Screw Ships": International Shipbuilding Progress, January 1963.
- [1-11] J.D. van Manen; "The Effect of Cavitation on the Interaction Between Propeller and Ship's Hull": International Shipbuilding Progress, January 1972.
- [1-12] E. Huse; "Pressure Fluctuations on the Hull Induced by Cavitating Propellers": Norwegian Ship Model Experiment Tank Publication No. 111, March 1972.
- [1-13] P. van Oossanen and J. van der Kooy; "Vibratory Hull Forces Induced by Cavitating Propellers": Trans. Royal Institution of Naval Architects, Vol. 115, 1973.
- [1-14] P. Sabathé et L. Guieysse; "Acoustique Sous-Marine": Dunod Paris, 1964.
- [1-15] P. van Oossanen; "Cavitation Testing of Marine Propellers": Schip en Werf, Vol. 39, no's 13 and 14, 1972.
- [1-16] J. Lockwood-Tayler; "Screw Propeller Theory": Trans. of the North East Coast Institution of Engineers and Shipbuilders, 1942.
- [1-17] L.C. Burrill; "Aerodynamics and Marine Propeller Design": Trans. of the North East Coast Institution of Engineers and Shipbuilders, Vol. 81, 1965.
- [1-18] K. Kafali; "An Investigation of the Pressure Distribution Around the Profiles Suitable for Marine Propellers":

Publication no. 64 of the Swedish State Shipbuilding  
Experimental Tank, 1968.

- [1-19] C.A. Johnsson; "On Theoretical Predictions of  
Characteristics and Cavitation Properties of  
Propellers": Publication no. 64 of the Swedish  
State Shipbuilding Experimental Tank, 1968.
- [1-20] K.O. Holden; "Type and Extent of Cavitation on Hydrofoils  
and Marine Propeller Blades": Det norske Veritas  
Report no. 72-2-M, 1972.
- [1-21] C.A. Johnsson; "Correlations of Predictions and Full  
Scale Observations of Propeller Cavitation":  
International Shipbuilding Progress, June 1973.

REFERENCES OF CHAPTER 2

- [2-1] A.B. Bailey; "The relationship between Flow Separation and Cavitation": Oxford University, Department of Engineering Science, Report No. 1111/70 July, 1970.
  
- [2-2] V.H. Arakeri; "Viscous Effects in Inception and Development of Cavitation on Axi-Symmetric Bodies": California Institute of Technology, Engineering and Applied Science Division, Report No. Eng. 183-1, January 1973.
  
- [2-3] P. van Oossanen; "Profile Characteristics in Cavitating and Non-Cavitating Flows": International Shipbuilding Progress, March 1971.
  
- [2-4] G. Kuiper; "Some Remarks on Lifting Surface Theory": International Shipbuilding Progress, Vol. 18, No. 199, 1971.
  
- [2-5] Wm.B. Morgan, V. Silovic and S.B. Denny; "Propeller Lifting Surface Corrections": Trans. Society of Naval Architects and Marine Engineers, Vol.76, 1968.
  
- [2-6] S. Tsakonas, C.Y. Cheng and W.T. Jacobs; "Unsteady Lifting Surface Theory for a Marine Propeller of Low Pitch Angle Distribution": Journal of Ship Research, Vol. 9, September 1965.
  
- [2-7] S. Tsakonas, W.R. Jacobs and P. Rank; "Unsteady Propeller Lifting Surface Theory with Finite Number of Chordwise Modes": Journal of Ship Research, Vol. 12, March 1968.
  
- [2-8] S. Tsakonas; "An Exact Linear Lifting-Surface Theory for a Marine Propeller in a Non-Uniform Flow Field":



Journal of Ship Research, Vol. 17, No. 4, Dec. 1973.

- [2-9] P. Verbrugh; "Unsteady Lifting Surface Theory for Ship Screws": Report no. 68-036-AH of the Netherlands Ship Model Basin, April 1968.
  
- [2-10] G. Kuiper; "Some Preliminary Results of an Exact Treatment of the Linearized Lifting Surface Integral Equation": Netherlands Ship Model Basin, Report no. 69-108-SP, 1969.
  
- [2-11] W. van Gent; "Unsteady Lifting Surface Theory for Ship Screws": To be published.
  
- [2-12] J.L. Hess and A.M.O. Smith; "Calculation of Potential Flow about Arbitrary Three-dimensional Lifting Bodies": Douglas Aircraft Company, Report no. MDC J5679-01, 1972.
  
- [2-13] O.W. Höiby; "Three-Dimensional Effects in Propeller Theory": Norwegian Ship Model Experiment Tank, Publication No. 105, May 1970.
  
- [2-14] K.O. Holden; "Type and Extent of Cavitation on Hydrofoils and Marine Propeller Blades": Det Norske Veritas, Report No. 72-2M, 1972.
  
- [2-15] C.A. Johnsson and T. Sjøntvedt; "Propeller Excitation and Response of 230.000 TDW Tankers": Det Norske Veritas, Publication No. 79, November 1972.
  
- [2-16] D. Küchemann; "A simple Method for Calculating the Span and Chordwise Loading on Straight and Swept Wings of any Given Aspect Ratio at Subsonic Speeds": Aeronautical Research Council, R&M. No. 2935, London, 1956.

- [2-17] J. Weber; "The Calculation of the Pressure Distribution over the Surface of Two-Dimensional and Swept Wings with Symmetrical Aerofoil Sections": Aeronautical Research Council, R&M. No. 2918, London 1956.
- [2-18] C.A. Johnsson; "Pressure Fluctuations Around a Marine Propeller: Results of Calculations and Comparison with Experiment": Publication no. 69 of the Swedish State Shipbuilding Experimental Tank, 1971.
- [2-19] S. Tsakonas and W.R. Jacobs; "Theoretical Calculations of Vibratory Thrust and Torque and Comparisons with Experimental Measurements": Stevens Institute of Technology, Davidson Laboratory Report No. 827, February 1961.
- [2-20] B. Vedeler; "On Marine Propeller Forces in Calm Water and Waves and the Strength of Propeller Shaft Systems in Single Screw Ships": Det Norske Veritas Report 68-12-M, 1968.
- [2-21] H. Tanibayashi; "Practical Approach to Unsteady Problems of Propellers": International Shipbuilding Progress, 1973.
- [2-22] C.F.L. Kruppa; "High Speed Propellers": Report of the University of Michigan, 1967.
- [2-23] V.E. Johnson, R.A. Barr. A. Thiruvengadam and A. Goodman; "Ship Cavitation Research at Hydronautics, Incorporated": Symposium on Testing Techniques in Ship Cavitation Research, Trondheim, 1967.
- [2-24] H.W. Lerbs; "Moderately Loaded Propellers with a Finite Number of Blades and an Arbitrary Distribution of Circulation": Trans. of the Society of Naval Architects and Marine Engineers, Vol. 60, 1952.

- [2-25] A. Betz; "Screw Propellers with Minimum Loss of Kinetic Energy": Reprinted in Vier Abhandlungen zur Hydro- und Aerodynamik by L. Prandtl and A. Betz, 1929.
- [2-26] S. Goldstein; "On the Vortex Theory of Screw Propellers": Proceedings of the Royal Society (London), Series A, Vol. 63, 1929.
- [2-27] C.N.H. Lock and D. Yeatman; "Tables for Use in an Improved Method of Airscrew Strip Theory Calculation": Reports and Memoranda no. 1674, Aeronautical Research Council, Her Majesty's Stationary Office, London, 1935.
- [2-28] K.N. Kramer; "Weiterführung von Goldsteins Lösung des Optimalproblems für Schraubenpropeller": Deutsche Versuchsanstalt für Luftfahrt, 1941.
- [2-29] S. Kawada; "On the Induced Velocity and Characteristics of a Propeller": Journal of the Faculty of Engineering, Tokyo, Imperial University, Vol.20,1933.
- [2-30] S. Kawada; "Induced Velocity by Helical Vortices": Journal of the Aeronautical Sciences, Vol.3, 1936.
- [2-31] J.W. Wrench; "The Calculation of Propeller Induction Factors": David Taylor Model Basin, Report no.1116, 1957.
- [2-32] C.A. Johnsson; "On Theoretical Predictions of Characteristics and Cavitation Properties of Propellers": Publication no. 64 of the Swedish State Shipbuilding Experimental Tank, 1968.
- [2-33] O.W Höiby; "Three-Dimensional Effects in Propeller Theory": Norwegian Ship Model Experiment Tank, Publication No. 105, May 1970.

- [2-34] W.R. Sears; "Some Aspects of Non-Stationary Airfoil Theory and its Practical Application": Journal of the Aeronautical Sciences, Vol. 8, no. 3, January 1941.
- [2-35] T. Sjøntvedt; "Theoretical Calculations of Hydrodynamic Loading on the Marine Propeller, Part I, Open-Water Performance": Det norske Veritas, Report no. 71-64-M, 1971.
- [2-36] L.C. Burrill; "Calculation of Marine Propeller Performance Characteristics": Trans. of the North East Coast Institution of Engineers and Shipbuilders, Vol. 60, 1944.
- [2-37] K. Minsaas and O.H. Slattelid; "Lifting Surface Corrections for 3 Bladed Optimum Propellers": International Shipbuilding Progress, Vol. 18, No. 208, Dec. 1971, pp. 437-452.
- [2-38] R.A. Cumming, Wm.B. Morgan and R.J. Boswell; "Highly Skewed Propellers": Trans. Society of Naval Architects and Marine Engineers, Vol. 80, 1972.
- [2-39] J.D. van Manen; "On the Usefulness of a Test with a Propeller Model in a Cavitation Tunnel": Symposium on Testing Techniques in Ship Cavitation Research, Trondheim, 1967.
- [2-40] B. Thwaites; "Incompressible Aerodynamics": The Clarendon Press, 1960.
- [2-41] J.A. Geurst; "Linearized theory of two-dimensional cavity flows": Thesis, Delft, Technological University, 1961.
- [2-42] T. Theodorsen and I.E. Garrick; "General Potential Theory of Arbitrary Wing Sections": National Advisory Committee for Aeronautics, Report no. 452, 1933.

- [2-43] Krakowiak, Bindel and Brard; "Un programme algol pour le calcul de la repartition de pression sur un profil en courant uniforme": Bassin D'Essais Des Carèennes, Report no. 91306 BA-N-CM, 1954.
- [2-44] S. Goldstein; "Low-Drag and Suction Airfoils": Journal of the Aeronautical Sciences, Vol. 15, no. 4, april 1948.
- [2-45] E.J. Watson; "Formulae for the computation of the functions employed for calculating the velocity distribution about a given aerofoil": Rep.Memor. aero.Res.Coun.,London 2176, 1945.
- [2-46] I.H. Abbott and A.E. Von Doenhoff; "Theory of Wing Sections": Dover Publications, Inc. 1958.

REFERENCES OF CHAPTER 3

- [ 3-1 ] T. Theodorsen; "Theory of Wing Sections of Arbitrary Shape": National Advisory Committee for Aeronautics, Report no. 411, 1932
  
- [ 3-2 ] F.W. Riegels; "Aerofoil Sections": Butterworths, London 1961.
  
- [ 3-3 ] I.H. Abbott and A.E. Von Doenhoff; "Theory of Wing Sections": Dover Publications, Inc. 1958.
  
- [ 3-4 ] L.C. Burrill; "Calculation of Marine Propeller Performance Characteristics": Trans. North East Coast Institution of Engineers and Shipbuilders, Vol. 60, 1943-44.
  
- [ 3-5 ] J.G. Hill; "The Design of Propellers": SNAME, Vol. 57, 1949
  
- [ 3-6 ] P. van Oossanen; "Profile Characteristics in Cavitating and Non-Cavitating Flows": International Shipbuilding Progress, March 1971.
  
- [ 3-7 ] T.P. O'Brien; "Marine Screw Propellers": Hutchinson Scientific and Technical, London, 1962.
  
- [ 3-8 ] T. Sjøntvedt; "Theoretical Calculations of Hydrodynamic Loading on the Marine Propeller, Part I, Open-Water Performance": Det norske Veritas, Report no. 71-64-M, 1971
  
- [ 3-9 ] E.J. Glover; "A Design Method for the Heavily Loaded Marine Propeller": Paper issued by the Royal Institution of Naval Architects, 1973.



- [3-10] B. Thwaites; "Incompressible Aerodynamics": The Clarendon Press, 1960.
- [3-11] N. Curle and S.W. Skan; "Approximate Methods for Predicting Separation Properties of Laminar Boundary Layers": Aeronautical Quarterly 8, 257, 1957.
- [3-12] R. Michel; "Etude de la Transition sur les Profils d'Aile-Etablissement d'un Point de Transition et Calcul de la Traînée de Profil en Incompressible": Onera, Rapport 1/1578A, July 1951.
- [3-13] A.M.O. Smith; "Transition, Pressure Gradient, and Stability Theory": Proceedings of 9th International Congress of Applied Mechanics, Brussels, Belgium, Vol. 4, p. 234, 1956.
- [3-14] J.F. Nash and Miss A.G.J. Macdonald; "The Calculation of Momentum Thickness in a Turbulent Boundary Layer at Mach Numbers up to Unity": Aeronautical Research Council, C.P. No.963, 1967.
- [3-15] J.F. Nash; "Turbulent-boundary-layer Behaviour and the Auxiliary equation": AGARDograph 97. Aeronautical Research Council, C.P. 835, February 1965.
- [3-16] J.F. Nash and A.G.J. Macdonald; "A Turbulent Skin-Friction Law for Use at Subsonic and Transonic Speeds": Aeronautical Research Council, C.P.948, July 1966.
- [3-17] D.J. Hall and J.C. Gibbings; "Influence of Stream Turbulence and Pressure Gradient upon Boundary Layer Transition": Journal Mechanical Engineering Science, Vol. 14, No. 2, 1972.

- [3-18] C.A. Johnsson; "Pressure Fluctuations around a Marine Propeller: Results of Calculations and Comparison with Experiment": The Swedish State Shipbuilding Experimental Tank, Publ.No.69, 1971.
- [3-19] D.E. Cummings; "Numerical Prediction of Propeller Characteristics": Journal of Ship Research, March 1973.
- [3-20] T. Cebeci and A.M.O. Smith; "Calculation of Profile Drag of Airfoils at Low Mach Numbers": Journal of Aircraft, Vol. 5, No. 6, 1968.
- [3-21] M.W.C. Oosterveld and P. van Oossanen; "Recent Developments in Marine Propeller Hydrodynamics": Paper presented at International Jubilee Meeting on the Occasion of the 40th Anniversary of the Netherlands Ship Model Basin, August 30-September 1, 1972.
- [3-22] M.W.C. Oosterveld and P. van Oossanen; "Representation of Propeller Characteristics Suitable for Preliminary Ship Design Studies": International Conference on Computer Applications in Shipbuilding, Tokyo, 1973.
- [3-23] H.W. Lerbs; "On the Effect of Scale and Roughness on Free Running Propellers": Journal of the American Society of Naval Engineers, Inc. Vol. 63, no. 1, February 1951.
- [3-24] S.F. Hoerner; "Fluid Dynamic Drag": Published by the Author, 1971.
- [3-25] M.A. Efroymsen; "Multiple Regression Analysis": Numerical Methods, Vol. I, edited by Ralston and Wilf, Wiley 1959.

- [3-26] R.M. Pinkerton; "Calculated and Measured Pressure Distributions over the Midspan Section of the NACA 4412 Airfoil": National Advisory Committee for Aeronautics, Rep.no. 563, 1936.

REFERENCES OF CHAPTER 4

- [4-1] E.N. Harvey, W.D. McElroy and A.H. Whitely; "On Cavity Formation in Water": Journal Applied Physics, 18, no. 2, 1947.
- [4-2] R.T. Knapp, J.W. Daily and F.G. Hammitt; "Cavitation": McGraw-Hill Book Company 1970.
- [4-3] V.H. Arakeri; "Viscous Effects in Inception and Development of Cavitation on Axi-Symmetric Bodies": California Institute of Technology, Engineering and Applied Science Division, Report No. Eng. 183-1, January 1973.
- [4-4] A.J. Alexander; "An Investigation of the Relationship Between Flow Separation and Cavitation": National Physical Laboratory, TM 230, November 1968.
- [4-5] A.B. Bailey; "The relationship between Flow Separation and Cavitation": Oxford University, Department of Engineering Science, Report No. 1111/70, July 1970.
- [4-6] B.R. Parkin and J.W. Holl; "Incipient-Cvitation Scaling Experiments for Hemispherical and 1.5 Calibre Ogive-Nosed Bodies": Report Nord 7958-264, Ordnance Research Laboratory, The Pennsylvania State University, May 1954.
- [4-7] R.M. Pinkerton; "Calculated and Measured Pressure Distributions over the Midspan Section of the NACA 4412 Airfoil": National Advisory Committee for Aeronautics, Rep.no. 563, 1936.
- [4-8] J.W. Daily; "Force and Cavitation Characteristics of the NACA 4412 Hydrofoil": California Institute of Technology, HML No. ND-19, June 1944. See also

"Cavitation Characteristics and Infinite Aspect Ratio Characteristics of a Hydrofoil Section": Trans. American Society of Mechanical Engineers, Vol. 71, pp. 269-284, April 1949.

- [4-9 ] R.W. Kermeen; "Water Tunnel Tests of NACA 4412 and Walchner Profile 7 Hydrofoils in Noncavitating and Cavitating Flows": California Institute of Technology, Report No. 47-5, February 1956.
- [4-10] R.W. Kermeen; "Water Tunnel Tests of NACA 66, -012 Hydrofoil in Noncavitating and Cavitating Flows": California Institute of Technology, Report No. 47-7, February 1956.
- [4-11] A.M.O. Smith; "Transition, Pressure Gradient, and Stability Theory": Proceedings of 9th International Congress of Applied Mechanics, Brussels, Belgium, Vol. 4, p.234, 1956.
- [4-12] T. Cebeci, G.J. Mosinskis and A.M.O. Smith; "Calculation of Viscous Drag of Two-Dimensional and Axisymmetric Bodies in Incompressible Flows": American Institute of Aeronautics and Astronautics, Paper No. 72-1, 1972.
- [4-13] C.A. Johnsson and T. Sjøntvedt; "Propeller Excitation and Response of 230.000 TDW Tankers": Det Norske Veritas, Publication No. 79, November 1972.
- [4-14] J.D. van Manen; "On the Usefulness of a Test with a Propeller Model in a Cavitation Tunnel": Symposium on Testing Techniques in Ship Cavitation Research, Trondheim, 1967.
- [4-15] D.K. Brown; "Air Content, Surface Tension and Cavitation Inception": Admiralty Experiment Works, Technical

Memorandum, No. 7/73, March 1973.

- [4-16] A.P. Keller; "Investigations Concerning the Modeling of Flow Cavitation": University of Michigan, Report No. UMICH 01357-28-T, March 1973.
- [4-17] J.W. Holl; "The Estimation of the Effect of Surface Irregularities on the Inception of Cavitation": American Society of Mechanical Engineers, Symp. on Cavitation in Fluid Machinery, G.M. Wood et al, (editors), 1965.
- [4-18] R.T. Knapp; "Cavitation Mechanics and Its Relation to the Design of Hydraulic Equipment": Proceedings Institute Mechanical Engineers (London), A, 166, 150-163, 1952.
- [4-19] Lord Rayleigh; "On the Pressure Developed in a Liquid During the Collapse of a Spherical Cavity": Philosophical Magazine, 34, 94-98, August 1917.
- [4-20] O. Walchner; "Contributions to the Design of Ship Propellers without Cavitation": M.A.P. Völkenrode, A.V.A. Monographs.
- [4-21] J. Balhan; "Metingen aan enige bij Scheepsschroeven Gebruikelijke Profielen in Vlakke Stroming met en zonder Cavitatie": Doctor's Thesis 1951. Delft. Publ.no. 99 of the Netherlands Ship Model Basin.
- [4-22] P. van Oossanen; "Report on Experiments with Typical Screw Propeller Type Sections in Cavitating and Non-Cavitating Flow": Report of the Netherlands Ship Model Basin, No. W.O. 179, December 1969.
- [4-23] P. van Oossanen; "Profile Characteristics in Cavitating and Non-Cavitating Flows": International



Shipbuilding Progress, March 1971.

- [4-24] W.P.A. van Lammeren, J.D. van Manen and M.W.C. Oosterveld; "The Wageningen B-Screw Series": Trans. Society of Naval Architects and Marine Engineers, Vol. 77, 1969.
- [4-25] J.A. Geurst; "Linearized Theory of Two-Dimensional Cavity Flows": Delft University of Technology, 1961.
- [4-26] T. Hanaoka; "Linearized Theory of Cavity Flow Past a Hydrofoil of Arbitrary Shape": Journal Society of Naval Architects of Japan, Vol. 115, 1964.
- [4-27] F. Gutsche; "Sammlung und Auswertung von Unterlagen über Kavitation und Theoretische Propellerberechnung": Schiffbauforschung, Heft 1, 1962.
- [4-28] F. Gutsche; "Der Einfluss der Kavitation auf die Profileigenschaften von Propellerblattschnitten": Schiffbauforschung, Heft 1, 1962.
- [4-29] O. Walchner; "Profilmessungen bei Kavitation. Hydromechanische Probleme des Schiffsantriebes": Hamburgische Schiffsbau-Versuchsanstalt, 1932, S.256.
- [4-30] H.P. Rader; Discussion on Session 5 (Papers 15, 16, 17), Symposium on Cavitation in Hydrodynamics, National Physical Laboratory Teddington, England. September 1955.

REFERENCES OF CHAPTER 5

- [5-1] M.W.C. Oosterveld and P. van Oossanen. "Recent Developments in Marine Propeller Hydrodynamics": Paper presented at International Jubilee Meeting on the Occasion of the 40th Anniversary of the Netherlands Ship Model Basin, August 30-September 1, 1972.
- [5-2] W. van Gent and P. van Oossanen; "Influence of Wake on Propeller Loading and Cavitation": Paper held at Second Lips Propeller Symposium, Drunen, Holland, 1973. See also International Shipbuilding Progress, 1973.
- [5-3] Wm.B. Morgan, V. Silovic and S.B. Denny; "Propeller Lifting Surface Corrections": Trans. Society of Naval Architects and Marine Engineers, Vol. 76, 1968.
- [5-4] R.A. Cumming, Wm.B. Morgan and R.J. Boswell; "Highly Skewed Propellers": Trans. Society of Naval Architects and Marine Engineers, Vol. 80, 1972.
- [5-5] M.W.C. Oosterveld and P. van Oossanen; "Representation of Propeller Characteristics Suitable for Preliminary Ship Design Studies": International Conference on Computer Applications in Shipbuilding, Tokyo, 1973.
- [5-6] W.P.A. van Lammeren, J.D. van Manen and M.W.C. Oosterveld; "The Wageningen B-Screw Series": Trans. Society of Naval Architects and Marine Engineers, Vol. 77, 1969.
- [5-7] P. van Oossanen; "A Method to Minimize the Occurrence of Cavitation on Propellers in a Wake": International Shipbuilding Progress, September 1971. Netherlands Ship Model Basin, publ.no.388.

REFERENCES OF APPENDIX

- [A-1] Wm.B. Morgan, V. Silovic and S.B. Denny; "Propeller Lifting Surface Corrections": Trans. Society of Naval Architects and Marine Engineers, Vol. 76, 1968.
- [A-2] K. Minnaas and O.H. Slattelid; "Lifting Surface Corrections for 3 Bladed Optimum Propellers": International Shipbuilding Progress, Vol. 18, No. 208, Dec. 1971, pp. 437-452.
- [A-3] R.A. Cumming, Wm.B. Morgan and R.J. Boswell; "Highly Skewed Propellers": Trans. Society of Naval Architects and Marine Engineers, Vol. 80, 1972.
- [A-4] H.M. Cheng; "Hydrodynamic Aspect of Propeller Design Based on Lifting Surface Theory: Part I-Uniform Chordwise Load Distribution": David Taylor Model Basin Report 1802, 1964 and "Hydrodynamic Aspect of Propeller Design Based on Lifting Surface Theory: Part II-Arbitrary Chordwise Load Distribution": David Taylor Model Basin Report 1803, 1965.
- [A-5] J.E. Kerwin and R. Leopold; "A Design Theory for Subcavitating Propellers", Trans. Society of Naval Architects and Marine Engineers, vol. 72, 1964, pp. 294-335.
- [A-6] G.G. Cox; Report of Propeller Committee to the 13th International Towing Tank Conference, Hamburg and Berlin, 1972.
- [A-7] M.A. Efroymsen; "Multiple Regression Analysis": Numerical Methods, Vol. I, edited by Ralston and Wilf, Wiley 1959.

NOMENCLATURE

UPPER CASE LETTERS

$A_1, A_2$	constants in least squares method for determination of effective camber distribution in non-uniform flow
$A_E$	expanded area of propeller blades
$A_N$	Fourier coefficient in expansion of conformal transformation parameters $\psi$ and $\epsilon$
$A_R$	Fourier coefficients in expansion of conformal transformation parameters $\psi$ and $\epsilon$
$A_O$	disc area of propeller
$B_1, B_2$	constants in least squares method for determination of effective camber distribution in non-uniform flow
$BTF_x$	blade thickness fraction based on maximum thickness of blade section
$C_1, C_2$	constants in least squares method for determination of effective camber distribution in non-uniform flow
$C_D$	drag coefficient, $C_D = D/\frac{1}{2}\rho U^2 c$
$C_{D_0}$	drag coefficient for $\sigma = 0$
$C_{D_3}$	three-dimensional part of $C_D$
$C_{D_{max}}$	maximum value of drag coefficient due to cavitation
$C_{D_{min}}$	minimum value of drag coefficient of blade section

$C_{D_\infty}$	value of drag coefficient in non-cavitating flow
$C_f$	skin-friction coefficient
$C_L$	three-dimensional value of lift coefficient, $C_L = L/\frac{1}{2}\rho U^2 c$
$C_{L_0}$	lift coefficient for $\sigma = 0$
$C_{L_2}$	two-dimensional value of lift coefficient
$C_{L_2P}$	two-dimensional value of lift coefficient in potential flow
$C_{LP}$	three-dimensional value of lift coefficient in potential flow
$C_{L_\infty}$	lift coefficient for non-cavitating flow
$C_p$	pressure coefficient, $C_p = 1 - (v/U)^2$
$C_{p_{x_c}}$	pressure coefficient on profile or blade section at $x_c$
$D$	drag force and propeller diameter
$D_x$	drag force at $x$
$G$	shape factor of boundary layer and non-dimensional value of circulation
$G_m$	Fourier coefficients in expansion for radial distribution of non-dimensional circulation
$H$	shape factor of boundary layer
$I, \bar{I}$	induction factor

$I_A$	axial induction factor
$I_n^A$	Fourier coefficients in expansion for radial distribution of axial induction factor
$I_n^T$	Fourier coefficients in expansion for radial distribution of tangential induction factor
$I_T$	tangential induction factor
$J$	advance ratio, $J = \bar{V}_A / nD$
$K$	ratio of value of Knapp's similarity parameter for decline to that for growth
$K_C$	lifting surface correction factor for camber
$K_S$	lift curve-slope factor for effect of viscosity
$K_T$	thrust coefficient, $K_T = T / \rho n^2 D^4$
$K_Q$	torque coefficient , $K_Q = Q / \rho n^2 D^5$
$K_t$	angle of attack lifting surface correction factor for thickness
$K_\alpha$	lifting surface correction factor for ideal angle of incidence
$K_{\alpha_0}$	zero-lift angle of attack factor for effect of viscosity
$L$	lift force



$L_e$	distance of leading edge to generator line
$L_x$	lift force at x
N	number of chordwise points at which effective camber is calculated
P	pitch of blade section and non-dimensional ordinate along pitch line from position of maximum thickness to leading and trailing edges for use in formula for coordinates of B-series propellers
$P_o$	effective atmospheric pressure
$P_v$	vapour pressure at prevailing temperature
Q	torque
$Q_x$	coordinate of radial distribution of torque at x
R	bubble radius and radius of propeller
$R_x$	resultant of lift and drag forces on blade section
$R_{x_s}$	Reynolds number based on free-stream velocity and coordinate $x_s$ along blade section surface
$R_{x_{ci}}$	Reynolds number based on free-stream velocity at the position of cavitation inception
$R_{x_{tr}}$	Reynolds number based on free-stream velocity and distance of position of point of transition from leading edge
$R_\theta$	Reynolds number based on momentum thickness of boundary layer

$R_{\theta ci}$	Reynolds number based on momentum thickness and local velocity at the position of cavitation inception
$R_{\theta tr}$	Reynolds number based on momentum thickness and local velocity at the position of transition
T	thrust
$T_x$	coordinate of radial distribution of thrust at x
U	undisturbed free-stream velocity
$\bar{U}$	induced velocity
$U_A$	axial induced velocity component
$U_s$	velocity induced by straight line vortex
$U_r$	tangential induced velocity component
$U_\infty$	undisturbed velocity
V	resultant velocity at blade section
$V_A$	average value of axial inflow velocity component along lifting line
$\bar{V}_A$	average value of axial inflow velocity component over propeller disc
$V_a$	local value of axial inflow velocity component
$\bar{V}_a$	average value of axial inflow velocity component along chord line of blade section
$V_r$	local value of radial inflow velocity component

$\bar{V}_r$	average value of radial inflow velocity component along chord line of blade section
$V_t$	local value of tangential inflow velocity component
$\bar{V}_t$	average value of tangential inflow velocity component along chord line of blade section
$V_1, V_2$	coefficients
$Z$	number of propeller blades

LOWER CASE LETTERS

$a$	conformal transformation parameter
$a_i$	power of $Z$ in polynomial for derivative of $C_D$ with respect to $\alpha$ for B-series propellers and power of $x$ in polynomials for lifting surface correction factors for high skews
$b_i$	power of expanded blade area ratio in polynomial for derivative of $C_D$ with respect to $\alpha$ for B-series propellers and power of $Z$ in polynomials for lifting surface correction factors for high skews
$c$	chord length of blade section
$c_i$	power of pitch-diameter ratio in polynomial for derivative of $C_D$ with respect to $\alpha$ for B-series propellers and power of $\theta_s$ in polynomials for lifting surface correction factors <sup>x</sup> for high skews
$d_i$	power of $\alpha$ in polynomial for derivative of $C_D$ with respect to $\alpha$ for B-series
$e_i$	power of $Z$ in polynomial for $C_L$ of B-series propellers

- $f$  maximum camber of blade section
- $f_i$  power of expanded blade area ratio in polynomial for  $C_L$  of B-series propellers
- $f_{g_k}$  ordinates of geometric camber distribution of blade section at  $k$  th position on chord
- $\Delta f_{g_k}$  change in geometric camber at  $k$  th position on chord due to curvature of undisturbed flow along chord
- $f_{g_{x_c}}$  ordinate of geometric camber distribution of blade section at  $x_c$
- $f_x$  position along chord of blade section where the camber is maximum
- $f_{x_c}$  ordinate of effective camber distribution of blade section at  $x_c$
- $\Delta f_{g_{x_c}}$  change in geometric camber at  $x_c$  due to curvature of undisturbed flow along chord
- $f_1$  function of  $x_c/c$  for determination of two-dimensional zero-lift angle of attack in potential flow
- $f_3$  function of  $x_c/c$  for determination of two-dimensional ideal angle of attack in potential flow
- $g$  acceleration due to gravity
- $g_i$  power of pitch-diameter ratio in polynomial for  $C_L$  of B-series propellers
- $h_i$  power of angle of attack in polynomial for  $C_L$  of B-series propellers

- $h_m^A$  part of expression for axial induced velocity which can be simplified by means of the Glauert integral
- $h_m^T$  part of expression for tangential induced velocity which can be simplified by means of the Glauert integral
- $\bar{i}$  unit vector along u-axis
- $\bar{j}$  unit vector along v-axis
- $\bar{k}$  unit vector along w-axis
- $k_i$  coefficients in polynomial for derivative of  $C_D$  with respect to  $\alpha$  for B-series propellers
- $k_{i_1}$  coefficients in equation for two-dimensional value of zero-lift angle of attack in potential flow
- $k_{i_3}$  coefficients in equation for two-dimensional value of ideal angle of incidence in potential flow
- $\bar{l}$  vector along lifting line
- $l_{hub}$  length along lifting line from origin to hub radius
- $l_{tip}$  length along lifting line from origin to propeller tip
- $m$  integer used in Fourier series expansion for radial distribution of non-dimensional circulation
- $n$  revolutions per second of propeller and integer used in Fourier series expansion for the radial distribution of the value of the induction factors
- $p$  conformal transformation parameter and integer defining location of points on profile shape in conformal mapping procedure

$\Delta p$	effective liquid tension causing growth or decline of cavity
$r, r_0$	radial coordinates
$r_h$	radius of propeller hub
$\bar{s}$	vector distance between vortex element of bound vortex line and point at which induced velocity is calculated
$s_i$	power of $Z$ in polynomials for lifting surface correction factors
$t$	integration parameter in Poisson's integral for the conjugate function occurring in conformal transformation procedure and time of growth or decline of cavity
$t_i$	power of tangent of local skew angle in polynomials for lifting surface correction factors
$t_{l.e.}, t_{t.e.}$	extrapolated blade section thickness at leading and trailing edges
$(t_{max})_x$	maximum thickness of blade section
$t_R$	ratio of given thickness ordinates of blade section to ordinates of elliptical thickness distribution
$t_s$	effective wake thickness of profile or propeller blade section
$u$	cartesian coordinate
$u_i$	power of expanded blade area ratio in polynomials for lifting surface correction factors
$v$	cartesian coordinate and local velocity on profile



$v_i$	power of induced advance ratio in polynomials for lifting surface correction factors
$v_{x_c}$	local velocity on blade section or profile at $x_c$
$w$	cartesian coordinate
$x$	non-dimensional radial coordinate, $x = r/R$
$x_c$	coordinate along chord of blade section
$x_{c_k}$	coordinate of $k$ th position along chord of blade section
$x_{c_1}$	position on profile or blade section at which $-C_p$ equals the cavitation index nearest to the leading edge
$x_{c_2}$	position on profile or blade section at which $-C_p$ equals the cavitation index furthest from the leading edge
$x_{c_3}$	position on profile or blade section at which cavity terminates
$x_E$	thrust eccentricity of propeller blade
$x_h$	non-dimensional radius of propeller hub, $x_h = r_h/R$
$x_s$	non-dimensional arc length along surface of blade section or profile
$y$	cartesian coordinate and ordinate of suction and pressure sides of profile or blade section
$y_e$	ordinate of elliptical blade section thickness distribution

$y_{\text{face}}, y_{\text{back}}$	vertical ordinate of point on blade section of B-series propellers on face and back with respect to pitch line
$y_g$	ordinate of given blade section thickness distribution
$y_{s_p}, y_{s_s}$	ordinate on pressure and suction side of profile or blade section at location of turbulent separation

GREEK SYMBOLS

$\alpha$	angle of attack
$\alpha_{\text{eff}}$	effective angle of attack in approximate three-dimensional pressure distribution calculation
$\bar{\alpha}_g$	average incidence of undisturbed flow over blade section with respect to nose-tail line
$\Delta\alpha_g$	variation in incidence angle along blade section with respect to average value $\bar{\alpha}_g$
$\alpha_{g_k}$	incidence of undisturbed flow at k th position along blade section with respect to nose-tail line
$\Delta\alpha_{g_k}$	variation in incidence angle along blade section at k th position with respect to average value
$\alpha_i$	three-dimensional value of ideal angle of attack
$\alpha_{i_2}$	two-dimensional value of ideal angle of attack
$\alpha_{i_2p}$	two-dimensional value of ideal angle of attack in potential flow
$\alpha_{\text{NT}}$	angle of attack with respect to nose-tail line of profile or blade section

$\alpha_0$	three-dimensional value of zero-lift angle of attack
$\alpha_0_2$	two-dimensional value of zero-lift angle of attack
$\alpha_0_2^p$	two-dimensional value of angle of zero-lift in potential flow
$\beta$	advance angle and conformal transformation parameter (equal to the two-dimensional value of angle of attack for zero-lift in potential flow)
$\beta_I$	hydrodynamic pitch angle
$\beta_k$	advance angle at k th position along chord of blade section
$\beta_\alpha$	corrected value of zero-lift angle of attack for effect of viscosity
$\Gamma$	circulation
$\gamma_0$	effective pitch angle of propeller blade section
$\gamma_{NT}$	angle between nose-tail line of blade section with respect to pitch line
$\delta^*$	displacement thickness of boundary layer
$\delta_{S_P}^*, \delta_{S_S}$	displacement thickness of boundary layer on pressure and suction side at the location of turbulent separation
$\epsilon$	conformal transformation parameter
$\epsilon_\alpha$	corrected value of $\epsilon$ for effect of viscosity
$\epsilon_{\alpha_{eff}}$	effective three-dimensional value of $\epsilon$ used in pressure distribution calculation

$\eta_0$	open-water efficiency, $\eta_0 = \frac{K_T \cdot J}{2\pi K_Q}$
$\theta$	momentum thickness of boundary layer and angular polar coordinate
$\theta_{inc}$	momentum thickness at location of cavitation inception
$\theta_k$	angular polar coordinate of k th position along blade section
$\theta_s$	skew angle at blade tip
$\theta_{s_x}$	skew angle at radius x
$\theta_x$	angular polar coordinate of lifting line at x
$\theta_0$	angular polar coordinate of radial vector to x on lifting line
$\lambda_i$	induced advance ratio
$\nu$	kinematic viscosity
$\pi$	pressure gradient parameter of boundary layer
$\rho$	fluid density
$\rho_l$	radius of curvature of leading edge of profile or blade section
$\rho_t$	radius of curvature of trailing edge of profile or blade section
$\sigma$	cavitation index based on resultant velocity for

propeller blade section and based on free-stream velocity for profile

- $\sigma_{crit}$  value of cavitation index for begin of lift or drag loss
- $\sigma_i$  value of cavitation index at cavitation inception
- $\sigma_N$  cavitation number based on rotational tip speed
- $\tau_w$  wall shear stress
- $\phi, \phi_0$  variable substituted for  $x$  and  $x$  in Fourier expansion for radial distribution of induction factors and non-dimensional circulation
- $\phi$  conformal transformation parameter
- $\psi$  conformal transformation parameter
- $\psi_l, \psi_t$  value of  $\psi$  at leading and trailing edge
- $\psi_0$  conformal transformation parameter

SUMMARY

In this thesis a method is developed for the calculation of the performance characteristics and of the extent and type of cavitation on propellers. The effects of viscosity and non-uniform inflow on these aspects are considered.

The Lerbs induction factor method forms the basis of the propeller theory presented in chapter 2. For the present purpose the inverse application of this method is required. Convergence is reached by means of introducing an extra iteration for the hydrodynamic pitch angle. The effect of non-uniform flow is considered by repeating the calculations at every required blade position. The average of the undisturbed inflow velocities over the blade sections is used to determine the advance angle at each blade position. The effect of the variation of the undisturbed inflow velocities over each blade section is accounted for by effectively distorting the geometric camber distribution. The effect of the bound vortices is included because of their non-zero contribution to the induced velocity in a non-uniform flow. The calculation of the pressure distribution on the blades at each blade position is carried out after further distorting blade section camber and by defining an effective angle of attack such that a three-dimensional approximation is obtained with a two-dimensional method.

For the correct prediction of propeller performance, particularly in off-design conditions, it is necessary to account for viscous effects on the lift and drag properties of propeller blade sections. This topic is considered in chapter 3. Viscous effects on the lift coefficient are accounted for by means of boundary layer theory. A correlation is obtained between the lift-curve slope and the effective thickness of the wake in the absence of laminar boundary layer separation. The effect of viscosity on the angle of zero-lift is found to be dependent on the relative wake thickness of suction and pressure sides. A calculation procedure for the drag coefficient is developed from the results of an "equivalent profile" analysis of the experimental characteristics of the Wageningen B-series propellers.



An analytical method for the assessment of cavitation characteristics of propellers is presented in chapter 4. A boundary layer analysis of the results of cavitation inception studies on profiles revealed that cavitation inception always occurs in the laminar-turbulent transition region of the boundary layer. A criterium for the extent of cavitation is derived by calculating the value of Knapp's dynamic similarity parameter for spherical cavities for growth and decline from the results of cavitation measurements on profiles. A study of measured pressure distributions at various angles of attack and values of the cavitation index leads to an approximate method for the calculation of the pressure distribution on a cavitating profile. With this result a general procedure for the change in lift and drag due to cavitation can be deduced.

In chapter 5 various results of calculations are presented which demonstrate the validity of the developed theory.

### SAMENVATTING

In dit proefschrift wordt een methode gegeven voor de berekening van de voortstuwingeigenschappen en van de omvang en het type van cavitatie op schepsschroeven. De invloeden van viscositeit en niet-uniforme aanstroming op deze aspecten worden in aanmerking genomen.

De inductiefactormethode van Lerbs vormt de basis van de schroeftheorie, die gegeven wordt in hoofdstuk 2. Voor het onderhavige doel is toepassing van deze methode in omgekeerde zin vereist. Convergentie werd verkregen door middel van het invoeren van een extra iteratie voor de hydrodynamische spoedhoek. De invloed van niet-uniforme aanstroming wordt in aanmerking genomen door herhaling van de berekeningen op iedere gewenste bladpositie tijdens een omwenteling. Het gemiddelde van de ongestoorde instroomsnelheden over de bladsecties wordt gebruikt om de snelheidsgraad op iedere bladpositie te bepalen. De invloed van de variatie van de ongestoorde instroomsnelheden over iedere bladsectie wordt in rekening gebracht door de geometrische welvingsverdeling te vervormen. De invloed van de gebonden wervels wordt meegerekend vanwege hun eindige bijdrage tot de geïnduceerde snelheid in een niet-uniforme stroming. De berekening van de drukverdeling op de bladen voor iedere bladstand tijdens een omwenteling wordt uitgevoerd na een verdere vervorming van de welving van de bladsecties en door het definiëren van een effectieve invalshoek zodanig dat een drie-dimensionale benadering wordt verkregen met een tweedimensionale methode.

Voor de juiste voorspelling van de voortstuwingeigenschappen van de schroef, speciaal onder omstandigheden die afwijken van het ontwerp, is het noodzakelijk de viskeuze invloeden op de lift- en weerstandseigenschappen van schroefbladsecties in rekening te brengen. Dit onderwerp wordt behandeld in hoofdstuk 3. Viskeuze invloeden op de liftcoëfficiënt worden in rekening gebracht door middel van grenslaagtheorie. Een relatie wordt verkregen tussen de helling van de liftkromme en de effectieve dikte van het zog zonder laminaire grenslaagloslating. De invloed van de viscositeit